Faculté des Sciences Appliquées
Université de Liège
Belgique

Numerical and experimental study of bluff body aerodynamics

Amandine Guissart

Thesis submitted in partial fulfillment of the requirements for the degree of
Doctor of Philosophy in Engineering Sciences

September, 2017

Faculté des Sciences Appliquées
Université de Liège
Belgique

Numerical and experimental study of bluff body aerodynamics

Amandine Guissart

Thesis submitted in partial fulfillment of the requirements for the degree of
Doctor of Philosophy in Engineering Sciences

September, 2017

Members of the examination committee

Prof. **B. Dewals** (Committee President)	University of Liège, Liège, Belgium
Prof. **V. E. Terrapon** (Advisor)	University of Liège, Liège, Belgium
Prof. **G. Dimitriadis** (Co-advisor)	University of Liège, Liège, Belgium
Prof. **X. Amandolèse**	École Polytechnique, Paris, France
Dr. Ir. **T. Andrianne**	University of Liège, Liège, Belgium
Prof. **L. P. Bernal**	University of Michigan, Ann Arbor, USA

Résumé

Cette thèse étudie la dynamique des écoulements autour de corps non-profilés et les charges aérodynamiques en résultant. Ces aspects sont primordiaux, entre autres dans le contexte de l'ingénierie du vent. Deux géometries sont considérées: un cylindre de section rectangulaire 4:1 et une plaque plane, soit immobile et à grande incidence, soit soumise à un mouvement de tangage d'amplitude élevée. Des expériences et des simulations sont réalisées, leurs résultats étant comparés à l'aide de la "Proper Orthogonal Decomposition" et la "Dynamic Mode Decomposition".

L'écoulement autour du cylindre de section rectangulaire 4:1 est étudié à l'aide de mesures de pression dynamique sur une section et de résultats provenant de simulations dites "Unsteady Reynolds-Averaged Navier Stokes" (URANS) et "Delayed-Detached Eddy Simulation" (DDES). Cette étude poursuit deux buts: i) enrichir les connaissances à propos de la physique de l'écoulement, des charges aérodynamiques qui en découlent et de leur variation avec l'incidence et la vitesse de l'écoulement amont, et ii) déterminer si les simulations URANS et DDES estiment avec précision les variations spatio-temporelles de l'écoulement ainsi que les charges aérodynamiques, et ce pour plusieurs incidences. On montre que l'écoulement est alternativement séparé et réattaché, et très sensible au nombre de Reynolds (Re). En particulier, la pente du coefficient de portance $\overline{c_l}_\alpha$ augmente rapidement dans la gamme $3.1 \times 10^4 \leqslant \mathrm{Re} \leqslant 7.6 \times 10^4$. On montre aussi que les simulations URANS et DDES n'estiment pas l'écoulement avec suffisamment de précision. La URANS permet de déterminer quantitativement l'évolution des tourbillons pour une incidence inférieure à l'angle de décrochage $\alpha = 4^\circ$, une valeur pouvant être estimée par la DDES uniquement.

Les écoulements autour de la plaque plane permettent de tester une technique de mesure indirecte des charges aérodynamiques à partir de champs de vitesse obtenus par vélocimétrie par images de particules (PIV). Cette technique est particulièrement adaptée à l'étude de phénomènes impliquant des corps en mouvement pour lesquels la réponse de la structure peut entacher les charges mesurées directement. Deux formulations basées sur un bilan de quantité de mouvement sont testées. La première utilise la forme intégrale des équations de Navier-Stokes et la seconde est basée sur la "flux equation" proposée par Noca et al. (1999). Cette seconde méthode est étendue au calcul indirect des moments qui n'était pas possible avec la formulation originale. Les effets des paramètres d'entrée nécessaires aux méthodes indirectes sur l'estimation des charges sont étudiés. De plus, des résultats numériques sont utilisés pour mieux comprendre les limitations des approches indirectes. On montre que ces approches fournissent des résultats similaires pour les écoulements détachés considérés. Les charges moyennées en temps sont estimées avec précision et celles moyennées en phase sont déterminées raisonnablement, pour autant que les champs PIV correspondant à chaque phase soient suffisamment convergés. Des effets tridimensionnels et une faible répétabilité des phénomènes impactent généralement négativement les résultats instationnaires. Les paramètres d'entrée les plus critiques sont identifiés et des recommandations guidant le choix de l'utilisateur sont proposées.

Cette thèse démontre qu'il est très utile de combiner des approches numériques et expérimentales, en particulier dans le cadre de l'ingénierie du vent, où l'aérodynamique des structures non profilées utilisées en génie civil est très difficile à étudier numériquement. Les deux approches sont complémentaires et permettent une meilleure compréhension de la physique du phénomène.

Abstract

This thesis investigates the dynamics of detached flows around bluff bodies and the resulting aerodynamic loads, which are of primary importance in wind engineering. Two canonical geometries are considered: a 4:1 rectangular cylinder and a flat plate that is either fixed at large incidence or undergoing a large pitching motion. The different studies are conducted through both experimental measurements and numerical simulations. Their results are compared by using Proper Orthogonal Decomposition and Dynamic Mode Decomposition.

The flow around the 4:1 rectangular cylinder is studied through dynamic pressure measurements along a cross-section combined with Unsteady Reynolds-Averaged Navier-Stokes (URANS) and Delayed-Detached Eddy Simulation (DDES) results. The main objectives are two-fold: i) to improve the general knowledge about the spatio-temporal flow features, the resulting aerodynamic loads, and their variations with the incidence angle and the freestream velocity, and ii) to assess the capabilities of URANS and DDES approaches to provide a sufficiently accurate estimation of the flow and aerodynamic loads at several incidences. It is shown that the rectangular cylinder involves complex separation-reattachment phenomena that are highly sensitive to the Reynolds number (Re). Consequently, the mean lift slope $\overline{c_l}_\alpha$ increases rapidly in the investigated range $3.1 \times 10^4 \leqslant \mathrm{Re} \leqslant 7.6 \times 10^4$. Additionally, it is shown that both URANS and DDES simulations fail to accurately approximate the flow at the different incidence angles considered. Only the URANS approach is able to qualitatively estimate the spatio-temporal variations of vortices for incidences below the stall angle $\alpha = 4^\circ$. Nonetheless, this stall angle is only captured by DDES.

The flows around a flat plate with different configurations are selected as test cases to assess an indirect load measurement technique that uses Particle Image Velocimetry (PIV) velocity fields. This technique is well suited to analyze phenomena involving moving bodies where direct load measurements could be contaminated by the structural response. The capabilities of two formulations based on the momentum balance are tested. The first method uses the integral form of the Navier-Stokes equation (INSE), and the second is based on the flux equation derived by Noca et al. (1999) (NOCA). This second method is extended to the indirect estimation of aerodynamic moments that is not provided by the original formulation. The user-defined parameters required by the INSE and NOCA methods are studied to evaluate their effects on the indirect estimation. Additionally, numerical results are used to better understand the limitations of the indirect approaches. It is shown that the INSE and the NOCA methods perform similarly for the detached flows considered. They are able to accurately estimate the mean loads, and the phase-averaged time responses are also estimated with a reasonable accuracy as long as the corresponding PIV phase-averaged fields are sufficiently converged. The unsteady results are generally negatively impacted by three-dimensional effects and the lack of a clear single shedding frequency. The user-defined parameters that have the most significant effects on the accuracy of the indirect load estimations are identified and guidelines for their setting are proposed.

Overall, this thesis demonstrates the added-value of integrating numerical and experimental studies, especially in the context of wind engineering where the aerodynamics of bluff civil engineering structures is very challenging to study numerically. The two approaches are complementary and enable a deeper understanding of the physics.

Acknowledgments

I wish to thank everyone who contributed to this project. In particular, I would like to thank my advisor Professor Vincent E. Terrapon for what I learned throughout this research work and my co-advisor Professor Greg Dimitriadis for his valuable insights and careful proofreading of this manuscript. I would also like to express my deep gratitude to Professor Luis P. Bernal for his guidance and enthusiastic encouragement during my research stay at the University of Michigan. Thomas Andrianne deserves my special thanks for his great help and advice regarding both scientific and non-scientific topics. I am particularly grateful to Professors Xavier Amandolèse, Luis P. Bernal, Benjamin Dewals and Doctor Thomas Andrianne who accepted to be members of the examination committee of this thesis. Their valuable advice help to improve the present manuscript. Finally, I would like to extend my thanks to my colleagues, friends and family for their kind support and encouragement who made this experience less stressful and more enjoyable.

Amandine Guissart
August 2017

Contents

CHAPTER 1

Context and motivation

This chapter explains the context and motivation of this thesis. It also exposes the different pursued objectives and presents the outline of this work.

1.1 Context

Fluid flows are ubiquitous in nature, everyday life and industrial problems. The study of fluid mechanics is thus necessary to understand physical phenomena but also to provide improvements in a large field of domains. For instance, the air flow within street canyons is studied to understand the dispersion of traffic induced pollution in cities (Leitl and Meroney, 1997). The creation of river meanders is investigated in order to better understand the river dynamics and provide help to safely decide the location of new bridges or homes (Edwards and Smith, 2002). The water waves forming a tsunami are studied to improve the monitoring of such events and help the governments better react to them (Stefanakis et al., 2011). The dynamic of blood flow is investigated to help doctors identify weak spots on a vessel that may lead to a failure (Messaris et al., 2016). Water-repelling properties of the lotus plant leaves or of some aquatic insects can provide new friction drag reduction strategies for numerous applications (Xu et al., 2014). Another example is the study of the wind flow around large football stadiums to assess the comfort of pedestrians on the circulation deck of the building and the surrounding streets and squares (Blocken and Persoon, 2009).

Aerodynamics is a particular topic of fluid mechanics. It is dedicated to the study of the fluid motion and particularly how the fluid interacts with moving objects. It aims to understand how the fluid motion along a body generates aerodynamic forces and moments. It has impacted considerably the development of aviation from the historical first flight of the Wrigth brothers (Anderson, 2010) to the new double-deck airliner Airbus A380 (Reckzeh, 2003). The importance of aerodynamics for such streamlined bodies is obvious as obtaining optimal aerodynamic properties is the main purpose of their design. Conversely, the architectural design of civil engineering buildings aims to satisfy structural requirements, aesthetic considerations, functional aspects or environmental sustainability goals. Therefore, the relevance of applying aerodynamic studies to such structures may not seem evident. Nonetheless, the consideration of wind induced loads is crucial, particularly for large structures or new construction methods. This is the purpose of wind engineering.

In the context of wind engineering, the air flow is often not able to follow smoothly the walls of the structures. Such flows are said to be detached and one of their features is the formation of large regions of rotating flow called vortices. Detached flows and vortices are characterized by their intrinsic unsteadiness and their turbulent behavior. Such flows induce aerodynamic excitations to the structure which might lead to undesirable phenomena. A first example is the alternate

(a) The Normandie bridge.

(b) The Burj Khalifa in Dubai.

(c) The Tacoma Narrows bridge.

Figure 1.1: Examples of civil engineering structures subjected to severe aerodynamic excitations.

excitations created by the vortex shedding behind a tall building. This may induce a large dynamic response and in turn result in small amplitude motions of the building called vortex induced vibrations. These motions may cause in the best case discomfort to the occupants and in the worst case structural problems (Irwin, 2008). A number of suspension bridges such as the Normandie bridge depicted in Fig. 1.1a have been reported to experience wind-induced vibrations of long suspenders nearby the towers. Because the suspenders represent the major connecting component for force transmission, their integrity directly impacts the integrity of the whole bridge structure (Li et al., 2017). Skyscrapers are also subject to vortex induced vibrations. As an example, the design of the Burj Khalifa, the tallest building in the world depicted in Fig. 1.1b, includes a variation of the cross section with the height. This helps to mitigate the coherence of the shed vortices along the entire height of the tower and thus prevent large resulting loads (Irwin, 2010). Another example of wind-induced phenomenon is the ice galloping of power lines. It is caused by the asymmetric modification of the cable section due to frozen water. The wind on the iced section causes a lift force that can lead to high amplitude oscillations of the power lines in the crosswind direction (Païdoussis et al., 2014). The power lines can then hit each other, damage themselves enough to cause a power outage, or even fall to the ground (Chan et al., 2009). Wind can also induce torsional flutter, the phenomenon that caused the famous failure of the Tacoma Narrows bridge in 1940 (Billah and Scanlan, 1991). Torsional flutter is characterized by a self induced aerodynamic excitation that leads to a large amplitude pitching motion, as depicted in Fig. 1.1c. All these examples involve a complex interplay between the structural and flow dynamics, and are thus part of the field of fluid-structure interaction and aeroelasticity. Because the occurrence of such phenomena is typically undesirable, studying the aerodynamic and aeroelastic behavior of civil engineering structures is critical.

The description of aerodynamic phenomena first relied on a combination of theoretical and experimental tools. Experiments have been used from the early history of aerodynamics to observe phenomena and verify hypothesis (Anderson, 1999). Nowadays, they enable qualitative and quantitative studies mainly conducted in wind tunnels. A wind tunnel, whose first design and operating is credited to Frank H. Wenham in 1871 (Anderson, 1999), is a facility that creates a flow in which a model of the body of interest is placed. Large bodies or structures can be tested since scaled models can be used, as long as the key parameters describing the problem are conserved. This is called scale-similarity. By using wind tunnels, the actual physics is represented and information can be collected about different variables (Barlow et al., 1999). The flow can be visualized by using smoke visualization (Bomphrey et al., 2009) and global flow parameters such as aerodynamic loads or shedding frequency can be measured through load balances or velocity probes (Barlow et al., 1999). Local information, such as velocity and pressure fields, can also be measured by using for instance Particle Image Velcometry (Raffel et al., 2013) and pressure sensors (Barlow et al., 1999), respectively. Therefore, wind tunnels and more generally experimental aerodynamics have been and are still now a cornerstone in fundamental research and industrial development. However, experiments have also some limitations such as the unavoidable measurement errors and the imperfect control of the conditions. Many flows depend on several key parameters and it is not always possible to achieve scale-similarity. In some cases, it is very difficult if not impossible to acquire data without disturbing the flow with the measuring equipment. In other cases, some quantities simply cannot be measured, or with only insufficient accuracy, even by state-of-the-art techniques. Finally, the use of experimental facilities are costly and time consuming. This is particularly true for the early development phases of industrial projects where many different configurations need to be considered.

Computational fluid dynamics, known as CFD, can nowadays be used as a complement to experiments. CFD consists in a set of methodologies to simulate the flow (Hirsch, 2007), i.e., to solve numerically the governing equations, which have most of the time no analytical solution. CFD was born in the end of the 60s. The rapid growth of computer power and affordability enabled it to evolve from an initial tool to a strategic factor in industrial developments. It overcomes many limitations of experiments. In particular, all parameters can be fully controlled and information about all variables is available everywhere. The use of CFD shortens the design process and, in some cases, eliminates the need for experimental testing. It also allows access to design solutions that were previously unreachable. For these reasons, CFD plays nowadays a major role in industrial R&D (Johnson et al., 2005). Nonetheless, despite its tremendous variation, CFD has not come close to replacing experiments in development of projects involving aerodynamic problems. Many complex phenomena remain very challenging to solve numerically, such as, for instance, turbulent detached flows. More generally, CFD simulations always impose a trade-off between fidelity and computational cost. Lower fidelity approaches are easily feasible in an industrial context, but their accuracy is limited. On the other hand, high-fidelity methods provide a very accurate solution, but their cost is prohibitive for most realistic applications.

Beyond their intrinsic differences, experimental measurements and numerical simulations are very complementary. Numerical results guide the design of experiments. Conversely, experiments are essential for the validation of numerical models. As such, leveraging the synergistic properties of both simulations and experiments in an integrated approach can provide an invaluable insight into the flow physics.

1.2 Motivation and objectives

The main concern of this thesis is the investigation of the dynamics of detached flows around bluff bodies, and of the resulting aerodynamic loads. The analysis leverages both experimental measurements and numerical simulations. In particular, this work focuses on two canonical geometries: a rectangular cylinder, and a flat plate that is either fixed at large incidence or undergoing a large pitching motion. Despite their geometrical simplicity, these cases involve rich and challenging flow physics that are representative of more complex configurations typically found in civil engineering applications.

The first aspect investigated in this work is the fundamental flow around a 4:1 rectangular cylinder. The cross-section of this cylinder is a rectangle whose width is four times longer than its height. This very basic geometry approximates several elongated civil engineering buildings such as bridges and towers. Despite the simple two-dimensional body shape, the subsequent flow is three-dimensional. Moreover, unsteady flow separation and reattachment occur along the upper and lower surface of the rectangular cylinder. The flow can also be sensitive to the velocity and turbulent intensity of the incoming flow. All this makes the flow around a rectangular cylinder highly complex. This case is studied both experimentally and numerically. As CFD simulations, and in particular those based on the Reynolds-averaged Navier-Stokes equations, are largely used in industrial applications, it is important to determine if these techniques are able to provide a sufficiently accurate estimation of such detached flows (Huang et al., 2007; Patruno, 2015). A comparison of computational and experimental global and local results is therefore required. The integration of numerical and experimental approaches is an important but difficult step, particularly in the case of local quantities related to unsteady flows. This comparison is made through two decomposition methods: the Proper Orthogonal Decomposition and the Dynamic Mode Decomposition.

In the context of civil engineering, the study of the dynamic interaction between the flow and the structure requires the determination of the aerodynamic loads. Numerically, this type of study remains very challenging (Löhner et al., 2015) and therefore experimental studies are often more appropriate. However, the direct measurement of loads with force balance can become challenging when the body is moving. In such cases the load sensor is also moving, which might impact the measurements. Moreover, the load sensor cannot differentiate the aerodynamic from the structural loads, which are not negligible in wind tunnel experiments. For phenomena involving structural motion, another possible approach is to determine the loads directly from the flow field. This can be done by using the pressure field measured through pressure sensitive paint, Pitot tube wake rakes or pressure taps (Barlow et al., 1999). An interesting alternative to these methods is to use the velocity field to indirectly calculate the aerodynamic loads. This motivates the second field of investigation of this thesis, which is mostly experimental and aims to study the indirect estimation of loads from the velocity field. Practically, the velocity field can be measured through Particle Image Velocimetry (PIV), from which the loads can be indirectly computed by using a momentum balance. In particular, this thesis compares the capabilities of two formulations: i) a formulation based on the integral Navier-Stokes equations and ii) a formulation derived by Noca et al. (1999) called the flux equation. The accuracy and efficiency of these formulations are tested in the context of detached flows. To this end, they are applied to the flow around a 16:1 plate that is either fixed at large incidence or undergoing a forced large pitching motion.

To summarize, the research presented in this thesis is conducted in the context of detached flows. It is based both on experimental and numerical techniques and its main objectives are:

- To improve the general knowledge of the flow around a 4:1 rectangular cylinder and, in particular, the effect of the rectangle incidence and freestream velocity on the variation of the flow topology and the aerodynamic loads.
- To assess the capability of two CFD techniques to provide a sufficiently accurate estimation of the flow around a 4:1 rectangular cylinder at incidence and the subsequent aerodynamic loads. In particular, the two CFD approaches chosen are the Unsteady Reynolds-Averaged Navier-Stokes simulation (URANS) and the Delayed-Detached Eddy simulation (DDES).
- To evaluate the accuracy of two methods based respectively on the integral Navier-Stokes equations and the flux equation proposed by Noca et al. (1999) to indirectly estimate the aerodynamic loads on a flat plate from the velocity fields acquired by PIV.
- To extend the methodology based on the flux equation proposed by Noca et al. (1999) to the indirect estimation of the aerodynamic moments.

- To provide guidelines for efficiently applying the indirect load measurements based on PIV data.

1.3 Outline

This thesis is composed of five chapters, including the present introduction. Chapter 2 is dedicated to the presentation of the theoretical background and the fundamental tools used throughout this work. First, some basics of the physics occurring in detached flows are presented. Then, the different CFD techniques used in this thesis are detailed by explaining how the different approaches represent turbulence. The PIV methodology is then described as it is used to measure the flow velocity field required to indirectly estimate the aerodynamic loads. This is followed by the presentation of the key equations underlying the indirect force calculation. In this context, an extension of the method proposed by Noca et al. (1999) is also derived. Finally, the Proper Orthogonal Decomposition (POD) and the Dynamic Mode Decomposition (DMD) are presented as two possible techniques enabling the comparison of numerical and experimental data.

Chapter 3 focuses on the analysis of the flow around the 4:1 rectangular cylinder. In particular, the effects of a variation of incidence are investigated and the capabilities of URANS and DDES simulations to estimate this effect are studied. Chapter 3 starts by reviewing the main results of previous research conducted on the flow around a rectangular cylinder. The setups of the performed measurements and simulations are then described and the main flow features are presented. The aerodynamic load and pressure coefficients obtained numerically are then compared to experimental results by using statistics together with decomposition methods. This enables to determine the accuracy of the numerical estimations. Finally, the impact of a variation of the freestream velocity is investigated experimentally. In particular, Chap. 3 aims to answer the following key questions:

- How does a variation of incidence impact the flow?
- How does a variation of the freestream velocity impact the flow?
- How does the flow evolve within a shedding cycle?
- Do URANS and DDES simulations provide a sufficiently accurate estimation of the flow?
- Are URANS and DDES able to accurately determine the effect of a modification of incidence?
- Do DDES simulations enable a better estimation of the flow than URANS?

Chapter 4 discusses the capability of two indirect approaches to calculate the loads from the velocity fields obtained through PIV. In particular, the method based on the integral Navier-Stokes equations is tested together with an approach based on the flux equation proposed by Noca et al. (1999). Experimental data are obtained in a water channel for both a plate undergoing a large amplitude imposed pitching motion and a static plate at high angle of attack. These two flows are used as test cases to apply the indirect calculation of loads. Chapter 4 begins therefore with the description of the experimental measurements and an overview of the flow dynamics involved in the test cases. Then, the effect of the user-defined parameters required for the two indirect methodologies are investigated. Finally, the capabilities of these methods to provide an accurate estimation of the loads are compared and discussed by integrating direct measurements and numerical results. In particular, the goal of Chap. 4 is to answer the following key questions:

- How accurate are the indirect computations of loads compared to direct measurements?
- Does one of the two methodologies tested perform better?
- How do the setup of the PIV experiment and the user-defined parameters impact the accuracy of the results?
- How do the flow features impact the accuracy of the results?
- How should the user-defined parameters be chosen?

Chapter 5 concludes this thesis. It provides a summary of each chapter and highlights the main original contributions of this thesis. Finally, some directions for future work are proposed.

CHAPTER 2

Theoretical background and fundamental tools

This chapter introduces the theoretical concepts and tools needed in the context of this thesis. It is divided into four main parts. First, the physics associated with the flows studied is described and the basic concepts used throughout this work are exposed. Then, the different models chosen to perform numerical simulations are detailed. Subsequently, the basic idea behind PIV *is explained and two methodologies chosen to indirectly calculate aerodynamic loads are described. Finally, the last part of this chapter is dedicated to the description of the decomposition methods selected to analyze and compare the spatio-temporal data obtained numerically or experimentally.*

2.1 Fundamental principles of the flow physics

The basic equations describing the physics of flows are known since the second part of the 19th century. The conservation of mass, momentum and energy leads to a complicated system of non-linear partial differential equations that, for most cases, has no analytical solution. For some applications, several simplifications can be introduced and the complexity of the fluid motion equations can be reduced.

The Mach number is a dimensionless quantity defined as the ratio of the flow velocity to the local speed of sound. For a freestream flow of velocity U_∞, the freestream Mach number reads

$$\mathrm{M}_\infty = \frac{U_\infty}{a_\infty}. \tag{2.1}$$

The term a_∞ is the speed of sound defined as $a_\infty = \sqrt{\gamma R T_\infty}$, where γ is the specific heat ratio of a gas, R is the specific gas constant and T_∞ is the temperature of the freestream. The value taken by this Mach number indicates the local flow regime. Depending on the value of M, the flow can be subsonic if $\mathrm{M} < 1$, sonic if $\mathrm{M} = 1$ or supersonic if $\mathrm{M} > 1$. Moreover, the value of the Mach number is related to the importance of the compressibility effects. In particular, for subsonic flows with $\mathrm{M}_\infty < 0.3$, these effects can be neglected and the aerodynamic problem can be modeled as being incompressible. The fluid density ρ can then be considered as a constant without any loss of accuracy (Anderson, 2010). The cases considered in the present work can be considered as incompressible. Moreover, heat transfer phenomena can be neglected, so that the fluid remains isothermal. This simplification leads to the decoupling of the energy equation from the mass and momentum equations.

Therefore, the equations governing the flows considered in this work are the incompressible Navier-Stokes equations. For a Newtonian fluid, the viscous shear stress τ_{ij} reads

$$\tau_{ij} = \mu \left(\partial_i u_j + \partial_j u_i \right), \tag{2.2}$$

where u_i is the i-component of the velocity vector **u** and μ the dynamic viscosity. In that context, the Navier-Stokes equations are written in a Cartesian coordinate system as

$$\begin{aligned} \partial_i u_i &= 0, \\ \rho \partial_t u_i + \rho u_j \partial_j u_i &= -\partial_i p + \mu \partial_{jj}^2 u_i, \end{aligned} \tag{2.3}$$

where p is the pressure.

A body immersed in an airflow is subject to aerodynamic forces and moments due to the pressure and shear stress distributions over its surface. In particular, the wall shear stress is defined as

$$\tau_w = \mu \partial_y u_x |_{y=0}, \tag{2.4}$$

where y is the distance perpendicular to the wall. The integration of p and τ_w over the complete body surface results in a three-dimensional aerodynamic force **F** and moment **M**, the latter being defined with respect to a given point. As depicted in Fig. 2.1, **F** can be split into components according to the wind axes defined by the freestream velocity U_∞. Therefore, by definition, the component of **F** perpendicular to U_∞ is called the lift L while the component parallel to U_∞ is called the drag D. The resultant moment **M** can also be separated into different components according to the wind axes. In particular, the component about the z-axis is called the pitching moment M_z. By convention, M_z is considered to be positive when it acts to pitch the airfoil in the nose-up direction. When the flow is two-dimensional, the forces and moment are denoted by l, d and m_z. Dimensionless force and moment coefficients can be defined from L, D and M_z. For three-dimensional flows the lift, drag and pitching moment coefficients are

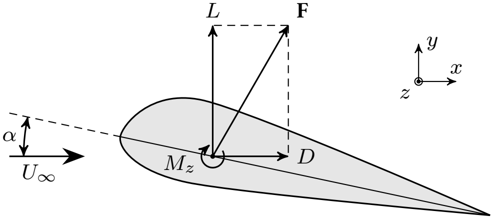

Figure 2.1: Resultant aerodynamic force and definition of lift and drag. Adapted from Anderson (2010).

$$c_L = \frac{L}{1/2 \rho U_\infty^2 S}, \quad c_D = \frac{D}{1/2 \rho U_\infty^2 S}, \quad \text{and} \quad c_M = \frac{M_z}{1/2 \rho U_\infty^2 S l_c}, \tag{2.5}$$

where S is a reference surface area and l_c is a characteristic length. For two-dimensional cases, the aerodynamic coefficients are

$$c_l = \frac{l}{1/2 \rho U_\infty^2 l_c}, \quad c_d = \frac{d}{1/2 \rho U_\infty^2 l_c}, \quad \text{and} \quad c_m = \frac{m_z}{1/2 \rho U_\infty^2 l_c^2}. \tag{2.6}$$

The flows investigated in this thesis are characterized by moderate values of the freestream Reynolds number Re_∞ with typical values belonging to the interval $[20\,000, 80\,000]$, where

$$\mathrm{Re}_\infty = \frac{U_\infty l_c}{\nu}, \tag{2.7}$$

with $\nu = \mu/\rho$ the kinematic viscosity. The Reynolds number represents the ratio of inertia to viscous forces (Anderson, 2010). For high Reynolds numbers, the flow can be divided into different regions (Prandtl, 1905). More specifically, a dimensional analysis of the Navier-Stokes equations shows that the viscous effects can be neglected in most of the flow away from the body. However, they are not negligible near the body surface. In particular, the relative flow velocity at a solid surface is zero. Going far away from the body, the flow accelerates until the velocity reaches the freestream velocity. Therefore, there is a thin region adjacent to the wall where the velocity gradients are large. In this region of height δ and called boundary layer, the flow viscosity cannot be neglected. The viscous effects are responsible for the profile drag, whose two contributions are i) the pressure drag resulting from a non-zero integrated pressure distribution, and ii) the friction drag due to the friction at the wall. Figure 2.2 summarizes schematically these two regions and the concept of boundary layer.

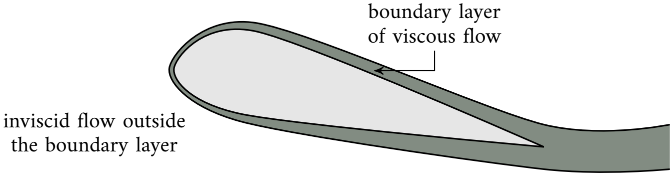

Figure 2.2: Schematic view of the division of a flow into an inviscid region away from the body and a thin viscous boundary layer. Adapted from Anderson (2010).

As depicted on the lower surface of the airfoil in Fig. 2.3, a boundary layer can develop smoothly along the body surface, the streamlines following the body curvature. In this case, the flow and the boundary layer are said to be attached. However, under a strong adverse pressure gradient, the flow near the surface can reverse its direction and move upstream. Because of this reversed-flow phenomenon, the boundary layer separates from the body surface. The flow is then detached and a large region of recirculating flow is created downstream of the separation point. The upper surface of the airfoil in Fig. 2.3 illustrates schematically this phenomenon. Because separation causes a decrease in pressure over the rear part of the body, it induces a large imbalance in pressure. Detached flows are thus associated with large pressure drag. The relative importance of pressure and friction drag to the total profile drag depends on the body shape and orientation with respect to the flow. Figure 2.4 illustrates how these two contributions compare for different body shapes.

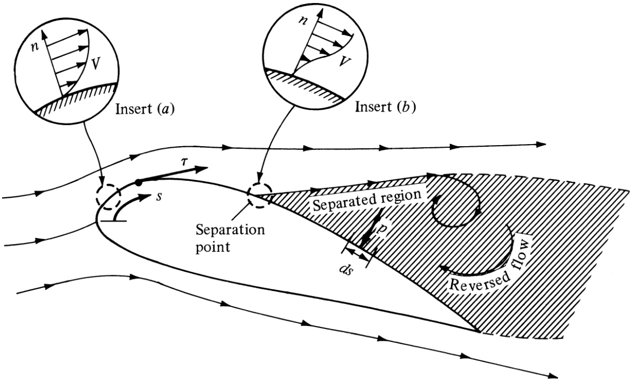

Figure 2.3: Schematical view of attached and detached flows. Reproduced from Anderson (2010).

This relative contribution between friction and pressure drag leads also to the definition of two generic body shapes: i) a streamlined body for which the profile drag stems mostly from friction drag, and ii) a bluff body for which the pressure drag dominates. As an example, in Fig. 2.3, all the profiles but the airfoil correspond to bluff bodies.

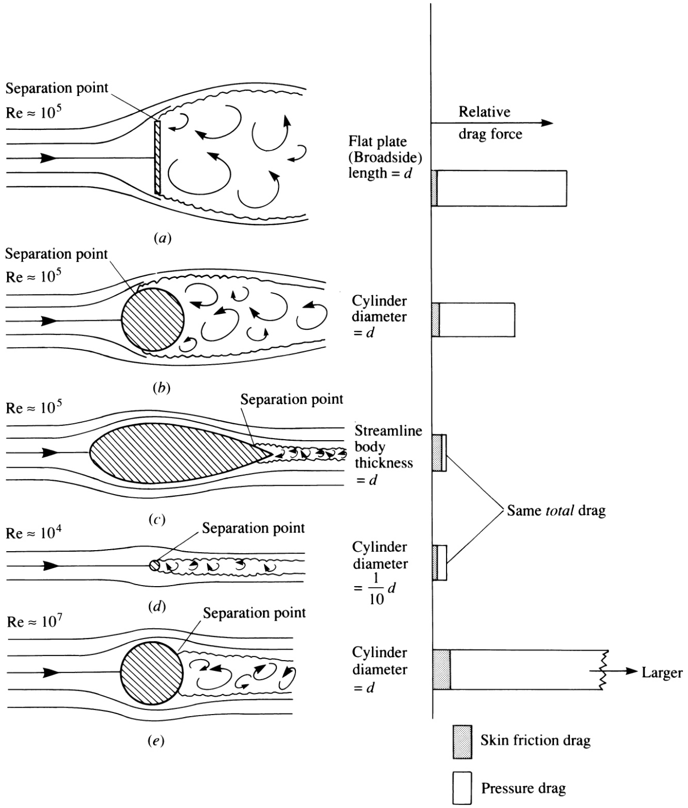

Figure 2.4: Relative comparison between friction and pressure drag for various aerodynamic shapes. Reproduced from Anderson (2010).

Detached flows typically exhibit a certain regularity. In particular vortices are often shed at a regular frequency f. In the context of oscillating flow problems, one can define a dimensionless frequency named after Strouhal (1878), the Strouhal number

$$\mathrm{St} = \frac{f l_c}{U_\infty}, \tag{2.8}$$

represents the ratio of the characteristic length l to the distance $^{U_\infty}/_f$. This distance corresponds to the length covered during a time $^1/_f$ by a fluid particle at velocity U_∞. Because $^1/_f$ corresponds to the period of the shedding phenomenon, the Strouhal number provides an estimation of the distance between two consecutive vortices shed from the same side of the body.

Viscous flows can be separated into two regimes: laminar and turbulent flows. These regimes are illustrated in Fig. 2.5 and defined according to the flow response to a small disturbance. Since the relative importance of the viscous term is inversely proportional to the Reynolds number, the stability of a flow to a perturbation depends on Re (Moran, 2003). At low Reynolds numbers, the disturbances are damped. The flow remains stable, smooth and regular: this is the laminar regime. For Reynolds numbers higher than a critical value, any small disturbance in the flow is amplified and creates new disturbances. This leads to a transition to turbulence, i.e., a complex irregular flow with a large range of scales. Turbulent flows are chaotic, and thus not predictable

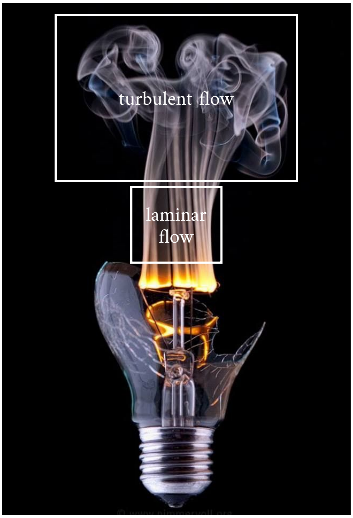

Figure 2.5: Artistic illustration of laminar and turbulent flows (Nimmervoll, 2013).

in detail, although they are governed by the deterministic Navier-Stokes equations (2.3). All these characteristics originate in the non-linear convective term. Because of the stochastic nature of turbulent flows, a statistical description is required. In particular, first and higher order statistics are typically analyzed.

Turbulent flows contain a large range of scales across which the turbulent kinetic energy k is distributed. The turbulent kinetic energy per unit mass is expressed as

$$k = \frac{1}{2}\overline{u_i' u_i'}. \tag{2.9}$$

where u_i' is a velocity fluctuation and $\bar{\cdot}$ represents the average of a stochastic quantity. Richardson (1922) introduced the concept of energy cascade in which this energy is transferred from the large scales to smaller ones through instabilities. More precisely, the mean shear generates large eddies associated with large kinetic energy. This phenomenon is thus responsible for the production of turbulent kinetic energy. The large eddies are controlled by the external geometry and are relatively insensitive to viscous effects. Because they are unstable, they break up into smaller ones. Through this mechanism, the turbulent kinetic energy is transferred to smaller and smaller scales. Sufficiently small eddies are stable and do not break up (Pope, 2000). These eddies are associated with the smallest scales called Kolmogorov scales (Kolmogorov, 1941). Although viscous effects do not impact large and intermediate scales, they are important for the smallest ones. In particular, the turbulent kinetic energy is dissipated by viscous action taking place at the smallest scales (Pope, 2000). The intermediate range of scales where the energy is transferred without being produced nor dissipated is called the inertial subrange. Kolmogorov (1941) demonstrated that at sufficiently high Reynolds number, the energy of the eddies increases with their size to the $^2\!/_3$ power in the inertial subrange. In the spectral space, the $^2\!/_3$ law becomes a $-^5\!/_3$ law which is known as Kolmogorov $-^5\!/_3$ spectrum (Durbin and Pettersson Reif, 2011). It is represented in Fig. 2.6 which depicts the distribution of the energy spectrum $E(\kappa)$. In this figure, κ is the wave number defined as $\kappa = {}^{2\pi}\!/_{l_e}$, where l_e is the eddy size. Moreover, η and u_η are the length scale and the velocity associated with the smallest eddies, i.e. the Kolmogorov scale. The ranges of scales corresponding to production and dissipation of kinetic energy are also represented, as well as the intermediate range.

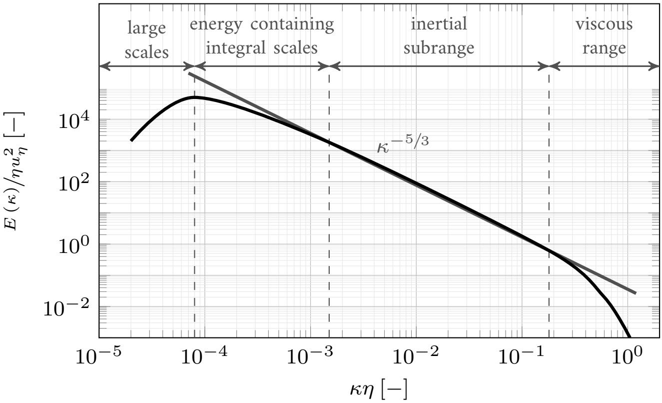

Figure 2.6: Turbulent energy spectrum as a function of the wave number κ non-dimensionalized by the Kolmogorov length and velocity scale, η and u_η. Adapted from Pope (2000).

The complex stochastic motion in a turbulent flow impacts significantly the behavior of the boundary layer. The velocity profile in a laminar and a turbulent boundary layer are depicted in Fig. 2.7 for illustration. The turbulent fluctuations increase the rate of mixing of momentum near the body surface. Therefore, higher-momentum fluid elements from the outer regions of the flow are transported closer to the wall. Compared to the laminar case, the average flow velocity near the surface is then larger for a turbulent boundary layer. It follows that the velocity gradient at the surface is much larger. Consequently, the wall shear stress τ_w and the friction drag are also larger. Because of the stronger mixing by turbulent fluctuations, turbulent boundary layers are also thicker, grow faster and are less sensitive to adverse pressure gradients than laminar ones. Therefore, a turbulent flow is less likely to separate from the body surface (Anderson, 2010).

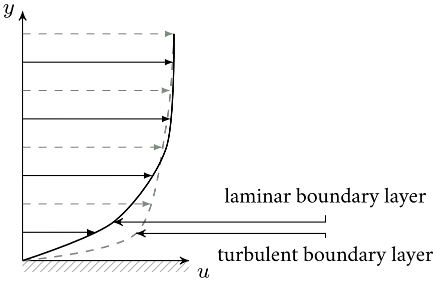

Figure 2.7: Schematic view of velocity profiles for laminar and turbulent boundary layers. Adapted from Anderson (2010).

The structure of a turbulent boundary layer can be described by introducing the concept of wall units. Wall units are non dimensional variables defined using the so-called viscous scales. In particular, the friction veloctiy is defined as

$$u^* = \sqrt{\frac{\tau_w}{\rho}}, \tag{2.10}$$

where τ_w is the wall shear stress defined in Eq. 2.4. The wall units y^+ and $\overline{u}^+$ are then obtained as

$$y^+ = \frac{u^* y}{\nu} \quad \text{and} \quad \overline{u}^+ = \frac{\overline{u}_x}{u^*}, \tag{2.11}$$

where $\overline{u}_x$ is the mean of u_x, the velocity in the direction parallel to the wall. Expressed in terms of wall units, the structure of a turbulent boundary layer is depicted schematically in Fig. 2.8. It is composed of two main overlapping regions: the inner layer or law-of-the-wall region, and the outer layer or law-of-the-wake region. The inner layer is adjacent to the wall and consists of three sub-regions. From the wall to the law-of-the-wall region, the inner layer is composed of: i) the viscous sublayer, ii) the buffer layer and iii) the log-law region extending from $y^+ \approx 40$ to $y < 0.2\delta$. Note that the log-law region also belongs to the outer layer and its size varies with the Reynolds number (Pope, 2000). The mean velocity profile inside the inner layer is fully determined by viscous scales. In other words, the mean velocity profile non-dimensionalized with inner units is universal, independent of the geometry, pressure gradient, or Reynolds number. Conversely, the direct effect of viscosity is negligible in the outer layer (Pope, 2000; Durbin and Pettersson Reif, 2011). As the log-law region overlaps both the law-of-the-wall and law-of-the-wake regions, it shares properties of both, meaning that the mean velocity profile is independent of the outer flow and not impacted by viscosity. From those considerations, the velocity profile in the log-law region can be determined as

$$\overline{u}^+ = \frac{1}{\kappa} \ln y^+ + B, \tag{2.12}$$

where the value of the von Karman constant $\kappa \approx 0.41$ and of $B \approx 5.1$ are obtained from experimental measurements.

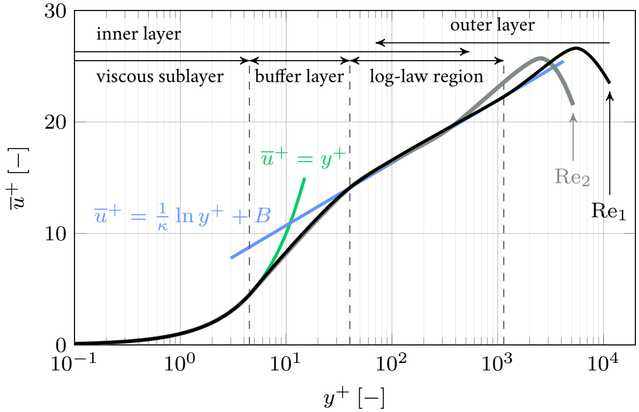

Figure 2.8: Mean velocity profile in a turbulent boundary layer for two different Reynolds numbers (Re$_1$ > Re$_2$). The location of the different regions are also indicated for Re$_1$. Adapted from Pope (2000).

These characteristics of turbulent flows and the structure of turbulent boundary layers have a major impact on the simulation approaches, as described below.

2.2 Modeling turbulence in numerical simulations

Computational fluid dynamics (CFD) is the set of numerical methodologies that can be used to solve numerically the Navier-Stokes equations, or more generally to simulate fluid flows. This section briefly describes the different components of the CFD simulations. It also presents the theoretical background of turbulence modeling in CFD. More information about these topics can be found for instance in the work of Hirsch (2007) and Durbin and Pettersson Reif (2011).

For laminar flows, the computing power available nowadays allows generally to solve the Navier-Stokes equations (2.3) without difficulties. However, most of the flows occurring in nature and industrial applications are turbulent. As such, they contain a large range of time and length scales. Direct Numerical Simulation (DNS) of turbulent flows aims to compute the turbulent statistical fluctuations at all the relevant physical scales. The computational cost of this type of simulations increases dramatically with the Reynolds number to scale approximately as Re^3. Therefore, DNS requires large computational capacities which are out of reach for most applications with the exception of fundamental research on the mechanisms of turbulence in canonical configurations and at moderate Reynolds numbers. Consequently, the Navier-Stokes equations (2.3) cannot be solved usually directly, and other strategies must be followed.

Several levels of approximation exist. By descending degree of fidelity, the main ones are the Large Eddy Simulation (LES), the Detached Eddy Simulation (DES) and the Unsteady Reynolds-averaged Navier-Stokes Simulation (URANS). The idea of LES emerges from the observation that most of the computational cost is dedicated to resolving the smallest scales. As explained in Sec. 2.1, these small scales have, to some extent, a universal character and their role is to dissipate energy. On the contrary, the largest scales are affected by the flow geometry and consequently are not universal. Therefore, in the context of LES, the computational cost is reduced by resolving only these large scales. A dissipative model is added to mimic the impact of the smallest scales (Pope, 2000; Durbin and Pettersson Reif, 2011). Figure 2.9 illustrates which regions of the energy spectrum are resolved and which are modeled in LES. In URANS, the goal is to solve only for mean quantities. The simplification approach is thus much more severe since the complete turbulence spectrum is modeled, as illustrated in Fig. 2.9. Moreover, URANS simulations can be two-dimensional while the techniques permitting turbulent eddying must be three-dimensional. The possibility to use coarse two-dimensional grids allows to drastically reduce the computational cost. URANS is based on the Navier-Stokes equations (2.3) that have been averaged. This averaging process leads however to unclosed terms due to the non-linearity of the convective term. In particular, the so-called Reynolds stress tensor cannot be directly related to the mean flow (Hirsch, 2007), and must therefore be modeled. Consequently, the accuracy of URANS results depends strongly on the ability of the closure model to capture the physics of interest. Finally, DES is an hybrid method combining LES away from walls and URANS close to them. The fine grid resolution needed by LES in a boundary layer is thus overcome. In this thesis, two turbulence modeling approaches are chosen: URANS and Delayed-Detached Eddy Simulation (DDES), the second approach being a variant of DES. Therefore, URANS and DDES techniques are further explained in the next subsections.

Once a mathematical model describing the flow is selected, the problem has to be solved numerically. The first step is to define a computational domain that approximates as well as possible the physical one. For the external flows considered in this work, the infinite space has to be modeled by appropriate boundary conditions. Those boundary conditions are imposed at the boundaries of the finite computational domain. Therefore, the size of this domain has to be determined carefully to minimize the impact of boundary conditions on the results. The continuous space is then divided into a number of discrete cells forming the mesh. The discretization of the physical domain has a major impact on the result accuracy. Therefore, the effect of the mesh coarseness has to be studied for each application. In this work both geometry and mesh are built using Gmsh (Geuzaine and Remacle, 2009).

The continuous equations describing the mathematical model have to be discretized. Implemented properly on a solver, their resolution leads to the sought numerical solution. This implementation requires the conversion of differential or integral equations into arithmetic operations on mesh-related unknowns. Different methods are available to perform this conversion. One can cite the finite difference method (FDM), the finite element method (FEM) or the finite volume method (FVM). More information about these methods can be found in the work of Hirsch (2007). The present work uses FVM and the simulations are performed with the open-source cell-centered code OpenFOAM (Weller et al., 1998). More precisely, the transient solver for incompressible flows `pimpleFoam` is selected. It is based on a combination of the PISO and SIMPLE algorithms (Ferziger

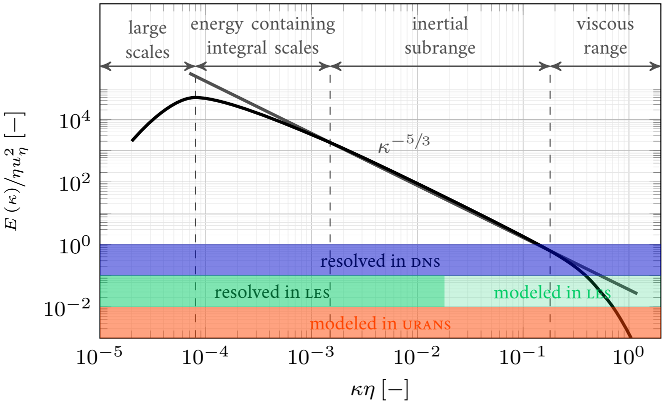

Figure 2.9: Definition of the modeled and resolved regions as a function of the non-dimensional wave number $\kappa\eta$ for URANS, LES and DNS with respect to the non-dimensional turbulent energy spectrum. Adapted from Pope (2000).

and Perić, 1996) and allows a large time-step.

The following subsections describe in details the two levels of approximation used in this thesis. Computational domain, grid related issues and chosen numerical schemes are discussed for each particular case in the following respective chapters.

2.2.1 Reynolds-Averaged Navier-Stokes Simulation

Using the Reynolds decomposition, a turbulent stochastic quantity **a** can be separated into

$$\mathbf{a} = \bar{\mathbf{a}} + \mathbf{a}', \tag{2.13}$$

where $\bar{\mathbf{a}}$ and $\mathbf{a}'$ represent the mean and the fluctuating part of **a**, respectively. Statistical results are of primary importance for engineering applications. The computation of **a** followed by the calculation of its mean requires to perform DNS to obtain **a** which is extremely costly. Therefore, the goal of the URANS approach is to compute directly the mean $\bar{\mathbf{a}}$. In practice, this mean can be approximated by an average over different realizations, over a long period of time of the same realization, or over homogeneous directions.

URANS simulations are based on the Navier-Stokes equations that are averaged over the whole spectrum of turbulence. The statistical procedure used to obtain those equations is called the Reynolds averaging (Reynolds, 1895). It consists in two steps: i) the introduction of the Reynolds decomposition (2.13) into the incompressible Navier-Stokes equations (2.3) and then ii) the averaging of the equation. The Reynolds averaging procedure leads to the URANS equations

$$\begin{aligned} \partial_i \overline{u}_i &= 0, \\ \rho\partial_t \overline{u}_i + \rho\overline{u}_j\partial_j\overline{u}_i &= -\partial_i\overline{p} + \mu\partial^2_{jj}\overline{u}_i - \partial_j\overline{u'_j u'_i}, \end{aligned} \tag{2.14}$$

where $\overline{u'_i u'_j}$ is the Reynolds stress. The Reynolds stress arises from the non-linear convective term in Eq. (2.3). Comparing Eq. (2.3) and Eq. (2.14), it can be concluded that the different behavior between laminar and mean turbulent flows is attributable to this Reynolds stress (Pope, 2000). Moreover, there is no intrinsic relation between the Reynolds stress and the mean flow quantities and the URANS equations (2.14) are thus unclosed. Solving Eq. (2.14) requires the introduction of a closure model providing a consitutive equation for the Reynolds stress. Numerous closure models have been developed based on theoretical considerations and empirical information. However, they remain a major source of errors because of their empirical nature and the approximations involved in their derivation.

Most common techniques used to close the URANS equations are based on the Boussinesq approximation (Boussinesq, 1877), also called the linear eddy viscosity hypothesis. By analogy with the viscous stress (2.2), it assumes that the deviatoric part of the Reynolds stress is proportional to the mean strain rate $\overline{S}_{ij} = {}^1\!/\!_2 \left(\partial_j \overline{u}_i + \partial_i \overline{u}_j\right)$. Therefore, under the Boussinesq approximation, the Reynolds stress reads

$$-\overline{u_i' u_j'} = 2\nu_T \overline{S}_{ij} - \frac{2}{3} k \delta_{ij}, \tag{2.15}$$

where the proportionality constant ν_T is called the turbulent or eddy viscosity. The turbulent kinetic energy k given in Eq. (2.9) corresponds to the trace of the Reynolds stress tensor. The turbulence models based on Eq. (2.15) are called eddy viscosity models (EVM).

For many flows the turbulent viscosity hypothesis (2.15) is not valid. Pope (2000) cites several examples such as strongly swirling flows (Weber et al., 1990), flows with significant streamline curvature (Bradshaw, 1973; Patel and Sotiropoulos, 1997) and fully developed flows in ducts of non-circular cross-section (Melling and Whitelaw, 1976; Bradshaw, 1987). In those cases, EVM models fail and higher fidelity closure models have to be used. One possibility is to rely on transport equations for the Reynolds stress directly instead of using the turbulent viscosity hypothesis. This aims to increase the physical content in the ensuing turbulence models that are called Reynolds stress transport (RST), Reynolds stress modeling (RSM), or second-moment closure (SMC). These transport equations are derived from the fluctuating velocity. They model the variation of the Reynolds stress in terms of production, dissipation, redistribution and turbulent transport (Durbin and Pettersson Reif, 2011). However, several of these terms are unclosed, which requires additional empirical closure models. Therefore, more equations have to be solved and the computational cost increases. Another possibility is to introduce approximations in the equations governing SMC models. The ensuing equations form an algebraic stress model (ASM). Such models are inherently less general and less accurate than SMC models but are relatively simple (Pope, 2000). Finally, additional non-linear terms can be introduced into the stress-strain relation (2.15). This makes the Reynolds stresses a more general function of the mean strain and vorticity. Moreover, this better reflects the highly non-linear aspect of turbulence. Turbulence models based on a non-linear turbulent viscosity hypothesis are called non-linear viscosity models (NLEVM). More information about SMC, ASM and NLEVM modeling approaches can be found for instance in the work of Pope (2000) and Durbin and Pettersson Reif (2011). The present work uses two different EVM turbulence models: the $k-\omega$ shear stress transport (SST) model and the Spalart-Allmaras (SA) model. Both are described in details in the following.

2.2.1.1 $k-\omega$ shear stress transport turbulence model

The $k-\omega$ shear stress transport model was introduced by Menter (1994). It is a two-equations model based on the Boussinesq approximation (2.15) that combines the $k-\varepsilon$ model proposed by Chien (1982) and the $k-\omega$ model developed by Wilcox (1993). The SST model aims to combine the respective advantages of the $k-\omega$ and $k-\varepsilon$ models, while overcoming their deficiencies. The two aforementioned models determine the turbulent viscosity ν_T as the product of a velocity $u^\star$ and a length $l^\star$. The velocity $u^\star$ is determined by using the turbulent kinetic energy k and the length $l^\star$ is based on the dissipation rate of kinetic energy ε or the specific dissipation rate $\omega = {}^\varepsilon\!/\!_k$. Both k and ε (or ω) are obtained by solving a corresponding transport equation. The $k-\varepsilon$ model is numerically robust. However, it has been shown that in some cases the ε-equation fails to determine the length $l^\star$ in the near wall region. In particular, Rodi and Scheuerer (1986) showed that the model fails for flows with an adverse pressure gradient. The $k-\varepsilon$ model is then unable to approximate properly the behavior of separated flows. Wilcox (1993) introduced an equation for the specific dissipation rate ω to predict the length $l^\star$. This equation replaces the $\varepsilon-$equation and the near wall behavior of the model is improved. Consequently, the $k-\omega$ model leads to a better prediction of flows with moderate adverse pressure gradients (Menter, 1993). However, this model suffers from a strong sensitivity to the freestream value of ω (Menter, 1992) and overpredicts the level of shear stress in adverse pressure-gradient boundary layers. Menter (1994) developed the SST model to overcome these problems. It is a combination of the $k-\omega$ and the $k-\varepsilon$ models. More precisely, the $k-\omega$ model is used near the walls while the $k-\varepsilon$ model is used elsewhere. Additionally, a shear-stress limiter and blending functions are introduced.

The model used in this thesis is based on the work of Menter and Esch (2001) with updated coefficients (Menter et al., 2003). The eddy viscosity reads

$$\nu_T = \frac{a_1 k}{\max\left(a_1\omega, \overline{S}F_2\right)}, \tag{2.16}$$

where a_1 is a coefficient of the model, $\overline{S} = \sqrt{2\overline{S}_{ij}\overline{S}_{ij}}$ is the invariant measure of the strain rate and F_2 is a blending function. The two transport equations in conservative form are

$$\begin{aligned} \partial_t\left(\rho k\right) + \partial_j\left(\rho\overline{u}_j k\right) &= \mathcal{P}^k - \mathcal{D}^k + \partial_j\left(\Gamma_k\partial_j k\right), \\ \partial_t\left(\rho\omega\right) + \partial_j\left(\rho\overline{u}_j\omega\right) &= \mathcal{P}^\omega - \mathcal{D}^\omega + \partial_j\left(\Gamma_\omega\partial_j\omega\right) + \frac{2\rho\sigma_{\omega 2}}{\omega}\left(1-F_1\right)\partial_j k\partial_j\omega. \end{aligned} \tag{2.17}$$

The blending function F_1, the production and destruction terms $\mathcal{P}$ and $\mathcal{D}$ associated with k and ω, the variables Γ_k and Γ_ω and the constant $\sigma_{\omega 2}$ are documented in the work of Menter and Esch (2001) and Menter et al. (2003).

Finally, boundary conditions are required for k and ω. For an external flow, the freestream value k_∞ is calculated from the freestream turbulence intensity I as $k_\infty = {}^3\!/_2\left(U_\infty I\right)^2$. The specific dissipation rate ω_∞ is calculated to verify $10^{-5} < {}^{\nu_T}\!/_{\nu} < 10^{-2}$, as proposed by Menter (1994). Two possibilities exist for the wall treatment: i) one can fully resolve the near-wall region above the viscous sublayer ($y^+ \approx 1$) or ii) one can resolve only the part above a point located in the log-layer ($y^+ \approx 100$) and assume a universal behavior below that point. The first possibility corresponds to wall-resolved URANS. In this case, the turbulent kinematic energy at the wall is zero by definition. Moreover, Wilcox (1993) established that the specific dissipation rate in the viscous sublayer reads

$$\omega_{vis} = \frac{6\nu}{0.075y^2}, \tag{2.18}$$

where, y corresponds to the distance between the wall and the first calculation point away from it. Therefore, for wall-resolved URANS, boundary conditions correspond to $k_w = 0$ and $\omega_w = \omega_{vis}$. The second possibility corresponds to the use of a wall function. It takes advantage of the structure of turbulent boundary layers under the approximation of large Reynolds number, as previously described and illustrated in Fig. 2.8. When a wall function is used, the first grid point adjacent to the wall is located in the log-law region, so that the turbulent properties can be estimated. In particular, the specific dissipation rate in the log-law region reads

$$\omega_{log} = \frac{u^*}{0.3\kappa y}. \tag{2.19}$$

The use of a wall function allows the use of much coarser grids since the inner layer is not resolved. However, a wall function introduces additional hypotheses and imposes strict limitations on the grid generation. Moreover, wall functions are not adequate for detached flows.

The present work investigates flows through wall-resolved URANS simulations. Therefore, the different grids are generated in such a way that the first calculation point away from a wall satisfies $y^+ \approx 1$. In practice, the simulations use an automatic near-wall treatment proposed by Menter and Esch (2001). In particular, this model determines ω_w by combining the values calculated from Eq. (2.18) and Eq. (2.19). To this end, it uses a blending function defined as

$$\omega_w = \sqrt{\omega_{vis}^2 + \omega_{log}^2}. \tag{2.20}$$

For low y values the term in ${}^1/_{y^2}$ dominates and therefore ω_w corresponds approximately to ω_{vis}. Conversely, for larger values of y, ${}^1/_y$ is dominant and ω_{log} is recovered.

2.2.1.2 Spalart-Allmaras turbulence model

Baldwin and Barth (1990) suggested to formulate a transport equation directly for the eddy viscosity ν_T. The goal is to replace the indirect calculation of ν_T from $u^\star$ and length $l^\star$. This aims to avoid numerical difficulties occurring with the $k - \varepsilon$ model and to improve fidelity. In this spirit, Spalart and Allmaras (1994) developed a model being by design computationally simple and numerically forgiving.

In the Spalart-Allmaras model (SA), the Boussinesq approximation is further simplified. In particular, the term $-\frac{2}{3}k\delta_{ij}$ in Eq. (2.15) is discarded because k is not readily available. Note that this does not introduce any error for incompressible flows, as this term is usually integrated into the pressure. Therefore, the Reynolds stress is expressed as

$$-\overline{u_i'u_j'} = 2\nu_T\overline{S}_{ij}. \tag{2.21}$$

The eddy viscosity is defined as

$$\nu_T = \tilde{\nu} f_{v1}, \tag{2.22}$$

where $\tilde{\nu}$ is an effective viscosity and f_{v1} is a non-linear function of ${}^{\tilde{\nu}}/_{\nu}$. The transport equation

$$\partial_t\tilde{\nu} + \overline{u}_j\partial_j\tilde{\nu} = \mathcal{P}^{\tilde{\nu}} - \mathcal{D}^{\tilde{\nu}} + \frac{1}{\sigma}\left[\partial_j\left(\left(\nu + \tilde{\nu}\right)\partial_j\tilde{\nu}\right)\right] \tag{2.23}$$

describes the variation of $\tilde{\nu}$. The function f_{v1}, the production term $\mathcal{P}^{\tilde{\nu}}$, the destruction term $\mathcal{D}^{\tilde{\nu}}$ and the value of the constant σ appearing in Eq. (2.23) are documented in the original work of Spalart and Allmaras (1994). Note that the transport equation (2.23) implemented in the OpenFOAM framework is slightly different from the one originally proposed. More precisely, it does not contain the trip term intended to model transition.

Finally, the model requires boundary conditions. At walls, the Reynolds stress and the eddy viscosity have to vanish. Consequently, $\tilde{\nu}_w$ is zero. The boundary conditions for the farfield must represent a fully turbulent behavior. As proposed by Spalart (2000) and Spalart and Rumsey (2007), $\tilde{\nu}_\infty$ is set to verify $3 < {}^{\tilde{\nu}_\infty}/_{\nu} < 5$. The corresponding ν_T can be then calculated from Eq. (2.22).

2.2.2 Delayed-Detached Eddy Simulation

In the context of turbulent flows, URANS simulations model all scales of turbulence. Therefore, if the model is not adapted to the computed physics, it can lead to inaccurate results. On the other hand, DNS requires very fine grids to capture all the turbulent scales, which is most of the time computationally too expensive. This section introduces different modeling techniques lying between DNS and URANS in terms of fidelity. In particular, LES, DES and DDES are described.

As explained before, LES aims to resolve the large eddies that contain the bulk of energy and are dependent on the flow geometry. The small dissipative scales and part of the inertial subrange are not resolved and need thus to be modeled. Practically, the Navier-Stokes equations (2.3) are filtered in space leading to

$$\begin{aligned} \partial_i\widehat{u}_i &= 0, \\ \rho\partial_t\widehat{u}_i + \rho\widehat{u}_j\partial_j\widehat{u}_i &= -\partial_i\widehat{p} + \mu\partial_{jj}^2\widehat{u}_i - \partial_j\tau_{ji}^{\text{SGS}}, \end{aligned} \tag{2.24}$$

where $\widehat{\cdot}$ represent the filtered variables being resolved. In Eq. (2.24), τ_{ij}^{SGS} is the unclosed sub-grid scale (SGS) stress. It is modeled by using semi-empirical laws that represent the effects of the unresolved eddies, and in particular the dissipation of energy. The SGS model developed by Smagorinsky (1963) is probably the most popular one. It is based on a linear eddy viscosity assumption that links the SGS stress to the filtered strain rate $\widehat{S}_{ij} = {}^1/_2\left(\partial_j\widehat{u}_i + \partial_i\widehat{u}_j\right)$. Mathematically, this reads

$$-\tau_{ij}^{\text{SGS}} = 2\nu_{\text{SGS}}\widehat{S}_{ij}, \tag{2.25}$$

where the eddy viscosity is modeled by

$$\nu_{\text{SGS}} = (C_S\Delta)^2\,\widehat{S}. \tag{2.26}$$

In Eq. (2.26), $\widehat{S} = \sqrt{2\widehat{S}_{ij}\widehat{S}_{ij}}$, C_S is the Smagorinsky coefficient and Δ is function of the grid spacing. Note that $C_S\Delta$ is a length scale called the Smagorinsky length scale.

For a free shear layer, LES requires a number of mesh points proportional to $\mathrm{Re}^{3/2}$ to accurately capture the smallest resolved scales. Taking into account the time integration, the number of floating-point operations required for LES is proportional to $\mathrm{Re}^{9/4}$ (Hirsch, 2007). It is significantly lower than DNS requirements but still high. On the other hand, for wall-bounded flows, the size of the scales that are responsible for the turbulence production is similar to the viscous length scale (Pope, 2000). Therefore, a DNS-like resolution is needed in the near-wall region so that a wall-resolved LES is still computationally too costly for high Re flows. In that case, a special wall treatment is needed to allow a coarser resolution near the wall.

In this context, Spalart et al. (1997) proposed a modeling technique called detached eddy simulation (DES). It combines an LES approach away from the walls and URANS close to them. In particular, Spalart et al. (1997) used SA as URANS model (Spalart and Allmaras, 1994). DES is based on EVM models and it consists in limiting the eddy viscosity away from the wall. If the eddy viscosity is kept low, natural instabilities are able to develop into turbulence (Durbin and Pettersson Reif, 2011). A length scale $\tilde{d}$ determines the shift from URANS to LES behavior. It is defined as

$$\tilde{d} = \min\left(\underbrace{d}_{\text{RANS mode}}, \underbrace{C_{DES}\Delta}_{\text{SGS mode}}\right), \tag{2.27}$$

where C_{DES} is an adjustable constant of order one. The term d is the distance to the wall appearing in the SA model (Spalart and Allmaras, 1994) and Δ is a measure of the mesh size. Typically, for cartesian grids, Δ is defined as the largest grid spacing in all the three directions of space or, mathematically, $\Delta = \max(\Delta x, \Delta y, \Delta z)$. Spalart et al. (1997) obtained then a hybrid technique that performs as SA near to the wall as $\tilde{d}$ reduces to d. Farther from the wall, it acts as a SGS model since $\tilde{d} = C_{DES}\Delta$ tends to the Smagorinsky length scale appearing in Eq. (2.26). Finally, although originally developed with a SA model, DES can be employed with any URANS model by defining properly a length scale with the available turbulent variables. As an example, Menter et al. (2003) extended this idea to the $k-\omega$ SST model.

DES simulations are thus designed to treat the entire boundary layer using a URANS model and to apply LES treatment elsewhere. The regions subjected to URANS or LES do not have to be explicitly identified *a priori*. However, the user defines them implicitly since the grid strongly impacts the location of the switch between URANS and SGS treatment. Figure 2.10 illustrates this phenomenon by comparing two grids in a boundary layer. The grids differ by their streamwise density and have a largest grid spacing $\Delta = \Delta x \approx \Delta z$. The grid displayed in Fig. 2.10a is typical of URANS or DES use. For such a mesh, Δ is always much larger than the distance to the wall d. Therefore, using Eq. (2.27), DES would be in its URANS mode throughout the boundary layer as expected. However, for the grid shown in Fig. 2.10b, there exists a region where Δ is smaller than the distance d. The DES would then activate its SGS mode in the upper two-thirds of the boundary layer. The grid in this area however is not fine enough to accurately resolve the velocity fluctuations. Therefore, LES would be under-resolved in the boundary layer which might lead to “grid-induced separation”. It means that the onset of the separation is altered by the mesh, which results to a flow detaching too far upstream (Mellen et al., 2002; Menter and Kuntz, 2004). However, this second type of grid can be justifiably desired, for example, for a grid convergence study, a design adapted to geometry features or a properly discretized thick boundary layer.

Menter et al. (2003) addressed this deficiency by identifying the boundary layer and preventing a switch to the LES mode within it. This identification is performed by using the blending functions

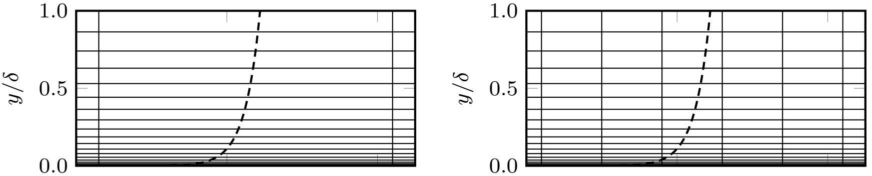

(a) Type I: natural DES.

(b) Type II: ambiguous grid spacing.

Figure 2.10: Two DES grids in a boundary layer. The dashed lines represent the mean velocity and δ is the boundary layer thickness. The grid spacing in the third dimension is similar to the streamwise grid spacing, i.e., $\Delta z \approx \Delta x$. Adapted from Spalart et al. (2006).

of the SST turbulence model. Spalart et al. (2006) extended this concept to other URANS models involving an eddy viscosity. To this end, a function f_d that takes the value 1 in the LES region and 0 elsewhere is defined

$$f_d = 1 - \tanh\left([8r_d]^3\right), \tag{2.28}$$

with

$$r_d = \frac{\nu_T + \nu}{\sqrt{\partial_j \widehat{u}_i \partial_j \widehat{u}_i \kappa^2 d^2}}. \tag{2.29}$$

The term r_d is equal to 1 in the logarithmic layer and falls to 0 towards the edge of the boundary layer. Moreover, this new approach requires to re-define the original DES length scale $\tilde{d}$ given by Eq. (2.27) as

$$\tilde{d} = d - f_d \max\left(0, d - C_{DES}\Delta\right). \tag{2.30}$$

This methodology delays the LES mode of DES. Consequently, Spalart et al. (2006) named it the Delayed Detached-Eddy Simulation (DDES). Finally, the constants appearing in Eq. (2.28) are determined from the application of the SA-based DDES on a flat-plate boundary layer. An adjustment of those constants may be required for DDES based on other turbulence models. In the present work, the DDES simulations carried out use the SA-based DDES methodology and, more precisely, the version proposed by Spalart et al. (2006).

2.3 Indirect calculation of loads by the use of Particle Image Velocimetry

Particle Image Velocimetry (PIV) is an optical technique that enables the measurement of a instantaneous flow velocity field by using images of particles seeded in the fluid. Developed during the eighties, PIV has become increasingly popular and is nowadays a well-recognized experimental tool to study complex flows. Initially PIV provided two-dimensional velocity fields in a plane, i.e. two velocity components in a two-dimensional space (2C2D). The technique was then extended to the acquisition of the out-of-plane velocity component (3C2D) and nowadays to fully tri-dimensional measurements in a volume (3C3D).

Aerodynamic loads on a body can be indirectly estimated from PIV measurements. A first methodology was proposed by Lin and Rockwell (1996) who used the vorticity field computed from PIV data to estimate the instantaneous lift. As the method requires the knowledge of the entire vorticity history, the PIV window should theoretically be infinite if the vorticity is convected by the flow. Lin and Rockwell (1996) circumvented this limitation by applying the formulation to a cylinder oscillating in still fluid, so that the vorticity remained confined in a finite domain that could be captured by the PIV window.

The method was then extended by Noca et al. (1997) to eliminate the domain size limitation. Derived from the integral form of the momentum equation applied to a control surface surrounding the geometry of interest, his formulation expresses the forces solely in terms of the velocity field and its derivatives by re-writing the pressure term. This approach requires an accurate evaluation of the vorticity on the entire control surface, including the region near the body. However, obtaining the velocity field in the vicinity of geometries, especially moving ones, can be challenging due to reflections of the laser sheet. To alleviate this drawback, Noca et al. (1999) proposed alternative approaches, where the knowledge of the velocity and vorticity fields are required only on the contours of the control surface.

In parallel to the work of Noca et al. (1999), Unal et al. (1997) showed that the classical integral form of the momentum equation can be directly used to estimate the loads on a body. In this case both contour and surface integrals of the velocity and pressure fields are required. Nonetheless, the pressure can be itself obtained from the PIV data through the application of the Navier-Stokes equations.

In this work, the so-called flux equation proposed by Noca et al. (1999) is extended to the calculation of moments as the original formulation allowed the calculation of forces only. In Chap. 4, this extended formulation and the integral form of the Navier-Stokes equations are applied to spatio-temporal data obtained from separated flows. The following sections describe first the basic concepts of 2C2D PIV. Note that more information about this topic can be found for instance in the practical guide of Raffel et al. (2013) or in the Lecture Series of the Von Karman Institute (Anthoine et al., 2009). Then, the two methodologies allowing the indirect calculation of aerodynamic loads through PIV are presented. The corresponding sections begin with the respective formulation and end with the validation of the implementation based on CFD data.

2.3.1 Particle Image Velocimetry

Particle Image Velocimetry is a non-intrusive optical measurement technique allowing the indirect acquisition of velocity fields. Originating in solid mechanics, PIV has its roots in laser speckle velocimetry (LSV), a technique that measures displacements through scattered laser light. Dudderar and Simpkins (1977) were the first to seek possibilities to apply LSV to fluid flows. A systematic approach was then proposed by Meynart (1983) and Adrian and Yao (1984). The technique was initially limited to the acquisition of two velocity components in a two-dimensional velocity field and was thus called 2C2D PIV. The measurement of the third velocity component was enabled by the emergence of stereoscopic 3C2D PIV (Prasad, 2000). This technique consists in the simultaneous recording of two different views of a single plane. The combination of these two views enables the reconstruction of the three velocity components. Nowadays, if sufficient illumination power is available, the light sheet can be expanded into a thick region such that three dimensional PIV measurements are possible within a volume (3C3D).

Basic 2C2D PIV determines the flow velocity by measuring the displacement of tracer particles in a plane illuminated by a light sheet over a short interval of time. The flow is generally seeded with tracer particles. These particles are then illuminated in a plane twice within a short time interval Δt and a camera records the light scattered by the tracers in these two different time frames. The displacement $\Delta\mathbf{x}$ of the particles between two light pulses is then determined by comparison of the two frames and classical image processing techniques. After the removal of potential outliers, the two components of the velocity in the two dimensional plane are obtained as $\mathbf{u} = {}^{\Delta\mathbf{x}}/_{\Delta t}$. Therefore, a typical PIV system consists of several sub-systems as depicted in Fig. 2.11: tracer particles, a laser and the corresponding optics necessary to generate a light sheet, and a camera to record images.

Because PIV measures the velocity of the tracers and not directly the flow velocity, the tracers have to be chosen so as to avoid significant discrepancy between fluid and particle motion. By analogy with Stokes' drag law, the velocity lag in a continuously accelerating fluid reads

$$\mathbf{u}_p - \mathbf{u}_f = d_p^2 \frac{\rho_p - \rho_f}{18\mu_f} \mathrm{d}_t \mathbf{u}_f, \tag{2.31}$$

where d_p is the particle diameter and indices p and f stand for variables related to particle and fluid, respectively (Raffel et al., 2013). Therefore, to reduce the velocity lag, the seeding and the

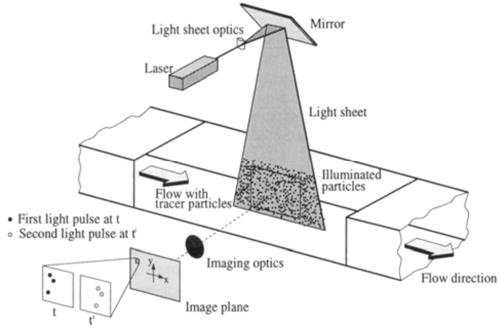

Figure 2.11: Typical arrangement setup for 2C2D PIV experiment. Reproduced from Raffel et al. (2013).

fluid should have similar densities. When the particle density is much greater than the fluid density, the particle response time τ_p is

$$\tau_p = \frac{d_p^2 \rho_p}{18 \mu_f}. \tag{2.32}$$

The Stokes number Stk characterizes the behavior of particles suspended in a fluid flow by comparing the time response of a particle τ_p and the characteristic time of the flow τ. This non-dimensional number is defined as

$$\mathrm{Stk} = \frac{\tau_p}{\tau}. \tag{2.33}$$

For turbulent flows, the smallest time scale corresponds to the Kolmogorov time scale τ_k. Therefore, for a seeding such that $\rho_p \gg \rho_f$, the Stokes number $\mathrm{Stk} = {}^{\tau_p}/_{\tau_k}$ should tend to zero. Consequently, the diameter of the particles should be very small in order to ensure good tracking (Raffel et al., 2013). In the case of a gas flow such as air, matching density is difficult and the seeding density is generally higher than the fluid density. Very small particles must thus be used which usually deteriorates their light scattering property. Typical tracers for a gas are solid titanium or glass micro-spheres, smoke, liquid oil. For liquid flows, it is much simpler to find seeding particles with matching density. Common solid materials used in that context are polystyrene, aluminum flakes, hollow glass spheres or granules for synthetic coatings.

A laser beam is generally used as a high-power light source. Cylindrical lenses or rotating mirrors transform the beam into a sheet that illuminates the tracers. Argon-ion and Neodym:YAG lasers are frequent choices for applications requiring continuous and pulsed light, respectively. Pictures of the seeding were previously recorded by the use of photography technique but, nowadays, images are mainly digital and acquired by CCD or CMOS cameras enabling the recording of several distinct PIV frames within microseconds. The availability of high-speed PIV camera and high-speed laser led to time-resolved PIV, a technique that allows the acquisition of the instantaneous flow field even for high frequency phenomena. Finally, the most frequently used recording method is the double frame/single exposure PIV which provides a single illuminated image of the flow for each of the two illumination pulses. As the frames are distinct, this technique eliminates the need to resolve directional ambiguity that occurs with the single frame/multi-exposure approach.

Once PIV frames are recorded, the velocity field is obtained from the displacement $\Delta\mathbf{x}$. Unlike particle tracking techniques which follow individual tracers, here the position of a set of particles is analyzed through statistical methods. In the context of a digital approach with double frame/single exposure, this analysis consists in the calculation of the cross-correlation between patterns of tracers. As depicted in Fig. 2.12, an interrogation window is defined around a point (x_0, y_0) in frames A and B distant in time by Δt. The interrogation windows in frames A and B are called IWa_0 and IWb_0, respectively. The minimal size of these interrogation windows is defined by the one quarter rule, i.e the maximum displacement that can be measured is limited to roughly a quarter of the interrogation window size (Raffel et al., 2013). The displacement $\Delta\mathbf{x}$ is obtained by measuring the degree of matching between IWa_0 and IWb_0 through a cross-correlation function. More specifically, a cross-correlation map having the same size as the interrogation window is computed by using frequency domain multiplications. The location with the highest value in the resulting cross-correlation map represents a direct estimation of the particle displacement $\Delta\mathbf{x}$. Note that this peak location is determined using a Gaussian fit which allows subpixel accuracy. Knowing the displacement $\Delta\mathbf{x}$ at the point (x_0, y_0) and the time interval Δt between two light pulses, the corresponding velocity at this location can be easily computed. The method inherently provides a first order approximation of the velocity field because a constant velocity is assumed between two images. Finally, this process is repeated for each points belonging to a defined grid to retrieve an entire velocity field.

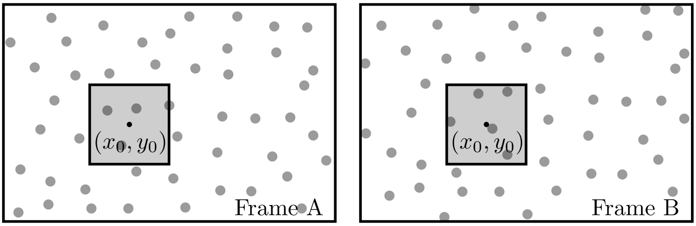

Figure 2.12: Interrogation windows in the context of single pass PIV. Adapted from Raffel et al. (2013).

The dynamic range is the ability to represent large range of velocity scales in the flow field. With the basic procedure described previously, this dynamic range is limited by the size of the interrogation window. The one-quarter rule imposes a large interrogation window in order to capture large displacements, i.e., high velocities. This simultaneously decreases the smallest scales that can be detected, and thus the resolution. The dynamic range can be enlarged by using advanced interrogation techniques. The PIV algorithm used in the context of this thesis is based on the window displacement iterative multigrid (WIDIM) interrogation method (Scarano and Riethmuller, 1999) which takes advantage of multiple pass interrogations with window displacement and grid refinement. The idea behind this procedure is to calculate a first displacement $\Delta\mathbf{x}_0$ through a first correlation map determined by using the interrogation windows IWa_0 and IWb_0 defined at point (x_0, y_0) as explained previously for the basic procedure. Then, the process is repeated for a second pass where a second interrogation window is defined for each frame A and B. These two new interrogation widows are respectively called IWa_1 and IWb_1 and are offset with respect to point (x_0, y_0). To obtain a central difference interrogation and eventually a second order velocity field, the center of IWa_1 and IWb_1 are respectively given by $(x_1, y_1)_{\mathrm{A}} = (x_0, y_0) - {}^{\Delta\mathbf{x}_0}\!/_2$ and $(x_1, y_1)_{\mathrm{B}} = (x_0, y_0) + {}^{\Delta\mathbf{x}_0}\!/_2$, as depicted in Fig. 2.13. This second pass increases the fraction of matched tracers in the two windows and thus the signal-to-noise ratio of the correlation peak. The number of passes can be fixed or the process can be repeated until the calculated displacement is converged. In the context of this work, the number of passes is constant and set to two. The multiple pass interrogation algorithm can be further improved by using an approach in which the size of the interrogation window is reduced as a new pass is considered. This procedure is called iterative multigid and combines a large first interrogation window with as smaller second one. Therefore, it increases the achievable dynamic range.

After the processing of the PIV images, a certain number of incorrectly determined velocity vectors called outliers can frequently be found by visual inspection of the raw data. In order to automatically detect these incorrect vectors, the raw velocity field obtained after each pass of the

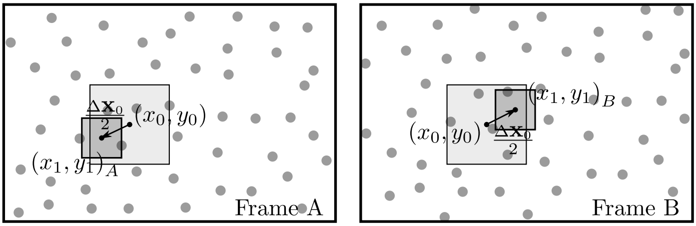

Figure 2.13: Interrogation windows in the context of double pass PIV using WIDIM. Adapted from Raffel et al. (2013).

PIV algorithm has to be validated. For this purpose, two validation tests are performed on the cross-correlation map that leads to a velocity vector: i) the location of the peak must be within a predetermined range in the x and y-directions and, ii) the peak magnitude should be at least three standard deviations above the mean value of the cross-correlation map. If data validation fails, the incorrect displacement vector is discarded and replaced using a median filter, i.e., the new value is the median of the neighboring displacement vectors. For time or phase-averaged velocity fields, a $3-\sigma$ filter is additionally applied. This filter requires several PIV images and their respective particle displacement fields. Averaged $\overline{\Delta \mathbf{x}}$ and standard deviation $\Delta \mathbf{x}'$ are calculated using K particle displacement fields $(\Delta \mathbf{x})^k$, where k stands for the k^{th} image. Then, each displacement field $(\Delta \mathbf{x})^k$ is compared to the averaged $\overline{\Delta \mathbf{x}}$. For each field $(\Delta \mathbf{x})^k$, only the displacement vectors satisfying $\overline{\Delta \mathbf{x}} - 3\Delta \mathbf{x}' \leqslant (\Delta \mathbf{x})^k \leqslant \overline{\Delta \mathbf{x}} + 3\Delta \mathbf{x}'$ are retained, the others being discarded. Finally, statistics on the K particle displacement fields $(\Delta \mathbf{x})^k$ are re-calculated considering only the remaining vectors. The velocity field is finally computed by using the time between pulses Δt and the magnification produced by the camera lens.

The overall algorithm used in the present work is given in Algo. 1. The first phase consists in the definition of the region of interest (ROI) and the grid where the velocity field is calculated. During this initialization phase, the user also sets the size of the interrogation windows required for first and second passes. Then, and for each pair of images, the particle displacement $\Delta \mathbf{x}_0$ associated with each point of the grid is calculated through a first pass and the validity of the obtained values is verified. This first pass completed, each detected outlier is replaced by applying a median filter. A second pass is then applied using $\Delta \mathbf{x}_0$ to shift the interrogation window associated with each calculation point. The particle displacement field $\Delta \mathbf{x}_1$ is subsequently post-processed to remove outliers. Finally, for time or phase-averaged flows, a $3-\sigma$ filter is applied. As discussed before, it is possible to indirectly estimate the aerodynamic loads from PIV results. The subsequent Secs. 2.3.2, 2.3.3 and 2.3.4 are dedicated to that purpose.

2.3.2 Approach based on the integral form of the Navier-Stokes equations

The simplest and most trivial indirect approach to calculate the aerodynamic loads from PIV data is the direct application of the integral form of the Navier-Stokes equations. This section describes the physical explanation of this formulation and the challenges appearing when it is applied to PIV measurements.

2.3.2.1 Loads from the integral form of the Navier-Stokes equations

The integration of the differential form of the Navier-Stokes equations (2.3) on a control volume $\mathcal{V}$ gives the integral form of the Navier-Stokes equations

$$\mathrm{d}_t \int_{\mathcal{V}} \rho \mathbf{u} \, \mathrm{d}\mathcal{V} = \int_{\mathcal{S}} \mathbf{n} \cdot \left[-p\mathbf{I} - \rho \mathbf{u}\mathbf{u} + \boldsymbol{\tau} \right] \, \mathrm{d}\mathcal{S}, \tag{2.34}$$

Algorithm 1: Calculation of PIV velocity field.

```
Input: Snapshots containing pair of images temporally distant of $\Delta t$
Output: Velocity field on a grid and associated with a ROI
/* Initialization                                                        */
define grid and ROI;
define size of interrogation window for first and second pass;
/* Analyze of each snapshot                                              */
foreach pair of images do
    /* First pass: calculation of displacement $\Delta x_0$               */
    foreach point of the grid $(x_0, y_0)$ do
        foreach point inside the interrogation window $(x_i, y_i)$ do
            calculate the cross-correlation associated with $(x_i, y_i)$;
        end
        fit the cross-correlation map with Gaussian function;
        determine the displacement $\Delta \mathbf{x}_0$;
        check the validity of $\Delta \mathbf{x}_0$;
    end
    /* First pass: treatment of outliers                                 */
    foreach detected outlier do
        replace outlier by the median of neighboring values;
    end
    /* Second pass: calculation of displacement $\Delta x = \Delta x_1$   */
    foreach point of the grid $(x_0, y_0)$ do
        calculate the location of the interrogation window: $(x_1, y_1)_A$ and $(x_1, y_1)_B$;
        foreach point inside the interrogation window $(x_i, y_i)$ do
            calculate the cross-correlation associated with $(x_i, y_i)$;
        end
        fit the cross-correlation map with Gaussian function;
        determine the displacement $\Delta \mathbf{x}_1$;
        check the validity of $\Delta \mathbf{x}_1$;
    end
    /* Second pass: treatment of outliers                                */
    foreach detected outlier do
        replace outlier by the median of neighboring values;
    end
end
/* Filter based on several snapshots                                     */
apply a $3 - \sigma$ filter;
```

where $\mathcal{V}$ consists only in the fluid volume, and is fixed in space and bounded by a control surface $\mathcal{S}$. In Eq. 2.34, $\mathbf{n}$ is the unit normal vector determining the orientation of surface $\mathcal{S}$ and is defined as positive when pointing away from volume $\mathcal{V}$. This equation is simply a formulation of Newton's second law applied to a fluid volume. The left-hand side of Eq. (2.34) corresponds to the time rate of change in momentum in the volume $\mathcal{V}$ due to unsteady flow fluctuations while the right-hand size is the sum of the surface forces acting on the control surface $\mathcal{S}$ (Anderson, 2010). Note that the body forces have been neglected.

To calculate the aerodynamic force on a body, Eq. (2.34) has to be modified to take into account the impact of this body on the fluid. This can be done by choosing a control volume $\mathcal{V}$ enclosing the body of volume $\mathcal{V}_b$, as in Fig. 2.14, where $\mathcal{V}_b$ is excluded from the fluid control volume. In other words, $\mathcal{V}$ is bounded by the two surfaces $\mathcal{S}_\infty$ and $\mathcal{S}_b$. Note that unlike $\mathcal{S}_\infty$, $\mathcal{S}_b$ is not fixed in space and time as $\mathcal{V}_b$ can move. The aerodynamic force on the body corresponds to the reaction to the force applied by the body on the fluid, i.e. the integrated contribution of the pressure and shear stress acting on the surface $\mathcal{S}_b$. It is assumed here that there is no flow through the body surface. Therefore, neglecting body forces, Newton's second law can be written as

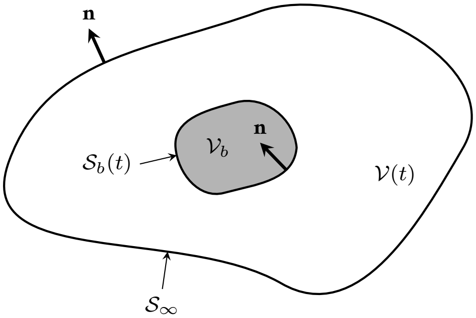

Figure 2.14: Domain of integration for the determination of aerodynamic forces on a body (in dark gray) using momentum-based approaches.

$$\mathrm{d}_t \int_{\mathcal{V}} \rho \mathbf{u} \, \mathrm{d}\mathcal{V} = \oint_{\mathcal{S}_\infty} \mathbf{n} \cdot [-p\mathbf{I} - \rho\mathbf{u}\mathbf{u} + \boldsymbol{\tau}] \, \mathrm{d}\mathcal{S} + \oint_{\mathcal{S}_b} \mathbf{n} \cdot [-p\mathbf{I} + \boldsymbol{\tau}] \, \mathrm{d}\mathcal{S}, \tag{2.35}$$

where the second term on the right-hand side represents the force applied by the body on the fluid. Therefore, the aerodynamic force $\mathbf{F}$ exerted by the fluid on the body is

$$\mathbf{F} = -\mathrm{d}_t \int_{\mathcal{V}} \rho \mathbf{u} \, \mathrm{d}\mathcal{V} + \oint_{\mathcal{S}_\infty} \mathbf{n} \cdot [-p\mathbf{I} - \rho\mathbf{u}\mathbf{u} + \boldsymbol{\tau}] \, \mathrm{d}\mathcal{S}. \tag{2.36}$$

The formulation for torques created by the fluid with respect to a point R directly follows from Eq. (2.36). To obtain the aerodynamic moments, each elemental surface or volume force has to be multiplied by the lever arm connecting point R to the point of the elemental force application. In vector notation, this takes the form of a cross product where the lever arm is a location vector $\mathbf{r}$. Therefore, the moment vector is the sum of these elemental contributions, which is expressed by volume or surface integral. Finally, the aerodynamic moment with respect to point R is written as

$$\mathbf{M} = -\mathrm{d}_t \int_{\mathcal{V}} \rho \mathbf{u} \times \mathbf{r} \, \mathrm{d}\mathcal{V} + \oint_{\mathcal{S}_\infty} (\mathbf{n} \cdot [-p\mathbf{I} - \rho\mathbf{u}\mathbf{u} + \boldsymbol{\tau}]) \times \mathbf{r} \, \mathrm{d}\mathcal{S}. \tag{2.37}$$

Note that, using Eq. (2.37), the resulting moment is negative according to the right-hand rule definition to conform with the convention of positive pitch-up moment used in aerodynamics.

Equations (2.36) and (2.37) allow the general calculation of forces and moments based on a momentum-balance. The only assumptions made are that there is no flow through the body surface, $\mathcal{S}_\infty$ is fixed and body forces are neglected. However, the specific applications considered here require some adaptation of the general formulation given by Eqs. (2.36) and (2.37). First, since the available velocity fields correspond to 2C2D PIV fields, the momentum-balance is applied to a two-dimensional surface $\mathcal{S}$ whose contour is composed of the external and body borders, $\mathcal{C}_\infty$ and

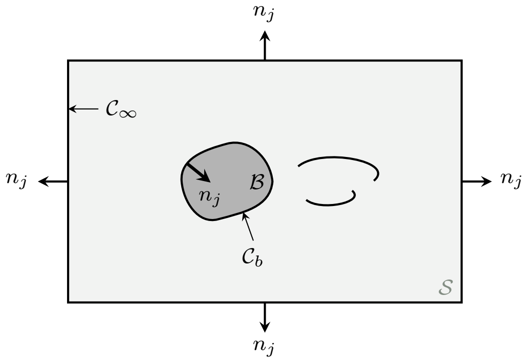

Figure 2.15: Schematic view of the control surface $\mathcal{S}$ and its countours $\mathcal{C}_\infty$ and $\mathcal{C}_b$ around the geometry $\mathcal{B}$ of interest.

$\mathcal{C}_b$, respectively. Moreover, the surface $\mathcal{S}$ is assumed to be rectangular, as depicted in Fig. 2.15. Although the body is free to move, the external border $\mathcal{C}_\infty$ is assumed to be static.

Because of the low acquisition frequency of the PIV apparatus used in this work, the evaluation of instantaneous loads is not possible. Moreover, since the flows studied in the following are turbulent, only statistical mean fields are considered. The momentum balance must thus be derived from the Reynolds-averaged Navier-Stokes equations (2.14). This provides the two-dimensional average aerodynamic force

$$\overline{F}_i = -\mathrm{d}_t \int_{\mathcal{S}} \rho \overline{u}_i \,\mathrm{d}\mathcal{S} - \oint\limits_{\mathcal{C}_\infty} \overline{p} n_i \,\mathrm{d}\mathcal{C} + \oint\limits_{\mathcal{C}_\infty} \left(-\rho \overline{u}_i \overline{u}_j + \overline{\tau}_{ij} - \rho \overline{u_i' u_j'}\right) n_j \,\mathrm{d}\mathcal{C}, \tag{2.38}$$

and the average pitching moment about point R defined positive nose up

$$\begin{aligned} \overline{M}_z = & -\mathrm{d}_t \int_{\mathcal{S}} \rho \overline{u}_l r_m \epsilon_{lm} \,\mathrm{d}\mathcal{S} - \oint\limits_{\mathcal{C}_\infty} \overline{p} n_l r_m \epsilon_{lm} \,\mathrm{d}\mathcal{C} \\ & + \oint\limits_{\mathcal{C}_\infty} \left(-\rho \overline{u}_l \overline{u}_j + \overline{\tau}_{lj} - \rho \overline{u_l' u_j'}\right) n_j r_m \epsilon_{lm} \,\mathrm{d}\mathcal{C}, \end{aligned} \tag{2.39}$$

where $\overline{u_i' u_j'}$ is the Reynolds stress tensor introduced in Sec. 2.1 and ϵ_{ij} is the two-dimensional Levi-Cevita symbol. Equations (2.38) and (2.39) represent the core of the indirect load measurement methodology based on the integral Navier-Stokes equations and will be hereafter referred to as INSE. Finally, note that the average $\overline{\cdot}$ does not necessarily imply a time averaging procedure so that the average force and moment can be time dependent.

Each term in the above expressions can be calculated by averaging the velocity field u_i obtained from PIV measurements. In particular, the average viscous stress tensor $\overline{\tau}_{ij}$ is computed from the average velocity gradients

$$\overline{\tau}_{ij} = \mu \left(\partial_i \overline{u}_j + \partial_j \overline{u}_i\right). \tag{2.40}$$

The average pressure field $\overline{p}$ is not explicitly known, but can be determined indirectly as explained in the following.

2.3.2.2 Obtaining the pressure field from PIV measurements

As shown by Eqs. (2.38) and (2.39), the indirect calculation of loads based on the integral form of the Navier-Stokes equations requires the knowledge of the pressure. However, as pressure is not explicitly acquired by PIV measurements, it has to be indirectly calculated from the velocity field. This has been extensively reviewed by van Oudheusden (2013) and used in several studies which focused on the pressure field calculation from PIV (Gurka et al., 1999; Dabiri et al., 2014; Laskari et al., 2016; Schneiders et al., 2016; van Gent et al., 2017). Two approaches can be considered, both based on the knowledge of the average pressure derivatives calculated from the averaged Navier-Stokes equations

$$\partial_i \overline{p} = -\rho \partial_t \overline{u}_i - \rho \overline{u}_j \partial_j \overline{u}_i + \mu \partial^2_{jj} \overline{u}_i - \partial_j \overline{u'_j u'_i}. \tag{2.41}$$

The first option is to solve the Poisson equation that is obtained by taking the divergence of Eq. (2.41). Boundary conditions of Neumann type can be applied using Eq. (2.41). The second option consists in integrating along $\mathcal{C}_\infty$ the component of the pressure gradient $\partial_i \overline{p}$ that is tangential to the contour. Because the use of the pressure Poisson equation increases the computational time without improving results significantly (Albrecht et al., 2012), the second option has been chosen here. Since the integration path is closed, the average pressure computed at the last point E depicted in Fig. 2.16 should be equal to the initial value at point A, i.e., $\overline{p}_\mathrm{E} = \overline{p}_\mathrm{A} = \overline{p}_{init}$. In practice, a discrepancy between these two values is typically observed because the PIV data are only available at discrete points and entail measurement errors. Nonetheless, the integration error $\varepsilon_{\overline{p}} = \overline{p}_\mathrm{A} - \overline{p}_\mathrm{E}$ can be used to improve the pressure calculation.

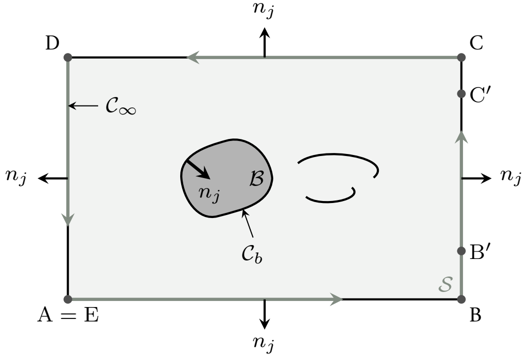

Figure 2.16: Schematic view of the integration path used to calculate the pressure from its derivatives.

The approach used here is based on the work of Kurtulus et al. (2007), who estimated the pressure from Bernoulli's equation outside the viscous wake, represented by the segments A-B-B′ and C′-C-D-E in Fig. 2.16, and integrated Eq. (2.41) in the wake region, depicted by the segment B′-C′. The value obtained in C′ is then compared to the one computed by Bernoulli's equation and the discrepancy is redistributed with a linear weighting along B′-C′. In the present work, Eq. (2.41) is used along the entire contour $\mathcal{C}_\infty$ but the correction is only applied in the wake region. The assumption that most of the error is generated in the wake, and then simply propagated along the rest of the contour, seems reasonable since the edge B-C is the zone where the spatio-temporal variations of the velocity and pressure are the largest, and, thus, the numerical integration of the pressure gradient is the most challenging. Based on this assumption, the error $\varepsilon_{\overline{p}}$ is simply removed from the computed value $\overline{p}$ along edges E-D-C-C′. Similarly to Kurtulus et al. (2007), it is assumed that the error $\varepsilon_{\overline{p}}$ increases linearly in the wake, i.e. along the segment B′-C′, and the pressure is corrected accordingly.

The wake is here defined as the region of large-scale vorticity. This region is identified by the Γ_2 function (Graftieaux et al., 2001), which provides the location of the large-scale vortex boundary based on the topology of the velocity field. This method was preferred to the one based on the vorticity proposed by Kurtulus et al. (2007), as the velocity field is less noisy than its spatial derivatives. The value of the Γ_2 function at a point P is given by the integral over a small area A around P

$$\Gamma_2\left(\mathrm{P}\right) = \frac{1}{A}\int_{\mathrm{M}\in A} \frac{\left[\left(\mathbf{x}^{\mathrm{M}}-\mathbf{x}^{\mathrm{P}}\right)\times\left(\mathbf{u}^{\mathrm{M}}-\tilde{\mathbf{u}}^{\mathrm{P}}\right)\right]\cdot\mathbf{e}_z}{\left\|\left(\mathbf{x}^{\mathrm{M}}-\mathbf{x}^{\mathrm{P}}\right)\right\|\left\|\mathbf{u}^{\mathrm{M}}-\tilde{\mathbf{u}}^{\mathrm{P}}\right\|}\,\mathrm{d}A, \tag{2.42}$$

where, as depicted in Fig. 2.17, $\mathbf{x}^{\mathrm{M}}$ is the location of a point M that lies on surface A, and $\mathbf{e}_z$ is the unit vector normal to the measurement plane. Moreover, $\mathbf{u}^{\mathrm{M}}$ is the velocity vector associated with M and $\tilde{\mathbf{u}}^{\mathrm{P}}$ is a local convection velocity around P defined as $\tilde{\mathbf{u}}^{\mathrm{P}} = {}^{1}\!/\!{}_{A}\int_A \mathbf{u}\,\mathrm{d}A$, the mean velocity on A. The wake is identified as the region for which $\|\Gamma_2\| > \Gamma_2^{\mathrm{thres}}$, where $\Gamma_2^{\mathrm{thres}}$ is a threshold value to be chosen. The pressure correction on edge B-C then consists of three parts: on C$'$-C, the error $\varepsilon_{\overline{p}}$ is removed from the initially computed $\overline{p}$; on B$'$-C$'$, $\varepsilon_{\overline{p}}$ is removed linearly; and on B-B$'$, the initially calculated pressure is not corrected.

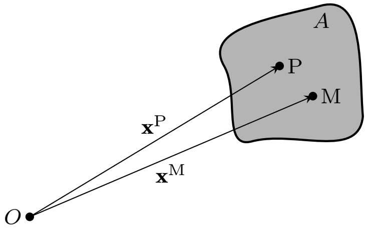

Figure 2.17: Schematic view of the calculation of Γ_2.

2.3.3 Approach based on Noca's flux equation

Using the integral form of the momentum equation is not the only existing possibility to indirectly calculate the loads from PIV measurements. In his thesis, Noca (1997) derived several formulations allowing the estimation of forces. Among them, the so-called flux equation is a formulation of the momentum balance which does not require the knowledge of pressure, nor the integration over the control volume $\mathcal{V}$ but only over the bounding surface $\mathcal{S}$. The following section describes this formulation and extends it to the calculation of moments.

2.3.3.1 Forces from Noca's flux equation

As stated before, Noca's flux equation derives from the integral momentum equation given by Eq. (2.36). It is written as

$$\mathbf{F} = \oint\limits_{\mathcal{S}_\infty} \mathbf{n}\cdot\left(\boldsymbol{\gamma}^{Ft}+\boldsymbol{\gamma}^{Fp}-\rho\mathbf{u}\mathbf{u}+\boldsymbol{\tau}\right)\,\mathrm{d}\mathcal{S} - \mathrm{d}_t\oint\limits_{\mathcal{S}_b}\mathbf{n}\cdot\left(\rho\mathbf{u}\mathbf{x}\right)\mathrm{d}\mathcal{S}, \tag{2.43}$$

with

$$\begin{aligned}
\boldsymbol{\gamma}^{Ft} &= -\,\rho(\partial_t\mathbf{u})\mathbf{x},\\
\boldsymbol{\gamma}^{Fp} &= \frac{\rho}{2}\|\mathbf{u}\|^2\mathbf{I} + \frac{\rho}{\mathcal{N}-1}\left[\boldsymbol{\omega}(\mathbf{x}\times\mathbf{u})-\mathbf{u}(\mathbf{x}\times\boldsymbol{\omega})\right]\\
&\quad - \frac{\rho}{\mathcal{N}-1}\left[(\mathbf{x}\cdot\partial_t\mathbf{u})\mathbf{I}-\mathbf{x}\partial_t\mathbf{u}\right]\\
&\quad + \frac{1}{\mathcal{N}-1}\left[\mathbf{x}\cdot(\nabla\cdot\boldsymbol{\tau})\mathbf{I}-\mathbf{x}(\nabla\cdot\boldsymbol{\tau})\right].
\end{aligned} \tag{2.44}$$

The term $\boldsymbol{\gamma}^{Fp}$ represents the pressure contribution, while the sum of $\boldsymbol{\gamma}^{Ft}$ and the last integral in Eq. (2.43) corresponds to the temporal term in the Navier-Stokes equations. Moreover, $\mathbf{I}$ is the unit tensor, $\mathcal{N}$ is the dimension of space, $\mathbf{x}$ is a location vector with respect to some arbitrary origin and $\boldsymbol{\omega}$ is the vorticity. The original formulation proposed by Noca et al. (1999) is more general. In particular, Eqs. (2.43) and (2.44) assume that the external border $\mathcal{S}_\infty$ is fixed and there is no flow through the body surface $\mathcal{S}_b$. More information about the derivation of Eqs. (2.43) and (2.44) is available in App. A.2.

Similarly to the INSE methodology, this three-dimensional formulation has to be adapted to planar PIV fields with low sampling frequency. In this case, the two-dimensional formulation for the average force reads

$$\overline{F}_i = \oint\limits_{\mathcal{C}_\infty} \left(\overline{\gamma}_{ji}^{Ft} + \overline{\gamma}_{ji}^{Fp} - \rho \overline{u}_j \overline{u}_i + \overline{\tau}_{ji} - \rho \overline{u'_j u'_i} \right) n_j \, \mathrm{d}\mathcal{C} - \mathrm{d}_t \oint\limits_{\mathcal{C}_b} \rho n_j \overline{u}_j x_i \, \mathrm{d}\mathcal{C}, \tag{2.45}$$

where tensors $\overline{\gamma}_{ij}^{Ft}$ and $\overline{\gamma}_{ij}^{Fp}$ are defined as

$$\begin{aligned} \overline{\gamma}_{ij}^{Ft} &= -\rho \partial_t \overline{u}_i x_j, \\ \overline{\gamma}_{ij}^{Fp} &= -\rho \overline{u}_i x_k \overline{\omega}_z \epsilon_{jk} + \frac{\rho}{2} \overline{u}_k \overline{u}_k \delta_{ij} + \rho x_i \partial_t \overline{u}_j \\ &\quad - \rho x_k \partial_t \overline{u}_k \delta_{ij} + x_l \partial_k \overline{\tau}_{kl} \delta_{ij} - x_i \partial_k \overline{\tau}_{kj} \\ &\quad + \rho x_i \partial_k \overline{u'_k u'_j} - \rho x_l \partial_k \overline{u'_k u'_l} \delta_{ij}. \end{aligned} \tag{2.46}$$

In Eqs. (2.45)-(2.46), $\mathcal{C}_b$ is the closed-path contour defining the body boundary as shown in Fig. 2.15, δ_{ij} is the Kronecker delta and $\overline{\omega}_z = \partial_l \overline{u}_m \epsilon_{lm}$ is the average vorticity. Note that unlike Eq. (2.38), Eq. (2.45) enables the calculation of loads by using only closed-path integrals and does not need the knowledge of pressure.

Finally, the last term in Eq. (2.45) requires the spatio-temporal variation of the body location. This can be difficult to obtain directly from PIV measurements due to reflections appearing near the surface. Nonetheless, in cases of rigid body motion, this term can be directly expressed in terms of the overall body kinematics. The body displacement can be decomposed into a rigid translation at velocity u_i^t and a rotation around the z-axis at angular velocity $\dot{\alpha}_z^r$, here defined positive clockwise. The velocity of the body surface is then

$$u_i^b = u_i^t - \dot{\alpha}_z^r \left(x_k^r - x_k \right) \epsilon_{ik}, \tag{2.47}$$

where x_i^r is the position of the center of rotation. Finally, the integral along $\mathcal{C}_b$ in Eq. (2.45) required to compute $\overline{F}_i$ can be written as

$$-\mathrm{d}_t \oint\limits_{\mathcal{C}_b} \rho n_j \overline{u}_j x_i \, \mathrm{d}\mathcal{C} = \rho \mathcal{B} \mathrm{d}_t u_i^t + \rho \mathcal{B} \overline{x}_j^r \mathrm{d}_t \dot{\alpha}^r \epsilon_{ij}, \tag{2.48}$$

where $\mathcal{B}$ is the area of the body cross-section, and $\overline{x}_i^r$ the location vector of the centroid defined with respect to the pivot point. The term requiring the spatio-temporal variation of the body location is thus calculated from the known kinematics without using PIV measurements. The derivation of this result can be found in App. A.2.

2.3.3.2 Derivation of a formulation for the calculation of moments

It is also possible to obtain a formulation for the aerodynamic moment that does not require the pressure nor the volume integral. For the methodology based on the Navier-Stokes equations, the formulation for the moment directly derives from the equation allowing the calculation of forces. However, the expression for the moment cannot be established from the flux equation. The reason is that the so-called pressure identity, a relation used by Noca et al. (1999) to rewrite the pressure term and derive the flux equation, is not applicable when a lever arm multiplies the pressure contribution. Therefore, a new formulation has to be derived from the expression for the moment with respect to point R, Eq. (2.37), recalled here for convenience,

$$\mathbf{M} = -\mathrm{d}_t \int_{\mathcal{V}} \rho \mathbf{u} \times \mathbf{r} \, \mathrm{d}\mathcal{V} + \oint_{\mathcal{S}_\infty} (\mathbf{n} \cdot [-p\mathbf{I} - \rho \mathbf{u}\mathbf{u} + \boldsymbol{\tau}]) \times \mathbf{r} \, \mathrm{d}\mathcal{S}. \tag{2.37}$$

The derivation is then similar to what was done by Noca et al. (1999) to establish the flux equation. It consists of two steps: i) the elimination of pressure and ii) the rewriting of the volume integral into surface integrals. Note that, as for the force formulation, it is assumed that the external surface $\mathcal{S}_\infty$ is static and that there is no flow through the body surface.

Elimination of pressure To rewrite the pressure, Noca et al. (1999) uses the so-called pressure identity. However, as mentioned before, it cannot be directly used for the calculation of moments. Instead, the pressure term in Eq. (2.37) can be rewritten using the extended pressure identity which is derived from the pressure identity as explained in App. A.4. The extended pressure identity reads

$$-\oint_{\mathcal{S}} \phi \, (\mathbf{n} \times \mathbf{x}) \, \mathrm{d}\mathcal{S} = \frac{1}{\mathcal{N}} \oint_{\mathcal{S}} \mathbf{x} \times [\mathbf{x} \times (\nabla \phi \times \mathbf{n})] \, \mathrm{d}\mathcal{S}, \tag{2.49}$$

where ϕ is an arbitrary scalar. Note that the domain enclosed by $\mathcal{S}$ can be multiply-connected. Using Eq. (2.49) with $\phi = p$, one has

$$-\oint_{\mathcal{S}} p \, (\mathbf{n} \times \mathbf{x}) \, \mathrm{d}\mathcal{S} = \frac{1}{\mathcal{N}} \oint_{\mathcal{S}} \mathbf{x} \times [\mathbf{x} \times (\nabla p \times \mathbf{n})] \, \mathrm{d}\mathcal{S}. \tag{2.50}$$

The pressure gradient can then be written as a function of the velocity field using the differential form of the Navier-Stokes equations

$$\nabla p = -\rho \partial_t \mathbf{u} - \nabla(\frac{\rho}{2} \|\mathbf{u}\|^2) + \rho \mathbf{u} \times \boldsymbol{\omega} + \nabla \cdot \boldsymbol{\tau}. \tag{2.51}$$

Finally, using the vector identity

$$\mathbf{x} \times (\mathbf{x} \times [\mathbf{a} \times \mathbf{n}]) = \mathbf{n} \cdot \left(\{[\mathbf{a} \times \mathbf{I}] \cdot \mathbf{x}\} \, \mathbf{x} - \|\mathbf{x}\|^2 \, [\mathbf{a} \times \mathbf{I}] \right), \tag{2.52}$$

and imposing $\mathbf{r} = \mathbf{x}$, the pressure term can be written as

$$-\oint_{\mathcal{S}_\infty} p \, (\mathbf{n} \times \mathbf{x}) \, \mathrm{d}\mathcal{S} = \oint_{\mathcal{S}_\infty} \mathbf{n} \cdot \boldsymbol{\gamma}^{Mp} \, \mathrm{d}\mathcal{S}, \tag{2.53}$$

where $\boldsymbol{\gamma}^{Mp}$ is

$$\begin{aligned} \boldsymbol{\gamma}^{Mp} = & -\frac{\rho}{2} \, \|\mathbf{u}\|^2 \, (\mathbf{x} \times \mathbf{I}) \\ & - \frac{\rho}{\mathcal{N}} \, ([\partial_t \mathbf{u} \times \mathbf{I}] \cdot \mathbf{x}) \, \mathbf{x} + \frac{\rho}{\mathcal{N}} \|\mathbf{x}\|^2 \, (\partial_t \mathbf{u} \times \mathbf{I}) \\ & + \frac{\rho}{\mathcal{N}} \, ([\{\mathbf{u} \times \boldsymbol{\omega}\} \times \mathbf{I}] \cdot \mathbf{x}) \, \mathbf{x} - \frac{\rho}{\mathcal{N}} \|\mathbf{x}\|^2 \, (\{\mathbf{u} \times \boldsymbol{\omega}\} \times \mathbf{I}) \\ & + \frac{1}{\mathcal{N}} \, ([\{\nabla \cdot \boldsymbol{\tau}\} \times \mathbf{I}] \cdot \mathbf{x}) \, \mathbf{x} - \frac{1}{\mathcal{N}} \|\mathbf{x}\|^2 \, (\{\nabla \cdot \boldsymbol{\tau}\} \times \mathbf{I}) \, . \end{aligned} \tag{2.54}$$

Note that in the two-dimensional case, i.e. $\mathcal{N} = 2$, the first term on the right-hand side of Eq. (2.52) vanishes, leading to a simplification of Eq. (2.54).

Elimination of volume integral By using the Reynolds transport theorem and imposing $\mathbf{r} = \mathbf{x}$, the volume integral in Eq. (2.37) can be written as

$$-\,\mathrm{d}_t \int_{\mathcal{V}} \rho\mathbf{u}\times\mathbf{x}\,\mathrm{d}\mathcal{V} = \int_{\mathcal{V}} \rho\mathbf{x}\times\partial_t\mathbf{u}\,\mathrm{d}\mathcal{V} - \oint_{\mathcal{S}_b} \left(\mathbf{u}^b\cdot\mathbf{n}\right)\left(\rho\mathbf{u}\times\mathbf{x}\right)\,\mathrm{d}\mathcal{S}, \tag{2.55}$$

where $\mathbf{u}^b$ is the velocity at the body surface. In order to express the volume integral on the right-hand side of Eq. (2.55) as a surface integral, the quantity $\mathbf{x}\times\partial_t\mathbf{u}$ is rewritten in terms of field derivatives. This is achieved by starting from the identity

$$\mathbf{x}\times\partial_t\mathbf{u} = \frac{1}{2}\nabla\times\left(\|\mathbf{x}\|^2\partial_t\mathbf{u}\right) - \frac{1}{2}\|\mathbf{x}\|^2\partial_t\boldsymbol{\omega}, \tag{2.56}$$

and taking advantage of the vorticity equation

$$\partial_t\boldsymbol{\omega} = \left(\boldsymbol{\omega}\cdot\nabla\right)\mathbf{u} - \left(\mathbf{u}\cdot\nabla\right)\boldsymbol{\omega} + \nu\nabla^2\boldsymbol{\omega}. \tag{2.57}$$

Then, the following identities are used

$$\|\mathbf{x}\|^2\left(\mathbf{u}\cdot\nabla\right)\boldsymbol{\omega} = \nabla\cdot\left(\|\mathbf{x}\|^2\mathbf{u}\boldsymbol{\omega}\right) - 2\left(\mathbf{x}\cdot\mathbf{u}\right)\boldsymbol{\omega}, \tag{2.58}$$

$$\|\mathbf{x}\|^2\left(\boldsymbol{\omega}\cdot\nabla\right)\mathbf{u} = \nabla\cdot\left(\|\mathbf{x}\|^2\boldsymbol{\omega}\mathbf{u}\right) - 2\left(\mathbf{x}\cdot\boldsymbol{\omega}\right)\mathbf{u}, \tag{2.59}$$

$$\|\mathbf{x}\|^2\nabla^2\boldsymbol{\omega} = \nabla^2\left(\|\mathbf{x}\|^2\boldsymbol{\omega}\right) - \nabla\cdot\left(4\mathbf{x}\boldsymbol{\omega}\right) + 2\mathcal{N}\boldsymbol{\omega}, \tag{2.60}$$

$$\begin{aligned}\left(\mathbf{x}\cdot\mathbf{u}\right)\boldsymbol{\omega} = {} & -\nabla\times\left[\frac{1}{2}\|\mathbf{u}\|^2\mathbf{x} - \left(\mathbf{u}\mathbf{u}\right)\cdot\mathbf{x}\right] \\ & -\nabla\cdot\left[\left(\mathbf{u}\times\mathbf{x}\right)\mathbf{u}\right] + \left(\mathbf{x}\cdot\boldsymbol{\omega}\right)\mathbf{u},\end{aligned} \tag{2.61}$$

to obtain

$$\begin{aligned}\mathbf{x}\times\partial_t\mathbf{u} = {} & \nabla\times\left(\frac{1}{2}\|\mathbf{x}\|^2\partial_t\mathbf{u}\right) + \nabla\cdot\left(\frac{1}{2}\|\mathbf{x}\|^2\mathbf{u}\boldsymbol{\omega}\right) \\ & + \nabla\times\left(\frac{1}{2}\|\mathbf{u}\|^2\mathbf{x} - \left[\mathbf{u}\mathbf{u}\right]\cdot\mathbf{x}\right) \\ & + \nabla\cdot\left(\left[\mathbf{u}\times\mathbf{x}\right]\mathbf{u}\right) - \nabla\cdot\left(\frac{1}{2}\|\mathbf{x}\|^2\boldsymbol{\omega}\mathbf{u}\right) \\ & - \nabla\cdot\left(\nabla\left[\frac{\nu}{2}\|\mathbf{x}\|^2\boldsymbol{\omega}\right]\right) + \nabla\cdot\left(2\nu\mathbf{x}\boldsymbol{\omega}\right) - \nabla\times\left(\nu\mathcal{N}\mathbf{u}\right).\end{aligned} \tag{2.62}$$

Finally, Gauss' theorem is used to express the volume integral as a surface integral. Thus, equation (2.55) becomes

$$-\,\mathrm{d}_t \int_{\mathcal{V}} \rho\mathbf{u}\times\mathbf{x}\,\mathrm{d}\mathcal{V} = \oint_{\mathcal{S}_\infty+\mathcal{S}_b} \mathbf{n}\cdot\boldsymbol{\gamma}^{Mt}\,\mathrm{d}\mathcal{S} - \oint_{\mathcal{S}_b}\left(\mathbf{u}^b\cdot\mathbf{n}\right)\left(\rho\mathbf{u}\times\mathbf{x}\right)\,\mathrm{d}\mathcal{S}, \tag{2.63}$$

with $\boldsymbol{\gamma}^{Mt}$ given by

$$\begin{aligned}\boldsymbol{\gamma}^{Mt} = {} & -\frac{\rho}{2}\|\mathbf{x}\|^2\,\partial_t\mathbf{u}\times\mathbf{I} + \rho\left(\mathbf{u}\times\mathbf{x}\right)\mathbf{u} \\ & + \frac{\rho}{2}\|\mathbf{x}\|^2\,\mathbf{u}\boldsymbol{\omega} - \frac{\rho}{2}\|\mathbf{x}\|^2\,\boldsymbol{\omega}\mathbf{u} \\ & - \frac{\rho}{2}\|\mathbf{u}\|^2\,\mathbf{x}\times\mathbf{I} + \rho\left(\left[\mathbf{u}\mathbf{u}\right]\cdot\mathbf{x}\right)\times\mathbf{I} \\ & + \mu\mathbf{x}\boldsymbol{\omega} + \mu\mathcal{N}\mathbf{u}\times\mathbf{I} - \frac{\mu}{2}\|\mathbf{x}\|^2\nabla\boldsymbol{\omega}.\end{aligned} \tag{2.64}$$

Note that if $\mathcal{N} = 2$, the vortex stretching term in Eq. (2.57) vanishes and several terms in Eq. (2.64) disappear.

Finally, a formulation similar to Noca's flux equation is obtained for the aerodynamic moment with respect to a point R,

$$\begin{aligned}\mathbf{M} = & \oint\limits_{\mathcal{S}_\infty + \mathcal{S}_b} \mathbf{n} \cdot \boldsymbol{\gamma}^{Mt} \, \mathrm{d}\mathcal{S} - \oint\limits_{\mathcal{S}_b} \left(\mathbf{u}^b \cdot \mathbf{n} \right) \left(\rho \mathbf{u} \times \mathbf{x} \right) \, \mathrm{d}\mathcal{S} \\ & + \oint\limits_{\mathcal{S}_\infty} \mathbf{n} \cdot \boldsymbol{\gamma}^{Mp} \, \mathrm{d}\mathcal{S} - \oint\limits_{\mathcal{S}_\infty} \mathbf{n} \cdot \left(\left[\rho \mathbf{u}\mathbf{u} - \boldsymbol{\tau} \right] \times \mathbf{x} \right) \, \mathrm{d}\mathcal{S},\end{aligned} \tag{2.65}$$

where the tensors $\boldsymbol{\gamma}^{Mp}$ and $\boldsymbol{\gamma}^{Mt}$ are given by Eqs. (2.54) and (2.64), respectively. Note again that the moment is defined positive nose-up, i.e., it is negative according to the right-hand rule. Moreover, this formulation requires the origin of the location vector **x** to be located at point R.

The integral along the body surface involves the vorticity, which is very difficult to compute accurately from PIV data. In practice, it is often better to keep the temporal term as a volume integral. Therefore, in the case of a two-dimensional turbulent flow, the pitching moment around R is

$$\begin{aligned}\overline{M}_z = & - \mathrm{d}_t \int_{\mathcal{S}} \rho \overline{u}_l x_m \epsilon_{lm} \, \mathrm{d}\mathcal{S} + \oint\limits_{\mathcal{C}_\infty} n_l \overline{\gamma}_l^{Mp} \, \mathrm{d}\mathcal{C} \\ & + \oint\limits_{\mathcal{C}_\infty} \left(-\rho \overline{u}_l \overline{u}_j + \overline{\tau}_{lj} - \rho \overline{u_l' u_j'} \right) n_j x_m \epsilon_{lm} \, \mathrm{d}\mathcal{C},\end{aligned} \tag{2.66}$$

where

$$\begin{aligned}\overline{\gamma}_i^{Mp} = & - \frac{\rho}{2} x_k x_k \partial_t \overline{u}_j \epsilon_{ij} - \frac{\rho}{2} x_k x_k \overline{\omega}_z \overline{u}_i \\ & + \frac{\rho}{2} \overline{u}_k \overline{u}_k x_j \epsilon_{ij} + \frac{1}{2} x_k x_k \partial_l \overline{\tau}_{lj} \epsilon_{ij} \\ & - \frac{\rho}{2} x_k x_k \partial_l \overline{u_l' u_j'} \epsilon_{ij}.\end{aligned} \tag{2.67}$$

Again, the origin must be defined at point R, so that $r_i = x_i$. To estimate the pitching moment about a different point, the contribution of the forces calculated by Eq. (2.45) has to be added to the value provided by Eq. (2.66). Equations (2.45) and (2.66) are the core of the methodology based on Noca's flux equation and its extension for the moment calculation. It will be hereafter referred to as NOCA.

2.3.4 Implementation and verification based on CFD

The INSE and NOCA formulations given by Eqs. (2.38), (2.39), (2.45) and (2.66) must be discretized in order to be applied to discrete PIV data. This section gives first the details of the implementation and then presents a verification procedure and its results.

2.3.4.1 Implementation

Different schemes are used to discretize the equations. For both INSE and NOCA methodologies, spatial derivatives are only required along the contour $\mathcal{C}_\infty$ shown in Fig. 2.16. They are calculated by using central finite difference schemes of fourth order for the first spatial derivatives and of second order for the second spatial derivatives. The temporal derivatives $\partial_t \overline{u}_i$ appearing in the NOCA methodology are computed with a fourth order central scheme.

The average pressure needed for the INSE methodology is calculated by integrating the average pressure gradient obtained from Eq. (2.41) along the closed path $\mathcal{C}_\infty$ as illustrated in Fig. 2.16. The integration path starts at point A where the pressure is chosen to be $\overline{p}_{init}$ and goes along $\mathcal{C}_\infty$ counterclockwise until point $\mathrm{E} = \mathrm{A}$. For each of the N points, a relation between the pressure and its derivatives can be written using a finite difference scheme. A non-symmetric third order scheme is used for all points except the corners A, B, C, D and E, where a third order forward/backward scheme is used. This discretization can be expressed as a system of N equations that is solved for the N unknown pressure values. Once this system is solved, the pressure is corrected according to the methodology described in Sec. 2.3.2.2.

As explained previously, this correction needs the knowledge of the function Γ_2 on edge B-C. To be more general, it is calculated at each point of $\mathcal{S}$ by applying

$$\Gamma_2\left(\mathrm{P}\right) = \frac{1}{n}\sum_i \frac{\left(\mathbf{x}^{\mathrm{M}_i} - \mathbf{x}^{\mathrm{P}}\right) \times \left(\mathbf{u}^{\mathrm{M}_i} - \tilde{\mathbf{u}}^{\mathrm{P}}\right)}{\left\|\left(\mathbf{x}^{\mathrm{M}_i} - \mathbf{x}^{\mathrm{P}}\right)\right\| \left\|\mathbf{u}^{\mathrm{M}_i} - \tilde{\mathbf{u}}^{\mathrm{P}}\right\|}, \tag{2.68}$$

which is the discrete version of Eq. (2.42). In Eq. (2.68), the summation is performed on the n points contained in A, a square of length l depicted in Fig. 2.18. The PIV grid being uniform and larger than the surface $\mathcal{S}$, the calculation of Γ_2 can be done using this definition everywhere without modification. Note that it has been demonstrated that the length l has no significant impact on the vortex detection (Graftieaux et al., 2001).

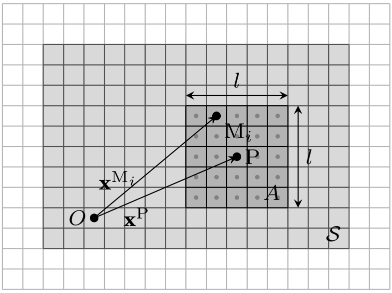

Figure 2.18: Schematic view of the calculation of Γ_2 applied on the PIV grid.

The loads are calculated by integrating the different terms on the contour $\mathcal{C}_\infty$ and surface $\mathcal{S}$. The rectangle rule is chosen to perform these calculations. Finally, when required, the temporal derivative of the volume integral is calculated with a fourth order central scheme.

2.3.4.2 Test case used for verification

To verify the correctness of their implementation, the two indirect methodologies are applied to data obtained from a CFD study. To this end, a numerical simulation is performed on the a two-dimensional flow around a square cylinder. A low Reynolds number $\mathrm{Re} = 50$ is chosen so that the flow remains laminar and the computational cost limited.

For the purpose of this study, a transient solver for incompressible laminar flows based on the PISO algorithm is used. The backward Euler scheme advances the equations in time and the time step is chosen in such a way that the Courant-Friedrichs-Lewy number (CFL) remains below 0.9. The computational domain is represented in Fig. 2.19a. It consists of a square of size $20c \times 20c$ surrounding the square cylinder of size $c \times c$ at its center. An intermediate square of length $5c$ is used to build the computational grid which is composed of square cells. The mesh is divided into two regions: i) the external part with a grid spacing of $\Delta x^E = {}^c/_{40}$ and ii) the internal part with a grid spacing equals to $\Delta x^I = {}^c/_{100}$. A grid convergence study has shown that the grid is fine enough to accurately capture the solution. The numerical solution can thus be considered as representative of the real physics. This is corroborated by the obtained $\overline{c_d}$ which is similar to the value reported by Sohankar et al. (1999).

At the body surface, a no-slip condition is imposed for the velocity and a zero-gradient boundary condition is set for the pressure. At the inlet, the freestream velocity is prescribed while a zero-gradient boundary condition is imposed on the pressure. At the outlet, a mixed condition is chosen. Most of the time, it enforces the pressure and imposes a zero-gradient boundary condition for the velocity. However, in case of backward flow, the boundary condition becomes the same as for the inlet. Finally, a slip condition is imposed for the upper and lower boundaries.

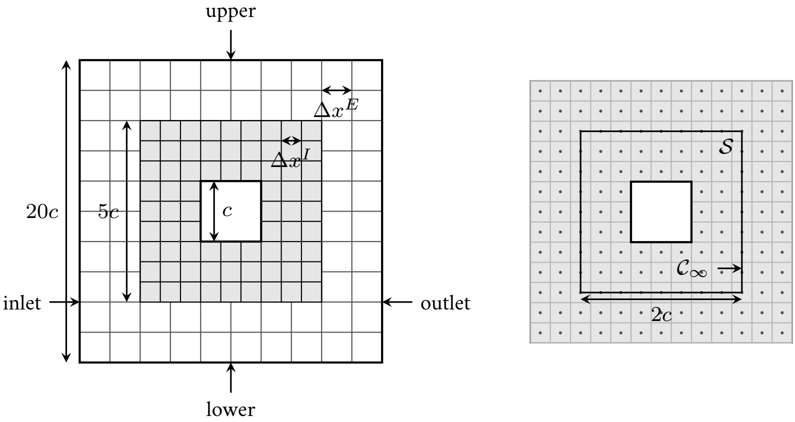

(a) Computational domain and grid.

(b) Chosen control surface.

Figure 2.19: Schematic view of the PIV-like grid used to apply the indirect methodologies. Figure (a) represents the CFD mesh and (b) the PIV-like grid. The gray area corresponds to the sampled zone and the small circles are the points of the PIV-like grid.

2.3.4.3 Results of numerical simulation

The numerical results for the flow around the square cylinder are presented in Fig. 2.20. Four phases of the vortex shedding cycle are depicted, corresponding successively to zero, maximum, zero and minimum lift coefficient. Both the streamlines and the pressure coefficient field are shown. It appears that two vortices are alternatively shed from the upstream corners into the wake. This causes the unsteadiness in the time response of the aerodynamic coefficients shown in Fig. 2.21. The pressure variations along the surfaces of the square cylinder are very low, which explains the low amplitude exhibited by the temporal response of c_l, c_d and c_m. A higher Reynolds number would lead to higher amplitudes.

2.3.4.4 Results of verification

The CFD solution is used to build sets of data on which the two indirect load calculation techniques can be applied. More precisely, a PIV-like grid is built sampling the center of the cells in the shaded zone as shown in Fig. 2.19b. Since the CFD code is based on a cell-centered technique, the fields at these points correspond to the solution of the Navier-Stokes equations. The two indirect methods are then applied to these discrete velocity fields to compute the aerodynamic forces and moment acting on the square cylinder. The aerodynamic loads obtained with different PIV-like grid resolutions are finally compared to the exact numerical loads. Three PIV-like grids are considered: the

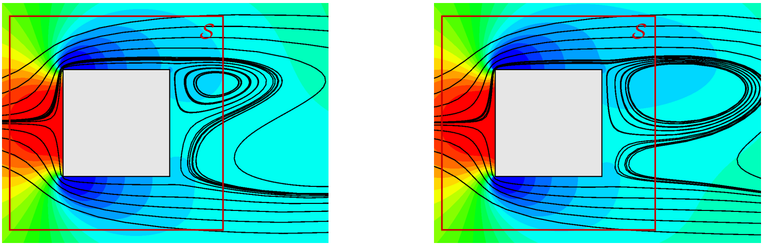

(a) $\varphi = 0$ and $c_l = 0$. (b) $\varphi = 0.25$ and $c_l = \max$.

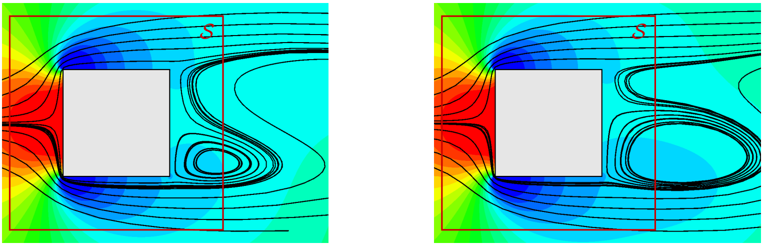

(c) $\varphi = 0.5$ and $c_l = 0$. (d) $\varphi = 0.75$ and $c_l = \min$.

Figure 2.20: Instantaneous streamlines and pressure coefficient field around a square cylinder at 0° of incidence and $\mathrm{Re} = 50$. Four different phases of a shedding period T are shown, corresponding to the zero, maximum and minimum values of the lift coefficient c_l. The pressure coefficient ranges from 1 (red) to -1 (blue) and each variation of color represents a step $\Delta C_p = 0.1$. The red square corresponds to the contour $\mathcal{C}_\infty$ of the control surface $\mathcal{S}$ used to indirecly compute the loads.

finest grid has the same resolution as the CFD grid, a coarser one uses every second CFD grid point and the coarsest every fourth point, which corresponds to a grid spacing of $^c/_{100}$, $^c/_{50}$ and $^c/_{25}$, respectively. The contour $\mathcal{C}_\infty$ surrounding the control surface $\mathcal{S}$ is a square of length $2c$ centered on the body, as depicted in Figs. 2.19b and 2.20.

The time responses of the loads obtained with the two indirect formulations on the three grids are shown in Fig. 2.21 together with the CFD loads. The results show that the lift, drag and moment coefficients converge to the CFD solution for both INSE and NOCA methods when the PIV-like grid is refined. Moreover, it seems that the INSE method converges slightly faster than the NOCA approach. The small discrepancy remaining between the finest mesh and the numerical solution is most likely due to the finite grids used for both the CFD and indirect load calculations. Nonetheless, the convergence of the results with finer grids indicates that the two indirect methods have been implemented correctly.

2.4 Decomposition methods

Spatio-temporal quantities describing unsteady aerodynamic flows are analyzed through modal decomposition in order to extract their dominant behavior. The goal is to study a sequence of N snapshots $\mathbf{v}_n$. Each snapshot $\mathbf{v}_n$ is a column vector containing M two or three-dimensional spatial data and the N snapshots are temporal instances equidistant in time. Different methods decompose the matrix of snapshots $\mathbf{V}_1^N = \{\mathbf{v}_1, \mathbf{v}_2, \ldots, \mathbf{v}_N\}$ of size $M \times N$ into a variable-separated finite sum

$$\mathbf{V}_1^N(\mathbf{x}, t) = \sum_{k=1}^{K} \mathbf{q}_k(t)\, \boldsymbol{\phi}_k(\mathbf{x}), \tag{2.69}$$

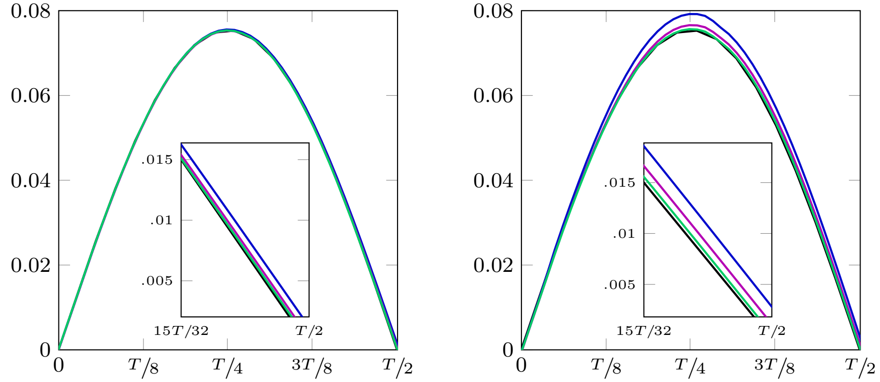

(a) c_l INSE. (b) c_l NOCA.

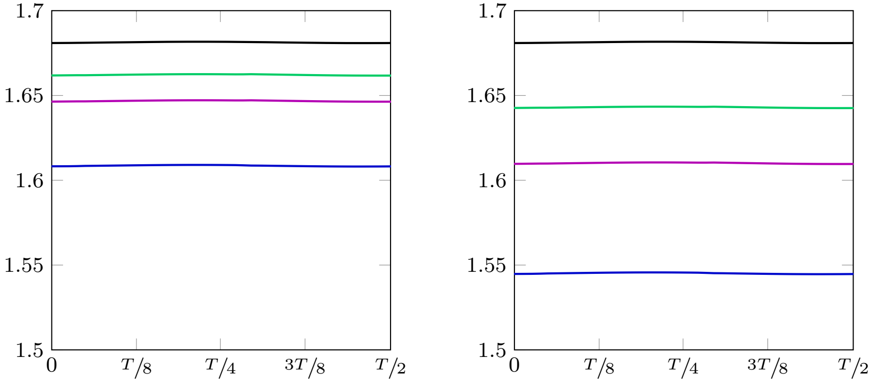

(c) c_d INSE. (d) c_d NOCA.

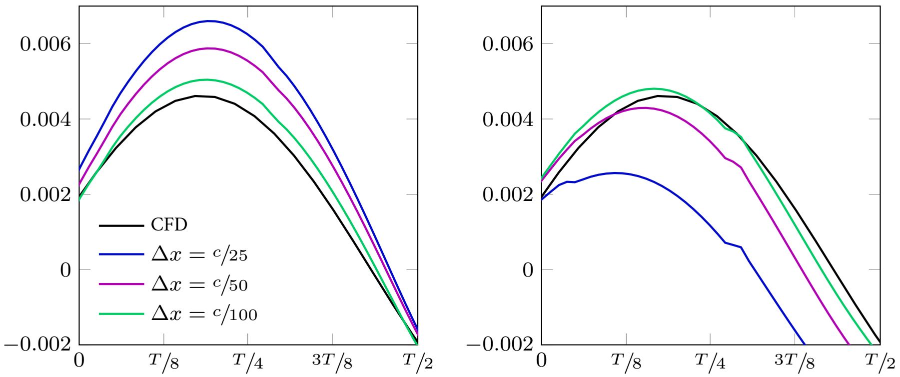

(e) c_m INSE. (f) c_m NOCA.

Figure 2.21: Verification of the implementation of INSE and NOCA methodologies: lift, drag and pitching moment coefficients as a function of time for a half shedding period obtained for different grid spacing.

where $\mathbf{q}_k$ are the generalized coordinates representing the time response, and $\boldsymbol{\phi}_k$ is the k^{th} spatial mode shape that only depends on the spatial coordinates. Both $\mathbf{q}_k$ and $\boldsymbol{\phi}_k$ are vectors of length N and M, respectively, and the number of modes $K = \min(M, N)$. The decomposition given by Eq. (2.69) is not unique and the choice for $\boldsymbol{\phi}_k$ defines the specific decomposition. Depending on the chosen decomposition, different types of information on the simulated and/or measured flow can be obtained. This section introduces the two decomposition methods considered in the context of this thesis: Proper Orthogonal Decomposition (POD) and Dynamic Mode Decomposition (DMD). More information on POD and DMD can be found in the work of Liang et al. (2002) and Schmid (2010), respectively.

2.4.1 Proper Orthogonal Decomposition

Proper Orthogonal Decomposition aims to capture the dominant components of a process in the most efficient way, i.e. using as few spatial modes as possible (Liang et al., 2002). This technique has been used for many years under different denominations and in many disciplines such as image processing (Kirby and Sirovich, 1990), structural vibration (Feeny and Kappagantu, 1998) or atmospheric science (Hannachi et al., 2007). It is known as Principal Component Analysis (PCA), Karhunen-Loève Decomposition (KLD) but also as Empirical Orthogonal Functions (EOF) or Singular Value Decomposition (SVD). In fluid dynamics, POD has been popularized by Lumley (1967) but the technique was introduced independently by different authors: Kosambi (1943), Loeve (1945), Karhunen (1946), Pugachev (1953), Obukhov (1960), Holmström (1963), Roukhovetz (1963) and Lumley (1970).

The goal of POD is to find a set of ordered orthonormal basis vectors $\boldsymbol{\phi}_k^{\text{POD}}$ and the corresponding $\mathbf{q}_k^{\text{POD}}$ such that $\mathbf{V}_1^N$ can be expressed optimally using the first l modes $\boldsymbol{\phi}_k^{\text{POD}}$. Mathematically, if the minimization of the mean-square error is used as a measure of optimality, this problem can be written as

$$\min_{\boldsymbol{\phi}_k^{\text{POD}}} \varepsilon^2(l) = \min_{\boldsymbol{\phi}_k^{\text{POD}}} \mathbb{E}\left\{\|\mathbf{V}_1^N - \left(\widehat{\mathbf{V}}_1^N\right)_l^{\text{POD}}\|^2\right\}. \tag{2.70}$$

In Eq. (2.70), the right-hand side stands for the expectation of the mean square error obtained if $\mathbf{V}_1^N$ is approximated by $\widehat{\mathbf{V}}_1^N$, the sum of the first l modes of the POD decomposition. If the entire POD basis is considered, this decomposition reads

$$\begin{aligned} \mathbf{V}_1^N(\mathbf{x}, t) &= \sum_{k=1}^{K} \mathbf{q}_k^{\text{POD}}(t)\, \boldsymbol{\phi}_k^{\text{POD}}(\mathbf{x}), \\ \text{s.t.} \quad \boldsymbol{\phi}_i^{\text{POD}^T} \boldsymbol{\phi}_j^{\text{POD}} &= \delta_{ij} \quad i, j = 1, 2, \dots K. \end{aligned} \tag{2.71}$$

The POD modes are computed from matrix $\mathbf{V}_1^N$ by solving an eigenvalue problem or equivalently through a SVD decomposition. The subsequent paragraphs expose first the derivation of the eigenvalue problem in the context of PCA as explained by Liang et al. (2002), then, the relationship with SVD is highlighted.

The condition given by Eq. (2.70) is equivalent to imposing that the first l generalized coordinates $\mathbf{q}_k^{\text{POD}}$ contain most of the variation present in the original matrix $\mathbf{V}_1^N$. Mathematically, this corresponds to maximizing the variance

$$\max_{\mathbf{q}_k^{\text{POD}}} \sum_{k=1}^{l} \mathbb{E}\left\{\left(\mathbf{q}_k^{\text{POD}} - \mathbb{E}\left\{\mathbf{q}_k^{\text{POD}}\right\}\right)^2\right\}. \tag{2.72}$$

The generalized coordinates can be written as $\mathbf{q}_k^{\text{POD}} = \boldsymbol{\phi}_k^{\text{POD}^T} \mathbf{V}_1^N$, so that Eq. (2.72) becomes

$$\begin{aligned} \max_{\boldsymbol{\phi}_k^{\text{POD}}} & \sum_{k=1}^{l} \boldsymbol{\phi}_k^{\text{POD}^T} \boldsymbol{\Sigma}_{\mathbf{V}_1^N} \boldsymbol{\phi}_k^{\text{POD}} \\ \text{s.t.} \quad & \boldsymbol{\phi}_i^{\text{POD}^T} \boldsymbol{\phi}_j^{\text{POD}} = \delta_{ij} \quad i, j = 1, 2, \dots l, \end{aligned} \tag{2.73}$$

where $\boldsymbol{\Sigma}_{\mathbf{V}_1^N} = \mathbb{E}\left\{\left(\mathbf{V}_1^N - \mathbb{E}\left\{\mathbf{V}_1^N\right\}\right)\left(\mathbf{V}_1^N - \mathbb{E}\left\{\mathbf{V}_1^N\right\}\right)^T\right\}$ is the $M \times M$ covariance matrix and the orthonormality of the POD modes comes from a normalization constraint. For a sufficient number of snapshots $\mathbf{v}_n$ (Liang et al., 2002), the covariance matrix can be obtained from $\mathbf{V}_1^N$ through

$$\boldsymbol{\Sigma}_{\mathbf{V}_1^N} = \frac{1}{N}\mathbf{V}_1^N\left(\mathbf{V}_1^N\right)^T. \tag{2.74}$$

The constrained optimization problem given by Eq. (2.73) can be solved using the method of Lagrange multipliers. The Lagrange function $\mathcal{L}$ is then written as

$$\mathcal{L} = \sum_{k=1}^{l}\left[\boldsymbol{\phi}_k^{\text{POD}\,T}\boldsymbol{\Sigma}_{\mathbf{V}_1^N}\boldsymbol{\phi}_k^{\text{POD}} - \sum_{j=1}^{l}\lambda_j^{\text{POD}}\left(\boldsymbol{\phi}_k^{\text{POD}\,T}\boldsymbol{\phi}_j^{\text{POD}} - \delta_{kj}\right)\right], \tag{2.75}$$

where λ_j^{POD} are the Lagrange multipliers. Differentiating function $\mathcal{L}$ with respect to $\boldsymbol{\phi}_k^{\text{POD}}$ yields

$$\partial_{\boldsymbol{\phi}_k^{\text{POD}}}\mathcal{L} = \sum_{k=1}^{l}\left[\boldsymbol{\Sigma}_{\mathbf{V}_1^N}\boldsymbol{\phi}_k^{\text{POD}} - \lambda_k^{\text{POD}}\boldsymbol{\phi}_k^{\text{POD}}\right], \tag{2.76}$$

which has to be zero to satisfy Eq. (2.73). Therefore, the POD modes satisfying the condition given by Eq. (2.72), and consequently (2.70), are determined by solving the eigenvalue problem

$$\boldsymbol{\Sigma}_{\mathbf{V}_1^N}\boldsymbol{\phi}^{\text{POD}} = \boldsymbol{\lambda}^{\text{POD}}\boldsymbol{\phi}^{\text{POD}}, \tag{2.77}$$

where $\boldsymbol{\lambda}^{\text{POD}}$ and $\boldsymbol{\phi}^{\text{POD}}$ are respectively the vector of eigenvalues λ_k^{POD} and the matrix containing the $\boldsymbol{\phi}_k^{\text{POD}}$ modes. Finally, it can be shown that the mean-square error $\varepsilon(l)^2$ in Eq. (2.70) is related to λ_l^{POD} by

$$\varepsilon^2(l) = \sum_{k=l+1}^{M}\lambda_k^{\text{POD}}. \tag{2.78}$$

Equations (2.71), (2.74) and (2.77) constitute the core of the POD procedure. However, the solution of the eigenvalue problem given by (2.77) is not the only way to compute the POD modes. Another procedure consists in using the singular value decomposition of matrix $\boldsymbol{\Sigma}_{\mathbf{V}_1^N}$ to determine the modes $\boldsymbol{\phi}_k^{\text{POD}}$. The matrix of snapshots can be expressed as

$$\mathbf{V}_1^N = \mathbf{U}\boldsymbol{\Sigma}\mathbf{W}^*, \tag{2.79}$$

where $\mathbf{U}$ and $\mathbf{W}$ are unitary matrices of size $M \times M$ and $N \times N$, respectively, $\boldsymbol{\Sigma}$ is a $M \times N$ rectangular diagonal matrix containing the singular values of $\mathbf{V}_1^N$ and $(\cdot)^*$ stands for the conjugate transpose. Inserting this last expression into the definition of the covariance matrix (2.74) and using the properties of matrices $\mathbf{U}$, $\boldsymbol{\Sigma}$ and $\mathbf{W}$ one obtains

$$\boldsymbol{\Sigma}_{\mathbf{V}_1^N}\mathbf{U} = \frac{1}{N}\boldsymbol{\Sigma}^2\mathbf{U}. \tag{2.80}$$

Comparing Eqs. (2.77) and (2.80), it can be seen that the matrix of POD modes $\boldsymbol{\phi}^{\text{POD}}$ is equivalent to the matrix of left singular vectors $\mathbf{U}$ obtained by SVD and the associated λ_k^{POD} are the corresponding squared singular values divided by N, i.e. Σ_k^2/N. The core procedure describing the POD methodology is summarized in Algo. 2, and is implemented in Matlab.

2.4.2 Dynamic Mode Decomposition

Dynamic Mode Decomposition was introduced by Schmid (2010) who intended to develop a technique to extract dynamical flow features without knowing the underlying governing equations.

Algorithm 2: POD decomposition.

```
Input: $\mathbf{V}_1^N$
Output: $\boldsymbol{\phi}^{\text{POD}}$, $\mathbf{q}^{\text{POD}}$ and $\boldsymbol{\lambda}^{\text{POD}}$
/* Initialization                                                    */
$\mathbf{V}_a = \mathbf{V}_1^N$
/* Calculation of dynamic process characteristics                     */
calculate singular value decomposition: $\mathbf{V}_a = \mathbf{U}\boldsymbol{\Sigma}\mathbf{W}^*$;
calculate effective number of POD modes: $K = \min(M, N)$;
calculate POD modes: $\boldsymbol{\phi}^{\text{POD}} = \mathbf{U}(:,1{:}K)$;
calculate Lagrangian multipliers: $\boldsymbol{\lambda}^{\text{POD}} = {}^1\!/_N\boldsymbol{\Sigma}^2(K,K)$;
calculate generalized coordinates: $\mathbf{q}^{\text{POD}} = \left(\boldsymbol{\phi}^{\text{POD}}\right)^{-1}\mathbf{V}_a$;
```

Since its introduction, DMD has been applied to a wide variety of flows (e.g. Schmid, 2010; Grilli et al., 2012; Massa et al., 2012; Muld et al., 2012) and some modifications to the basic procedure have been proposed (Chen et al., 2012; Goulart et al., 2012; Tu et al., 2014).

The original version of DMD is based on numerical or experimental data composing the matrix $\mathbf{V}_1^N$ in Eq. (2.69). The method decomposes these outputs into single frequency modes $\boldsymbol{\phi}_k^{\text{DMD}}$ describing the dynamic process. Therefore, the time response represented by the $\mathbf{q}_k$ in Eq. (2.69) can be expressed as $\mathbf{q}_k^{\text{DMD}} = q_k^{\text{DMD}} \exp\left(\lambda_k^{\text{DMD}}\mathbf{t}\right)$, where λ_k is the complex frequency associated with the k^{th} DMD mode while $\mathbf{t}$ is the line vector containing the N time-steps. Thus, in the context of DMD, the modal decomposition given by Eq. (2.69) becomes

$$\mathbf{V}_1^N(\mathbf{x}, t) = \sum_{k=1}^{K} q_k^{\text{DMD}} \boldsymbol{\phi}_k^{\text{DMD}} \exp\left(\lambda_k^{\text{DMD}}\mathbf{t}\right). \tag{2.81}$$

A linear mapping $\mathbf{A}$ is assumed between two consecutive snapshots of the flow, such that $\mathbf{v}_{i+1} = \mathbf{A}\mathbf{v}_i$. Moreover, assuming that the linear mapping is approximately the same over the entire time interval considered, the series of N snapshots separated by a constant sampling time Δt can then be formulated as a Krylov sequence

$$\mathbf{V}_1^N = \{\mathbf{v}_1, \mathbf{A}\mathbf{v}_1, \mathbf{A}^2\mathbf{v}_1 \ldots, \mathbf{A}^{N-1}\mathbf{v}_1\}, \tag{2.82}$$

which, for a non-linear process, corresponds to a linear tangent approximation. From Eq. (2.82), the sequence beginning at time-step 2 can be written as

$$\mathbf{V}_2^N = \mathbf{A}\{\mathbf{v}_1, \mathbf{v}_2, \mathbf{v}_3 \ldots, \mathbf{v}_{N-1}\} = \mathbf{A}\mathbf{V}_1^{N-1}. \tag{2.83}$$

The objective of DMD is to extract the dynamic characteristics of the process described by the $M \times M$ matrix $\mathbf{A}$. However, $\mathbf{A}$ is usually not known a priori and therefore, it needs to be approximated from the sequence of snapshots $\mathbf{V}_1^N$. To this end, it is assumed that, beyond a critical number of snapshots, the vectors $\mathbf{v}_i$ become linearly dependent. The last snapshot $\mathbf{v}_N$ can thus be approximated as a linear combination of $\mathbf{v}_i$,

$$\begin{aligned} \mathbf{v}_N &= a_1\mathbf{v}_1 + a_2\mathbf{v}_2 + \cdots + a_{N-1}\mathbf{v}_{N-1} + \mathbf{r}, \\ &= \mathbf{V}_1^{N-1}\mathbf{a} + \mathbf{r}, \end{aligned} \tag{2.84}$$

where a_i are the coefficients of the linear combination. The residual vector $\mathbf{r}$ indicates how accurately the vector $\mathbf{v}_N$ is approximated by previous snapshots $\mathbf{v}_i$. In matrix form, considering that the i^{th} column of $\mathbf{V}_2^N$ is identical to the $(i+1)^{\text{th}}$ column of $\mathbf{V}_1^{N-1}$, for $i = 1, \ldots, N-1$, this linear combination can be written as

$$\mathbf{V}_2^N = \mathbf{A}\mathbf{V}_1^{N-1} = \mathbf{V}_1^{N-1}\mathbf{S} + \mathbf{r}\mathbf{e}_{N-1}^T \,, \tag{2.85}$$

where the vector $\mathbf{e}_{N-1}^T = (0, \ldots, 0, 1)$ and $\mathbf{S}$ is the $(N-1) \times (N-1)$ companion matrix

$$\mathbf{S} = \begin{pmatrix} 0 & & & & a_1 \\ 1 & 0 & & & a_2 \\ & \ddots & \ddots & & \vdots \\ & & 1 & 0 & a_{N-2} \\ & & & 1 & a_{N-1} \end{pmatrix} . \tag{2.86}$$

For a series of snapshots leading to a sufficiently low residual, the dynamics extracted from $\mathbf{S}$ provides a good approximation of the dynamics contained in $\mathbf{A}$ that describes the dynamics of the process. In particular, the vector of eigenvalues of $\mathbf{A}$ is approximated by $\boldsymbol{\mu}$, the vector of eigenvalues of $\mathbf{S}$. Then, the eigenvalue μ_k is related to the complex frequency λ_k^{DMD} in Eq. (2.81) by $\lambda_k^{\text{DMD}} = \log(\mu_k)/\Delta t$. The $M \times K$ matrix of DMD modes $\boldsymbol{\phi}^{\text{DMD}}$ contains the eigenvectors of $\mathbf{A}$ expressed in the snapshot basis, where each computed vector has been normalized. Mathematically, a column vector of this matrix is approximated by $\boldsymbol{\phi}_k^{\text{DMD}} = \mathbf{v}_1^{N-1}\mathbf{x}_k/\|\mathbf{v}_1^{N-1}\mathbf{x}_k\|$, where the matrix $\mathbf{x}$ comes from the eigenvalue problem $\mathbf{S}\mathbf{x}_k = \mu_k\mathbf{x}_k$. Finally, to retrieve the matrix of snapshots $\mathbf{V}_1^{N-1}$, the temporal contribution of the modal decomposition (2.69) should be the $K \times N$ matrix $\mathbf{q}^{\text{DMD}} = \|\mathbf{V}_1^{N-1}\mathbf{x}\|\mathbf{x}^{-1}$. Therefore, the amplitude q_k^{DMD} of each DMD mode can be calculated through $q_k^{\text{DMD}} = \mathbf{q}_{k,1}^{\text{DMD}}/\exp\left(\lambda_j^{\text{DMD}}\mathbf{t}_1\right)$, where index 1 associated with the two vectors corresponds to their first entry.

The solution of the least square problem (2.84) is required to build the companion matrix $\mathbf{S}$. This can be obtained as

$$\mathbf{a} = \left(\mathbf{V}_1^{N-1}\right)^+ \mathbf{v}_N \,, \tag{2.87}$$

where $\left(\mathbf{V}_1^{N-1}\right)^+$ is the pseudoinverse of $\mathbf{V}_1^{N-1}$,

$$\left(\mathbf{V}_1^{N-1}\right)^+ = \begin{cases} \left(\mathbf{V}_1^{N-1}\right)^* \left[\mathbf{V}_1^{N-1}\left(\mathbf{V}_1^{N-1}\right)^*\right]^{-1} & \text{if } M < N, \\ \left[\left(\mathbf{V}_1^{N-1}\right)^* \mathbf{V}_1^{N-1}\right]^{-1} \left(\mathbf{V}_1^{N-1}\right)^* & \text{if } M > N. \end{cases} \tag{2.88}$$

The pseudoinverse matrix itself can be obtained through a singular value or a **QR** decomposition of $\mathbf{V}_1^{N-1}$. However, the latter can only be used if $M > N$. In this case $\left(\mathbf{V}_1^{N-1}\right)^+ = \mathbf{R}^{-1}\mathbf{Q}^*$. The singular value decomposition $\mathbf{V}_1^{N-1} = \mathbf{U}\boldsymbol{\Sigma}\mathbf{W}^*$ is usually preferred to avoid an ill-conditioned problem. Moreover, it highlights more explicitly the close connection between POD and DMD. In that context, the pseudoinverse is written as $\left(\mathbf{V}_1^{N-1}\right)^+ = \mathbf{W}\Sigma^+\mathbf{U}^*$.

In a practical implementation, the use of the companion matrix $\mathbf{S}$ can lead to an ill-conditioned algorithm. Therefore, Schmid (2010) proposed a more robust implementation that uses a dense matrix $\tilde{\mathbf{S}}$ defined using the singular value decomposition of $\mathbf{V}_1^{N-1}$ as

$$\tilde{\mathbf{S}} = \mathbf{U}^*\mathbf{V}_2^N\mathbf{W}\boldsymbol{\Sigma}^{-1}. \tag{2.89}$$

Matrix $\tilde{\mathbf{S}}$ is related to $\mathbf{A}$ through the similarity transformation $\mathbf{A} = \mathbf{U}\tilde{\mathbf{S}}\mathbf{U}^*$. Since $\mathbf{U}$ contains the POD modes computed from the snapshots sequence $\mathbf{V}_1^{N-1}$, the matrix $\tilde{\mathbf{S}}$ is then the result of a projection of the linear operator $\mathbf{A}$ onto the POD basis. Moreover, this procedure allows to reduce the number of DMD modes by considering only the most important POD modes. Note that this corresponds to $\mathbf{V}_1 \approx \tilde{\mathbf{U}}\tilde{\boldsymbol{\Sigma}}\tilde{\mathbf{W}}^*$ in Algo. 4 that summarizes the present methodology. Some of the eigenvalues and eigenvectors of $\mathbf{A}$ are obtained as the solution of the eigenvalue problem $\tilde{\mathbf{S}}\mathbf{y}_k = \mu_k \mathbf{y}_k$. As stated previously, the dynamics of the process is fully described by $\mathbf{A}$. Therefore, the complex frequency λ_k^{DMD} associated with each mode is $\lambda_k^{\text{DMD}} = \log(\mu_k)/\Delta t$. The normalized DMD modes are calculated with $\boldsymbol{\phi}_k^{\text{DMD}} = {}^{\mathbf{U}\mathbf{y}_k}\!/\!_{\|\mathbf{U}\mathbf{y}_k\|}$ while the temporal component is $\mathbf{q}_k^{\text{DMD}} = \|\mathbf{U}\mathbf{y}_k\| \left(\mathbf{y}^{-1}\boldsymbol{\Sigma}\mathbf{W}^*\right)_k$. Finally, the amplitude q_k^{DMD} of each DMD mode is calculated as previously using $q_k^{\text{DMD}} = {}^{\mathbf{q}_{k,1}^{\text{DMD}}}\!/\!_{\exp\left(\lambda_j^{\text{DMD}}\mathbf{t}_1\right)}$, which completes the modal decomposition in Eq. (2.81).

To summarize, the two algorithms used in the context of this thesis and implemented in Matlab are exposed in Algos. 3 and 4. Algorithm 3 is based on the companion matrix $\mathbf{S}$ and is usable for any shape of matrix $\mathbf{V}_1^N$, while Algo. 4 is based on matrix $\tilde{\mathbf{S}}$ and should therefore be used with $\mathbf{V}_1^N$ for which $M \geqslant N+1$.

Algorithm 3: DMD decomposition based on companion matrix **S**.

```
Input: $\mathbf{V}_1^N$ and $\mathbf{t}$
Output: $\boldsymbol{\phi}^{\text{DMD}}$, $\boldsymbol{\lambda}^{\text{DMD}}$, $\mathbf{q}^{\text{DMD}}$ and $\mathbf{r}$
/* Initialization                                                          */
$\mathbf{V}_a = \mathbf{V}_1^N(:,1{:}N-1)$ and $\mathbf{v}_N = \mathbf{V}_1^N(:,N)$;
$\Delta t = \mathbf{t}(N) - \mathbf{t}(N-1)$ and $t_1 = \mathbf{t}(1)$;
/* Calculation of companion matrix S and residual r                        */
calculate pseudoinverse $\mathbf{V}_a^+$;
solve least square problem: $\mathbf{a} = \mathbf{V}_a^+\mathbf{v}_N$;
calculate residual: $\mathbf{r} = \mathbf{V}_a\mathbf{a} - \mathbf{v}_N$;
build companion matrix $\mathbf{S}$ using $\mathbf{a}$;
/* Calculation of dynamic process characteristics                          */
solve eigenvalue problem: $\mathbf{S}\mathbf{x} = \boldsymbol{\mu}\mathbf{x}$;
calculate normalized DMD modes: $\boldsymbol{\phi}_k^{\text{DMD}} = {}^{\mathbf{V}_a\mathbf{x}_k}/_{\|\mathbf{V}_a\mathbf{x}_k\|}$;
calculate frequency and growth-rate: $\boldsymbol{\lambda}^{\text{DMD}} = {}^{\log(\boldsymbol{\mu})}/_{\Delta t}$;
calculate matrix of time response: $\mathbf{q}^{\text{DMD}} = \|\mathbf{V}_a\mathbf{x}\|\mathbf{x}^{-1}$;
calculate amplitude: $q_k^{\text{DMD}} = {}^{\mathbf{q}^{\text{DMD}}(k,1)}/_{\exp(\lambda_k^{\text{DMD}}t_1)}$;
```

Algorithm 4: DMD decomposition based on matrix $\tilde{\mathbf{S}}$.

```
Input: $\mathbf{V}_1^N$, $\mathbf{t}$ and $\text{nb}^{\text{POD}}$
Output: $\boldsymbol{\phi}^{\text{DMD}}$, $\boldsymbol{\lambda}^{\text{DMD}}$, $\mathbf{q}^{\text{DMD}}$ and $\mathbf{r}$
/* Initialization */
$\mathbf{V}_a = \mathbf{V}_1^N(:,1{:}N-1)$, $\mathbf{V}_b = \mathbf{V}_1^N(:,2{:}N)$ and $\mathbf{v}_N = \mathbf{V}_1^N(:,N)$;
$\Delta t = \mathbf{t}(N) - \mathbf{t}(N-1)$ and $t_1 = \mathbf{t}(1)$;
/* Calculation of matrix S̃ and residual r */
calculate single value decomposition: $\mathbf{V}_a = \mathbf{U}\boldsymbol{\Sigma}\mathbf{W}^*$;
if $nb^{POD} = N$ then
    $\tilde{\mathbf{U}} = \mathbf{U}(:,N)$, $\tilde{\boldsymbol{\Sigma}} = \boldsymbol{\Sigma}(N,N)$ and $\tilde{\mathbf{W}} = \mathbf{W}$;
else if $nb^{POD} < N$ then
    $\tilde{\mathbf{U}} = \mathbf{U}(:,\text{nb}^{\text{POD}})$, $\tilde{\boldsymbol{\Sigma}} = \boldsymbol{\Sigma}(\text{nb}^{\text{POD}},\text{nb}^{\text{POD}})$ and $\tilde{\mathbf{W}} = \mathbf{W}(:,\text{nb}^{\text{POD}})$;
else
    case not supported by this algorithm;
end
build matrix $\tilde{\mathbf{S}}$ : $\tilde{\mathbf{S}} = \tilde{\mathbf{U}}^*\mathbf{V}_b\tilde{\mathbf{W}}\tilde{\boldsymbol{\Sigma}}^{-1}$;
if $nb^{POD} = N$ then
    calculate residual: $\mathbf{R} = \tilde{\mathbf{U}}\tilde{\mathbf{S}}\tilde{\mathbf{U}}^*\mathbf{V}_a - \mathbf{V}_b$ and $\mathbf{r} = \mathbf{R}(:,N)$;
else
    calculation of residual not possible;
end
/* Calculation of dynamic process characteristics */
solve eigenvalue problem: $\tilde{\mathbf{S}}\mathbf{y} = \boldsymbol{\mu}\mathbf{y}$;
calculate normalized DMD modes: $\boldsymbol{\phi}_k^{\text{DMD}} = \tilde{\mathbf{U}}\mathbf{y}_k / \|\tilde{\mathbf{U}}\mathbf{y}_k\|$;
calculate frequency and growth-rate: $\boldsymbol{\lambda}^{\text{DMD}} = \log(\boldsymbol{\mu}) / \Delta t$;
calculate matrix of time response: $\mathbf{q}^{\text{DMD}} = \|\tilde{\mathbf{U}}\mathbf{y}\|\mathbf{y}^{-1}\tilde{\boldsymbol{\Sigma}}\tilde{\mathbf{W}}^*$;
calculate amplitude: $q_k^{\text{DMD}} = \mathbf{q}^{\text{DMD}}(k,1) / \exp(\lambda_k^{\text{DMD}} t_1)$;
```

CHAPTER 3

Detached flow around a 4:1 rectangular cylinder

This chapter is dedicated to the study of the flow around a 4:1 rectangular cylinder at different angles of incidence. Both experimental measurements and numerical simulations are performed to analyze the flow physics and, thus, improve the fundamental knowledge of the corresponding dynamical phenomena. Additionally, this chapter aims to assess the accuracy of the different numerical approaches in predicting aerodynamic loads and the separation-reattachment dynamics.

3.1 Introduction

The flow field around bodies of elongated rectangular cross section is of great interest for wind engineering applications. Examples are long span bridges or tall buildings. Despite the simple two-dimensional body geometry, the turbulent three-dimensional nature of such flows and the unsteady separation and reattachment dynamics are highly complex. This explains why rectangular cylinders at zero incidence have been extensively studied, first experimentally (Nakaguchi et al., 1968; Nakamura and Mizota, 1975; Washizu et al., 1978; Okajima, 1983; Stokes and Welsh, 1986) and then numerically (Tamura et al., 1993; Yu and Kareem, 1998; Shimada and Ishihara, 2002). These works have shown that the flow dynamics around such cross sections is mainly influenced by the ratio of the chord c to the depth d of the cross section. The impact of the flow parameters and geometry, such as Reynolds number, turbulence intensity or corner sharpness, depends on the $^{c}\!/_{d}$ ratio considered and the range of variability of these parameters.

Following the experimental studies conducted by Nakaguchi et al. (1968) and Stokes and Welsh (1986), Shimada and Ishihara (2002) investigated the impact of the $^{c}\!/_{d}$ ratio at zero incidence and $\mathrm{Re}_d = 2.2 \times 10^4$ through URANS simulations. They divided the aerodynamic behavior into three main categories based on the absence or presence of reattachment of the shear layer during a shedding cycle. These categories depend on the ratio $^{c}\!/_{d}$ and are illustrated in Fig. 3.1.

For short cylinders with $^{c}\!/_{d} \leqslant 2.8$, flow separation occurs at the leading edges and the rectangular cross section is too short to allow reattachment of the separated shear layer. This behavior is shown in Figs. 3.1a to 3.1c. The flow is thus fully separated and vortices are periodically shed from the leading edge forming a vortex street downstream of the body. As the upper and lower surfaces are entirely immersed in the separated region, rectangular cylinders with a ratio $^{c}\!/_{d} < 2.8$ are characterized by large fluctuations in lift. Depending on the ratio $^{c}\!/_{d}$, the vortex is shed close to or far away from the rear part of the cylinder, which impacts the shedding frequency and the drag. A peak in drag occurs at a ratio $^{c}\!/_{d} = 0.6$ (Nakaguchi et al., 1968), for which the shed vortex is located the closest to the rear part of the cross section as visible in Fig. 3.1a. Moreover, the Strouhal number $\mathrm{St} = {}^{fd}\!/_{U_\infty}$, where f is the shedding frequency, decreases as the vortices are shed farther away from the cylinder. A minimum St is observed for $^{c}\!/_{d} = 2$ and the corresponding flow is depicted in Fig. 3.1c. For rectangular cylinders with $2 \leqslant \frac{c}{d} \leqslant 2.8$, occasional reattachment

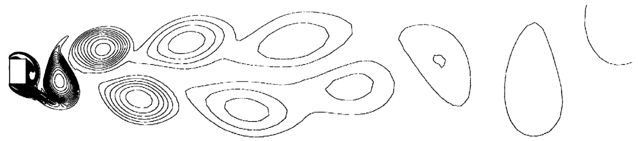

(a) $c/d = 0.6$.

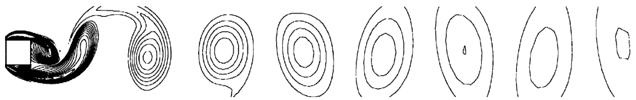

(b) $c/d = 1$.

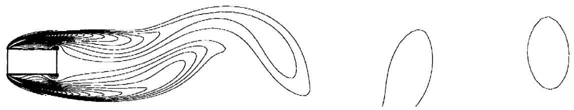

(c) $c/d = 2$.

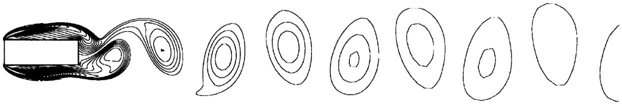

(d) $c/d = 3$.

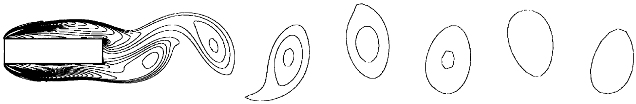

(e) $c/d = 4$.

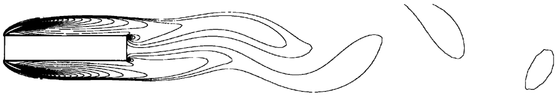

(f) $c/d = 5$.

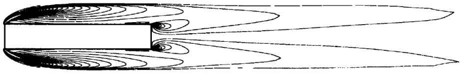

(g) $c/d = 6$.

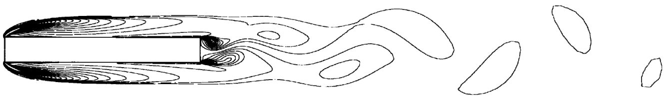

(h) $c/d = 8$.

Figure 3.1: Instantaneous vorticity contours around rectangular cylinders of different c/d ratio at the maximum lift. Reproduced from the work of Shimada and Ishihara (2002).

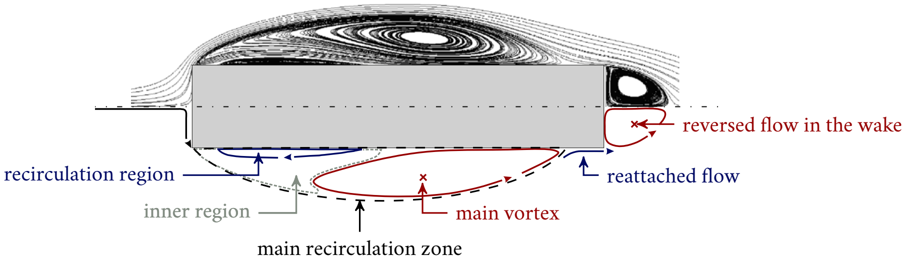

Figure 3.2: Streamlines averaged in time and along the spanwise dimension (top) and schematic of the most important mean flow structures (bottom). Adapted from Bruno et al. (2010).

may occur leading to a bi-modal vortex shedding frequency (Otsuki et al., 1974; Washizu et al., 1978). On rectangular cross sections with a ratio $2.8 < {}^{c}\!/_{d} < 6$, the shear layer reattaches periodically to the upper and lower surfaces upstream of the trailing edge, as shown in Figs. 3.1d to 3.1f. Moreover, vortex shedding occurs from both the leading and trailing edges. Finally, for longer rectangular cylinder with ${}^{c}\!/_{d} \geqslant 6$ depicted in Figs. 3.1g and 3.1h, the flow is fully reattached upstream of the trailing edge. A separation bubble grows and breaks randomly into vortices. Consequently, the vortex shedding becomes irregular and no clear vortex street is identified. For ratio ${}^{c}\!/_{d} > 8$, a stronger vortex shedding resumes from the trailing edge of the section.

Following these studies, the Benchmark on the Aerodynamics of a Rectangular Cylinder (BARC) has been proposed (Bartoli et al., 2008). The BARC aims to provide both experimental and numerical contributions within a homogeneous and fully-described setup. The rectangular cylinder specifically studied has a chord-to-depth ratio equal to 5. Bruno et al. (2014) summarized the first four years of activity of the BARC comparing among themselves more than 70 studies in terms of bulk parameters, flow and pressure statistics, as well as spanwise correlations. Among the principal conclusions, Bruno et al. (2014) showed that a narrow distribution of results is obtained for the Strouhal number or the mean drag coefficient $\overline{c_D}$ while those collected for the standard deviation of the lift coefficient are significantly dispersed. Bruno et al. (2014) argued that scattering of numerical and experimental results is due to the high sensitivity of the flow along the upper and lower surfaces of the rectangular cylinder.

In the context of the BARC, Bruno et al. (2010) described the different structures appearing in the mean flow around a 5:1 rectangular cylinder. As shown in Fig. 3.2, the mean flow can be divided into three main regions: the main recirculation zone, the reattached flow and the reversed flow in the wake. Moreover, the main recirculation zone, also called separation bubble, consists of three sub-regions. Near the leading edge, the approximately triangular inner region is responsible for the creation of vortices shed downstream. The coalescence of those vortices forms the main vortex. Below this inner region lies a thin recirculation region that rotates in the direction opposite to the main vortex. According to Bruno et al. (2010), the apparition of an inner region is characteristic of the flow field around a wedge. Therefore, the presence of an inner region is typical of the flow around a bluff body. The same authors also described what they found to be the main mechanism responsible for the lift generation. They demonstrated that the region lying between the main vortex core and the reattachment point is the most significant contributor to the lift generation. This region is called the mean pressure recovery region. Moreover, Bruno et al. (2010) associated the variation of the lift over a vortex-shedding cycle to the location of the vortices shed along the upper and lower surfaces. According to Shimada and Ishihara (2002) and as described above, the same type of flow is observed around rectangular cylinders with a ratio ${}^{c}\!/_{d} = 4$ and ${}^{c}\!/_{d} = 5$. Therefore, the flow topology and the lift generation process occurring for the rectangular cylinder studied in this chapter are expected to be the same as those detailed by Bruno et al. (2010).

For a rectangular cylinder with sharp edges, separation always occurs at the leading edges, irrespective of the Reynolds number. However, a variation of Re impacts the shear layer and, in particular, its reattachment along the upper and lower surfaces. Still within the framework of the BARC benchmark, Schewe (2013) investigated experimentally the impact of the Reynolds number on the aerodynamic coefficients, considering Reynolds numbers ranging between 2×10^4 and 2×10^6 and different angles of incidence. Schewe (2013) showed that the Reynolds number has a minor influence on both the drag coefficient and the Strouhal number, but significantly impacts the lift coefficient. Increasing the Reynolds number leads to a growth of the lift slope $\overline{c_L}_\alpha$ and a shift of the maximum lift towards lower incidence. In particular, an increase from $\mathrm{Re} = 3 \times 10^4$ to $\mathrm{Re} = 3 \times 10^5$ leads to a lift slope increasing from $5.7\ \mathrm{rad}^{-1}$ to $9.3\ \mathrm{rad}^{-1}$. Schewe (2013) argued that an increase in the turbulence level causes a modification of the location of the reattachment point on the lower surface. This reattachment point moves upstream and the recirculation bubble thus shortens. This modification of the flow topology impacts the pressure coefficient distribution and therefore the lift. Mannini et al. (2010) also investigated the influence of the Reynolds number through URANS simulations with different turbulence models. For most of them, they found a lift coefficient that is independent of the Reynolds number and poor agreement with experiments except at low Re. The Re sensitivity of the lift could only be reproduced using an Explicit Algebraic Reynolds Stress approach instead of the more classical turbulence models based on the linear Boussinesq hypothesis.

The present work investigates the flow around the elongated 4:1 rectangular cylinder by using both experimental and numerical techniques. Unsteady pressure measurements are performed in the wind tunnel of the University of Liege. Temporal pressure distributions for different incidences are acquired for several Reynolds numbers. The data are then analyzed to study the variation of the flow with the incidence and the Reynolds number. These results also provide a database for comparison with numerical simulations. The flow around the 4:1 rectangular cylinder is also investigated through CFD, by using both URANS and DDES approaches. The objective of the numerical study is two-fold: i) to assess the ability of the different CFD approaches to predict such flows, and ii) to further understand the underlying physics. The validation of the CFD simulations is done by comparing numerical and experimental bulk parameters. DMD is also used to identify similarities and potential discrepancies in the time response of the pressure distribution.

This chapter is thus organized in seven additional sections. Sections 3.2 and 3.3 are dedicated to the description of the experiments and the setup of the CFD simulations, respectively. Then, an overview of the flow topology around the 4:1 rectangular cylinder is exposed in Sec. 3.4. Both time-averaged and unsteady flow dynamics are considered. Experimental mean bulk parameters and pressure coefficients are discussed in Secs. 3.5 and 3.6, respectively. Moreover, a comparison with URANS and DDES results is performed in both cases for validation. Then, Sec. 3.7 presents and compares the variation of the experimental and numerical pressure coefficients within a shedding cycle, and Sec. 3.8 investigates the impact of the Reynolds number on the lift coefficient. Finally, this chapter closes with Sec. 3.9, which summarizes the conducted studies and exposes their main conclusions.

3.2 Experimental setup and measurements

The different experiments performed on the 4:1 rectangular cylinder are conducted in the wind tunnel of the University of Liege. They aim to measure the spatio-temporal pressure distribution along a section of the cylinder. The following sections describe the facility, the model and the experimental measurements.

3.2.1 Wind tunnel and model

The measurements are conducted in a Göttingen-type wind tunnel. The test section is $5\ \mathrm{m}$ long, $2.5\ \mathrm{m}$ wide and $1.8\ \mathrm{m}$ high. The freestream flow velocity ranges from $2\ \mathrm{m/s}$ to $40\ \mathrm{m/s}$ with a

(a) Front view of the mounting apparatus in the wind tunnel facility.

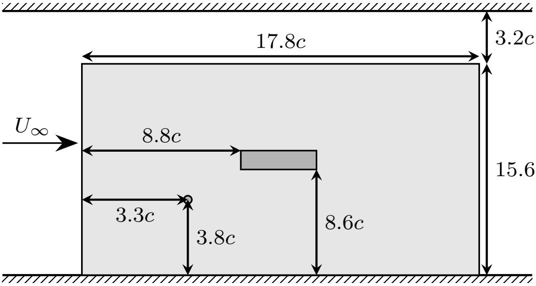

(b) Schematic side view of the mounting apparatus where the rectangular cylinder is depicted in dark gray and the small disk represents the point where the reference freestream velocity and static pressure are measured.

Figure 3.3: Picture and schematic view of the rectangular cylinder mounted in the wind tunnel.

turbulence intensity below 2%. The main Reynolds number studied in the following is $\mathrm{Re} = 4.2 \times 10^4$ which is based on a freestream velocity $U_\infty = 8.3\,\mathrm{m/s}$. Moreover, four additional freestream velocities are also considered to study the impact of the Reynolds number in the range between 3.1×10^4 and 7.6×10^4. These velocities are $U_\infty = 6\,\mathrm{m/s}$, $10.6\,\mathrm{m/s}$, $12.8\,\mathrm{m/s}$ and $15\,\mathrm{m/s}$. As explained below, these values take into account the blockage effect due to the model and support structure standing in the test section.

The model consists of a hollow rectangular aluminum tube of $2\,\mathrm{mm}$ thickness and $1.01\,\mathrm{m}$ length. The cross-section is $8\,\mathrm{cm} \times 2\,\mathrm{cm}$, where the first dimension corresponds to the chord c and the second to the depth d. As shown in Fig. 3.3a, one side of the tube is attached with ball bearings on a vertical beam. This assembly leads to a degree of freedom in pitch which is fixed once the desired incidence is imposed. The other side of the tube is located at a distance of $0.4c$ from the plexiglas window to reduce 3D flow effects. Note that the small size of the model and its cantilever mounting result from its initial development for PIV measurements (Andrianne, 2012) . A wooden plate of dimensions $15.6c \times 17.8c$ is added to the existing apparatus. It aims to reduce as much as possible the impact of the mounting on the flow around the rectangular cylinder. The initial setup without this plate showed clearly an asymmetrical pressure distribution at 0°. Therefore, the nearly symmetrical pressure coefficient distribution obtained at the same incidence with the addition of the plate suggests that it contributes to reduce three-dimensional effects. As depicted in Fig. 3.3b, the rectangular tube is located relatively far from the wooden plate edges and the boundary effects are thus assumed to be small.

The presence of this apparatus in the wind tunnel induces a blockage effect. The freestream velocity seen by the rectangular cylinder differs thus slightly from the user-imposed value. Therefore, the freestream velocity seen by the body of interest is measured through a Cobra 412 probe from Turbulent Flow Instrumentation (TFI) at different points. These points lie in a plane located at a distance of $5.5c$ upstream of the rectangular cylinder leading edge. Their distance from the wooden plate and from the wind tunnel bottom ranges from $1.3c$ to $10c$ and $3.8c$ to $8.8c$, respectively. The velocities measured at these points are within a range of 2%. The velocity measured by the Cobra 412 at the point located at a distance $2.6c$ of the wooden plate in the spanwise direction and $3.8c$ of the wind tunnel bottom wall is chosen as reference value. That particular location is represented by the disc in Fig. 3.3b. As mentioned above, the measured freestream velocities at that point correspond to $U_\infty = 6, 8.3, 10.6, 12.8$ and 15 m/s.

3.2.2 Pressure measurements

Dynamic pressure measurements are carried out to obtain the time response of the pressure distribution along a cross-section of the rectangular cylinder. The present section describes the acquisition device, the different configurations studied and the applied post-processing.

3.2.2.1 Pressure measurements apparatus

Pressure is measured with a multi-channel Dynamic Pressure Measurement System (DPMS) made by TFI. It is able to acquire pressure in a range from ± 10 kPa to ± 35 kPa. This transducer measures $p - p_\infty$, the difference between the pressure p at a tap and a reference pressure p_∞. In the context of this work, p_∞ is the static pressure measured at the reference point shown in Fig. 3.3b. As explained in Sec. 3.2.1, the velocity at this point is close to the freestream velocity. Therefore, p_∞ can be considered as the freestream static pressure.

The pressure is sampled at several pressure taps located on the rectangular cylinder as depicted in Fig. 3.4. As shown in Fig. 3.4a, a section located near the mid-span of the cylinder is covered with 36 taps separated by a distance of 5 mm or 6.25% of the chord. As the pressure taps were drilled manually, their location can vary within 1 mm. In the following, the taps are identified by their non-dimensional curvilinear abscissa $\overline{r} = {}^{r}/_{c}$, r being defined in Fig. 3.4. The pressure taps are connected to the DPMS transducer by Trans Continental Manufacturing tubes. These tubes are 1.34 m long and have a documented internal diameter of 1.32 mm. Each tube forms a pneumatic line that acts as a filter and causes amplitude and phase distortions of the unsteady pressure signal measured. Therefore, a correction is applied as a post-processing step to retrieve the original unsteady pressure. In particular, the theoretical correction proposed by Bergh and Tijdeman (1965) is chosen. The freestream velocity and static pressure being known, the pressure coefficient $C_p = \frac{p-p_\infty}{1/2\rho_\infty U_\infty}$ at each tap location can then be straightforwardly computed.

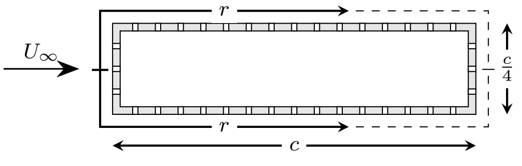

(a) Sectional view.

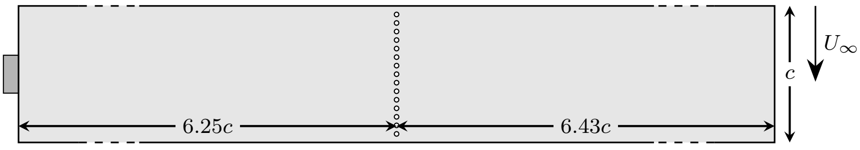

(b) View from the top.

Figure 3.4: Schematic view of the pressure taps located on the rectangular cylinder.

3.2.2.2 Experimental procedure

The pressure distribution is acquired for angles of attack ranging from -7° to 8°. The incidence angle is determined by using a graduated level having a resolution of 1°. The complete range of incidence angles is considered for two freestream velocities, $U_\infty = 8.3$ and 12.8 m/s. For the other freestream velocities, only 0°, 2° and 4° are considered. The sampling frequency f_s is set to 500 Hz. For the nominal freestream velocity $U_\infty = 8.2\,\mathrm{m/s}$, this sampling rate is equivalent to $10f$, where f is the shedding frequency and a value $\mathrm{St} = 0.13$ is assumed (Washizu et al., 1978). For the highest considered freestream velocity, $f_s = 5f$. Each set of experiments lasts 60 s, which corresponds to more than 3 000 shedding cycles for the nominal U_∞ and more than 2 000 for the lowest freestream velocity.

3.2.2.3 Post-processing

The pressure coefficient is first computed from the raw data and filtered using a Butterworth 12th order band-pass filter with a frequency band from 10 to 200 Hz. Then, the amplitude and phase distortions caused by the tube lines on the time response of C_p are corrected. To this end, the distortions are characterized by applying the method proposed by Bergh and Tijdeman (1965). The approach is based on a frequency response function (FRF) linking the true and measured C_p. The theoretical expression of the FRF depends on physical parameters, mainly the atmospheric pressure, and the geometry of the tubes and the transducer. A sensitivity analysis was conducted to determine the impact of parameter uncertainties on the corrected C_p. The results are reported in App. B.1 and show that the amplitude of C_p variations around $\overline{C_p}$ could be underestimated/overestimated by a maximum of 20%. However, this sensitivity analysis demonstrates that the shape of C_p' is not significantly impacted. Therefore, the overall shedding phenomenon is assumed to be captured accurately and the conclusions of the following studies to be robust to uncertainties. In the present context, since their geometric parameters are the same, a single FRF is considered for all tube lines. The Bode plot corresponding to this FRF is depicted in Fig. 3.5. It can be seen that large distortions occur at the shedding frequency of the rectangular cylinder and its first harmonic at the tested freestream velocities. Therefore, it is of primary importance to correct the temporal data by applying the inverse FRF. The implementation of the correction consists in three steps. First, as the FRF varies with the frequency, the temporal signal acquired for each pressure tab is converted to the frequency domain using the fast Fourier transform algorithm of Matlab. In order to reduce spectral leakage, a Hanning window is applied to the temporal data. Next, the Fourier coefficients defining the signal are divided by the FRF of a tube line. This step provides the Fourier coefficients of the corrected signal. Finally, the temporal corrected signal is retrieved by computing the inverse discrete Fourier transform and by applying the inverse of the Hanning window.

Aerodynamic loads applied on the rectangle can be calculated by integrating the C_p distribution along the rectangle edges. The integration is performed by using the trapezoidal rule. This leads to the two-dimensional sectional coefficients of lift c_l, drag c_d and pitching moment c_m, the latter being computed about the cross section center and defined positive nose up. The Strouhal number is computed through Fourier analysis performed on the lift coefficient. Since 15 pressure taps are used on both the upper and lower surfaces, a reasonable confidence can be expected for the lift and moment coefficients. However, c_d should be treated with caution since the upstream and downstream surfaces are discretized with only 3 points. Moreover, the aerodynamic coefficients represent only two-dimensional phenomena and the loads coefficients include only the pressure contribution.

First and second order statistics are computed on the pressure and aerodynamic load coefficients. The time-averaged values and the corresponding standard deviations are respectively denoted by $\bar{\cdot}$ and $\cdot'$. Moreover, the two decomposition methods presented in Sec. 2.4 are used to extract the dominant behavior of the spatio-temporal results. The POD decomposition is applied through Algo. 2 on the C_p obtained for $U_\infty = 8.3\,\mathrm{m/s}$. The distribution of the pressure coeffi-

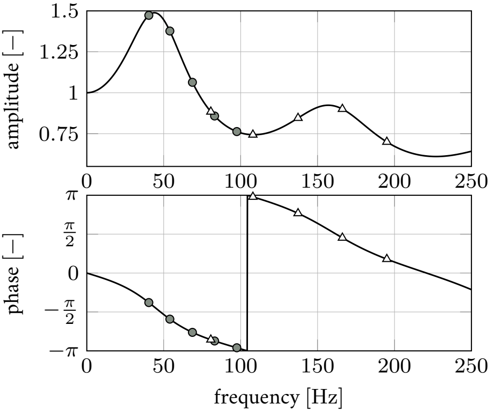

Figure 3.5: Bode plot of the pneumatic line FRF. Discs represent the shedding frequencies of the rectangular cylinder associated with the different freestream velocities and triangles their respective first harmonics.

cient at the n^{th} time step constitutes then the n^{th} column of the matrix $\mathbf{V}_1^N$ introduced in Sec. 2.4. To save computational power, only 250 shedding periods are considered, which has been found to be sufficient to obtain converged statistics. The DMD decomposition is also applied and, in this case, the time response of the load coefficients is added in matrix $\mathbf{V}_1^N$. In the context of the DMD based filtering explained below, this will provide a reference phase for the filtered time response of C_p. The resulting matrix $\mathbf{V}_1^N$ is decomposed using Algo. 3. As explained in Sec. 2.4, this algorithm leads to a number of modes ϕ_k^{DMD} that is equal to the largest dimension of matrix $\mathbf{V}_1^N$. Here, this corresponds to more than 2 000 modes. In order to identify the most relevant ones, the modes are first sorted by descending real part of λ_k^{DMD}, the latter being the complex frequency associated with each ϕ_k^{DMD}. This allows to discard the parasitic modes associated with high damping. Then, the modes are selected by descending amplitude q_k^{DMD}. This procedure identifies the modes associated with the mean and the shedding frequency as the most relevant ϕ_k^{DMD}. Finally, the selected spatial modes are used to reconstruct a lower-order approximation of the aerodynamic coefficients. More precisely, the approximation of the input matrix $\mathbf{V}_1^N$ reads

$$\widehat{\mathbf{V}}_1^N = \sum_{k^{\text{th}}\text{selected mode}} q_k^{\text{DMD}} \phi_k^{\text{DMD}} \exp\left(\Im(\lambda_k)^{\text{DMD}} \mathbf{t}\right), \tag{3.1}$$

where only the imaginary part of λ_k is kept to avoid spurious damping. DMD can thus be viewed as a filter and the time response of the reconstructed aerodynamic coefficients $\widehat{C_p}$, $\widehat{c_l}$, $\widehat{c_d}$ and $\widehat{c_m}$ can be analyzed within a shedding cycle.

3.3 Numerical setup

The flow around the rectangular cylinder is studied numerically by using both URANS and DDES techniques. This section presents the setup for the two types of simulation and the corresponding computational domain and mesh.

3.3.1 Unsteady Reynolds-Averaged Navier-Stokes simulation

The numerical results are first obtained from two-dimensional URANS simulations. The Menter $k-\omega$ SST model (Menter and Esch, 2001; Menter et al., 2003) is chosen to close the URANS equations, as it is known to better predict flow separation than the standard $k-\varepsilon$ model and to be less sensitive to freestream turbulence than the standard $k-\omega$ model (Casey and Wintergerste, 2000). The URANS equations are solved by using a transient solver for incompressible flow based on a combination of PISO and SIMPLE algorithms (Ferziger and Perić, 1996). Called PIMPLE, it enables stable simulations with time step leading to a large CFL number, the latter being roughly equal to 3.8 in the context of those simulations. The non-dimensional time step ${}^{\Delta t U_\infty}/_{c}$ is set to 10^{-3}, which corresponds to ${}^{1}/_{1700}{}^{\text{th}}$ of a typical shedding cycle. Therefore, the smallest time scales of the flow are assumed to be captured accurately. The second order implicit backward Euler scheme is used to advance the equations in time and second order schemes are chosen for spatial discretization. In particular , the term $\partial_i u_j$ is discretized through a second order, upwind-biased schemes in order to avoid spurious oscillations.

As depicted in Fig. 3.6a, the computational domain is a square of dimensions $50c \times 50c$ centered vertically on the center of the rectangular cylinder. This square is located horizontally in such a way that the upstream and downstream borders are respectively distant of $19.5c$ and $30.5c$ from the rectangle center. These dimensions are similar to those used in most of the numerical studies performed in the context of the BARC (Bruno et al., 2014). As shown in Fig. 3.6b, the mesh is divided into an unstructured and a structured part. The structured region consists of a disc of radius $15d$ centered on the rectangle. Moreover, the zone of the wake located downstream of the body is also part of the structured region. To allow this topology, the rectangular cross section has rounded corners. However, the flow is expected to be the same as for a cross-section with sharp corners, as the radius of curvature is less than one thousandth of the chord. In order to have an adequate resolution and accuracy in the critical flow regions, a fine mesh is used in the vicinity of the rectangle and in its wake. Finally, the simulations are wall-resolved and thus do not use wall-functions. Therefore, the first mesh point away from the rectangle surface is set such that $y^+ \approx 0.7$ for most of the cells around the rectangle.

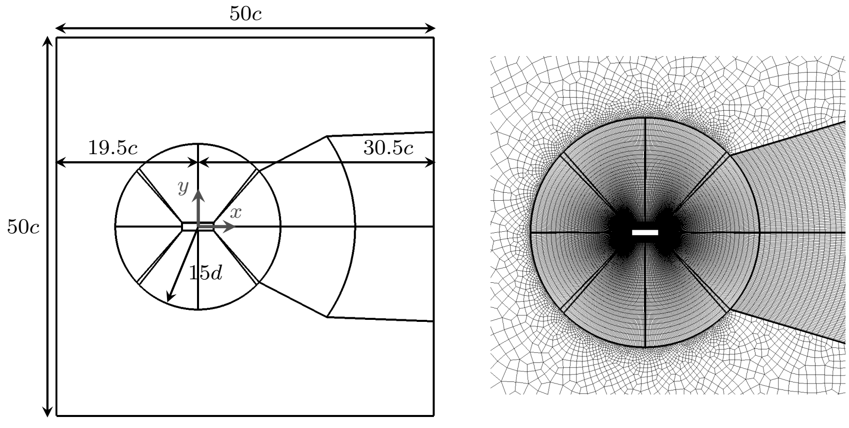

(a) Computational domain.

(b) Grid.

Figure 3.6: Computational domain and grid used for the URANS and DDES simulations.

At walls, the no-slip boundary condition is imposed for the velocity and an homogeneous Neumann condition is set for the pressure. Dirichlet conditions are imposed for the turbulent scalars as explained in Sec. 2.2.1. At the inlet, the freestream velocity and turbulent scalars are imposed. The value of the turbulent kinetic energy k_∞ is based on an inlet freestream turbulence intensity of 0.3%. The specific dissipation rate ω_∞ is calculated to obtain a turbulent eddy viscosity $\nu_T = 5 \times 10^{-3}\nu$, as suggested by Menter and Esch (2001) to avoid numerical issues. For the pressure, a Neumann boundary condition sets the pressure gradient to zero. The outlet corresponds to a zero-gradient for the velocity and turbulent scalars, while the pressure is enforced. Finally, a slip boundary condition is imposed for all variables at the upper and lower boundaries allowing only a streamwise variation.

A mesh convergence study is performed to select a grid leading to mesh independent results. The rectangle incidence with the freestream flow is set to 0° and 4°. Only the results corresponding to the non-zero incidence are presented in the following, this case being more challenging. Simulations are carried out on four different meshes whose main characteristics are presented in Tab. 3.1. The main differences between the grids are: i) the discretization of the chord and depth, ii) the number of cells along the radius of the circle surrounding the rectangle, and iii) the number of cells discretizing horizontally the wake. The results are presented in terms of Strouhal number as well as mean and standard deviation of lift, drag and moment coefficients. Figure 3.7 depicts the variation of the relative difference of each bulk parameter with the respective result calculated with the finest mesh. It can be seen that the results converge and mesh C leads to results within 2% of the ones calculated with mesh D, the finest mesh. Therefore, mesh C, which consists of 75 000, hexahedra is selected as the grid used for URANS computations.

	Number of cells				
	along chord	along depth	radially	wake	total
Mesh A	90	70	60	45	28 000
Mesh B	120	100	80	55	48 000
Mesh C	140	130	100	90	75 000
Mesh D	200	160	150	130	142 000

Table 3.1: Discretization of the main regions of the meshes used for the grid convergence study.

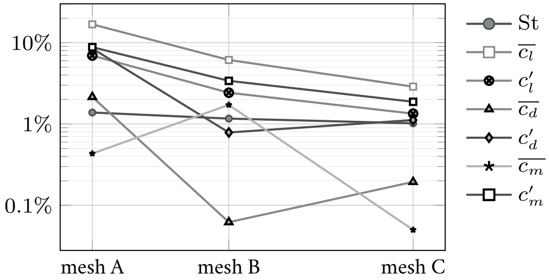

Figure 3.7: Percentage of difference on bulk URANS results compared to results obtained with mesh D in Tab. 3.1.

Finally, as URANS is based on averaged Navier-Stokes equations, simulations performed with such a level of approximation converge to a phase-averaged solution. Therefore, the computations are run until the aerodynamic coefficients have reached a fully-developed periodic behavior and only the last shedding cycle is analyzed.

3.3.2 Delayed-Detached Eddy Simulation

In addition to URANS, higher fidelity simulations are also performed using DDES based on the SA turbulence model (Spalart and Allmaras, 1994). More precisely, the original formulation proposed by Spalart et al. (1997) is used. The setup is very similar to that of URANS (Sec. 3.3.1), except for a few particular points specific to DDES.

As for URANS simulations, the transient incompressible solver PIMPLE is selected. For stability purposes, the non-dimensional time-step is decreased compared to the URANS cases and set to 6.25×10^{-4}. The corresponding CFL number is about 2.4 and one shedding cycle contains approximately 3 000 time-steps, which is assumed to be sufficient to capture the smallest time scales. Similarly to the URANS setup, a backward Euler scheme is chosen for temporal discretization. The same second-order schemes are also used for spatial discretization, except for the non-linear advective term, which is discretized with a Linear Upwind Stabilized Transport (LUST) scheme, as suggested by Patruno et al. (2016).

To enable the turbulent eddying process, DDES simulations have to be performed on a three-dimensional grid. The two-dimensional URANS computational domain is thus extruded along the z-direction to obtain a spanwise length $s = c$. This dimension has been used in LES studies performed on similar cases (e.g. Yu and Kareem, 1998; Bruno et al., 2010) and verifies the criterion ${}^{s}/_{c} \geqslant 1$ suggested by Tamura et al. (1998). Two DDES meshes, A and B, are considered, whose main characteristics are summarized in Tab. 3.2. The DDES mesh A corresponds to the URANS mesh (i.e., mesh C in Tab. 3.1) in the $x - y$ plane, with 32 cells along the span. This discretization satisfies the criterion ${}^{\Delta z}/_{c} \leqslant 0.1$ proposed by Tamura et al. (1998), and is finer than or similar to that used in many studies on rectangular cylinders performed in the context of the BARC (e.g. Yu and Kareem, 1998; Bruno et al., 2010; Arslan et al., 2011). In their "Young Person's Guide to Detached Eddy Simulation Grids", Spalart and Streett (2001) called the region where the geometry-dependent turbulence structures are generated the "focus region". They identified this region as the zone where a "particle can return from this point to the body". Spalart and Streett (2001) argued that the maximum grid spacing Δ_0 in that region is the principal measure of the spatial resolution in DES. In the present work, the "focus region" is assumed to extend until half a chord downstream of the rectangular cylinder trailing edges. For mesh A, the maximal grid spacing in that region is $\Delta_0^{\mathrm{A}} = (\Delta z)^{\mathrm{A}} = {}^{c}/_{32}$. Mesh B is designed to obtain $\Delta_0^{\mathrm{B}} = {}^{\Delta_0^{\mathrm{A}}}/_{2}$, a value similar to the one used by Mannini et al. (2011). Therefore, the spanwise discretization for mesh B is $(\Delta z)^{\mathrm{B}} = {}^{c}/_{64}$. Because Δ is defined as $\max{(\Delta x, \Delta y, \Delta z)}$, the grid in the $x - y$ plane has to be modified compared to grid A to keep the extent of the "focus region". Therefore, a finer grid is designed as reported in Tab. 3.2. Both meshes A and B are used in the following to investigate the impact of Δ_0 on the accuracy of the DDES results.

	Number of cells					
	along chord	along depth	radially	wake	along span	total
Mesh A	140	130	100	90	32	2 400 000
Mesh B	200	130	160	110	64	8 200 000

Table 3.2: Discretization of the main regions of the meshes used for the DDES simulations.

The boundary conditions for pressure and velocity are the same as the ones described in Sec. 3.3.1 for URANS. As a smooth freestream flow is assumed, a Dirichlet boundary condition $\tilde{\nu} = 0$ is imposed at the inlet while a Neumann condition is set for the outlet. A slip condition is imposed on the upper and lower boundaries. Finally, periodic boundary conditions are adopted on the two boundaries normal to the extrusion direction.

As the DDES methodology mixes URANS and LES techniques, the equations and consequently their results are no longer phase-averaged. It is therefore necessary to determine an appropriate size for the computed time window. To this end, a convergence study is performed on the mean and standard deviation of the aerodynamic coefficients obtained for a rectangular cylinder at 4° of incidence. The results presented below are computed based on the simulation run on mesh B but the conclusions are valid for both meshes. One hundred non-dimensional time units are first discarded in order to eliminate the transient response. The bulk parameters are then calculated for a first non-dimensional temporal window $\Delta T_1 = 25$, which corresponds roughly to 13 shedding cycles. The process is repeated increasing the window extent as $\Delta T_{i+1} = \Delta T_i + 25$ until an extent of 150 is achieved. This maximal extent corresponds roughly to 80 shedding cycles. The results are compared through a relative difference with those computed with the largest temporal window. Figure 3.8 shows the variation of these relative differences. It appears that a window of 125 leads to relative differences below 5% compared with results computed with the largest extent. However, Fig. 3.8 does not depict a smooth convergence of the aerodynamic coefficients. This could be due to the development of a low frequency phenomenon requiring a longer temporal extent to be fully established. Nonetheless, to limit the computational costs, it is chosen here to stop the simulation after 250 non dimensional times and to perform the analysis on the last 150 time instances.

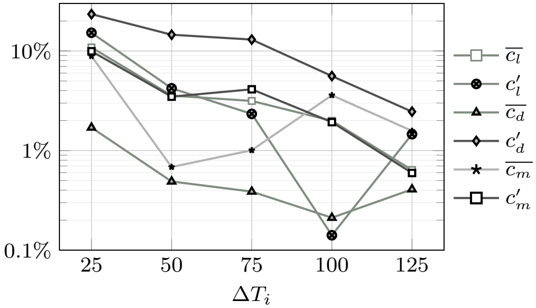

Figure 3.8: Percentage variation of the relative difference on aerodynamic coefficients computed by DDES with mesh B at 4° angle of attack for different time windows compared to those obtained with the largest window extent.

3.3.3 Post-processing

The loads and pressure coefficients resulting from both URANS and DDES simulations are post-processed before being analyzed. In particular, statistics are computed on the aerodynamic coefficients. Moreover, the decomposition methods described in Sec. 2.4 are applied to extract the dominant behavior of the URANS and DDES results.

First and second order statistics are computed on the time response of the coefficients. As the two-dimensional URANS simulations lead to phase-averaged data, a single shedding cycle is retained. The pressure distribution of interest corresponds to C_p along the cross-section of the rectangular cylinder. The three-dimensional pressure distributions resulting from DDES simulations are first averaged along the z-direction. Then, first and second order statistics are computed on the resulting $\langle C_p^{\text{DDES}}(\mathbf{x},t)\rangle_z$. More precisely, $\overline{C_p}^{\text{DDES}}(x,y) = \langle\langle C_p^{\text{DDES}}(\mathbf{x},t)\rangle_z\rangle_t$ and $C_p'^{\text{DDES}}(x,y) = \sqrt{\langle\langle C_p^{\text{DDES}}(\mathbf{x},t)\rangle_z^2\rangle_t - \left(\overline{C_p}^{\text{DDES}}\right)^2}$.

The POD and DMD decomposition methods are applied to CFD results reshaped in an input matrix $\mathbf{V}_1^N$. In particular, $\mathbf{V}_1^N$ consists of the time response of the C_p distribution when used as POD input, C_p being span-averaged in the context of DDES results. As for experimental results, $\mathbf{V}_1^N$ also contains the time response of the load coefficients when used as DMD input (see Sec. 3.2.2.3). Algorithms 2 and 4 are used to compute POD and DMD decompositions, respectively. As explained in Sec. 2.4.2, Algo. 4 performs the DMD decomposition by using only a reduced number of POD modes which eases the identification of the dominant DMD modes. Note that the number of POD modes selected has to be sufficient to capture a sufficient amount of energy in the flow. The use of Algo. 4 requires the $M \times N$ input matrix $\mathbf{V}_1^N$ to be such that $M \geqslant N$. This condition is verified in the context of URANS as $\mathbf{V}_1^N$ contains only a single shedding cycle. Conversely, the extent of the time response has to be reduced to apply DMD on DDES results. Therefore, to obtain a square matrix $\mathbf{V}_1^N$, the decomposition methods are applied to about 40 shedding cycles. As depicted in Fig. 3.8, this corresponds to a maximum relative error of 10% on the statistics of the aerodynamic coefficients. The DMD decomposition is then used to reconstruct an approximation of the CFD results. To this end, the most relevant ϕ_k^{DMD} are selected by descending order of amplitude q_k^{DMD} and the approximated matrix $\widehat{\mathbf{V}}_1^N$ is then calculated from

$$\widehat{\mathbf{V}}_1^N = \sum_{k^{\text{th}}\text{selected mode}} q_k^{\text{DMD}} \boldsymbol{\phi}_k^{\text{DMD}} \exp\left(\Im(\lambda_k^{\text{DMD}})\mathbf{t}\right). \tag{3.1}$$

The number of selected modes ϕ_k^{DMD} is chosen to obtain statistics computed on $\widehat{\mathbf{V}}_1^N$ similar to those computed on $\mathbf{V}_1^N$. Unless otherwise mentioned, it corresponds to the mean mode and the ϕ_k^{DMD} associated with the shedding frequency.

3.4 Overview of flow features

This section gives an overview of the flow around a 4:1 rectangular cylinder. To this end, snapshots of the flow computed by URANS simulations are depicted and commented. Note that, as shown in the following sections, URANS results are sufficiently representative to provide a qualitative understanding of the phenomena. However, URANS results should be considered extremely cautiously when examined quantitatively. In Sec. 3.4.1, the flow field is first analyzed in terms of time-averaged quantities. Section 3.4.2 is then dedicated to the study of the time response of the flow topology within a shedding cycle.

3.4.1 Time-averaged flow features

Figures 3.9 and 3.10 depict the mean flow from two perspectives : i) the streamlines and the vorticity and ii) the pressure coefficient and its associated iso-contours. Two incidences are considered: $\alpha = 0^\circ$ and $\alpha = 2^\circ$.

At 0° of incidence, the mean flow is symmetrical and the topology is the same for the upper and lower surfaces. This is shown in both Figs. 3.9a and 3.9b. Two large main vortices called A_U and A_L lie along each of the horizontal surfaces and each of them corresponds to a low pressure zone. Moreover, a free shear layer is visible along each of the two vortices. Despite their large extent, vortices A_U and A_L do not cover the entire surface and the mean flow reattaches at the rear part of the horizontal surfaces. Moreover, a region of high vorticity is visible near the two trailing edges. Finally, two symmetrical vortices B_U and B_L are located at the rear part of the rectangular cylinder, and are associated with a region of lower pressure.

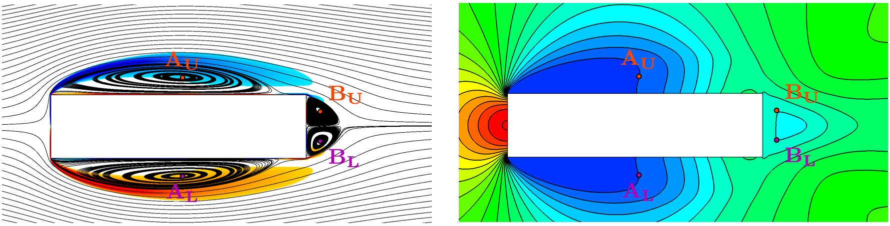

(a) Mean streamlines and $\overline{\omega}_z$.
(b) $\overline{C_p}$.

Figure 3.9: Mean flow around a rectangular cylinder at 0° and $\mathrm{Re} = 4.2 \times 10^4$ obtained by URANS. (a) Streamlines and vorticity (clockwise in blue and counter-clockwise in red), and (b) pressure coefficient C_p (high pressure in red and low pressure in blue) and associated iso-contours.

Increasing the incidence breaks the flow symmetry, as depicted in Figs. 3.10a and 3.10b for an incidence of 2°. Compared to a zero incidence, a positive angle of attack leads to an increase in the size of A_U, the main vortex along the upper surface, and a contraction of the main vortex A_L lying on the front part of the lower surface. Vortex A_U is in this case so large that there is no reattachment of the mean flow along the upper surface. Conversely, the reattachment along the lower surface occurs farther upstream. A vortex B_U is also visible at the rear part near the upper trailing edge. Moreover, a larger low pressure zone is present near the lower trailing edge but farther downstream from the body (see Fig. 3.10b). This low pressure zone indicates the presence of a vortex called vortex B_L. Finally, a high counter-clockwise vorticity zone is visible along the rear part of the lower surface and a small counter-clockwise rotating zone lies near the upper trailing edge, between vortices A_U and B_U.

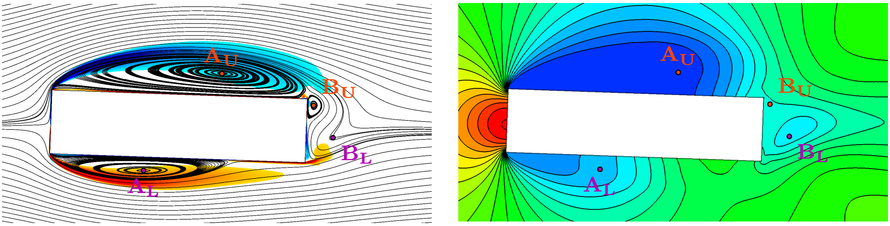

(a) Mean streamlines and $\overline{\omega}_z$. (b) $\overline{C_p}$.

Figure 3.10: Mean flow around a rectangular cylinder at 2° and $\mathrm{Re} = 4.2 \times 10^4$ obtained by URANS. (a) Streamlines and vorticity (clockwise in blue and counter-clockwise in red), and (b) pressure coefficient C_p (high pressure in red and low pressure in blue) and associated iso-contours.

3.4.2 Time response of flow features

Figures 3.11 and 3.12 show the variation of the flow around a rectangular cylinder at 0° and 2° of incidence during a shedding cycle. The beginning of the cycle $\varphi = {}^{t}\!/_{T} = 0$ is defined as the phase where the generated lift is minimum.

At 0° of incidence, the flow topology above and below the horizontal symmetry axis of the rectangle is identical but occurs at times distant by half a shedding period. Therefore, describing the time response of the flow above the upper surface is sufficient to entirely described the dynamics. At $\varphi = 0$, and as depicted by streamlines in Fig. 3.11a, a large clockwise rotating vortex, called vortex A_U^1, lies along the upper surface. The vorticity plot shows that the free shear layer does not impinge on the rear part of the upper surface, although the flow reattaches. Instead, it extends in the wake up to a zone of low pressure corresponding to a previously shed vortex denoted D_U^0, as depicted in Fig. 3.11b. As shown in Fig. 3.11c, vortex A_U^1 is then convected downstream while the free shear layer moves closer to the surface. A clockwise rotating zone lies along the rear part of the upper surface and rolls around the upper trailing edge of the cylinder, forming a small vortex denoted B_U^0. While vortex A_U^1 is being stretched and convected downstream, a new vortex A_U^2 forms at the leading edge of the cylinder. The emergence of this vortex is recognizable by the drop in pressure coefficient near the leading edge shown in Fig. 3.11f. Vortex A_U^2 then grows, pushing vortex A_U^1 further downstream, as depicted in Figs. 3.11g and 3.11h. At the same time, the free shear layer impinges the upper rear corner, feeding vortex B_U^0, which also grows and starts to detach from the rear surface. Vortices A_U^1 and B_U^0 eventually merge into a single vortex D_U^1, which is shed into the wake. Only vortex A_U^2 remains on the upper surface. This is depicted in Figs. 3.11i and 3.11j. Finally, vortices A_U^2 and D_U^1 are convected downstream and a new cycle resumes.

At an incidence of 2°, the flow topology is not anymore symmetric between the upper and lower surfaces. As depicted in Figs. 3.12a and 3.12b, a large clockwise rotating vortex called vortex

A_U^1 covers nearly the entire upper surface at $\varphi = 0$. The free shear layer follows the upper part of vortex A_U^1 and extends into the wake until the location of a vortex called A_U^0. Moreover, a small counter-clockwise vorticity zone lies at the upper trailing edge indicating the presence of a vortex called B_U^0. The same phase shows the emergence of a conter-clockwise rotating vortex called A_L^1 at the leading edge of the lower surface. Moreover, another vortex called A_L^0 and previously generated at the leading edge is still visible on the rear part of the lower surface. The free shear layer along vortices A_L^0 and A_L^1 impinges the rear part of the lower surface. This shear layer extends farther downstream, rolling around the lower trailing edge and feeding the counter-clockwise rotating vortex B_L^0 behind the rectangle. As shown in Figs. 3.12c and 3.12d, vortex A_U^1 elongates then downstream while the upper shear layer impinges the upper trailing edge and vortex B_U^0 vanishes. On the lower surface, vortex A_L^1 is convected downstream while vortex A_L^0 and B_L^0 merge into a single vortex called D_L^0 which is shed into the wake. At $\varphi = 0.5$, as depicted in Figs. 3.12e and 3.12f, a new vortex A_U^2 forms at the upper leading edge. The upper shear layer rolls around vortex A_U^1 and the upper trailing edge, impinging the rear surface. Along the lower surface, vortex A_L^1 is convected downstream and the free shear layer moves farther away from the surface. Simultaneously, a counter-clockwise vorticity zone starts to form and grows into a vortex B_L^1 at the lower trailing edge. This vortex appears clearly in Figs. 3.12g and 3.12h corresponding to $\varphi = 0.75$. At this stage, vortex A_L^1 lies alone on the lower surface. A couter-clockwise rotating vortical zone grows at the trailing edge of the upper surface and forms a small vortex B_U^1 while vortex A_U^2 keeps growing. Simultaneously, vortex A_U^1 becomes weaker as it extends progressively from the rear part of the upper surface into the wake. Vortex A_U^1 is finally completely shed at the end of the cycle (see vortex A_U^0 in Figs. 3.12a and 3.12b).

Some similarities and differences can be highlighted between the two incidence angles. For both cases, the main dynamics consists in the emergence of a vortex at the leading edge. This vortex grows and is convected downstream along the surface until it reaches the rear part of the cylinder and is shed into the wake. However, at 0° of incidence, the vortex generated at the leading edge merges with another vortex that has grown at the trailing edge. The result of this merging is then shed into the wake. For an incidence of 2°, the dynamics of the flow structures is similar along the lower surface. However, it differs along the upper surface where the vortex generated at the leading edge is convected and shed into the wake without merging with the vortex that has appeared at the trailing edge.

3.5 Load coefficient statistics and Strouhal number

This section details the experimental and numerical results in terms of bulk parameters: the statistics computed on the load coefficients and the Strouhal number. First, Sec. 3.5.1 presents and analyses the experimental results which are denoted by the superscript EXP. For the purpose of comparison, the results documented by Nakamura and Mizota (1975) and Washizu et al. (1978) are also included. Then, the results of URANS and DDES simulations are presented in Sec. 3.5.2 and the corresponding bulk parameters are identified by the superscripts URANS and DDES, respectively. In particular, this section discusses the DDES results obtained with two grids to illustrate the impact of the grid refinement. More precisely, DDES A and DDES B are associated with the results obtained for the coarser and finer grids, respectively (see Sec. 3.3.2). Moreover, Sec. 3.5.2 also compares the numerical and experimental results.

3.5.1 Experimental results

Figure 3.13 shows the aerodynamic coefficients and the Strouhal number as a function of the incidence α. The Reynolds number associated with the present experimental results is $\mathrm{Re} = 4.2 \times 10^4$. Experimental results reported by Nakamura and Mizota (1975) and Washizu et al. (1978) are also depicted for comparison. They were obtained from direct load measurements and in the context of studies on aeroelastic instabilities. Unfortunately, these authors specified only a

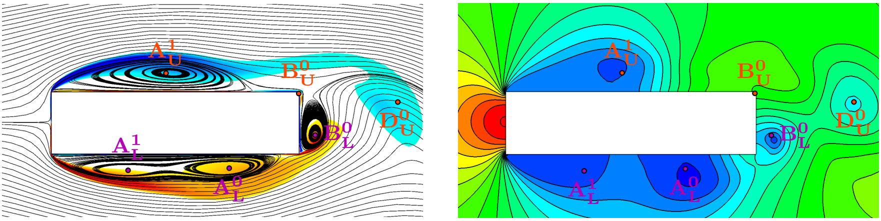

(a) Streamlines and ω_z at $\varphi = 0$.

(b) C_p at $\varphi = 0$.

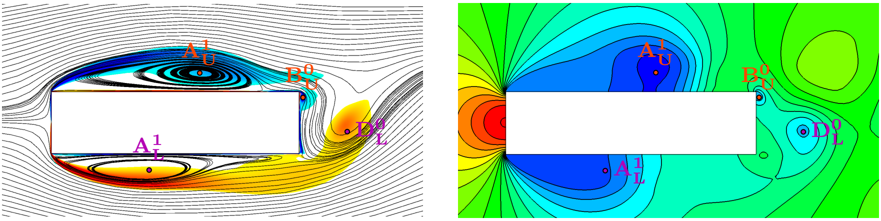

(c) Streamlines and ω_z at $\varphi = 0.25$.

(d) C_p at $\varphi = 0.25$.

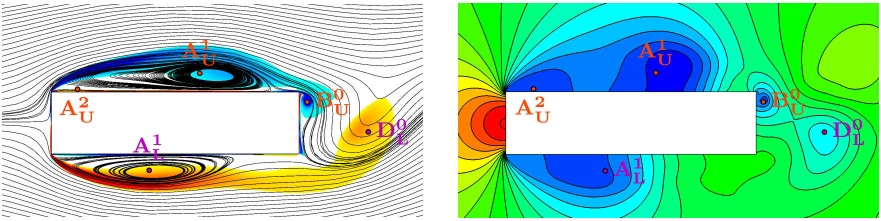

(e) Streamlines and ω_z at $\varphi = 0.375$.

(f) C_p at $\varphi = 0.375$.

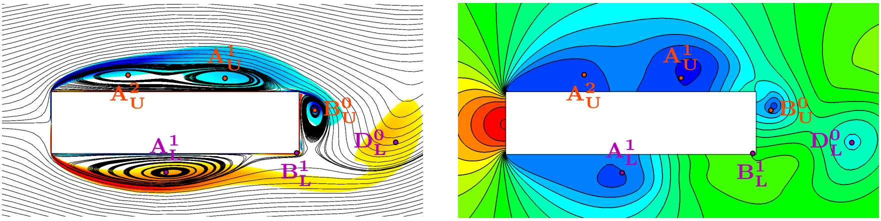

(g) Streamlines and ω_z at $\varphi = 0.5$.

(h) C_p at $\varphi = 0.5$.

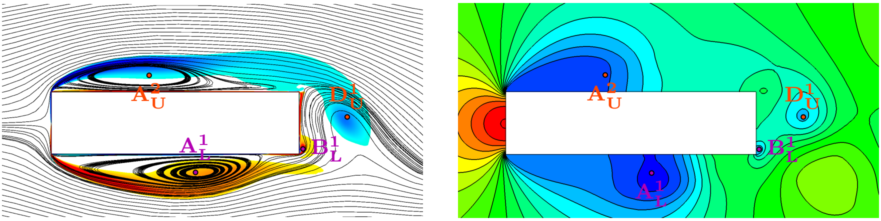

(i) Streamlines and ω_z at $\varphi = 0.75$.

(j) C_p at $\varphi = 0.750$.

Figure 3.11: Variation within a vortex shedding cycle of the flow around a rectangular cylinder at 0° and $\mathrm{Re} = 4.2 \times 10^4$ obtained by URANS. Left column: streamlines and vorticity (clockwise in blue and counter-clockwise in red). Right column: pressure coefficient C_p (high pressure in red and low pressure in blue) and associated iso-contours.

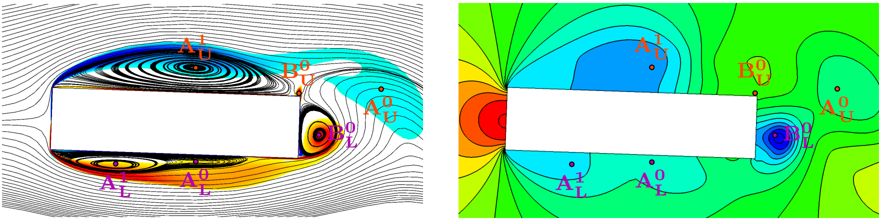

(a) Streamlines and ω_z at $\varphi = 0$.

(b) C_p at $\varphi = 0$.

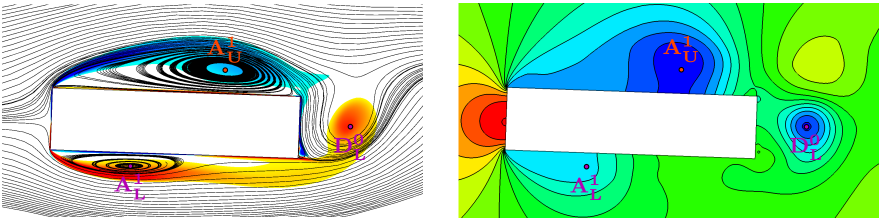

(c) Streamlines and ω_z at $\varphi = 0.25$.

(d) C_p at $\varphi = 0.25$.

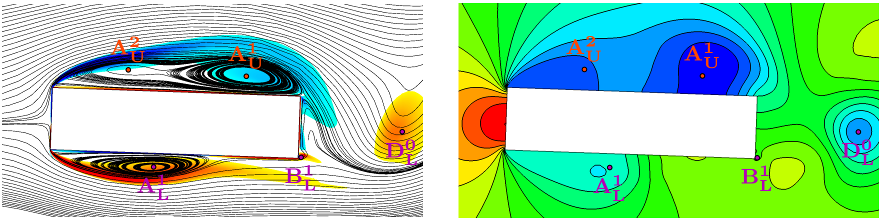

(e) Streamlines and ω_z at $\varphi = 0.5$.

(f) C_p at $\varphi = 0.5$.

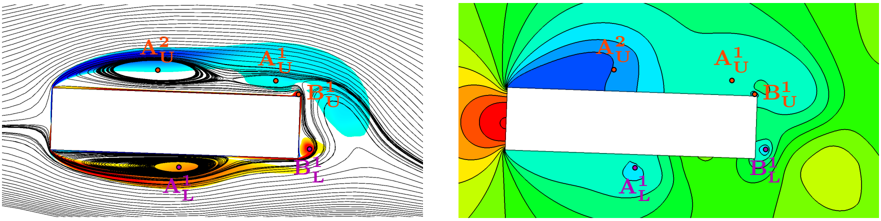

(g) Streamlines and ω_z at $\varphi = 0.75$.

(h) C_p at $\varphi = 0.75$.

Figure 3.12: Variation within a vortex shedding cycle of the flow around a rectangular cylinder at 2° and $\mathrm{Re} = 4.2 \times 10^4$ obtained by URANS. Left column: streamlines and vorticity (clockwise in blue and counter-clockwise in red). Right column: pressure coefficient C_p (high pressure in red and low pressure in blue) and associated iso-contours.

range of Reynolds numbers. In particular, Nakamura and Mizota (1975) documented results for $10^4 \leqslant \mathrm{Re} \leqslant 10^5$ and Washizu et al. (1978) for $8 \times 10^4 \leqslant \mathrm{Re} \leqslant 8 \times 10^5$. Therefore, it is not possible to infer precisely the Reynolds number associated with these results.

Figure 3.13a plots the mean lift coefficient against angle of attack. In particular, $\overline{c_l}^{\text{EXP}}$ clearly exhibits a linear increase with α from -4° to 4°. In this linear region, the slope $\overline{c_l}_{\alpha}^{\text{EXP}}$ is about 2.1π. For $|\alpha| > 5^\circ$, the absolute mean lift coefficient decreases and the rectangular cylinder is stalled. Finally, it appears that the variation of $\overline{c_l}^{\text{EXP}}$ is not perfectly symmetrical. More precisely, the absolute mean lift produced at a negative angle is higher than that for the corresponding positive incidence. The $\overline{c_l}^{\text{EXP}}$ curve would be nearly perfectly symmetrical if it was shifted downstream by 0.05. This asymmetrical behavior may be due to a freestream being slightly different along the upper and lower side of the plate. The mean drag and pitching moment coefficients are depicted in Fig. 3.13b. The variation of $\overline{c_d}^{\text{EXP}}$ exhibits a classical parabolic variation for absolute angles lower than 4°. For higher incidence, as the rectangular cylinder is stalled, the increase in drag saturates. Finally, the variation of the mean pitching moment about the center of the rectangular cylinder exhibits a linear decrease for incidence $|\alpha| \leqslant 2^\circ$. The corresponding negative slope is $\overline{c_{m\alpha}}^{\text{EXP}} \approx -0.35\pi$. This linear behavior is followed by a saturation. Finally, for $|\alpha| > 5^\circ$, the absolute $\overline{c_m}^{\text{EXP}}$ decreases slightly again. Note that, similarly to $\overline{c_l}$, the variation of both $\overline{c_d}^{\text{EXP}}$ and $\overline{c_m}^{\text{EXP}}$ are not perfectly symmetrical.

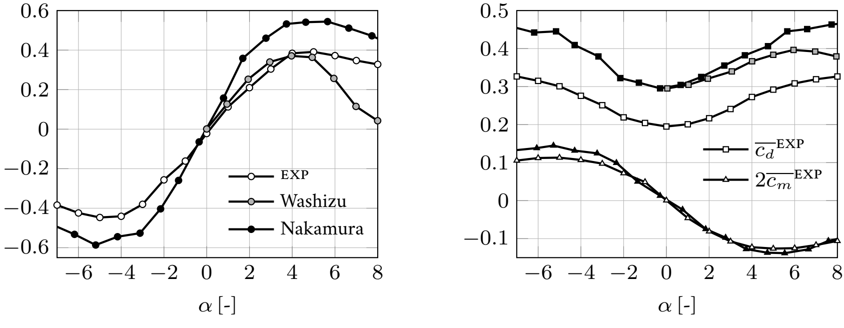

(a) $\overline{c_l}$.

(b) $\overline{c_d}$ and $\overline{c_m}$.

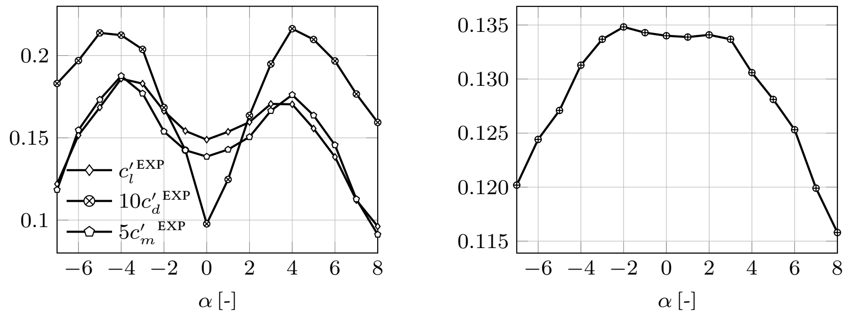

(c) c_l', c_d' and c_m'.

(d) St.

Figure 3.13: Statistics of the aerodynamic coefficients obtained from measured pressure distributions as a function of the angle of attack at $\text{Re} = 4.2 \times 10^4$. Experimental results of Nakamura and Mizota (1975) and Washizu et al. (1978) from direct load measurements at a similar Reynolds number are included for comparison.

The mean aerodynamic coefficients are compared to experimental results available in the literature. By doing so, several differences and similarities can be pointed out. First, the mean lift slope $\overline{c_{L\alpha}}$ obtained by Nakamura and Mizota (1975) and Washizu et al. (1978) are 3.3π and 2.3π, respectively. Therefore, the slope $\overline{c_{L\alpha}}^{\text{EXP}}$ is relatively close to the later but very different from the former. As mentioned in Sec. 3.1 and later illustrated in Sec. 3.8, the mean lift slope can be very sensitive to the Reynolds number. Therefore, as the Reynolds number associated with these external works are not known precisely, no conclusion can be drawn. The stall angle is similar for the three sets of results. However, the post-stall decrease in $\overline{c_L}$ is higher for the results presented by Nakamura and Mizota (1975) and even higher for the experiments carried out by Washizu et al.

(1978). The mean drag $\overline{c_D}$ at zero incidence is identical for the two studies from the literature. However, this value is higher by 0.1 compared to $\overline{c_d}^{\text{EXP}}$. For incidences $|\alpha| < 4^\circ$, the parabolic shape exhibited by the curve $\overline{c_d}^{\text{EXP}}$ is similar to the one obtained by Washizu et al. (1978). For higher $|\alpha|$, the $\overline{c_D}$ obtained by Washizu et al. (1978) first increases slower and then decreases for $|\alpha| > 6^\circ$. The $\overline{c_D}$ curve presented by Nakamura and Mizota (1975) also exhibits a parabolic behavior but the mean drag increases faster with the incidence. Some of those discrepancies can be explained by the difference in the load acquisition process. In particular, in the literature studies, forces are measured using strain-gauges (Otsuki et al., 1974), while the results obtained in the context of this work are computed by integrating $\overline{C_p}$. Therefore, $\overline{c_d}^{\text{EXP}}$ consists only of the pressure drag whereas the $\overline{c_D}$ documented by Washizu et al. (1978) and Nakamura and Mizota (1975) also includes the friction drag. Moreover, as explained in Sec. 3.2, most of the drag comes from the pressure distribution along the front and rear surfaces of the rectangular cylinder. Only three pressure taps are available on these surfaces, which might not be enough to obtain sufficient accuracy. Finally, the variation of $\overline{c_m}^{\text{EXP}}$ with α is comparable to the results reported by Nakamura and Mizota (1975). In particular, the slope in the linear part of the curves and the saturation behavior are similar. The discrepancies visible for $\alpha < -2^\circ$ are probably due to the non-symetical behavior of $\overline{c_m}^{\text{EXP}}$.

Figure 3.13c depicts the second order statistics of the aerodynamic coefficients as a function of α. The standard deviation associated with each of the load coefficients first increases until $|\alpha| = 4^\circ$, this angle corresponding to the end of the linear region in the curve $\overline{c_l}^{\text{EXP}}$. For $|\alpha| > 4^\circ$, the second order statistics decrease. Finally, the Strouhal number shown in Fig. 3.13d is calculated through a Fourier analysis of the lift coefficient. For $-3^\circ < \alpha < 3^\circ$, St^{EXP} is nearly constant and equal to 0.134. Then, for increasing incidence, St^{EXP} decreases linearly to reach $\text{St}^{\text{EXP}} = 0.125$ for $\alpha = 6^\circ$ and $\text{St}^{\text{EXP}} = 0.108$ for $\alpha = 10^\circ$ (not shown in Fig. 3.13d).

3.5.2 Comparison with numerical results

This section aims to present the CFD results and to discuss their validity. To this end, the bulk parameters obtained numerically are depicted in Fig. 3.14. The present experimental results as well as those from the work of Nakamura and Mizota (1975) and Washizu et al. (1978) are also shown for comparison.

The mean aerodynamic loads and the Strouhal number obtained from URANS is first investigated. Figure 3.14a shows that the mean lift coefficient $\overline{c_l}^{\text{URANS}}$ increases linearly with the angle of attack α until $\alpha = 3^\circ$. Beyond this value, the lift coefficient keeps increasing, but at a decreasing rate. The discrepancies with the experimental curve $\overline{c_l}^{\text{EXP}}$ are very large as both the URANS estimated slope $\overline{c_l}_\alpha$ and the behavior in the post-stall region differ dramatically. The slope $\overline{c_l}_\alpha^{\text{URANS}}$ is equal to 3.9π which is nearly twice the measured one. This slope is also very different from the result documented by Washizu et al. (1978). However, for incidence lower than 2°, $\overline{c_l}_\alpha^{\text{URANS}}$ is similar to the results presented by Nakamura and Mizota (1975). As mentioned before, the lift slope is known to be sensitive to the Reynolds number, a parameter that is not precisely documented by Nakamura and Mizota (1975). Nonetheless, based on the comparison of $\overline{c_l}^{\text{EXP}}$ and $\overline{c_l}^{\text{URANS}}$, it appears that the SST turbulence model is not able to provide an accurate estimation of the lift slope. Additionally, the behavior for angles of attack higher than 3° is not correctly captured by the URANS model. The three experimental data sets available depict a saturation of the mean lift followed by its decrease. For the three cases, the stall angle is located at around 4°. On the other hand, the lift curve estimated by URANS simulations does not exhibit any stall region for the considered range of incidences but only a monotonic increase at a decreasing rate. The $\overline{c_d}^{\text{URANS}}$ curve shown in Fig. 3.14b exhibits the expected quadratic behavior. The most visible discrepancy is the constant shift up of $\overline{c_d}^{\text{URANS}}$ compared to $\overline{c_d}^{\text{EXP}}$. However, as discussed in Sec. 3.5.1, $\overline{c_d}^{\text{EXP}}$ is not a complete drag estimate. Therefore, it is preferable to compare $\overline{c_d}^{\text{URANS}}$ with the results documented by Nakamura and Mizota (1975) and Washizu et al. (1978), for which the discrepancies are lower. In particular, for incidences lower than 3°, $\overline{c_d}^{\text{URANS}}$ approximates fairly accurately the literature results. For larger angles of attack, URANS simulations slightly overestimate the mean drag coefficient, this overestimation increasing with the incidence. Therefore, the SST model demonstrates

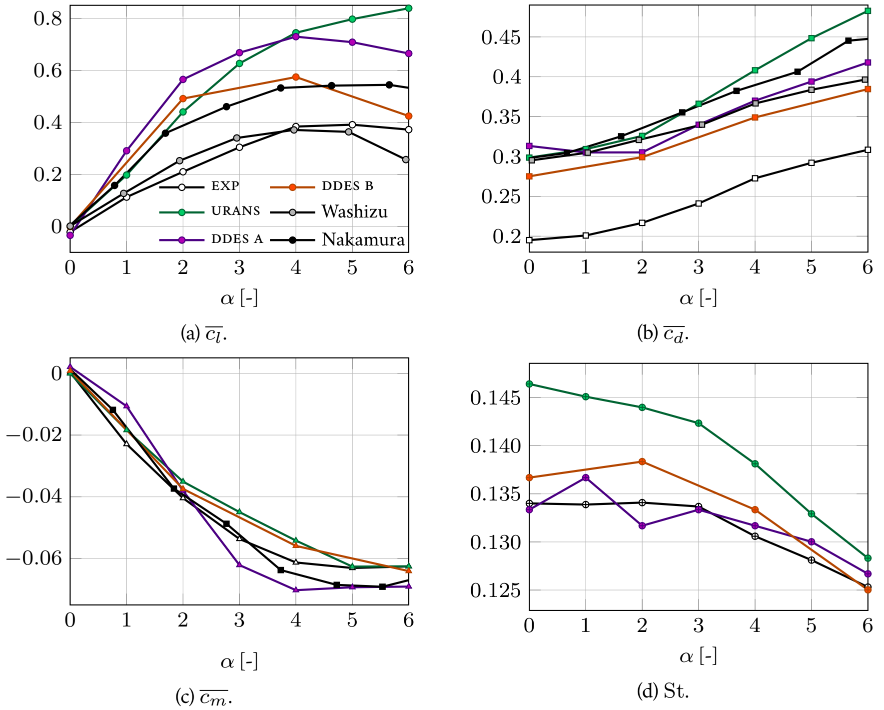

(a) $\overline{c_l}$.

(b) $\overline{c_d}$.

(c) $\overline{c_m}$.

(d) St.

Figure 3.14: Statistics of the aerodynamic coefficients obtained by URANS and DDES as a function of the angle of attack at $\mathrm{Re} = 4.2 \times 10^4$. Experimental results are included for comparison.

a reasonable ability to estimate the drag below the stall angle, $\overline{c_d}$ being overestimated for higher incidences. The dependence of the mean moment coefficient $\overline{c_m}^{\text{URANS}}$ on α in Fig. 3.14c shows a linear decrease followed by a saturation, in agreement with the experimental results of the present study and of Nakamura and Mizota (1975). Therefore, the SST turbulence model provides an accurate estimation of the mean pitching moment. The URANS estimated standard deviations (not shown) are much higher than the experimental results, especially for the drag at high incidence. Moreover, the decrease of the standard deviations for post-stall incidences depicted in Fig. 3.13c is not captured by URANS simulations. This discrepancy is expected since the $\overline{c_l}^{\text{URANS}}$ curve does not exhibit a stall region. As shown in Fig. 3.14d, the Strouhal number exhibits an initial linear decrease until $\alpha = 3^\circ$, followed by a second faster linear decrease. Compared to the experimental results, the Strouhal number obtained for different incidences is higher. Nonetheless, a modification of the slope at $\alpha = 3^\circ$ is also observed experimentally, although the value of the slopes differs quantitatively.

The DDES predictions are an improvement upon the URANS estimates but discrepancies with the experimental results still remain. Moreover, the predictions of the simulations computed on meshes A and B are also different. Figure 3.14a illustrates the mean lift coefficient. In particular, the slope obtained with mesh A is $\overline{c_{L}}_{\alpha}^{\text{DDES A}} \approx 5.2\pi$, which is even higher than that calculated by URANS. Refining the mesh leads to $\overline{c_{L}}_{\alpha}^{\text{DDES B}} \approx 4.5\pi$ which is closer to the value obtained by URANS but is still too high compared to experiments. Nonetheless, DDES simulations lead to a better $\overline{c_L}$ for incidence angles higher than 2°. In particular, a stall region characterized by a decrease in lift is captured but the estimated lift is still too high compared to the experimental results. The improved predictions obtained with DDES B suggest that using an even finer mesh could potentially improve the results. Figure 3.14b shows that DDES simulations lead to a better estimation of $\overline{c_D}$ than URANS for incidence angles higher than 2°. The curve $\overline{c_D}^{\text{DDES A}}$ is similar to the results presented by Washizu et al. (1978), although the parabolic behavior at $\alpha < 2^\circ$ is not correctly captured. This parabolic behavior is better represented better by the $\overline{c_D}^{\text{DDES B}}$ curve. The estimations provided by DDES A and B are quite close and meshes A and B seem to provide an accurate approximation of the drag. As shown in Fig. 3.14c, the mean pitching moment coefficient $\overline{c_M}^{\text{DDES}}$ is estimated with reasonable accuracy compared to the experimental measurements. The second order statistics computed from the DDES results (not shown) are also larger than the corresponding experimental values. However, these discrepancies are reduced compared to the URANS results. Moreover, ${c'_M}^{\text{DDES}}$ exhibits a modification of its slope for $\alpha > 4^\circ$ which is similar to the experimental results. Nonetheless, the improvement is not observed for ${c'_L}^{\text{DDES}}$ and ${c'_D}^{\text{DDES}}$. Finally, as depicted in Fig. 3.14d, the estimation of the Strouhal number is also improved by the use of DDES, although the plateau observed in EXP results for $0^\circ < \alpha < 3^\circ$ is not perfectly captured.

In conclusion, the URANS approach is not able to estimate $\overline{c_l}$ with a reasonable accuracy. In particular, the force normal to the chord axis is overestimated which impacts the results for $\overline{c_l}_\alpha$ and $\overline{c_d}$ at high incidence. Additionally, URANS modeling is not able to predict the stall angle. DDES yields better predictions for incidence angles in the stall region. The stall angle is correctly captured and the estimated lift is closer to the experimental values for post-stall incidences. Moreover, mesh B leads to a better estimation of the lift than the coarser mesh A. However, the estimation of $\overline{c_L}_\alpha^{\text{DDES}}$ is even worse than the URANS results. The use of a finer mesh could potentially improve this aspect, as the computations performed on mesh B give a better estimate of the lift curve slope than on mesh A. In order to explain these discrepancies, the next section analyzes the pressure coefficient distributions C_p obtained experimentally and numerically.

3.6 Pressure coefficient statistics

The present section examines the first and second order statistics of the pressure coefficient distribution C_p. Experimental and numerical results are discussed in Secs. 3.6.1 and 3.6.2, respectively. Additionally, Sec. 3.6.2 compares experimental and CFD results in order to explain the lack of accuracy of the URANS and DDES methodologies pointed out in Sec. 3.5.2.

3.6.1 Experimental results

This section examines the first and second order statistics of pressure coefficient distributions obtained experimentally for $\mathrm{Re} = 4.2 \times 10^4$. Figure 3.15 depicts the mean and standard deviation of C_p^{EXP} for several angles of attack. The distributions along the upper and lower surfaces of the rectangular cylinder are represented by plain and dashed lines, respectively. The distribution of $\overline{C_p}^{\text{EXP}}$ along the upstream face is not depicted in Fig. 3.15a for the sake of clarity. However, it exhibits the parabolic behavior expected for $\overline{C_p}$ around a stagnation point where $\overline{C_p} = 1$.

At zero incidence, the distribution of $\overline{C_p}^{\text{EXP}}$ is nearly identical for the upper and lower surfaces. Therefore, no lift is generated and $\overline{c_l}^{\text{EXP}} \approx 0$, as reported in Fig. 3.13a. The distribution $\overline{C_p}^{\text{EXP}}$ is almost constant with only a very weak decrease, in the first half of the upper and lower surfaces. It then increases rapidly but smoothly until the rear side of the rectangular cylinder. The beginning of this pressure recovery is located at around $\overline{r} = 0.5$. This location corresponds to the core of the main vortices appearing along both the upper and lower sides (Bruno et al., 2010). The mean pressure coefficient is positive along the upstream face and negative along the downstream face which leads to the positive $\overline{c_d}^{\text{EXP}}$ depicted in Fig. 3.13b.

For non-zero angles of attack the distribution of $\overline{C_p}^{\text{EXP}}$ is no longer symmetrical, which generates a lifting force and thus $\overline{c_l}^{\text{EXP}} > 0$. On the upper surface, increasing the angle of attack extends the plateau region further downstream and reduces the magnitude of the pressure recovery. Moreover, the pressure intensity of the $\overline{C_p}^{\text{EXP}}$ plateau region remains more or less the same

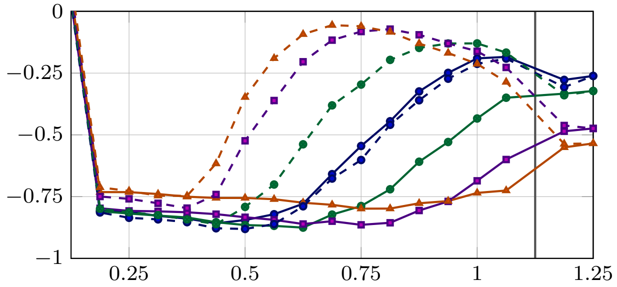

(a) $\overline{C_p}$.

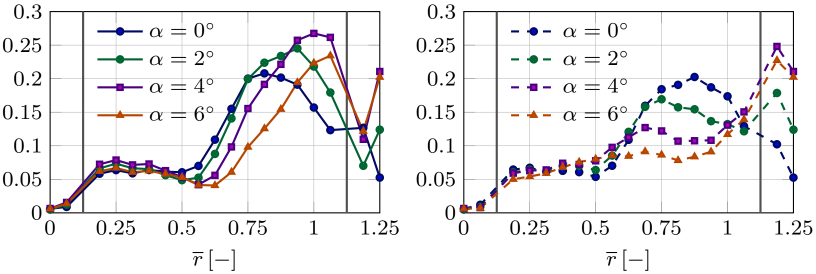

(b) C'_p along upper side.

(c) C'_p along lower side.

Figure 3.15: Mean and standard deviation of C_p along the rectangle surface obtained experimentally at $\mathrm{Re} = 4.2 \times 10^4$ for different angles of attack. The vertical gray lines represent the leading and trailing edges and the coordinate $\overline{r}$ is defined in Fig. 3.4. The plain and dashed lines in (a) corresponds to the legends in (b) and (c).

for small angles of attack. At $\alpha = 4°$, a slightly larger value is observed, which corresponds to the end of the linear region of the $\overline{c_l}^{\text{EXP}}$ curve shown in Fig. 3.13a. At $\alpha = 6°$, the distribution of $\overline{C_p}^{\text{EXP}}$ is nearly flat over the entire upper surface and its magnitude is significantly reduced compared to lower angles of attack. This is typical for a post-stall angle and explains the decrease of the mean lift coefficient $\overline{c_l}^{\text{EXP}}$. The opposite behavior is observed on the lower surface. The extent of the plateau region and the corresponding suction decrease with increasing angle of attack. Moreover, the pressure recovery is more abrupt and reaches a maximum value that increases and whose location moves upstream with α. The pressure then decreases downstream of this maximum to reach a value at the rear of the rectangular cylinder that is lower than for the $\alpha = 0°$ case. Finally, the pressure along the rear face decreases with α. As the pressure distribution on the front face is not significantly influenced by the incidence angle, the mean drag increases (see Fig. 3.13b). These changes in the pressure distribution can be related to changes in the mean flow structures around the rectangular cylinder. In particular, the beginning of the pressure recovery is directly correlated with the chordwise location of the main vortex core. In other words, the experimental pressure distribution suggests that with increasing α the main vortex core moves downstream on the upper surface and upstream on the lower surface. This is illustrated and further discussed in the next section through comparisons with numerical results.

The second order statistic C'_p represents the temporal variation around $\overline{C_p}$. Therefore, a high standard deviation along a particular region is representative of a high intensity vortex traveling across that zone. As depicted in Fig. 3.15b, the distribution of C'^{EXP}_p along the upper surface can be divided into two main parts: a region with low standard deviation from the leading edge to

$\overline{r} \approx 0.6$, followed by rapid increase and large values of C_p' up to the trailing edge. The standard deviation reaches a maximum in this second region. Increasing the incidence extends the first region further downstream and moves the location of the maximum C_p' closer to the trailing edge. The value of this maximum also increases until $\alpha = 4^\circ$, and then decreases for post-stall angles of attack. The same two regions are also present on the lower surface, as shown in Fig. 3.15c. Increasing the angle of attack has however the opposite effect of decreasing the extent of the first region and decreasing the peak C_p' in the second region. Moreover, for $\alpha \geqslant 4^\circ$, a second C_p' increase is observed just before the trailing edge.

3.6.2 Comparison with numerical results

This section presents the statistics computed on the pressure coefficient distribution obtained numerically through URANS and DDES simulations. Numerical and experimental results are compared, and their similarities and discrepancies are discussed.

Figure 3.16 depicts the statistics computed on results obtained experimentally and with CFD for different incidences. As explained in Sec. 3.3.3, $\overline{C_p}$ and C_p' are obtained from time averages. However, for the three-dimensional DDES results these averages are applied to results that have been previously averaged along the span. In other words, $C_p'^{\text{DDES}}$ represents the variation of the span-averaged pressure coefficient in time. Finally, the mean flow streamlines obtained by URANS and DDES are also depicted in Fig. 3.16. Results for DDES are shown for two different meshes, mesh B being the finer one.

As mentioned in the previous section, the numerical results shown in Fig. 3.16 suggest that the chordwise location of the vortex core corresponds well to the point where the mean pressure recovery starts. Moreover, the reattachment point, if present, correlates with the point where $\overline{C_p}$ reaches a maximum during the pressure recovery. Note that Matsumoto et al. (2003) suggested that the reattachment point lies between the point of minimum suction and the C_p' peak. Although this is consistent with the present results, it seems that the correlation with the point of minimum suction is stronger than with the point of maximum C_p'.

As depicted in Fig. 3.16a for 0° angle of attack, two symmetric vortices denoted A_U and A_L lie along the upper and lower surfaces. The flow reattachment point is located at a distance $0.92c$ from the leading edge for URANS and DDES A and $0.94c$ for DDES B. A distribution similar to $\overline{C_p}^{\text{EXP}}$ is obtained with both URANS and DDES A. The main difference is a shift down of $\overline{C_p}^{\text{URANS}}$ and $\overline{C_p}^{\text{DDES A}}$ compared to the experimental distribution. Moreover, the numerically computed pressure recovery begins slightly farther from the leading edge. These discrepancies can be explained by an erroneous estimation of the location of A_U and A_L. In particular, it seems that the URANS and DDES A vortex core is located slightly downstream compared to the presumed experimental location. However, since the distribution obtained by URANS is symmetrical, these differences have no impact on the expected mean lift coefficient $\overline{c_l}^{\text{URANS}} = 0$, as shown in Fig. 3.13. The distribution $\overline{C_p}^{\text{DDES A}}$ is not exactly symmetrical and therefore, a non-zero but very low $\overline{c_L}^{\text{DDES}}$ is observed. The use of a finer mesh for DDES simulation leads to different results. In addition to the shift down exhibited by URANS and DDES A, the shape of $\overline{C_p}^{\text{DDES B}}$ significantly differs from $\overline{C_p}^{\text{EXP}}$. In particular, the plateau region is followed by a zone where the suction increases before the pressure recovery. Moreover, the plateau corresponds to a lower suction than for the two other CFD results. Additionally, the pressure recovery begins at a location much farther downstream than for other results. These discrepancies are caused by differences in the shape of the mean vortices A_U and A_L. As shown by the streamlines, the mean vortex cores are situated farther downstream than for URANS and DDES A, which delays the pressure recovery. Additionally, the vortices are more tilted than for other CFD results. Therefore, the curvature of the mean streamlines is more important below the vortex cores, which could explain the suction peak at $\overline{r} = 0.75$. Large discrepancies appear between the experimental standard deviation of C_p and its estimations by CFD. The general shape consisting of a plateau followed by a growth and then a decrease of C_p' is overall retrieved, but the amplitude is largely overestimated. Another discrepancy is the nearly zero value of C_p' observed

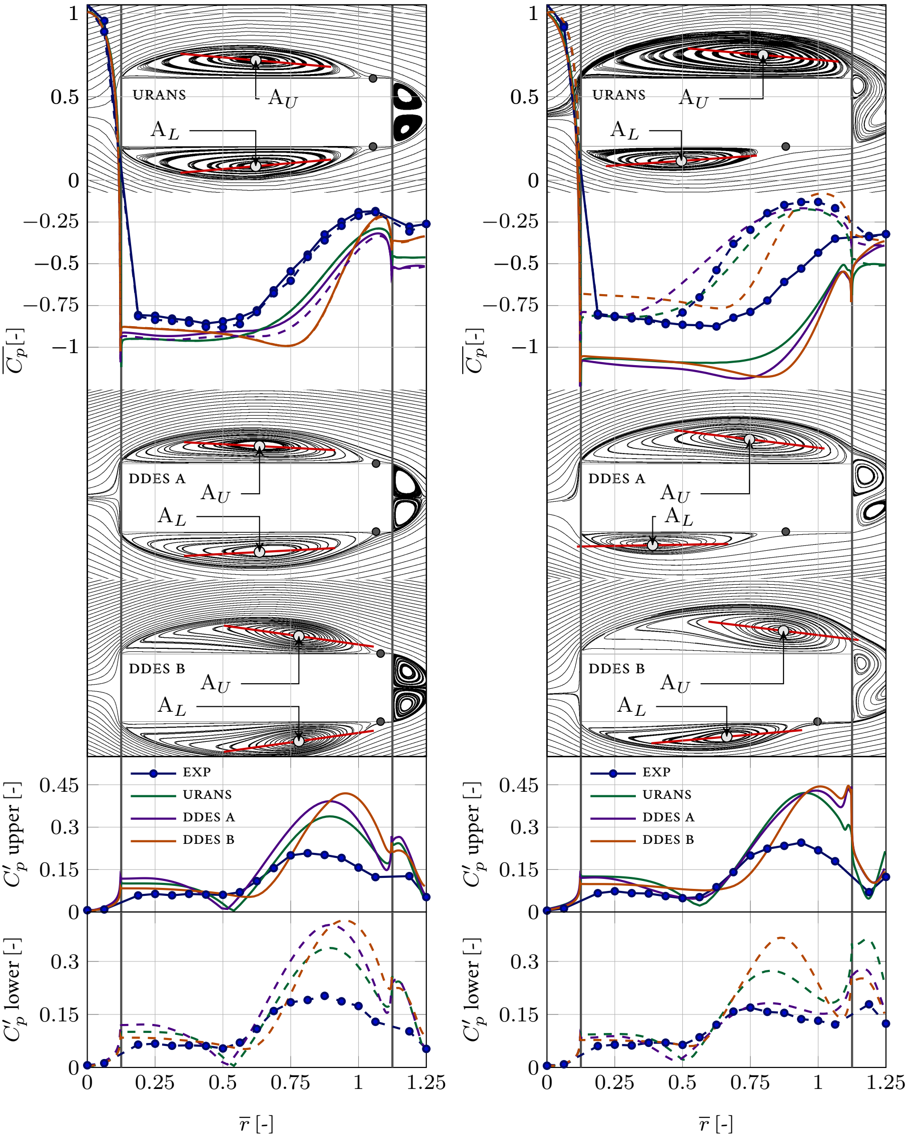

(a) $\alpha = 0^\circ$.

(b) $\alpha = 2^\circ$.

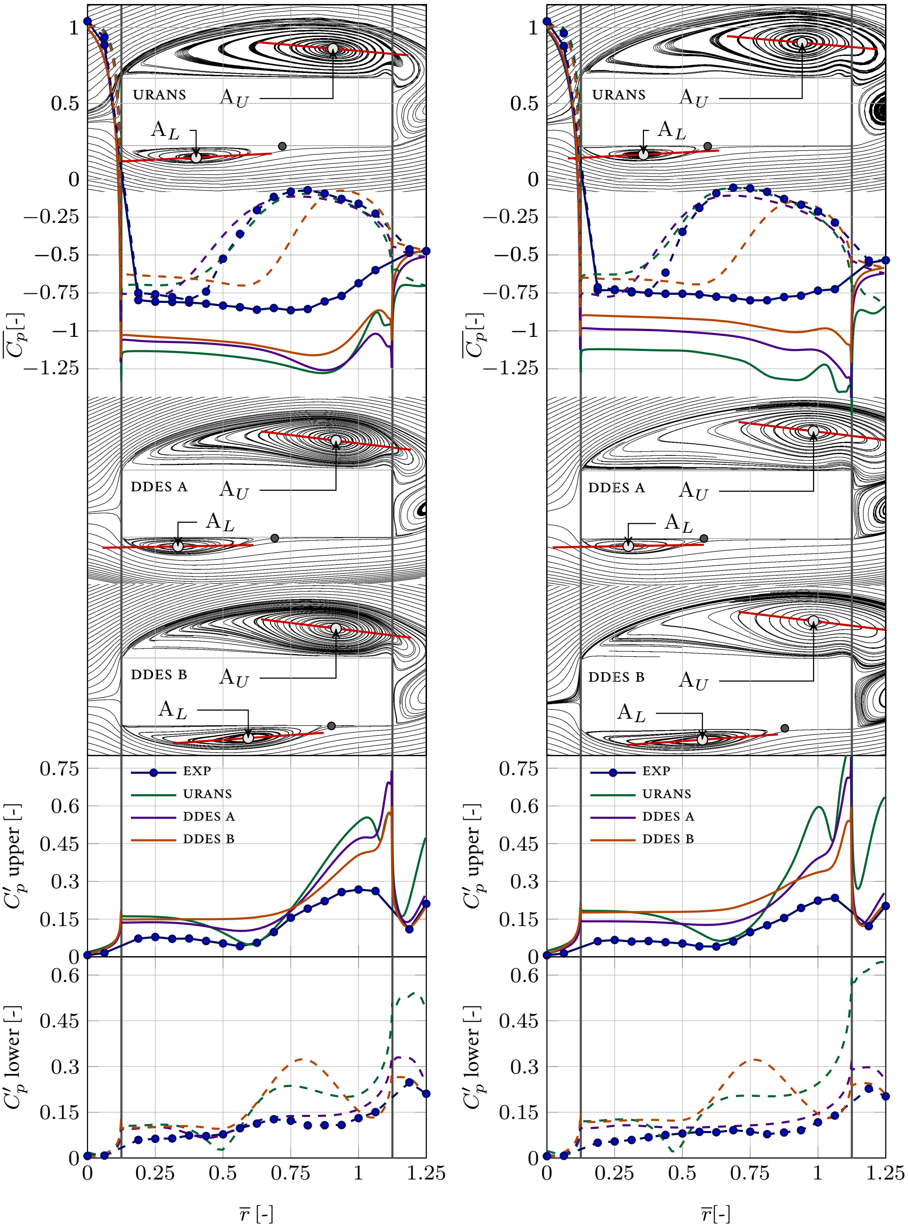

(c) $\alpha = 4^\circ$.

(d) $\alpha = 6^\circ$.

Figure 3.16: Mean streamlines calculated by URANS and DDES and statistics of the pressure coefficient along the rectangle surface obtained by URANS, DDES and EXP at $\mathrm{Re} = 4.2 \times 10^4$ for different angles of attack. Plain and dashed lines correspond to the upper and lower surface, respectively. The light gray disk corresponds to the main vortex core and the dark gray one to the reattachment point. The red line represents the major axis of the main vortex.

for URANS and DDES A results near $\overline{r} = 0.5$ which does not appear in experimental results. Note that this inconsistency was also noticed in the context of the BARC benchmark (Bruno et al., 2014). The use of a finer mesh for DDES improves this aspect as the results for DDES B are closer to the behavior of the experimental results for $\overline{r} < 0.6$. Finally, the mean streamlines can be compared to the experimental results obtained by Mizota (1981) at the same Reynolds number for a 4:1 rectangle at zero angle of attack. The results obtained by URANS and DDES A are similar to those depicted in Fig. 3.17. In particular, the reattachment of the flow occurs at the same location. However, this experimental study reports a slightly thinner vortex with a core located at $\overline{r} \approx 0.53$, i.e., slightly farther upstream than for URANS and DDES A. Conversely, the mean streamlines computed with DDES B are very different as the principal axis of the main vortex is too tilted and its core is located too far downstream. The streamlines depicted in Fig. 3.16a can also be analyzed in light of the study of Bruno et al. (2010) on a 5:1 rectangular cylinder (see Sec. 3.1). The present results do not exhibit the pseudo-triangular inner region illustrated in Fig. 3.2. Therefore, the recirculation bubble consists only of the main vortex A_U or A_L. This inner region has been reported to be case-insensitive by Bruno et al. (2010) after Pullin and Perry (1980). Its absence suggests that a URANS modeling approach of the boundary layer might not be sufficiently accurate.

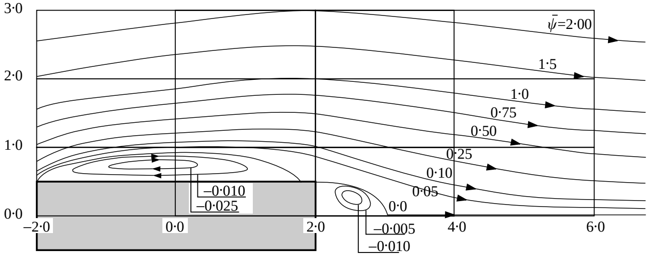

Figure 3.17: Mean streamlines measured by Mizota (1981) along upper surface of a 4:1 rectangular cylinder at 0° and $\mathrm{Re} = 4.28 \times 10^4$. Reproduced from Shimada and Ishihara (2002).

At larger angles of attack, vortex A_U grows and moves downstream, as seen in Figs. 3.16b to 3.16d. For $\alpha \geqslant 4^\circ$, vortex A_U wraps around the trailing edge, and from $\alpha = 2^\circ$ the flow does not reattach along the upper surface. Conversely, vortex A_L shrinks and is located further upstream, so that the reattachment point moves forward. The flow is no longer symmetrical. The suction is higher along the upper surface than along the lower one, which causes the increase of lift depicted in Fig. 3.14. Along the lower surface, the mean pressure distribution estimated by URANS and DDES A is similar to $\overline{C_p}^{\text{EXP}}$. However, $\overline{C_p}^{\text{DDES B}}$ is very different from experimental results, as the pressure recovery begins significantly downstream. This shift is due to the reattachment point and the vortex core that are estimated too far downstream. The numerically computed $\overline{C_p}$ along the upper surface is very different from $\overline{C_p}^{\text{EXP}}$. The suction intensity is largely overestimated, which causes the overestimation of $\overline{c_l}$ that was discussed in Sec. 3.5.2. Nonetheless, for $2^\circ \leqslant \alpha \leqslant 4^\circ$, the global shape of $\overline{C_p}^{\text{EXP}}$ along the upper surface is correctly estimated by URANS and, to a lesser extent, by DDES A. In particular, the pressure recovery and thus the location of the core of vortex A_U are fairly well estimated. For $2^\circ \leqslant \alpha \leqslant 6^\circ$, the pressure recovery of $\overline{C_p}^{\text{CFD}}$ along the upper surface exhibits a non-monotonous behavior just before the trailing edge. This modification in the trend of $\overline{C_p}$ is caused by a small counter-rotating vortex that cannot be detected experimentally because of the limited number of pressure taps. At $\alpha = 6^\circ$, the flow along the upper surface is better estimated by DDES, as Fig. 3.16d shows a decrease of the suction intensity compared to 4° (Fig. 3.16c). As explained in Sec. 3.6.1, this is also observed for $\overline{C_p}^{\text{EXP}}$ and causes a decrease of the lift for incidence angles higher than the stall angle. Moreover, the $\overline{C_p}^{\text{DDES}}$ distribution is nearly flat, which is also the case for the experimental results. Conversely, the suction intensity of $\overline{C_p}^{\text{URANS}}$ is similar for 4° and 6°. Therefore, $\overline{c_l}^{\text{URANS}}$ does not decrease for $\alpha > 4^\circ$ and URANS is not able to estimate the stall angle. The standard deviation of C_p is overestimated by URANS and DDES. This is consistent with the standard deviations of aerodynamic coefficients that are also overestimated by CFD (see Sec. 3.6.1). However, if CFD is able to accurately capture the chordwise location of the vortex core, the global shape of the experimental C_p' is also correctly estimated.

To summarize, the statistics computed on C_p demonstrate that it is very challenging to accurately capture the mean vortices A_U and A_L by using CFD. The second order statistics are even more difficult to approximate. Results from DDES A and B simulations are very different, particularly along the lower surface. This indicates that a finer mesh than mesh B may be required to obtained grid independent DDES results. The numerically computed suction intensity along the upper surface differs strongly from experimental results, which leads to a large overestimation of the lift. For incidences higher than the stall angle, it appears that DDES performs better than URANS along the upper surface. In particular, only the DDES approach is able to capture, qualitatively if not quantitatively, the decrease of suction occurring at these angles. This explains why the stall angle can be estimated from DDES but not URANS simulations. However, for $\alpha \leqslant 4^\circ$, URANS gives better results. Moreover, the flow along the lower surface is also better estimated by URANS, as DDES fails to approximate the location and size of vortex A_L.

3.7 Time response of pressure coefficient

This section aims to better understand the dynamics of the flow by analyzing the time response of the pressure distribution. Both experimental and numerical results are considered, but DDES results are only reported for the finer mesh (DDES B). The dominant POD modes are first presented. Then, the time response of the pressure distribution over a shedding cycle is discussed. In order to filter the random turbulent fluctuations and noise present in the DDES and experimental results, C_p is approximated through a reconstruction based on the main DMD modes. In all cases, DDES results have first been averaged along the span.

3.7.1 Comparison through POD

The POD decomposition reads

$$\mathbf{V}_1^N(\mathbf{x}, t) = \sum_{k=1}^{K} \mathbf{q}_k^{\text{POD}}(t)\, \boldsymbol{\phi}_k^{\text{POD}}(\mathbf{x}), \tag{2.71}$$

where the k^{th} POD mode $\boldsymbol{\phi}_k^{\text{POD}}$ is associated with an energy λ_k^{POD}. As explained in Sec. 2.4.1, λ_k^{POD} measures the contribution of the mode $\boldsymbol{\phi}_k^{\text{POD}}$ in the decomposition. Therefore, the dominant POD modes correspond to the modes with the largest λ_k^{POD}.

Figure 3.18a depicts the percentage of the total energy contained in the first six most energetic POD modes obtained for 0° of incidence. Most of the energy is contained in the first mode $\boldsymbol{\phi}_1^{\text{POD}}$. More precisely, this mode represents 97%, 94% and 93% of the total energy for EXP, URANS and DDES B results. As the mean has not been removed from C_p, this first mode corresponds to $\overline{C_p}$. Figure 3.18b shows the percentage of the remaining energy associated with modes $\boldsymbol{\phi}_2^{\text{POD}}$ to $\boldsymbol{\phi}_6^{\text{POD}}$. Modes $\boldsymbol{\phi}_2^{\text{POD}}$ and $\boldsymbol{\phi}_3^{\text{POD}}$ contain around 75% of the remaining energy for modes obtained from EXP and DDES B results and 96% for URANS results. The lower energy content of the higher URANS modes is simply due to the fact that URANS results are phase averaged and thus do not feature turbulent fluctuations or noise. The same behavior is observed for the POD method performed on C_p distributions at other incidences. In conclusion, for the incidences considered, only the mean and two additional modes are required to approximate $\mathbf{V}_1^N$ with an accuracy of more than 99%. Moreover, without considering the energy contained in the first mode, $\boldsymbol{\phi}_2^{\text{POD}}$ and $\boldsymbol{\phi}_3^{\text{POD}}$ capture a minimum of 75% of the remaining energy.

The shape of modes $\boldsymbol{\phi}_2^{\text{POD}}$ and $\boldsymbol{\phi}_3^{\text{POD}}$ is illustrated in Fig. 3.19. The mode $\boldsymbol{\phi}_1^{\text{POD}}$ is not presented as it corresponds to $\overline{C_p}$ shown in Fig. 3.16. The URANS modes $\boldsymbol{\phi}_2^{\text{POD}}$ and $\boldsymbol{\phi}_3^{\text{POD}}$ at $\alpha = 0$ are relatively

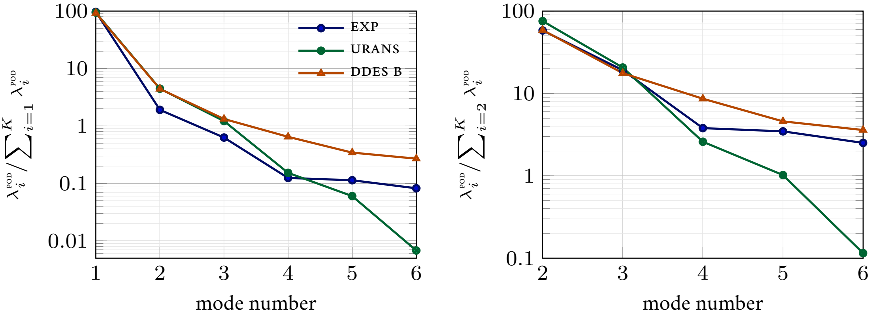

(a) All modes.

(b) Without the first mode.

Figure 3.18: Distribution of energy in the POD decomposition of the C_p distribution obtained for the flow around a rectangular cylinder at 0° of incidence and $\mathrm{Re} = 4.2 \times 10^4$.

close to the experimental ones, as shown in Fig. 3.19a. The main discrepancies are the amplitudes for $\overline{r} > 0.75$ which are overestimated by URANS and lead to the overestimation of the C_p'. The two POD modes corresponding to DDES appear to be shifted to the right compared to experimental results. This shift downstream also appears in ϕ_1^{POD}, as seen in Fig. 3.16a. Additionally, the amplitude is even more overestimated than in the URANS case. As the mean ϕ_1^{POD} is also better approximated by the URANS simulation, the POD decomposition demonstrates that the URANS technique leads to a better estimation of the spatial variation of C_p at zero incidence.

Figure 3.19b depicts ϕ_2^{POD} and ϕ_3^{POD} obtained for $\alpha = 2^\circ$. The increased incidence appears clearly as the spatial distributions are shifted upstream and downstream for the upper and lower surfaces, respectively. Moreover, the mode amplitude associated with the upper surface increases while the one corresponding to the lower surface decreases. As for $\alpha = 0^\circ$, the experimental POD modes are better approximated by the URANS than by DDES modes. In particular, the numerical modes are shifted downstream compared to experimental modes ϕ_2^{POD} and ϕ_3^{POD}, but this shift is smaller for the URANS results. In general, the second and third mode shapes are better estimated by URANS. Figure 3.16b shows that the shape of the mean mode ϕ_1^{POD} is also better approximated by the URANS approach.

The results obtained for incidences $\alpha = 4^\circ$ and $\alpha = 6^\circ$ are presented in Figs. 3.19c and 3.19d. Along the lower surface, the URANS modes ϕ_2^{POD} and ϕ_3^{POD} are close to the experimental results. However, significant discrepancies appear along the upper surface. In particular, the amplitude of the URANS modes overestimates the experimental results. Moreover, the URANS modes are shifted downstream and the mode shapes differ significantly for $\overline{r} > 0.75$, especially for mode ϕ_3^{POD}. Therefore, the URANS approach seems to fail to approximate the flow dynamics along the downstream part of the upper surface. Additionally, as depicted in Figs. 3.16c and 3.16d, the URANS mode shape of ϕ_1^{POD} is quite different from the corresponding experimental mode in that region. The POD modes obtained from DDES results are more difficult to analyze. In particular, the shape of ϕ_2^{POD} and ϕ_3^{POD} strongly differs from the experimental results. Therefore, no conclusion can be drawn in terms of the flow dynamics. Nonetheless, as shown in Figs. 3.16c and 3.16d, the shape and amplitude of the mean modes ϕ_1^{POD} along the upper surface are closer to the experimental results.

3.7.2 Comparison through DMD

The POD method is useful to compare modes among themselves but the physical insight of the flow dynamics provided by the method is limited. The DMD is thus used to further investigate the spatio-temporal variation of C_p. As explained in Sec. 2.4.2, the DMD procedure leads to a de-

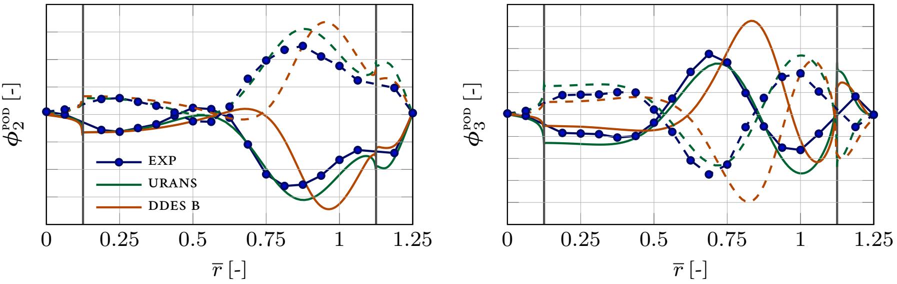

(a) $\alpha = 0°$.

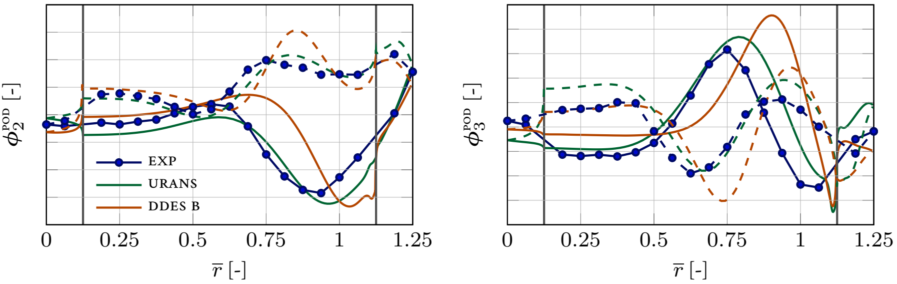

(b) $\alpha = 2°$.

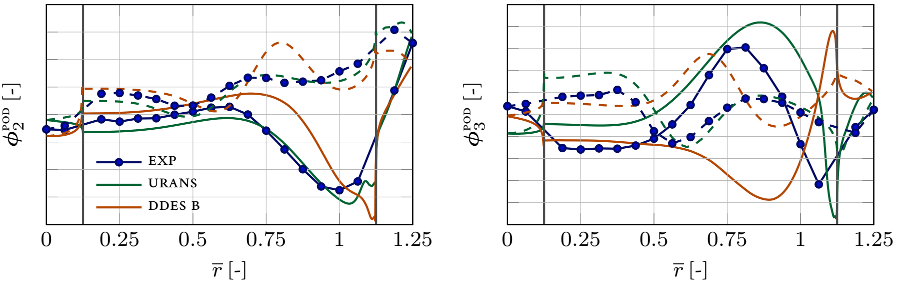

(c) $\alpha = 4°$.

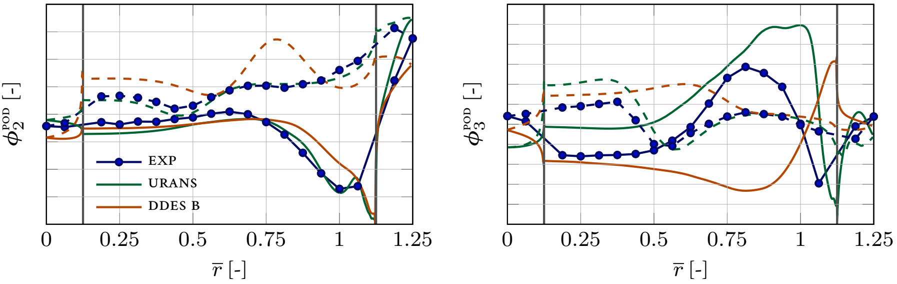

(d) $\alpha = 6°$.

Figure 3.19: Shape of modes ϕ_2^{POD} and ϕ_3^{POD} obtained for the flow around a rectangular cylinder at $\text{Re} = 4.2 \times 10^4$ several incidences. The POD decomposition is applied to experimental and CFD results (URANS and DDES B). Plain and dashed lines correspond to the upper and lower surface, respectively.

composition into modes oscillating at single frequencies. The most representative DMD modes for the experimental and numerical results are selected as explained in Secs. 3.2 and 3.3, respectively. Most of the time, two modes are required to accurately represent the physics: the mean mode ϕ_1^{DMD} and the mode ϕ_2^{DMD} associated with the shedding frequency. The first one corresponds to a frequency of zero and is purely real. Therefore, $\phi_1^{\text{DMD}} = \phi_1^{\text{POD}}$ and their shape at different incidences are depicted in Fig. 3.16. The mode shape ϕ_2^{DMD} is complex. The pressure coefficient is reconstructed from those most representative modes. This enables the comparison of the spatio-temporal $\widehat{C_p}$ obtained numerically and experimentally. This comparison approach is preferred to the comparison of the respective spatial mode shapes because its deeper physical insight. The spatio-temporal variation of $\widehat{C_p}$ is presented for $\alpha = 0^\circ$, 2° and 6° in Figs. 3.20, 3.21 and 3.22. Each of these figures depicts the spatial distribution of $\widehat{C_p}$ at four different phases φ. Similarly to Sec. 3.4, the beginning of a cycle $\varphi = 0$ corresponds to the minimum of $\widehat{c_l}^{\text{EXP}}$. The figures also show the URANS streamlines of the original flow field corresponding to each phase.

Figure 3.20 exposes the results for 0° of incidence and should be analyzed in light of the overview discussion presented in Sec. 3.4.2. As the flow field is symmetrical, the accuracy of the shedding phenomenon obtained numerically is assessed by comparing the variation of $\widehat{C_p}^{\text{EXP}}$ and $\widehat{C_p}^{\text{CFD}}$ along the upper surface only. The dynamics along the lower surface is very similar but distant in time by half a cycle. One can first observe that the URANS simulation predicts rather well the variation of pressure, despite a consistent larger suction on the entire upper and lower surfaces. Additionally, the pressure recovery starts slightly more downstream at $\varphi = 0.25$ and $\varphi = 0.5$. As for the mean flow, DDES results display much larger discrepancies with a larger suction peak and a pressure recovery displaced downstream. This is due to a larger and more tilted vortex A_U^1, whose core is located further downstream. Finally, the numerical results show larger variations in time, explaining the larger standard deviation in Fig. 3.16a. The relative good agreement between URANS and experimental results suggest that the streamlines from URANS provide a good representation of the flow dynamics, as described in Sec. 3.4.2. The strong correlations between the beginning of the pressure recovery and the vortex core, and between the location of maximum pressure and reattachment are again clearly visible. This is well illustrated at $\varphi = 0.5$, where the pressure recovery takes place in two stages, corresponding each to one of the two vortices A_U^1 and A_U^2.

Similar observations can be made for larger angles of attack (Figs. 3.21 and 3.22). Fairly good qualitative agreement is found between URANS and experimental results, but the quantitative discrepancies increase with the incidence angle. This is especially the case on the upper surface where suction is highly overestimated. On the other hand, DDES results show larger qualitative and quantitative discrepancies. The good qualitative agreement between URANS and experiments, especially regarding the chordwise location of the vortex cores and of the reattachment points, indicates that URANS also provides a good representation of the flow dynamics at larger angle of attack. There are two notable exceptions to this at $\alpha = 6^\circ$. First, URANS predicts a vortex A_L^1 that is too small at the beginning and end of the shedding cycle. This leads to a more upstream reattachment at $\varphi = 0$. Secondly, experimental measurements do not seem to indicate the presence of the small vortex on the upper surface just upstream of the trailing edge that is visible in URANS at $\varphi = 0$ and $\varphi = 0.75$. The overall dynamics is similar to the case at zero angle of attack, but amplified on the upper surface and reduced on the lower surface when α is increased. On the upper surface, vortex A_U^1 is larger and more energetic while being shed and the flow does not reattach during the entire cycle. On the lower surface, vortex shedding disappears. At $\alpha = 2^\circ$, vortex A_L^1 is still shed, but its size and strength have become very small. At $\alpha = 6^\circ$, vortex shedding no longer occurs. Vortex A_L^1 simply fluctuates in size and location, but no vortex A_L^2 is created. This explains why the pressure distribution on this surface remains relatively constant in time, as indicated by the low standard deviation in Figs. 3.16d.

To summarize, the comparison of the time response of $\widehat{C_p}$ within a shedding cycle demonstrates that URANS approximates better the flow along the lower surface than DDES. In particular, DDES does not capture correctly the location, size and dynamics associated with the vortex A_L^1.

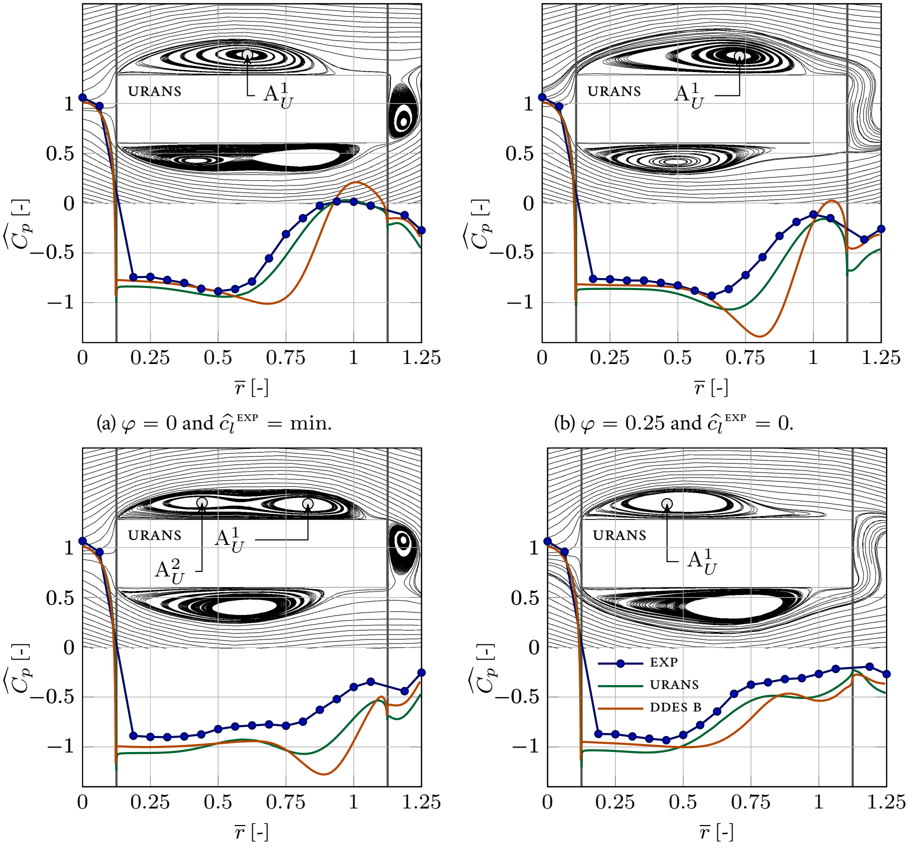

(a) $\varphi = 0$ and $\widehat{c_l}^{\text{EXP}} = \min$.

(b) $\varphi = 0.25$ and $\widehat{c_l}^{\text{EXP}} = 0$.

(c) $\varphi = 0.5$ and $\widehat{c_l}^{\text{EXP}} = \max$.

(d) $\varphi = 0.75$ and $\widehat{c_l}^{\text{EXP}} = 0$.

Figure 3.20: Distribution of the pressure coefficient along the upper surface reconstructed from the first two DMD modes at four different phases of the shedding cycle for the flow around a rectangular cylinder at $\alpha = 0^\circ$ and $\mathrm{Re} = 4.2 \times 10^4$. The streamlines of the original flow field obtained from URANS are also represented for easier interpretation.

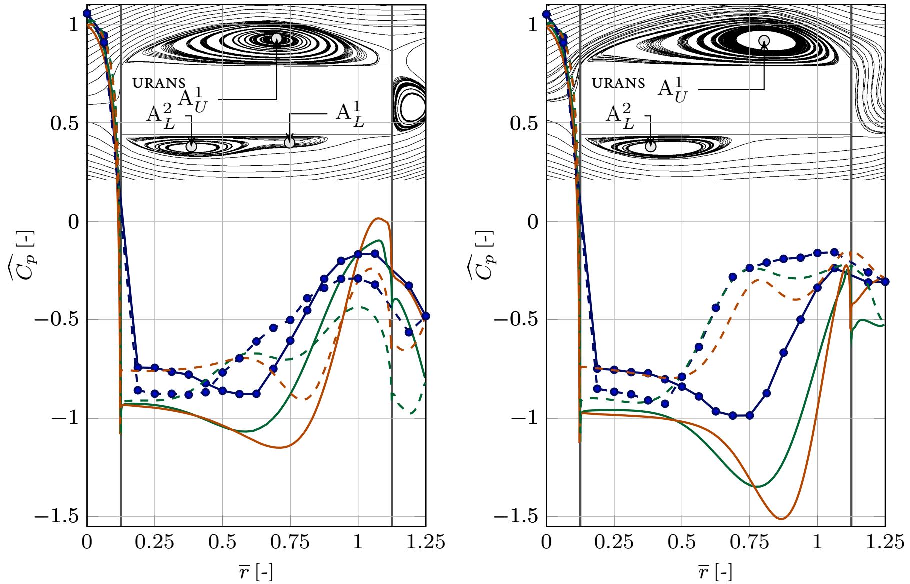

(a) $\varphi = 0$ and $\widehat{c_l}^{\text{EXP}} = \min$.

(b) $\varphi = 0.25$ and $\widehat{c_l}^{\text{EXP}} = 0$.

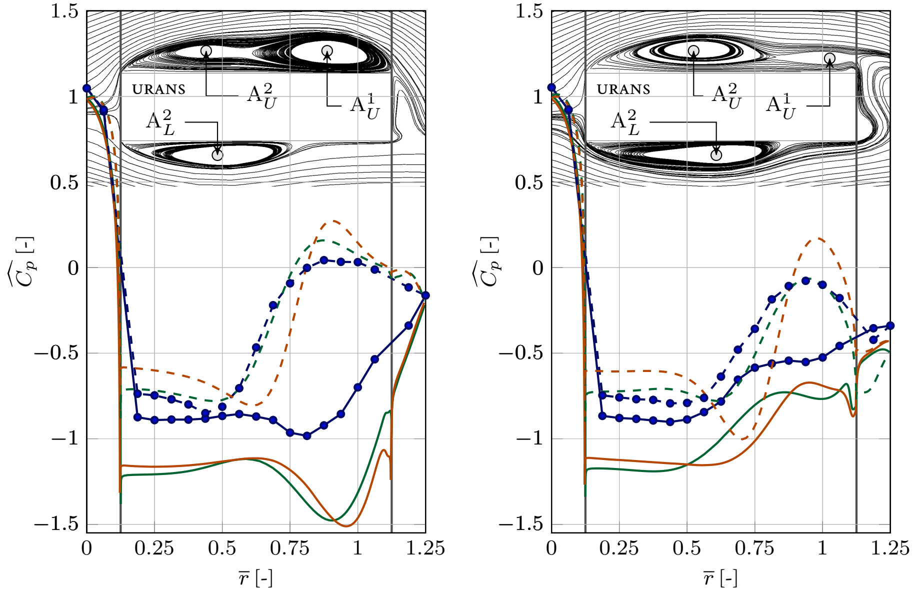

(c) $\varphi = 0.5$ and $\widehat{c_l}^{\text{EXP}} = \max$.

(d) $\varphi = 0.75$ and $\widehat{c_l}^{\text{EXP}} = 0$.

Figure 3.21: Distribution of the pressure coefficient reconstructed from the first two DMD modes at four different phases of the shedding cycle for the flow around a rectangular cylinder at $\alpha = 2^\circ$ and $\mathrm{Re} = 4.2 \times 10^4$. Plain and dashed lines correspond to the upper and lower surface, respectively. The streamlines of the original flow field obtained from URANS are also represented for easier interpretation.

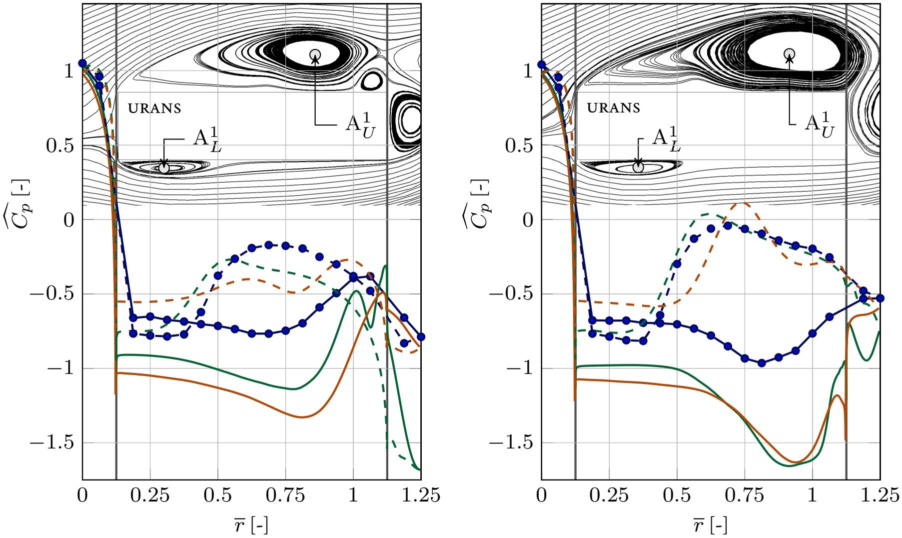

(a) $\varphi = 0$ and $c_l{}^{\text{EXP}} = \min$.

(b) $\varphi = 0.25$ and $c_l{}^{\text{EXP}} = 0$.

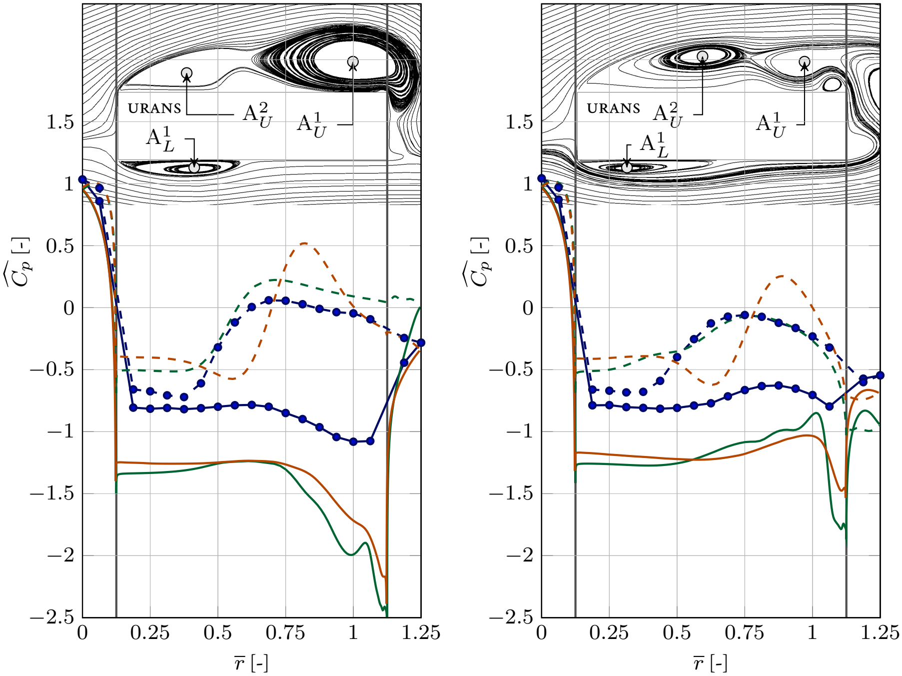

(c) $\varphi = 0.5$ and $c_l{}^{\text{EXP}} = \max$.

(d) $\varphi = 0.75$ and $c_l{}^{\text{EXP}} = 0$.

Figure 3.22: Distribution of the pressure coefficient reconstructed from the first two DMD modes at four different phases of the shedding cycle for the flow around a rectangular cylinder at $\alpha = 6^\circ$ and $\mathrm{Re} = 4.2 \times 10^4$. Plain and dashed lines correspond to the upper and lower surface, respectively. The streamlines of the original flow field obtained from URANS are also represented for easier interpretation.

For incidences lower than the stall angle, URANS also better estimates the flow along the upper surface. However, DDES performs better for higher angles of attack.

3.8 Reynolds number effects

This section studies the effects of the Reynolds number on the flow by analyzing the changes in the mean lift coefficient and in the statistics of the pressure coefficient. This aims to determine how the vortices lying along the upper and lower surfaces of the rectangular cylinder behave with a variation of the Reynolds number.

3.8.1 Mean lift coefficient

The mean lift coefficient $\overline{c_l}^{\text{EXP}}$ is represented for a large range of angles of attack and two different Reynolds number in Fig. 3.23a and for $\alpha = 2^\circ$ and $\alpha = 4^\circ$ but several Reynolds numbers in Fig. 3.23b. Both figures show that an increase of Reynolds numbers in the range considered here leads to a significant increase of the slope $\overline{c_l}_\alpha^{\text{EXP}}$. In particular, $\overline{c_l}_\alpha^{\text{EXP}} = 2.1\pi$ for $\text{Re} = 3.1 \times 10^4$ while $\text{Re} = 7.6 \times 10^4$ leads to $\overline{c_l}_\alpha^{\text{EXP}} = 3\pi$. Therefore, doubling the Reynolds number leads to a relative increase of 45% of the slope. Moreover, Fig. 3.23a suggests that increasing the Reynolds number also leads to a slight shift of the maximum lift to lower incidence. However, this cannot be definitively asserted since only two Reynolds numbers are available.

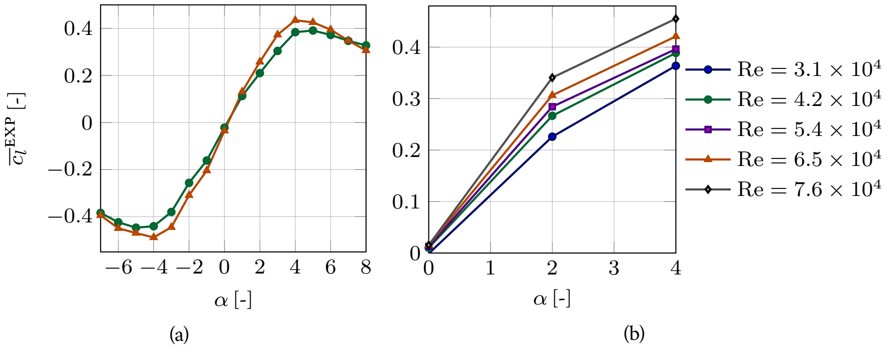

(a) (b)

Figure 3.23: Variation of the mean lift coefficient with Reynolds number.

As mentioned in Sec. 3.1, the sensitivity of the slope $\overline{c_l}_\alpha$ to the Reynolds number was studied by Schewe (2013) for a 5:1 rectangular cylinder. This author reported that the mean lift slope at $\alpha = 0^\circ$ increases by 63% when the Reynolds number increases from 3×10^4 to 3×10^5. Schewe (2013) suggested that the modification in the turbulence level associated with a change of the Reynolds number induces a modification of the flow structure along the lower surface of the rectangle. More precisely, this author argued that an increase of the Reynolds number results in a reattachment point located farther upstream, as depicted schematically in Fig. 3.24. Subsequently, the shape and curvature of the mean vortex A_L located on the lower side of the rectangular cylinder is modified. This causes a modification in the mean pressure distribution and consequently an increase of the mean lift compared to a lower Reynolds number. Schewe (2013) supported his explanation with numerical simulations performed by Mannini et al. (2010). These simulations were conducted for a Reynolds number varying from 2.6×10^4 to 1.85×10^6 and for an incidence of 4°. The results show an increase in $\overline{c_l}_\alpha$ of 26% and a reduction in the length of the mean vortex A_L of 14%.

If an increase of the Reynolds number leads to a reduction of the size of vortex A_L, the mean pressure distribution along the lower surface should also be modified, similarly to what has been

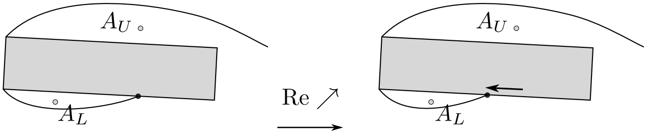

Figure 3.24: Modification of the flow topology caused by an increase of the Reynolds number as proposed by Schewe (2013).

reported for an increase of incidence (see Sec. 3.6.1). More precisely, the pressure recovery region should begin farther upstream, as depicted in Fig. 3.15a. Moreover, the point of maximum pressure during the pressure recovery, which has been found to correlate well with the reattachment point, should also move upstream. However, the pressure statistics shown in the next section do not support this argument. This suggests that the increase of lift with Reynolds number does not result from a shift upstream of the reattachment point on the lower surface.

3.8.2 Statistics on the pressure coefficient

Figure 3.25 depicts the mean and the standard deviation of the experimental pressure coefficient obtained at 2° and 4° of incidence, for $\mathrm{Re} = 4.2 \times 10^4$ and $\mathrm{Re} = 6.5 \times 10^4$. The general shape of both the mean and standard deviation does not change with the Reynolds number. In particular, the location of the maximum and minimum $\overline{C_p}^{\text{EXP}}$ and $C_p'^{\text{EXP}}$ remains constant. Moreover, the mean pressure recovery appears to begin at the same chordwise location $\overline{r}$. The main difference lies in the pressure magnitude: the mean suction is slightly larger on the upper surface and lower on the first and last third of the lower surface. Additionally, larger fluctuations, i.e., larger C_p', are observed at higher Reynolds number.

Using either the criterion of Matsumoto et al. (2003) based on the maximum $\overline{C_p}$ and maximum C_p', or the better correlation of the reattachment point with the maximum $\overline{C_p}$ observed here, these results indicate that the reattachment point on the lower surface does not move when the Reynolds number is increased. This is in contradiction with the mechanism proposed by Schewe (2013). As suggested by the results of the previous section, the changes in the magnitude of the pressure distribution, and thus the higher lift, could possibly originate in the vertical displacement of the vortex cores. This could also be linked to an increase/decrease of the vortex strength and/or thickness. In both cases, the chordwise location of the two vortices does not change.

3.9 Conclusions and future work

This chapter has studied numerically and experimentally the flow around a 4:1 rectangular cylinder at several angles of attack. In particular, dynamic pressure measurements have been performed to obtain the time response of the pressure coefficient C_p along a cross-section of the cylinder. The pressure distribution was used to compute and study the aerodynamic loads on the body and to analyze the flow dynamics. The sensitivity of the solution on the Reynolds number has been quantified by considering different Reynolds numbers ranging between 3.1×10^4 and 7.6×10^4. Additionally, URANS simulations based on the $k - \omega$ SST turbulence model and DDES simulations based on the SA model have been performed. For the latter, results on two different meshes have been presented. The pressure distribution along the cross-section of the cylinder resulting from numerical computations has been compared to the experimental results through statistical analysis and modal decomposition methods, namely POD and DMD. Moreover, numerical results have been used to visualize key flow structures and relate them to the variation of the pressure distribution.

Although the flow around a rectangular cylinder has been extensively studied, most of previous work has focused on a 5:1 rectangle. Furthermore, only few authors considered non-zero

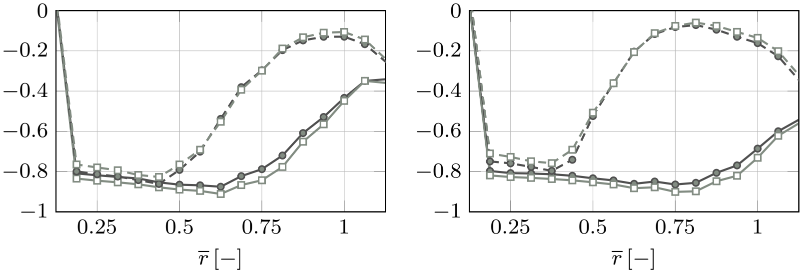

(a) $\overline{C_p}$ for $\alpha = 2^\circ$. (b) $\overline{C_p}$ for $\alpha = 4^\circ$.

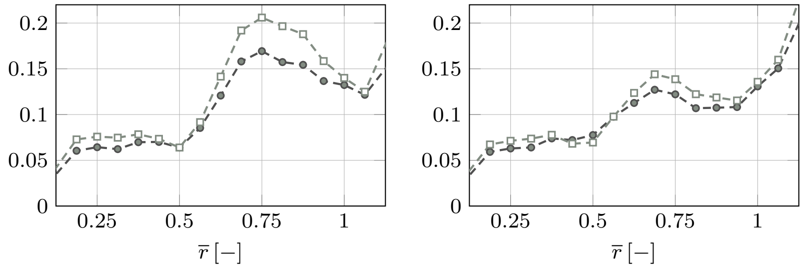

(c) C_p' along lower surface for $\alpha = 2^\circ$. (d) C_p' along lower surface for $\alpha = 4^\circ$.

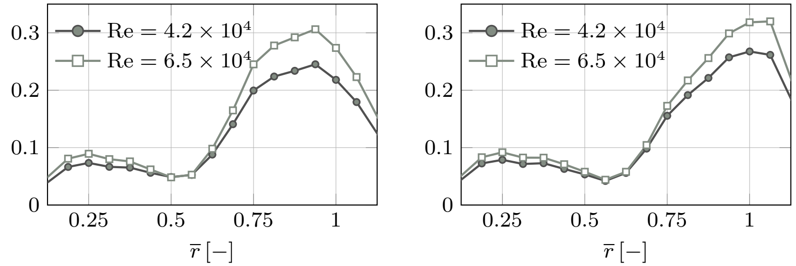

(e) C_p' along upper surface for $\alpha = 2^\circ$. (f) C_p' along upper surface for $\alpha = 4^\circ$.

Figure 3.25: Mean and standard deviation of C_p^{EXP} at $\alpha = 2^\circ$ and $\alpha = 4^\circ$ and for $\mathrm{Re} = 4.2 \times 10^4$ and $\mathrm{Re} = 6.5 \times 10^4$.

angles of incidence. The present study relies on a combined experimental and numerical study, focuses on a different geometry, and considers different angles of attack and different Reynolds numbers. It thus provides new data and insight to i) better understand the complex dynamics of the flow around a rectangular cylinder, and ii) quantitatively assess the ability of numerical methods to accurately represent such a flow. The results, on the one hand, confirm several observations or hypotheses made by other authors. On the other hand, this work provides new findings, and thus represents a useful contribution to better understand this type of flow.

- The variation with the incidence angle of the aerodynamic coefficients obtained through pressure measurement has been found to be close to those reported in previous studies (Nakamura and Mizota, 1975; Washizu et al., 1978). In particular, a stall angle of $\alpha \approx 4^\circ$ has also been observed. Two main discrepancies with the literature results have been highlighted: a lower drag and a difference in the lift slope. The differences are likely due to the load acquisition process for the drag and to the sensitivity to the Reynolds number for the lift.
- Similarly to what has been reported by Schewe (2013), a Reynolds number increase from 3.1×10^4 to 7.6×10^4 has been shown to impact strongly the flow around the rectangular cylinder. In particular, the mean lift slope $\overline{c_l}_\alpha$ strongly increases with Reynolds number. The pressure measurements have demonstrated that an increase of Reynolds number causes an increase/decrease of the suction along the upper/lower surfaces, respectively. This results in an increase of the mean lift coefficient. Unlike what was suggested by Schewe (2013), it is demonstrated that this increase is not due to an expansion of the mean recirculation bubble lying along the lower surface. It is argued that the modification in the mean pressure and the resulting variation of the mean lift slope are due to a modification of the mean vortex strength, size and/or distance of its core from the surface.
- Large discrepancies between numerical and experimental results have been highlighted. In particular, the mean suction intensity along the upper surface is largely overestimated by both URANS and DDES for all the incidence angles considered. This results in an overestimation of the lift coefficient for non-zero angles of attack. Conversely, the drag coefficient is captured with satisfying accuracy by both URANS and DDES. The high sensitivity of the pressure on the flow structures explains the rather poor numerical results. As separation and reattachment are particularly difficult to capture accurately with turbulence models, it might be no surprise to see large quantitative differences between numerical and experimental results.
- Although DDES should provide a more accurate representation of turbulence, URANS has been found to perform better than DDES for incidences below the stall angle. In particular, URANS gives a better approximation of the experimental pressure coefficient distribution, both in terms of statistics and time response. However, the stall angle is correctly estimated by DDES but not by URANS. More precisely, the decrease in suction intensity along the upper surface appearing for $\alpha > 4^\circ$ is only captured by DDES. Nonetheless, the reattaching flow along the lower surface is better approximated by URANS, also for incidences higher than the stall angle.
- DDES simulations have been performed on two meshes differing in their maximum grid spacing Δ_0 in the so-called "focus region". In particular, the Δ_0 corresponding to the coarsest and the finest meshes have been chosen as $\Delta_0 = c/32$ and $\Delta_0 = c/64$, respectively. These values are consistent with the grids adopted by other authors in the context of the BARC (Bruno et al., 2014). Large variations have been observed between the results obtained for the two meshes. Therefore, a maximum grid spacing $\Delta_0 = c/32$ is not fine enough to obtain conclusive DDES results. Moreover, $\Delta_0 < c/64$ might be required to obtained grid independent DDES results.
- The DMD filtering that has been applied to the numerical and experimental spatio-temporal pressure coefficient has demonstrated that URANS is able to correctly approximate the dy-

namics of pressure at the wall for incidence angles lower than 4°. The analysis of the URANS results has subsequently enabled the description of the flow dynamics. In particular, at $\alpha = 0^\circ$, it has been shown that vortices emerge and grow both at the leading and trailing edges. The leading edge vortex is convected downstream where it merges with the vortex at the trailing edge. The resulting vortex is then shed into the wake. For incidence angles $0^\circ < \alpha \leqslant 4^\circ$, the flow dynamics along the lower surface is similar. However, along the upper surface, the vortex generated at the leading edge is convected and shed into the wake without merging with the trailing edge vortex that vanishes.

Different simplifications and hypotheses have been made throughout this work. Moreover, various aspects have not been studied. Therefore, the flow around a 4:1 rectangular cylinder could be further investigated by performing additional numerical and experimental studies.

- The grid used for numerical studies assumed slightly rounded edges. Moreover, the experimental model cannot have perfectly sharp edges. Similarly to the high sensitivity of the flow to the Reynolds number, the sharpness of the edges could have a strong impact on the flow structures. Therefore, this aspect is worth further investigation. For the same reason, the effects of the incoming flow characteristics and the limitations/uncertainties associated with the experimental measurements should also be studied. This includes for instance the freestream turbulence level, the possible vibrations of the experimental setup, the uncertainty on the angle of attack or the alignment with the freestream.
- It has been shown that a maximum grid spacing $\Delta_0 < c/64$ in the "focus region" might be required to obtained grid independent DDES results. Consequently, additional DDES simulations on finer grids could be performed to assess whether the results are grid independent. Moreover, the numerical modeling of the flow was shown to be very sensitive to the near wall behavior. Therefore, URANS simulations based on a higher fidelity model than the Boussinesq hypothesis should be performed. Encouraging results were reported by Mannini et al. (2010) who showed that the Explicit Algebraic Reynolds Stress approach is able to partly capture the Reynolds number sensitivity of the flow. Additionally, higher fidelity simulations such as LES or DNS could be used.
- The present experimental studies are based on two-dimensional dynamic pressure measurements. Knowledge of the overall flow behavior would greatly benefit from velocity field measurements around the rectangular cylinder. This could be done through PIV measurements and would allow to determine how the flow varies with the Reynolds number. Moreover, the resulting data set would allow a better validation of numerical results.
- Finally, only two-dimensional aspects of the flow have been studied. Therefore, the three-dimensional effects could be further investigated, both numerically and experimentally.

CHAPTER 4

Detached flow around a flat plate

This chapter is dedicated to the study of the indirect calculation of aerodynamic loads from 2C2D PIV. In particular, this work presents, compares and discusses results obtained with the INSE and NOCA methods, two methodologies based on momentum balance. The indirect methods are applied to spatio-temporal data for different separated flows around a flat plate. The effect of the user-defined parameters required for the INSE and NOCA approaches are studied and the accuracy of the results is assessed by comparison with direct measurements and numerical results.

4.1 Introduction

Aerodynamic forces and moments are conventionally measured by means of a load balance. However, this approach has some limitations, such as high relative errors for small aerodynamic loads. Moreover, when the body is moving, these devices measure not only the aerodynamic forces and moments but also the structural response, which contaminates the measurements (Rival et al., 2009). For such cases, another option is to calculate the loads directly from the flow field. This calculation can be performed by using pressure sensitive paint (McLachlan and Bell, 1995), Pitot tube wake rakes (Jones, 1936) or pressure taps (Tropea et al., 2007). Although these approaches have been proven to be reliable and accurate, they also have limitations. Their accuracy can decrease with decreasing airspeed, they can be affected by zero drifting in time, they can be limited in frequency sampling or they have an intrusive effect, disturbing the flow (Tropea et al., 2007; Barlow et al., 1999). An interesting alternative to these methods is to use PIV velocity fields to indirectly calculate the aerodynamic loads.

In the present work, the INSE (Unal et al., 1997) and the NOCA (Noca et al., 1999) formulations are applied to spatio-temporal data obtained for the flow around a static or pitching flat plate. These two methods have been described in detail in Secs. 2.3.2 and 2.3.3, respectively. The INSE formulation has been applied to numerous cases, such as the steady flow around an airfoil (van Oudheusden et al., 2006), the unsteady flow around a square (Kurtulus et al., 2007), the steady supersonic flow around a bi-convex profile (van Oudheusden et al., 2007) or the phase-averaged flow around an airfoil undergoing dynamic stall (Gharali and Johnson, 2014). On the other hand, the NOCA method was used to compute the instantaneous forces on a cylinder (Tan et al., 2005) and, more recently, to estimate the unsteady loads on an airfoil with an actuated flap (Sterenborg et al., 2014). As shown by David et al. (2009) and Gharali and Johnson (2014), the velocity noise impacts the accuracy of the pressure calculation and thus of the load estimation. Moreover, the quality of the results is also affected by different parameters, such as the location and size of the PIV window, the spatio-temporal resolution (David et al., 2009; Albrecht et al., 2013; Gharali and Johnson, 2014) or the type of flow. The present work aims to extend these results by comparing the INSE and NOCA methods and by investigating the effect of several parameters.

The indirect formulations are applied to three different cases of unsteady flows around a plate having a 16:1 chord-to-thickness ratio. The first case considers a forced pitching motion with a large amplitude at a Reynolds number $\mathrm{Re} = 2 \times 10^4$ based on the chord c. The objective is to assess the ability of the INSE and NOCA methods to deal with moving bodies. A sinusoidal pitching motion $\alpha = \overline{\alpha} + \Delta\alpha \sin(2\pi f t)$ is imposed, with a mean angle of attack $\overline{\alpha} = 0^\circ$ and an amplitude $\Delta\alpha = 30^\circ$. The reduced frequency $k = {}^{\pi f c}/_{U_\infty}$ is 0.2 which corresponds to $f = 0.217\,\mathrm{Hz}$. Three pivot axes are considered: at mid-chord and at the leading and trailing edges, which are here denoted by LE and TE, respectively. The imposed pitching is used to synchronize the PIV apparatus with the motion of the plate so that several PIV frames can be obtained at the same specific phase of the motion. Consequently, the velocity field can be phase-averaged. Note that Gharali and Johnson (2014) studied through the INSE formulation the dynamic stall of an airfoil which is similar to this first test case.

The second case corresponds to a static plate at two different angles of attack, 30° and 45°, and a Reynolds number $\mathrm{Re} = 4 \times 10^4$. As the shedding is not perfectly periodic, it cannot be used to synchronize the PIV system as in the previous case. Moreover, the maximal sampling frequency of the PIV apparatus is too low to ensure a sufficient resolution of a single cycle. Therefore, only the mean flow is considered. This second test case aims to assess whether the indirect load calculations are able to predict the mean fluid dynamic load coefficients based on the mean velocity field. More specifically, in this particular case, the averaging operation in the INSE and NOCA formulations can be understood as time-averaging, or more precisely as an ensemble average over all PIV fields. Note that Albrecht et al. (2013) applied both the INSE and NOCA formulations to a similar case.

The third case attempts to alleviate the lack of reference for phase averaging by forcing the periodic shedding at a given frequency. To this end, a sinusoidal pitching motion $\alpha = \overline{\alpha} + \Delta\alpha \sin(2\pi f t)$ with a very small amplitude $\Delta\alpha$ is imposed around the mean angle of attack $\overline{\alpha}$. The pivot axis is located at the center of the plate and the frequency is chosen to be as close as possible to the shedding frequency of the static plate. The PIV apparatus can then be synchronized with the forcing frequency without strong alteration of the natural flow dynamics compared to the static plate (Lam and Leung, 2005). The PIV velocity field can therefore be obtained at selected phases and a phase-averaging procedure can be applied to analyze the time response of the velocity field and fluid dynamic loads within a cycle. Here again, the Reynolds number is $\mathrm{Re} = 4 \times 10^4$ and the mean angle of attack is set to 30° and 45°. The imposed amplitude $\Delta\alpha$ around the mean angle is 0.77° for the lowest mean incidence and 1.33° for the highest. In both cases, the non-dimensional frequency, i.e., the Strouhal number, $\mathrm{St} = {}^{f c \sin\overline{\alpha}}/_{U_\infty}$ is 0.155. The forcing frequency f equals $2.13\,\mathrm{Hz}$ and $1.47\,\mathrm{Hz}$ for the smallest and the largest angles, respectively.

This chapter is organized in six sections in addition to the present one. First, Sec. 4.2 details the experiments. In particular the PIV procedure, the direct load measurements and the flow visualization process are presented. The CFD simulations and their setup are then described in Sec. 4.3. In Sec. 4.4, the experimental and numerical results are used to describe the flow dynamics of the different test cases. Then, the INSE and NOCA formulations are applied to PIV fields. The different studies are presented in two sections. First, Sec. 4.5 describes the effects of the user-defined parameters. Then, Sec. 4.6 discusses the ability of the INSE and NOCA formulations to estimate the loads. Finally, this chapter closes with Sec. 4.7, which summarizes the main conclusions.

4.2 Experimental setup and measurements

The different experimental measurements are conducted in a low-turbulence free-surface water channel at the University of Michigan. The present section describes the facility shown in Fig. 4.1, the different experiments, the experimental devices and the post-processing applied to the data acquired.

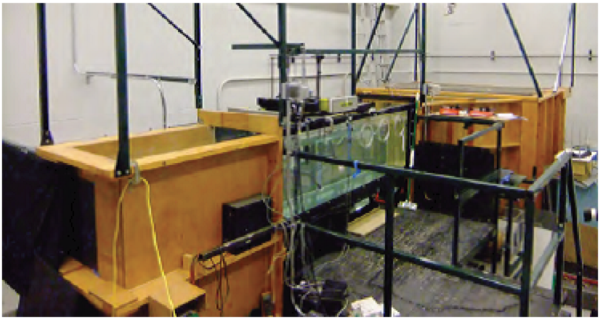

Figure 4.1: Overall view of the water channel facility (Vandenheede et al., 2012).

4.2.1 Water channel and model

The channel test cross-section has dimensions 61 cm $\times$ 61 cm as shown in Fig. 4.2, which corresponds to $8c \times 8c$, c being the chord length of the plate. The model is a polished stainless-steel flat plate with 7.6 cm chord length spanning the height of the test section. The plate thickness is 4.7 mm and the leading and trailing edges are rounded with a radius of half the plate thickness. As depicted in Fig. 4.2, the model is mounted vertically and the immersed span corresponds to $7.6c$. The distance between the model and the bottom wall of the test section is about 3 mm or $0.04c$ to minimize three-dimensional effects. In particular, the water channel bottom wall boundary layer thickness at the plate location is about 2.5 cm, approximately three times larger than the gap between the plate and the bottom wall. The gap is thus considered to be sufficiently small to minimize three-dimensional wing tip effects.

The flow in the water channel is generated by a propeller located in the lower part of the facility. The freestream velocity is controlled trough the frequency of the motor driving that propeller. In other words, the user does not directly impose the freestream velocity but the motor frequency. Since the latter impacts the flow rate in the test section, the freestream velocity depends on the motor frequency and the cross section, the latter varying with the water level. Through PIV measurements, Yu (2014) established an empirical correlation between the freestream velocity U_∞, the motor frequency f_M and the water level H,

$$U_\infty = 2.55 f_M \frac{H}{H_{ref}} - 0.58, \tag{4.1}$$

where $H_{ref} = 22\,{}^{11}/_{16}$ inch is the water level at which Eq. (4.1) was established. Note that the water levels are measured in inches and without flow, while the dimensions of the freestream velocity and the motor frequency are cm/s and Hz, respectively. Finally, the facility allows a freestream velocity ranging from 5 cm/s to 55 cm/s with a turbulence intensity of about 1%. The two freestream velocities used here are 26 cm/s and 52 cm/s, which corresponds to $\mathrm{Re} = 2\times10^4$ and 4×10^4, respectively. At these flow conditions the water surface does not deform significantly and, therefore, the free surface acts as a symmetry plane suppressing three-dimensional wing tip effects.

4.2.2 Plate motion and kinematics

The plate is initially located in the middle of the water channel and aligned with the flow. The plate motion is imposed by the mechanical system shown at the left of Fig. 4.2a. The position in the streamwise direction and perpendicular to the flow is set through two linear traverses (Velmex MN10-0400-E01-31 and MN10-0200-E04-31 BiSlide). The rotation around the span axis is imposed through a rotary stage (Velmex B4872TS Rotary Table).

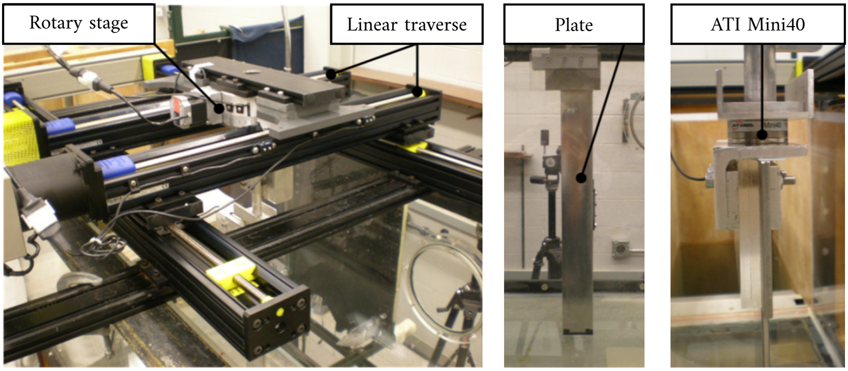

(a) Mounting in the water channel facility (Baik et al., 2012).

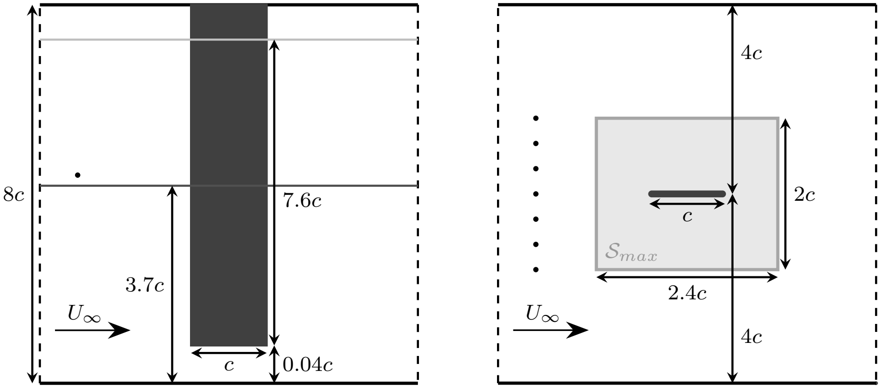

(b) Side view.

(c) Bottom view.

Figure 4.2: Pictures and schematic view of the plate mounted in the water channel. The seven small discs in (b) represent the location of the dye rake used in flow visualization (Sec. 4.2.3). The light and gray lines in (b) represent the water level and the laser sheet, respectively, and the light gray surface $\mathcal{S}_{max}$ in (c) corresponds to the PIV field of view (Sec. 4.2.4).

The pitching motions described in Sec. 4.1 are imposed through the rotary stage, which has an advance per step of $0.0125°$ and a maximum speed of $12.5°/\mathrm{s}$. The complete kinematics of the plate motion for the three different cases consists of three main parts. First, an initial motion imposes the initial orientation α_0 and rotational velocity $\dot{\alpha}_0$ of the pitching motion. Then, the desired sinusoidal pitching motion $\alpha = \overline{\alpha} + \Delta\alpha \sin(2\pi f t)$ is repeated several times. This repetition enables the phase-averaging done in the context of PIV and direct load measurements. Finally, a last motion brings the plate back to its reference orientation, i.e., aligned with the flow, to enable the quantification of the sensor drift. For the static case, the kinematics is very similar, except that the repetition of pitching motion is replaced by a constant orientation. This allows the time-averaging of direct load measurements. More details about the imposed kinematics can be found in App. C.1. > The rotary stage is driven by a stepper motor that is controlled through the COSMOS software. It requires to discretize the kinematics in such a way that it can be described by a succession of steps made at a specific value of the rotational speed. The COSMOS input files written for the three different cases can be found in App. C.2.

Finally, the stepper motor is able to send information while imposing a motion. More precisely, the stepper motor controller has two user outputs that can be modified through the input file. Specific commands enables to impose a "low" or a "high" output, corresponding to 0 V and 5 V, respectively. As this information is recorded, a specific phase can be identified which provides a reference to perform the phase-averaging of the loads.

4.2.3 Flow visualization

Dye visualization is used to obtain a qualitative overview of the flow for the different plate configurations. The apparatus consists of a camera, colored dyes and, as shown in Fig. 4.3, a dye rake and two syringe pumps. The rake is made of seven tubes of 0.8 mm outside diameter that are uniformly distributed over a distance of 15.2 cm or $2c$, as represented by the small circles in Fig. 4.2c. The syringe pumps generate blue and red streams made of food coloring dyes of $1012\ \mathrm{kg/m^3}$ density, which is close enough to the water density to minimize density effects. The dye rake is located at mid-span and a few chords upstream of the leading edge. The flow disturbances created by the rake are small enough to not significantly impact the measurements.

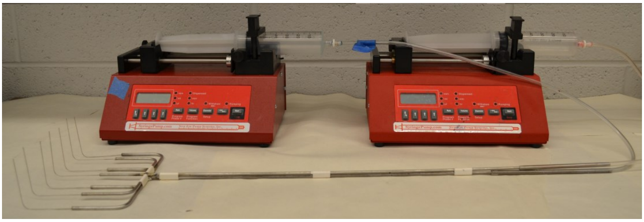

Figure 4.3: Syringe pumps and dye rake used for flow visualization (Yu, 2014).

The images are acquired at a frame rate of 30 Hz with a Nikkon D3100 camera. The flow is observed from both the side and bottom of the water channel. Because images acquired from the bottom suffer from a distracting background consisting of reflections from the water surface and view of the mounting system, a 5 mm thick white background board is fixed on the plate, parallel to the water level and just below it.

Dye visualization is carried out at a freestream velocity $U_\infty = 26.5\ \mathrm{cm/s}$ and provides streaklines that are used to observe the flow topology and three-dimensional effects for the different cases described in Sec. 4.1. When pitching motions are considered, the post-processing of the recorded movies consists in the extraction of pictures of the flow at specific phases of the cycle. However, the plate kinematics and the camera are not synchronized. Therefore, a reference phase is identified from the movies. Note that for the small amplitude pitching plate cases, the uncertainty on the phase can be important as the amplitude and the period of the motion are small.

4.2.4 PIV experiments

A quantitative study of the flow can be carried out through the analysis of PIV velocity fields. The technique is explained in Sec. 2.3.1 and the present section details the procedure used in this particular measurement campaign. It first describes the apparatus, then the experimental procedure and finally the applied post-processing.

4.2.4.1 PIV apparatus, seeding, synchronization and data acquisition

The PIV apparatus, depicted schematically in Fig. 4.4, consists of a double-pulsed laser, light sheet forming optics, a digital camera, control electronics and a computer which acquires images. Note that this apparatus is also described in the theses of Baik (2011) and Yu (2014).

The laser (Spectra Physics PIV 300) consists of two Nd-YAG cavities generating at a nominal frequency $f_{l_0} = 10$ Hz two distinct pulses of light, the laser beams. As shown in Fig. 4.4, each of the

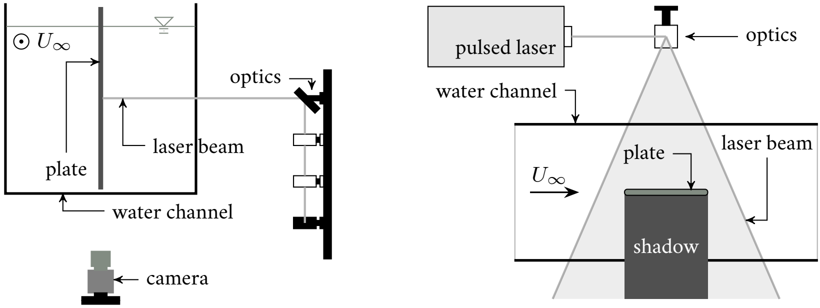

(a) Side view.

(b) Top view.

Figure 4.4: Schematic view of the PIV apparatus.

beams is transformed by mirrors and light sheet forming optics into a horizontal laser sheet of $2\,\mathrm{mm}$ thickness illuminating part of the water channel at a distance of $27.9\,\mathrm{cm}$, or $3.7c$, from the bottom, i.e. around the mid-span of the plate. Because of the flat water surface and the small gap between the bottom wall and the plate, the PIV measurements are not significantly affected by end-wall effects, which for unsteady flow phenomena may reach approximately one chord away from the walls (Gardner et al., 2014). Note that, as illustrated by Fig. 4.4b, a shadow region is present on one side of the plate where the velocity field cannot be measured. The two laser sheets are sightly distant in space. According to Baik (2011), they overlap along 75% of their thickness, i.e. in a region of $1.5\,\mathrm{mm}$ thickness, or 27 pixels for the magnification M imposed here by the camera lens. The imposed particle displacement between image pairs is chosen here as $\Delta x = 8$ pixels. The thickness of the laser sheet overlap enables to obtain image pairs of the same particle, and therefore accurate PIV fields, for a spanwise flow velocity up to $3U_\infty$. Finally, the second laser sheet is delayed with respect to the first one by a time Δt^e, the time between exposures which is of the order of a millisecond. This time Δt^e is determined by the imposed particle displacement and is a function of the freestream velocity (in $\mathrm{cm/s}$) and the magnification factor of the camera:

$$\Delta t^e = \frac{\Delta x}{10 M U_\infty}. \tag{4.2}$$

The seeding is done with a powder of $3\,\mu\mathrm{m}$ titanium dioxide particles (Sigma-Aldrich). Before each new experimental campaign, 3 g of this powder are added to the nearly $20\,\mathrm{m}^3$ of water contained in the water channel. The titanium dioxide is mixed with around $1\,\mathrm{cm}^3$ of dispersing agent (DARVAN C-N, Vanderbilt Minerals) which helps the particles to stay in suspension. The amount of 1 g of this powder is added every 24 h for experimental sessions lasting several days. The particles eventually settle at the channel bottom. Therefore, after a campaign of tests, the channel needs to be emptied, cleaned and refilled.

Images are acquired by a double frame digital camera (Cooke Corp. PCO.4000) equipped with a Micro-Nikkor $105\,\mathrm{mm}$ lens, which leads to a magnification M of approximately $18\,\mathrm{pixels/mm}$. The camera provides $4\,008 \times 2\,672$ pixels images, whose longer edge is aligned with the flow. The acquisition frequency is limited by the download speed of images from the camera to the computer. Here, the maximum acquisition frequency f_s^{max} is 1 Hz, which precludes the acquisition of more than one image per period for some of the cases described in Sec. 4.1.

The two pitching cases described in Sec. 4.1 are studied through phase-averaged PIV velocity fields. Therefore, it is necessary to acquire several pairs of images at the same phase of the motion. To this end, the nominal laser pulsing frequency f_{l_0} has to be adjusted to obtain a sampling frequency f_s as close as possible to the kinematic frequency f_k. Moreover, the camera shutter has to be opened at a specific phase of the motion. More details about the synchronization of the plate kinematics with the PIV sampling are given in App. C.3.

4.2.4.2 Experimental procedure

For each test case detailed in Sec. 4.1, PIV fields are measured by repeating several times a short acquisition of PIV images. For pitching cases, the short extent of a single acquisition prevents difference between the target phase and the actual phase being measured. This extent and thus the number of images per acquisition set are determined in such way that the maximum shift is lower than 1 ms, which is of the order of the time between the two components of a pair of PIV images. The chosen number of PIV images to perform the averaging process is 200 for each test case. For pitching cases, 20 phases uniformly distributed within the pitching cycle are considered. For static cases, images are acquired in four sets of 50 images at a frequency of 0.75 Hz. For these cases, dividing the complete acquisition into several sets has no other interest that providing redundancy. Finally, as previously mentioned, part of the flow around the plate is in a shadow region. However, the knowledge of the velocity field in that area is necessary to indirectly compute the loads from the PIV fields. To obtain these data, the experiment corresponding to static and small amplitude pitching cases is repeated with the plate mounted symmetrically with respect to the freestream direction, i.e. $\pm 30^\circ$ and $\pm 45^\circ$. For large amplitude pitching cases, as the motion is symmetrical with respect to the freestream direction, the sampled phases are sufficient to circumvent the problem.

4.2.4.3 Post-processing of raw images to obtain velocity fields

Raw images are post-processed using an in-house code developed at the University of Michigan. As explained in Sec. 2.3.1, the particle displacement field, and thus the velocity field, is determined in multi-passes using cross-correlation analysis. The first low-resolution and second high-resolution passes are performed using an interrogation window size of 64×64 pixels and 32×32 pixels, respectively. Two filters are then applied to remove outliers: a median filter based on spatially adjacent values and a $3 - \sigma$ filter based on a pre-computed mean and standard deviation at one particular point. The data are obtained on a cartesian grid with a spacing of 16 pixels, which corresponds to a physical spacing of about $c/85$. From this PIV grid, a window of size $2.4c \times 2c$ can be extracted. The location of this largest window $\mathcal{S}_{max}$ with respect to the plate is shown in Fig. 4.2c. Finally, for all cases of interest, the 200 PIV snapshots are used to calculate time or phase-averaged PIV fields. Second order statistics are also computed, leading to estimates of the standard deviation around the mean if the plate is static, and turbulent fluctuations when a motion is imposed.

4.2.4.4 Post-processing steps required to use INSE and NOCA methods

As explained in Secs. 2.3.2 and 2.3.3, the INSE and NOCA methodologies used to indirectly calculate the loads are based on a control volume approach. Therefore, they require velocity fields measured all around the plate, which is not possible to obtain with the setup described above. In other words, the shadow region depicted in Fig. 4.4b prevents a straightforward application of the INSE and NOCA methods, and an additional post-processing step is thus necessary.

In the present work, the missing data points are obtaining by exploiting the symmetry of the problem. To obtain the velocity field in the shadow region, the experiment is repeated with the plate mounted symmetrically with respect to the freestream direction as illustrated in Figs. 4.5a and 4.5b. The two sets of results are then stitched together. In particular, this stitching step is performed on the mean and fluctuation of the velocity field obtained after application of the PIV algorithm and phase or time-averaging. Since points are missing in the shadow region only, overlap regions exist between the images obtained for the two sides. These overlap regions are illustrated in Fig. 4.5c and are used to align the two sets of images. Despite this geometric overlap, the data usually do not match exactly. The two sets of data are thus stitched together based on a weighted-average in order to avoid discontinuities in the global velocity field.

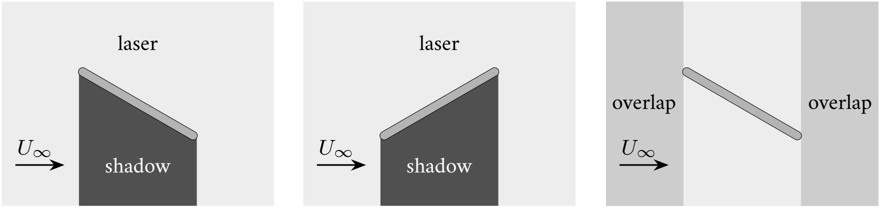

(a) Step 1: positive angle (b) Step 2: negative angle (c) Step 3: Overlap

Figure 4.5: Schematic view of the stitching post-processing step.

4.2.5 Direct load measurements

The fluid dynamic loads on the plate for the three flow configurations described in Sec. 4.1 are measured directly with a force/torque transducer. For each case, both $\mathrm{Re} = 2 \times 10^4$ and $\mathrm{Re} = 4 \times 10^4$ are considered. This section presents the apparatus, the experimental procedure and the post-processing applied to the acquired data.

4.2.5.1 Load measurement apparatus

Fluid dynamic forces and moments are directly measured with a six components ATI Mini40 silicon strain gauge sensor. The transducer is made by ATI Industrial Automation and is shown in the right side of Fig. 4.2a. The sensor is mounted as depicted in Fig. 4.6. Its sampling frequency is 5 000 Hz. As the device is attached as close as possible to the pivot axis, the reference axes move with the plate. Therefore, the forces and moments are measured at the pivot location and in the sensor axes which correspond to the plate axes. A projection is then needed to obtain lift, drag and moment around another point.

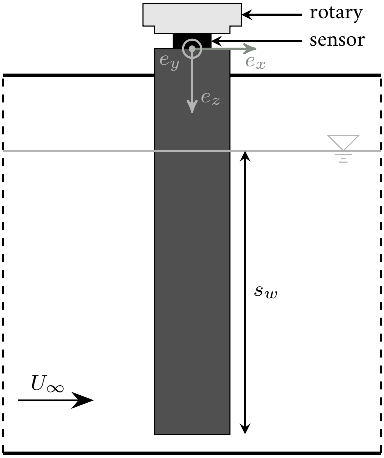

Figure 4.6: Schematic view of the ATI Mini40 mounting and resulting sensor axes.

The sensor with the SI-80-4 calibration used in the experiments is able to measure maximal forces of 80 N in the x and y-directions, 240 N in the z-direction and maximal torques of 4 Nm. The documented resolution for forces is $^1\!/_{50}$ N along the x and y-axes, and $^1\!/_{25}$ N in the z-direction, while a resolution of $^1\!/_{2000}$ Nm for torques is specified. The resolution can be expressed for load coefficients after normalization by $1/2\rho U_\infty^2 S_w$ and $1/2\rho U_\infty^2 S_w c$ for the forces and torques, respectively. The reference surface S_w corresponds to the surface of the plate under water $S_w = cs_w$, where s_w is the span under water equal to 59 cm or $7.6c$. The maximum force and torque coefficients and the corresponding resolution Δ are summarized in Tab. 4.1.

	c_{F_x} and c_{F_y}		c_{F_z}		c_{M_x}, c_{M_y} and c_{M_z}	
	max	Δ	max	Δ	max	Δ
$\mathrm{Re} = 2 \times 10^4$	52.8	1.32×10^{-2}	158.4	2.64×10^{-2}	34.7	4.34×10^{-3}
$\mathrm{Re} = 4 \times 10^4$	13.2	3.30×10^{-3}	39.6	6.60×10^{-3}	8.68	1.09×10^{-3}

Table 4.1: Maximal range and resolution of the ATI Mini40 sensor expressed in terms of load coefficients for the Reynolds numbers of interest.

4.2.5.2 Experimental procedure

Forces and moments are measured while the kinematics presented in Sec. 4.2.2 are imposed. The load acquisition for each kinematics is repeated several times to obtain sufficiently converged time or phase-averaged data. The repetition of short acquisitions is preferred to a single long acquisition to avoid sensor drifting. In particular, the longest acquisition time considered here is 275 s. To verify that the sensor has not drifted, forces and torques at the beginning and end of each measurement, i.e., while the plate is aligned with the flow, are compared. A relative difference on mean loads below 1% is typically obtained. For the static and small amplitude pitching cases, the acquisition is repeated 5 times, while for the large amplitude pitching case it is repeated 14 times. Additionally, to determine the variation of the load coefficients with the incidence angle for a static plate, the loads are measured for angles between -45° and 45° in steps of 2.5°.

In addition to the fluid dynamic loads, the sensor measures the structural static and dynamic loads due to gravity and inertia, respectively. These loads have to be subtracted from the sensor output. The major effect of gravity can be removed by subtracting a bias calculated at the beginning of each measurement. However, this bias corresponds only to the plate configuration at the time at which it is acquired, i.e. at $\alpha = 0^\circ$. Since the gravity impact changes with the incidence of the plate and the pivot location, a static calibration needs to be performed. It consists in the acquisition of loads at the different possible imposed plate incidences. The static calibration is performed for angles between -46° and 46° in steps of 2.5°, with additional steps of 1° around 45° and 30°. This procedure is repeated for both a full and empty water channel. Finally, inertial effects are determined by carrying out the measurements in an emptied water channel.

4.2.5.3 Post-processing

Data are acquired at a sampling frequency of 5 000 Hz so that the measurements contain high frequency noise which has to be removed. A Butterworth low pass filter of order six with a cutoff frequency of 10 Hz is used to this end. Note that this frequency is five times higher that the highest kinematic or shedding frequency.

Each set of raw data consists of different parts used to compute load coefficients but also to verify that the sensor is not drifting with time. They can be differentiated using the information sent by the stepper motor at different instants of the motion. Moreover, transient phenomena are contained in the measurements. Therefore, for static cases, the data corresponding to the first seconds are discarded. For pitching cases, transient effects are removed by discarding the data associated with the first cycles of each experiments. In all cases, the number of seconds or cycles discarded is determined by requesting that a perturbation is convected along a minimal distance of $20c$ within this time.

The acquired data correspond to loads in the sensor axes which move with the body. Therefore, the forces have to be projected onto the flow axes to obtain lift and drag. Moreover, the recorded pitching moment is modified to be defined positive nose-up and computed about the plate center. The lift, drag and pitching moment are calculated from

$$\begin{aligned} L &= -F_x \sin\alpha + F_y \sin\alpha, \\ D &= F_x \cos\alpha + F_y \sin\alpha, \\ M &= -M_z - \frac{ac}{2} L \sin\alpha - \frac{ac}{2} D \cos\alpha, \end{aligned} \tag{4.3}$$

where a stands for the location of the pivot axis with respect to the mid-chord. In particular, the leading edge corresponds to $a = -1$ and the trailing edge to $a = 1$.

As discussed earlier, the measurements carried out in water contain fluid dynamic loads but also structural inertial and gravity contributions that have to be removed. The structural inertial loads, appearing only for a pitching plate, are eliminated by removing the loads acquired during experiments performed in air. These data have to be post-processed as explained previously. The effect of gravity is determined through static calibration experiments conducted at different incidences. After being filtered, the loads corresponding to each incidence are determined. To this end, the transient part is removed and the mean loads are calculated based on 7.5×10^4 samples. Subsequently, the mean lift, drag and moment around the pivot axis are obtained using Eq. (4.3). Finally, the results are approximated by a second order polynomial for $\alpha \in [-46^\circ, 46^\circ]$. The contribution of gravity to measurements can thus be easily calculated and removed.

First and second order statistics are then applied. For the static case, the mean loads and the standard deviations are computed based on a minimum of 350 shedding periods. For the small and large amplitude pitching cases, the phase-averaged loads and the corresponding standard deviations are calculated using a minimum of 500 and 200 cycles, respectively. Subsequently, first and second order statistics are computed on the phase-averaged loads. Finally, these results are non-dimensionalized to obtain load coefficients.

4.3 Numerical setup

The flow around the 16:1 plate at an incidence of 30° is studied through DDES simulations. This CFD technique was preferred to URANS as Güner (2015) demonstrated that it provides a more accurate estimation of the flow. This section described the numerical setup. Two cases are considered, first the static plate and then the plate undergoing small amplitude pitching oscillations. For both cases, the Reynolds number is $\mathrm{Re} = 4 \times 10^4$.

The SA turbulence model (Spalart and Allmaras, 1994) closes the URANS equations appearing in the DDES methodology. The DDES equations are solved by means of a transient solver for incompressible flows called PIMPLE. It is based on a combination of the PISO and SIMPLE algorithms (Ferziger and Perić, 1996) and it allows the use of a large time-step. The non-dimensional time step ${}^{\Delta t U_\infty}\!/_{c}$ is set to 5×10^{-3} which leads to a CFL number of around 4. The smallest time scales of the flow are assumed to be captured accurately as the time step corresponds to $1/600^{\text{th}}$ of a typical vortex shedding cycle. The second order implicit backward Euler scheme is used to advance equations in time while second order schemes are chosen for the spatial discretization. In particular, the advective term $u_j \partial_j u_i$ is discretized through a LUST scheme (Patruno et al., 2016). The PIMPLE solver is combined with a moving mesh technique when a small amplitude pitching motion is imposed. In particular, the small pitching motion $\alpha = 30^\circ + 0.77^\circ \sin(2\pi f t)$ is imposed to the plate by enforcing a rigid body rotation of the cells inside the smallest disc depicted in Fig. 4.7a.

The computational domain is shown in Fig. 4.7a. It consists of two discs surrounding the plate. The largest disc of radius $50c$ is the external border of the computational domain while the smallest disc of radius $2.5c$ is used to impose the pitching motion. Inside this smallest disc, four arcs of ellipse result in cells with reasonable skewness around the plate edges. Finally, the plate is directly surrounded by a thin layer of $0.026c$ height that leads to a smooth mesh next to the walls. The grid is shown in Fig. 4.7b and consists of $17\,000$ quadrangles in the $x - y$ plane. The plate is discretized into 200 cells. Each straight part is divided into 66 cells distributed with a geometric progression equal to 1.3. Moreover, 34 cells are equally spread over each of the rounded edges. In the direction perpendicular to the wall, the layer next to the plate is composed of 15 cells distributed with a geometric progression of 1.26. The smallest and largest discs are discretized radially with 34 and 36 cells, distributed with a progression equal to 1.12 and 1.08, respectively. The ensuing mesh is non-conformal as the mesh nodes at the interface between the largest and smallest circles do not coincide. The two-dimensional grid is extruded along the z direction. Two span lengths are considered, $s = c$ and $s = 7.5c$, the latter being close to the span length of the plate used in the experiments. For both span lengths, the discretization along z is such that $\Delta z = c/32$. The two grids consist thus of $544\,000$ and $4\,080\,000$ hexahedra for the shorter and the longer span, respectively. These grids and the associated computational domain were designed based on the work of Güner (2015), which shows that the ensuing numerical results are mesh independent.

At walls, the no-slip condition is imposed for the velocity. A Neumann homogeneous condition is set for the pressure while the turbulent variable $\tilde{\nu}$ is zero. At the inlet, a Neumann homogeneous boundary condition is set for the pressure while a freestream velocity is imposed. The variable $\tilde{\nu}$ is set through a Dirichlet boundary condition such that $\tilde{\nu}/\nu_T = 6$, i.e., slightly above the upper limit suggested in Sec. 2.2. At the outlet, a combination of Neumann and Dirichlet conditions are set for the velocity, the pressure and the turbulent variable. For u_i and $\tilde{\nu}$, this combination leads to a zero-gradient boundary condition in case of an outflow. Conversely, if the flow enters the computational domain, u_i and $\tilde{\nu}$ are enforced through a Dirichlet condition setting the inlet values. For the pressure, the Neumann and Dirichlet boundary conditions are combined to lead to the opposite behavior. On the boundaries of the domain normal to the extrusion direction, periodic boundary conditions are adopted for all variables. Finally, a boundary condition that allows the passing of fluxes through non-conformal interfaces is set for faces between the largest and smallest discs.

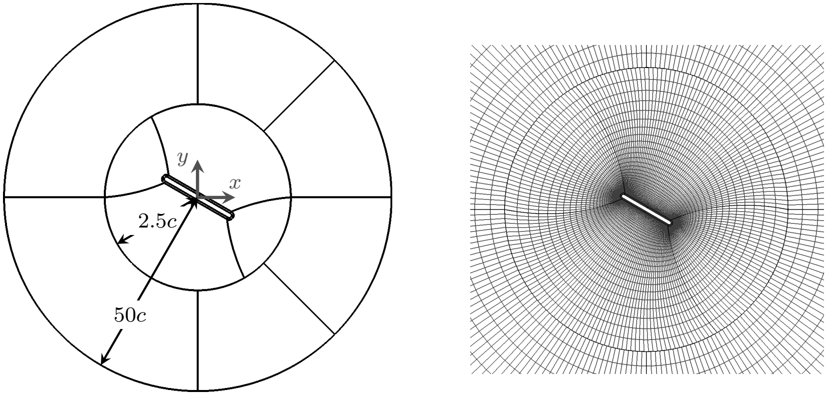

(a) Computational domain. (b) Grid.

Figure 4.7: Computational domain and grid used for the DDES simulations of the flow past a plate undergoing small amplitude pitching motion around an incidence of 30°.

Initial DDES simulations are first run until a fully-developed periodic response of the load coefficients is reached. Then, simulations are run for 150 additional non-dimentional time units.

This temporal window corresponds roughly to 45 shedding cycles, which has been shown to be sufficient in order to compute converged statistics (Güner, 2015).

4.4 Overview of flow features

This section presents the PIV results and the direct load measurements obtained for the three test cases. It aims to provide an overview of the flow features and phenomena. First, the flow around a flat plate undergoing large amplitude pitching oscillations is described. Then, the phenomena occurring for a static plate at high angle of attack are presented, the plate being first static and then undergoing small oscillations.

4.4.1 Large amplitude pitching case

This section presents an overview of the flow around a plate undergoing a sinusoidal pitching motion $\alpha = \Delta\alpha \sin(2\pi f t)$ where the amplitude is $\Delta\alpha = 30^\circ$. The flow features and loads are first described for a pivot axis located at the plate center. Then, the differences appearing when the location of the pivot axis is modified are highlighted.

The phase-averaged flow around a plate oscillating about its center obtained from PIV measurements is presented in Fig. 4.8 for the first half of the pitching cycle. It corresponds to the plate pitching up from 0° to 30° and then going back to zero incidence. The second half of the cycle is not shown since the flow is symmetrical with respect to the freestream: the flow features above and below the plate are the same but shifted in time by half a cycle. Therefore, the flow can be entirely described by analyzing the first half of the cycle, first considering the flow above the plate and then the flow below it. In Fig. 4.8a, the plate incidence is zero and the flow along the upper side of the plate is attached. As the angle of attack increases, a recirculation bubble appears at the leading edge of the plate. This is visible in Fig. 4.8c. Figure 4.8d shows that this recirculation bubble grows forming a clockwise vortex called LE vortex that lies on a counter-clockwise rotating zone of vorticity. When the incidence further increases, the LE vortex grows and is convected downstream while the counter-clockwise vorticity zone extends forming a conter-clockwise vortex. These phenomena are visible from Figs. 4.8d to Fig. 4.8f. Note that for the maximum incidence $\alpha = 30^\circ$, the phase-averaged flow is still attached despite an incidence much higher than the static stall angle $\alpha \approx 7^\circ$ (Granlund et al., 2013). When the incidence starts to decrease, the LE vortex detaches from the upper side of the plate. This allows the further growth of the counter-clockwise vortex visible in Fig. 4.8g. Between phase $\varphi = {}^{t}\!/_{T} = 0.3$ and $\varphi = 0.35$, the free shear layer below the plate rolls up around the TE to form a counter-clockwise vortex visible in Fig. 4.8h. This vortex merges with the counter-clockwise vortex below the LE vortex, which leads to the so-called TE vortex. This merging is depicted in Figs. 4.8h and 4.8i and occurs while the LE vortex is shed into the wake. As the plate incidence continues to decrease, the TE vortex is also shed. Between $\varphi = 0.45$ and $\varphi = 0.6$, the flow on the upper side of the plate exhibits a free shear layer extending from the plate LE. This is visible above the plate from Fig. 4.8j to Fig. 4.8k and below it from Fig. 4.8a to Fig. 4.8c. As the incidence decreases further, the flow reattaches and remains attached from the LE to the TE for the rest of the pitching cycle. This is visible below the plate from Fig. 4.8d to Fig. 4.8k.

The phase-averaged load coefficients are plotted as functions of time and incidence angle in Fig. 4.9. The variation of the load coefficients with the incidence angle for a static plate is also shown for comparison. In particular, the time response of the lift coefficient is depicted in Figs. 4.9a and 4.9b. At zero incidence, i.e. for $\varphi = 0$, the generated lift is zero. Then, the lift coefficient increases linearly with the incidence until $\alpha \approx 27^\circ$ or $\varphi \approx 0.18$. The lift slope is $c_{L\alpha} \approx 4.5$ which is lower than the slope measured for a static plate $c_{L\alpha} \approx 6.76$. Moreover, the linear increase in lift continues far beyond the saturation observed for $\alpha > 5^\circ$ for the static plate. The maximum lift is $c_L \approx 2.36$ and occurs at the maximal amplitude $\alpha = 30^\circ$. Figure 4.8 seems to indicate that the linear variation of the lift with the incidence angle corresponds to the emergence

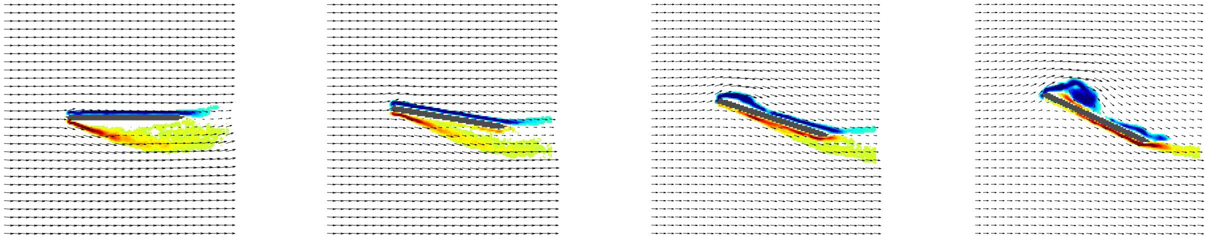

(a) $\varphi = 0$ and $\alpha = 0^\circ \uparrow$.

(b) $\varphi = 0.05$ and $\alpha = 9.3^\circ \uparrow$.

(c) $\varphi = 0.1$ and $\alpha = 17.6^\circ \uparrow$.

(d) $\varphi = 0.15$ and $\alpha = 24.3^\circ \uparrow$.

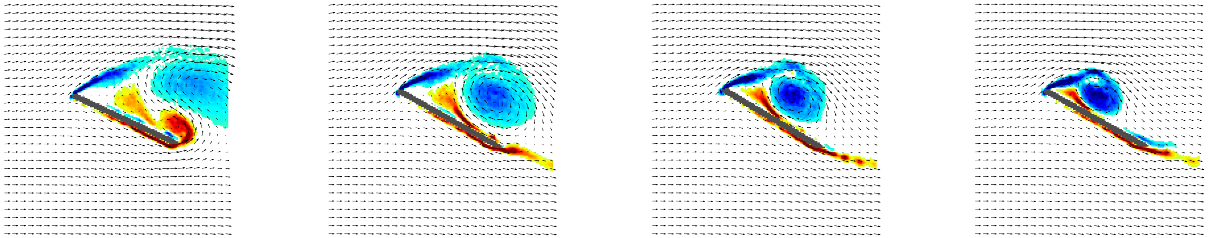

(h) $\varphi = 0.35$ and $\alpha = 24.3^\circ \downarrow$.

(g) $\varphi = 0.3$ and $\alpha = 28.5^\circ \downarrow$.

(f) $\varphi = 0.25$ and $\alpha = 30^\circ \downarrow$.

(e) $\varphi = 0.2$ and $\alpha = 28.5^\circ \uparrow$.

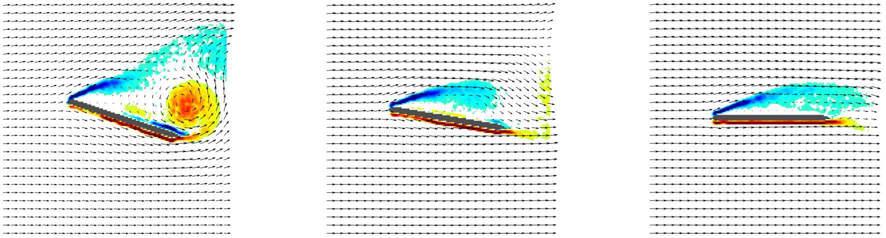

(i) $\varphi = 0.4$ and $\alpha = 17.6^\circ \downarrow$.

(j) $\varphi = 0.45$ and $\alpha = 9.3^\circ \downarrow$.

(k) $\varphi = 0.5$ and $\alpha = 0^\circ \downarrow$.

Figure 4.8: Phase-averaged PIV velocity and vorticity fields for half of the large amplitude pitching cycle about the plate center. The red and blue fields correspond, respectively, to positive and negative vorticity, i.e. counter-clockwise and clockwise vortices. The field of view corresponds to a square of size $2c$ centered on the plate center.

and growth of the LE vortex. The maximum lift occurs just before the shedding of the LE vortex. At this point, the plate is pitching down and the lift quickly decreases. From $\varphi = 0.35$ to $\varphi = 0.45$, the lift response exhibits a perturbation in its continuous decrease, which is probably due to the rolling up of the shear layer and the shedding of the TE vortex. As the plate returns to zero incidence, the lift reaches zero. Because the pitching motion is symmetrical, the time response of the phase-averaged lift during the second half of the pitching cycle is the same as during the first half but with negative values. One can finally observe that the maximum value of the lift coefficient is more than twice that of a static plate at the same incidence angle, for which $c_L \approx 1.04$ as shown in Fig. 4.9b. Note that stall delay is characteristic of dynamic stall (McCroskey, 1981). The response of the phase-averaged drag coefficient is shown in Figs. 4.9c and 4.9d. Because drag consists mostly in pressure drag, it exhibits a time response similar to that of the lift. It increases along the first quarter of the cycle, as the LE vortex emerges and grows. Then, the drag reaches its maximum value $c_D \approx 1.3$ at the maximum incidence. Again, this value is much larger than the corresponding static value $c_D \approx 0.65$ shown in Fig. 4.9d. The drag decreases then with incidence during the second quarter of the cycle, i.e., as the LE vortex is shed into the wake and convected downstream. The time response of the drag coefficient exhibits small oscillations around the phase-averaged value. Nonetheless, similarly to the lift, a perturbation due to the TE vortex is visible between $\varphi = 0.35$ to $\varphi = 0.4$. Finally, the variation of the phase-averaged pitching moment coefficient about the plate center is shown in Figs. 4.9e and 4.9f. Similarly to the lift, the time response of c_M is anti-symmetrical. Moreover, as for the lift and drag coefficients, its maximum, $c_M \approx 0.45$, is much larger than that of a static plate, for which $c_M = 0.12$ as shown in Fig. 4.9f. However, this maximum does not occur at the maximum incidence, but before, at $\varphi \approx 0.18$, which corresponds to an incidence $\alpha \approx 27.2^\circ$. This can be explained by the dynamics of the flow structures. At the beginning of the cycle, the growing LE vortex is located close to the leading edge. This location far from the plate center maximizes the lever-arm and thus its contribution to c_M. Therefore, because of the strong suction induced by the vortex, the pitching moment increases quickly with incidence. This can be visualized by comparing the variation of c_M in Fig. 4.9e and the flow field in Fig. 4.8 for phases $\varphi = 0$ to $\varphi = 0.15$. Then, as the incidence continues to increase, the vortex is convected downstream and finally past the plate center. The contribution of the LE vortex to c_M becomes negative and the pitching moment decreases. Similarly to the lift, the impact of the TE vortex is visible from $\varphi = 0.3$ to $\varphi = 0.5$, the drop in c_M being associated with the pitch down caused by the suction at TE due to the counter clockwise vortex.

In addition to the results for a pivot axis located at the plate center, Fig. 4.9 also depicts the time response of the phase-averaged coefficients associated with the two other pivot axis locations considered here, i.e., at the leading and trailing edges of the plate. The main impact of a change in the pivot axis location is clearly visible in Figs. 4.9a, 4.9c and 4.9e. It corresponds to a shift in time of the response associated with the load coefficients. Figures 4.10 and 4.11 show the phase-averaged PIV fields obtained for cases associated with a pivot located at the LE and TE of the plate. By comparing these figures with Fig. 4.8, it appears that the structure of the flow is similar but with a shift in the dynamics of the flow features. More precisely, compared to a pivot located a the plate center, a similar flow pattern occurs for lower and higher incidences for pivot located at the LE or TE, respectively. In particular, this shift can be seen by comparing Fig. 4.10b and Fig. 4.11c which both depict the emergence of the recirculation bubble at $\alpha = 9.3^\circ$ and $\alpha = 17.6^\circ$, for a pivot at LE and TE respectively. This is also clearly visible in Fig. 4.10f and Fig. 4.11g where the flow starts to detach at phase $\varphi = 0.25$ and $\varphi = 0.3$. Finally, a comparison of the flow structure for the three pivot locations at phase $\varphi = 0.35$ shows that the LE vortex center is located farther downstream when the pivot axis is closer to the LE of the plate.

The cause of this temporal shift can be determined by using the theoretical model proposed by Theodorsen (1935). Under the approximations of potential fully-attached flow, planar wake and the fulfillment of the Kutta condition, this theoretical approach provides an estimation of the

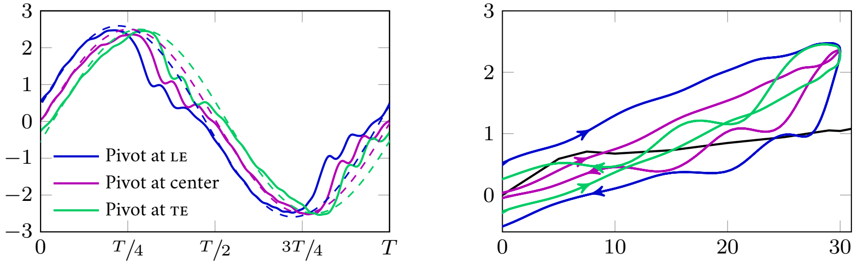

(a) c_L vs time. (b) c_L vs incidence.

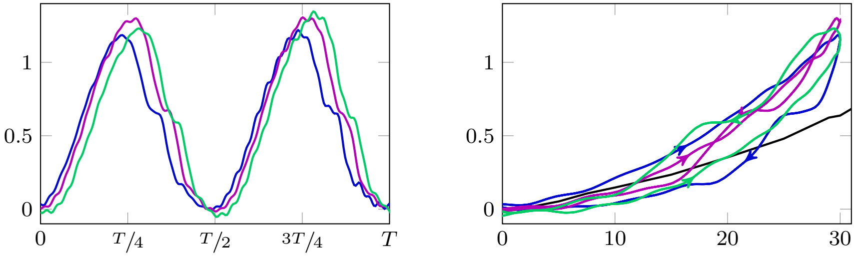

(c) c_D vs time. (d) c_D vs incidence.

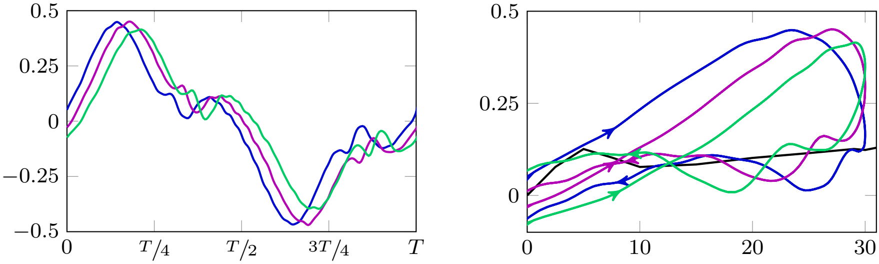

(e) c_M vs time. (f) c_M vs incidence.

Figure 4.9: Phase-averaged load coefficients obtained by direct load measurements for a plate undergoing large amplitude sinusoidal oscillations about three different pivot axes. (a,c,e) Time variation over a pitching period T: the dashed lines in (a) correspond to the theoretical predictions of Theodorsen's theory. (b,d,f) Variation as a function of the incidence angle for half a pitching period; the black line corresponds to a static plate.

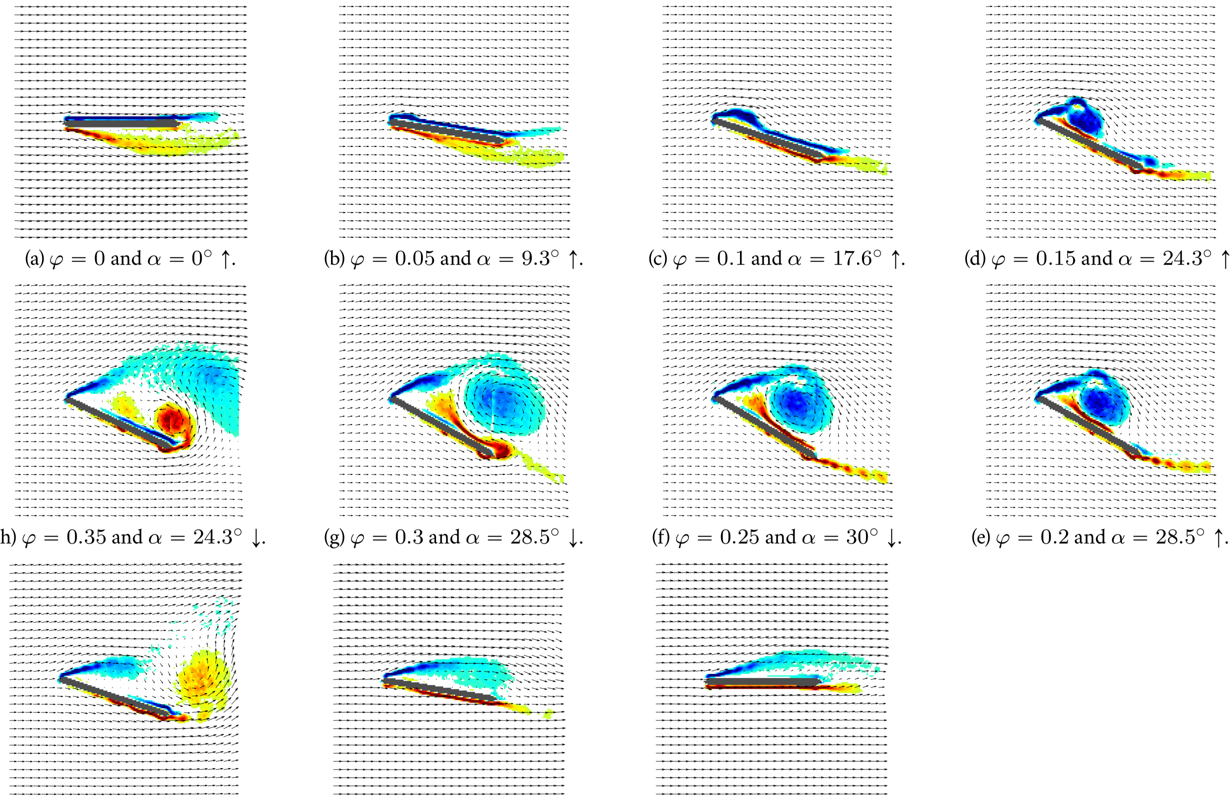

(a) $\varphi = 0$ and $\alpha = 0° \uparrow$.

(b) $\varphi = 0.05$ and $\alpha = 9.3° \uparrow$.

(c) $\varphi = 0.1$ and $\alpha = 17.6° \uparrow$.

(d) $\varphi = 0.15$ and $\alpha = 24.3° \uparrow$.

(h) $\varphi = 0.35$ and $\alpha = 24.3° \downarrow$.

(g) $\varphi = 0.3$ and $\alpha = 28.5° \downarrow$.

(f) $\varphi = 0.25$ and $\alpha = 30° \downarrow$.

(e) $\varphi = 0.2$ and $\alpha = 28.5° \uparrow$.

(i) $\varphi = 0.4$ and $\alpha = 17.6° \downarrow$.

(j) $\varphi = 0.45$ and $\alpha = 9.3° \downarrow$.

(k) $\varphi = 0.5$ and $\alpha = 0° \downarrow$.

Figure 4.10: Phase-averaged PIV velocity and vorticity fields for half of the large amplitude pitching cycle about the plate LE. The red and blue fields correspond, respectively, to positive and negative vorticity, i.e. counter-clockwise and clockwise vortices. The field of view corresponds to a square of size $2c$ centered on the plate center.

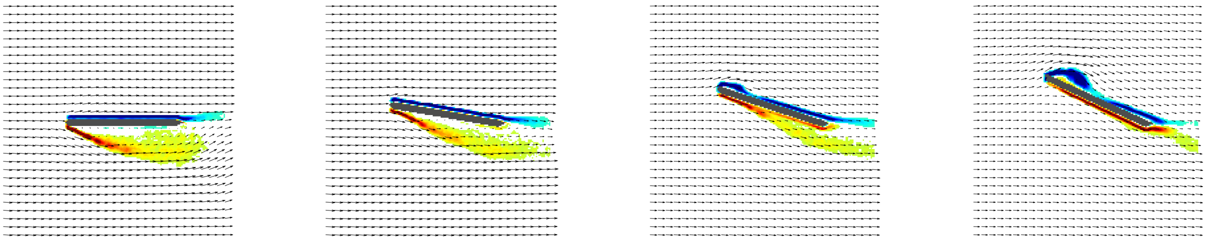

(a) $\varphi = 0$ and $\alpha = 0° \uparrow$. (b) $\varphi = 0.05$ and $\alpha = 9.3° \uparrow$. (c) $\varphi = 0.1$ and $\alpha = 17.6° \uparrow$. (d) $\varphi = 0.15$ and $\alpha = 24.3° \uparrow$.

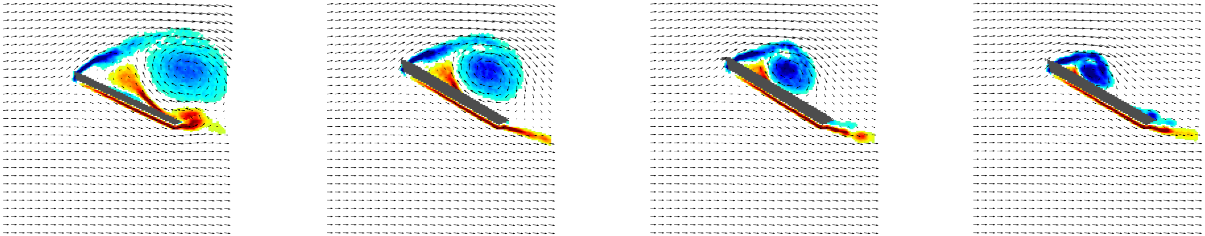

(h) $\varphi = 0.35$ and $\alpha = 24.3° \downarrow$. (g) $\varphi = 0.3$ and $\alpha = 28.5° \downarrow$. (f) $\varphi = 0.25$ and $\alpha = 30° \downarrow$. (e) $\varphi = 0.2$ and $\alpha = 28.5° \uparrow$.

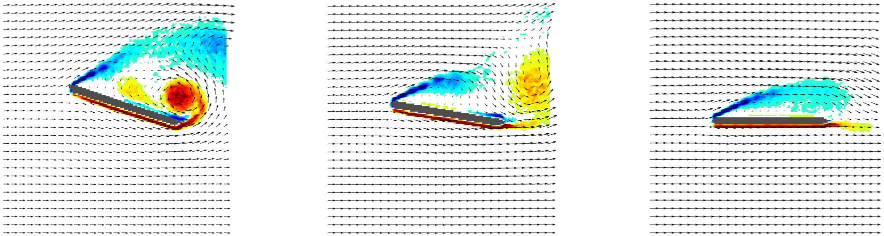

(i) $\varphi = 0.4$ and $\alpha = 17.6° \downarrow$. (j) $\varphi = 0.45$ and $\alpha = 9.3° \downarrow$. (k) $\varphi = 0.5$ and $\alpha = 0° \downarrow$.

Figure 4.11: Phase-averaged PIV velocity and vorticity fields for half of the large amplitude pitching cycle about the plate TE. The red and blue fields correspond, respectively, to positive and negative vorticity, i.e. counter-clockwise and clockwise vortices. The field of view corresponds to a square of size $2c$ centered on the plate center.

lift associated with unsteady aerodynamics. In the context of a purely pitching motion, it gives

$$c_l = \underbrace{\frac{\pi c}{2}\left(\frac{\dot{\alpha}}{U_\infty} - \frac{a\ddot{\alpha}}{2U_\infty^2}\right)}_{\text{non-circulatory lift}} + \underbrace{2\pi C\left(k\right)\left(\alpha + \frac{\dot{\alpha}c}{2U_\infty}\left[\frac{1}{2} - a\right]\right)}_{\text{circulatory lift}}, \tag{4.4}$$

where $\dot{\alpha}$ and $\ddot{\alpha}$ stand for the first and second temporal derivatives of the incidence angle. The complex-valued transfer function $C\left(k\right)$ is called Theodorsen's function and accounts for the influence of the vorticity shed into the wake. It acts as a filter that depends on the reduced frequency k. The results of this model applied to the present case are depicted by the dashed lines in Fig. 4.9a. Comparing the experimental and theoretical data shows that this model provides a very accurate estimation of c_l in the first part of the pitch-up motion. Discrepancies appear from $\varphi = 0.1$ to $\varphi = 0.25$, i.e., during the second part of the pitch-up motion. Nevertheless, the lift approximation is still quite accurate. In particular, the maximum c_L is very well approximated, both in value and location. As the theory proposed by Theodorsen (1935) assumes a fully attached flow, large discrepancies are observed during the pitch-down motion. Nonetheless, the temporal shift observed when modifying the pivot location is accurately modeled. Therefore, the causes of this shift can be determined by analyzing the different components of the lift predicted by Theodorsen's theory. In particular, Eq. (4.4) shows that the lift consists of a circulatory and a non-circulatory component. The non-circulatory contribution is caused by added mass effects while the circulatory contribution is due to a change in circulation. By comparing the variation of the different terms in Eq. (4.4) with the pivot location, it appears that the second term of the circulatory lift contributes the most to the temporal shift. Therefore, this temporal shift is mainly caused by a modification of the motion-induced angle of attack. Figure 4.12 shows the variation of the phase-averaged lift coefficient with the effective angle of attack $\alpha_{\text{eff}} = \alpha + \frac{\dot{\alpha}c}{2U_\infty}\left[\frac{1}{2} - a\right]$, for the three pivot axes. It shows that the curves $c_L\left(\alpha_{\text{eff}}\right)$ associated with the different pivot axes tend to match for the linear growth, contrary to what is depicted in Fig. 4.9b for $c_L\left(\alpha\right)$. This confirms the impact of the motion-induced angle of attack on the temporal shift. Finally, note that the same analysis could be conducted using the experimental lift slope $c_{L_\alpha} \approx 2.15\pi$ in Eq. (4.4) instead of the thin airfoil theory result $c_{l_\alpha} = 2\pi$. However, this would increase the modeled maximum lift and the modeled lift slope of the dynamic curve of about 10%.

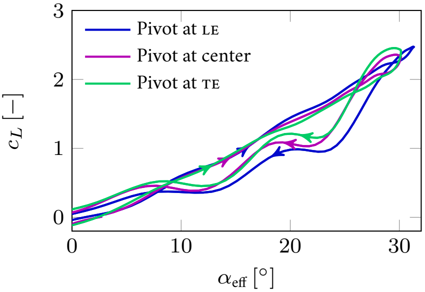

Figure 4.12: Phase-averaged lift coefficients obtained by direct load measurements for a plate undergoing large amplitude sinusoidal oscillations about three different pivot axes. Variation as a function of the effective incidence angle α_{eff} for half a pitching period.

4.4.2 Static case

The time-averaged flow fields around a plate at 30° and 45° incidence are depicted in Fig. 4.13. For both incidences, the mean flow is detached and two free shear layers extend downstream of the

LE and TE. Two vortices appear in the mean flow topology. A large clockwise vortex called the LE vortex lies above the upper surface of the plate. It extends from the LE shear layer to another vortex rotating conter-clockwise and called TE vortex and extending to the TE shear layer. Comparing Figs. 4.13a and 4.13b, it appears that both the LE and TE vortices become larger as the incidence increases. In particular, for $\alpha = 45^\circ$, the two vortices extend farther downstream.

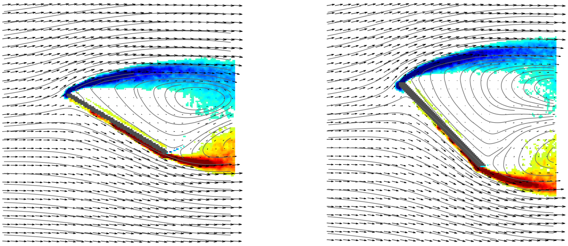

(a) $\alpha = 30^\circ$. (b) $\alpha = 45^\circ$.

Figure 4.13: Time-averaged PIV velocity and vorticity fields around a static plate at large incidence. The red and blue fields correspond, respectively, to positive and negative vorticity, i.e. counter-clockwise and clockwise vortices. The field of view corresponds to a square of size $2c$ centered on the plate center.

The mean load coefficients are shown in Tab. 4.2. The LE vortex induces suction along the upper surface of the plate. This suction combined with the positive pressure coefficient along most of the lower surface (Breuer et al., 2003; Lam and Wei, 2010) leads to a positive force perpendicular to the chord axis. This normal force corresponds to positive lift and drag forces, whose values are comparable to those reported by Granlund et al. (2013). The mean lift obtained for the two angles is almost the same. Note that the value of $\overline{c_L}$ obtained for $\alpha = 30^\circ$ is much lower than the c_L obtained for a similar angle when a large amplitude pitchig motion is imposed (see Sec. 4.4.1). This illustrates the difference between static and dynamic stall. For $\alpha = 45^\circ$, the pressure contributions to the lift and drag are equal. Therefore, the total drag reported in Tab. 4.2 is higher than the total lift due to friction effects. Finally, the reported mean pitching moment coefficient is positive and identical for the two incidences. This positive value is due to the mean pressure distribution along the lower side of the plate, which is positive for the first 60 percent of the plate and negative for the remaining part, while suction is almost constant along the upper side (Breuer et al., 2003; Lam and Wei, 2010). The mean flow leads thus to a nose-up moment at the plate center. The standard deviation of the load coefficients is also reported in Tab. 4.2. As the loads are time-averaged, the standard deviation provides an estimate of the amplitude of the variations around the mean. Note that the large values reported for $\alpha = 45^\circ$ may be partly caused by the plate vibrations observed during the experiments.

	$\overline{c_L}$	c'_L	$\overline{c_D}$	c'_D	$\overline{c_M}$	c'_M
$\alpha = 30^\circ$	0.99	0.055	0.63	0.036	0.12	0.005
$\alpha = 45^\circ$	1.01	0.304	1.09	0.345	0.12	0.011

Table 4.2: Time-average and standard deviation of the load coefficients for a static plate at large incidence angle and $\mathrm{Re} = 4 \times 10^4$.

4.4.3 Small amplitude pitching case

This section investigates the flow fields around a plate at an incidence of $\overline{\alpha} = 30^\circ$ and $\overline{\alpha} = 45^\circ$ undergoing small amplitude pitching oscillations, i.e., $\alpha = \overline{\alpha} + \Delta\alpha \sin\left({}^{2\pi t}/_{T}\right)$, where $\Delta\alpha = 0.77^\circ$ and 1.33° for the smallest and largest mean incidences, respectively. As explained in Sec. 4.2, these oscillations are imposed in order to provide a phase reference for the PIV measurements. The present section is divided into two parts. First, the impact of the imposed oscillations is investigated through experimental and numerical results. This aims to demonstrate that the imposed kinematics does not significantly impact the flow features. Then, the phase-averaged flow features obtained experimentally are depicted.

4.4.3.1 Impact of the imposed small amplitude pitching oscillations

The impact of the imposed pitching oscillations is investigated using both the measured load coefficients and the results of numerical simulations. The time-averaged load coefficients are reported in Tab. 4.3 for $\alpha = 30^\circ$. The results obtained for the static case are repeated to facilitate the comparison. The mean coefficients obtained with and without the imposed small amplitude oscillations are similar. In particular, their relative difference is below 10%. However, the standard deviations increase when a small pitching motion is imposed. As discussed below in more detail, this is likely due to an increase of the coherence of the flow along the span.

	$\overline{c_L}$	c_L'	$\overline{c_D}$	c_D'	$\overline{c_M}$	c_M'
EXP static	0.99	0.055	0.63	0.036	0.12	0.005
EXP small amplitude pitching	1.08	0.079	0.69	0.044	0.13	0.019
DDES static $s = c$	1.11	0.120	0.68	0.056	0.13	0.010
DDES static $s = 7.5c$	1.08	0.057	0.66	0.026	0.12	0.004
DDES small amplitude pitching $s = c$	1.17	0.250	0.73	0.130	0.12	0.026
DDES small amplitude pitching $s = 7.5c$	1.19	0.130	0.73	0.054	0.12	0.012

Table 4.3: Time-average and standard deviation of experimental and numerical load coefficients for a plate at an incidence angle $\alpha = 30^\circ$ and $\mathrm{Re} = 4 \times 10^4$. The plate is either static or undergoes small amplitude pitching oscillations around the mean angle of attack.

The impact of the imposed motion on the flow dynamics can be further investigated by using CFD. Table 4.3 presents the results of DDES simulations conducted for two span lengths, with and without forced pitching motion. For a static plate, the standard deviation of the load coefficients decreases when the span length is increased from $s = c$ to $s = 7.5c$. This indicates that the amplitude of the load coefficient time responses decreases. Conversely, the time-averaged load coefficients do not vary much with the span length. As discussed by Güner (2015) who investigated the same case, the variation of the standard deviation is due to three-dimensional phenomena. In particular, the flow is not entirely two-dimensional and therefore its coherence along the span is reduced. This is illustrated in Fig. 4.14a which depicts iso-surfaces of the pressure coefficient for a static plate of span length c at a time corresponding to a local maximum of the lift coefficient. When the span length increases, more flow structures can develop in the z-direction. Moreover, the impact of the periodic boundary conditions imposed on the borders of the computational domain perpendicular to the z-direction decreases. Therefore, the flow is more three-dimensional, which leads in turn to a decrease of the coherence in the z-direction, as depicted in Fig. 4.14b. This phenomenon causes a phase shift in the load distribution along the span. In particular, the minimum and maximum of the two-dimensional load coefficients along the plate do not occur at the same time within the shedding cycle. This impacts the time response of the three-dimensional load coefficients obtained by span-averaging the distribution of two-dimensional load coefficients. More precisely, as illustrated in Fig. 4.15, the amplitude of the load coefficient time responses decreases, which explains the decrease of the corresponding standard deviations. Finally, the comparison of the statistics of the load coefficients obtained from direct measurements and DDES simulations performed for $s = 7.5c$ indicates that the CFD is able to approximate the flow around a static plate. Note that this was demonstrated in detail by Güner (2015) who used DMD to compare the flow fields.

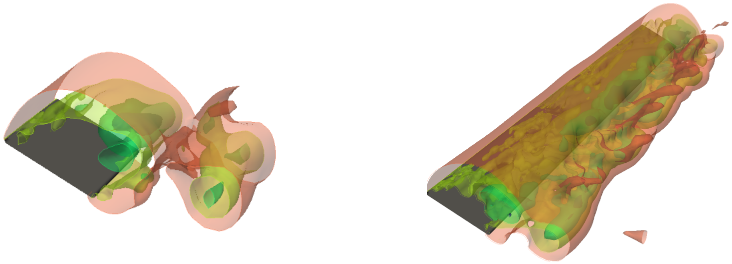

(a) Static case with $s = c$. (b) Static case with $s = 7.5c$.

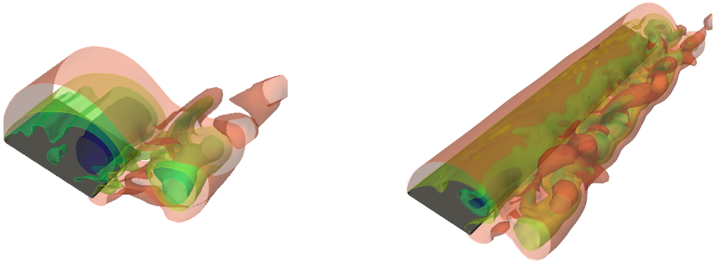

(c) Pitching case with $s = c$. (d) Pitching case with $s = 7.5c$.

Figure 4.14: Surfaces of constant pressure around a static and small amplitude pitching plate at $\alpha = 30^\circ$ obtained by DDES for different span lengths. The iso-surfaces correspond to equidistant values of C_p ranging from -0.6 to -1.9 (red to blue) and the time considered corresponds to the maximum lift in a shedding cycle.

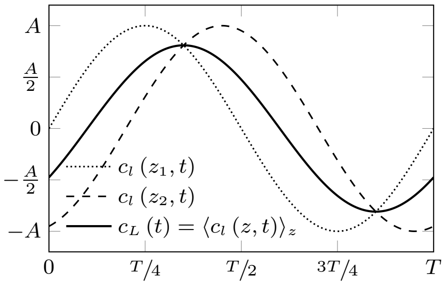

Figure 4.15: Schematic explanation of the decrease in amplitude caused by a phase shift in the two-dimensional load time responses at two spanwise positions z_1 and z_2.

When the plate undergoes small amplitude pitching oscillations, the statistics of the computed load coefficients vary with span length in a manner similar to that of the static case. An increase of the span length leads to a decrease of the standard deviations while time-averages do not vary significantly. This is reported in Tab. 4.3 and illustrated in Figs. 4.14c and 4.14d. More interestingly, by comparing the results obtained for the static plate and the forced motion, it is observed that the standard deviations of the coefficients increase when oscillations are applied, while the mean coefficients are not impacted. The imposed weak oscillation is likely sufficient to increase the flow coherence along the span as illustrated by Figs. 4.14b and 4.14d. As explained before, this increase of coherence causes an increase of the amplitude of the load coefficient responses and in turn of their standard deviation. Despite these differences, the load coefficients and the flow features do not seem to change much when small forced oscillations are applied.

In conclusion, it seems that the forcing of a pitching motion does not significantly impact the mean flow dynamics. Therefore, a better understanding of the flow features can be gained by studying the corresponding phase-averaged PIV fields.

4.4.3.2 Overview of flow features

The flow fields around a plate at incidence of $\overline{\alpha} = 30^\circ$ and $\overline{\alpha} = 45^\circ$ are shown in Figs. 4.16 and 4.17, respectively. In particular, these figures present the phase-averaged velocity and vorticity PIV fields. As explained before, the PIV fields are obtained by applying a small amplitude sinusoidal pitching motion to provide a phase reference for the PIV measurements. Mathematically, this motion is given by $\alpha = \overline{\alpha} + \Delta\alpha \sin\left({}^{2\pi t}/_{T}\right)$, where $\Delta\alpha = 0.77^\circ$ and 1.33° for the smallest and largest mean incidences, respectively.

The vortex shedding phenomenon that occurs for a mean incidence of $\overline{\alpha} = 30^\circ$ is depicted in Fig. 4.16. Similarly to the previous large amplitude pitching case, two vortices develop from the LE and TE of the plate, respectively. They are then convected downstream and shed into the wake. However, the flow is asymmetric about the wake centerline. The vortex appearing at the TE is small and has a high vorticity level at its center while the vortex developing from the LE is larger but less powerful (Lam and Wei, 2010). Moreover, the mechanisms leading to the vortex formation are very different.

The counter-clockwise rotating vortex forming next to the TE originates in the roll-up of the shear layer that extends from the trailing edge. The emergence and growth of the TE vortex are visible from Fig. 4.16g to Fig. 4.16j. During this stage, the TE vortex moves slowly. Subsequently, the velocity of the TE vortex center increases as the vortex is shed into the wake and convected downstream, as shown in Fig. 4.16a to Fig. 4.16e. Conversely, the formation and shedding of the clockwise vortex emerging from the leading edge does not involve the roll-up of the shear layer. In this case, a number of shear layer vortices are generated from the separation occurring at the LE, as visible in Figs. 4.16a or 4.16b. Breuer et al. (2003) demonstrated through LES that the small vortices result from a Kelvin-Helmholtz instability and are then convected downstream. Figures 4.16b to 4.16f show that these vortices progressively agglomerate into a large clockwise recirculation region called the LE vortex. At $\varphi = 0.6$, the LE vortex starts to detach from the upper part of the plate and is then shed into the wake, as depicted in Fig. 4.16h to Fig. 4.16k. Figures 4.16h and 4.16k illustrate the beginning of the LE and TE vortices detachment, respectively. These two vortices are shed approximately at the same downstream distance $0.65c$ from the plate center. According to Breuer and Jovičić (2001) and Lam and Leung (2005), there is a strong interaction between the LE and TE vortices. The size, detachment and shedding of the LE vortex is affected by the development of the TE vortex, and conversely. More precisely, the LE vortex has space to grow only after the shedding of the TE vortex, as shown in Fig. 4.16b. Moreover, the growing stage of the LE vortex stops as the TE vortex emerges, as seen in Fig. 4.16g. This is followed by an upward motion of the TE vortex as it grows, which causes the detachment of the LE vortex. This phenomenon is visible in Figs. 4.16h and 4.16i.

Finally, the measured load coefficients are presented in Fig. 4.16l while Tab. 4.4 reports their mean and standard deviation. The phase-averaged time responses of the lift, drag and pitching moment coefficients exhibit a nearly sinusoidal behavior. In particular, the maximum and mini-

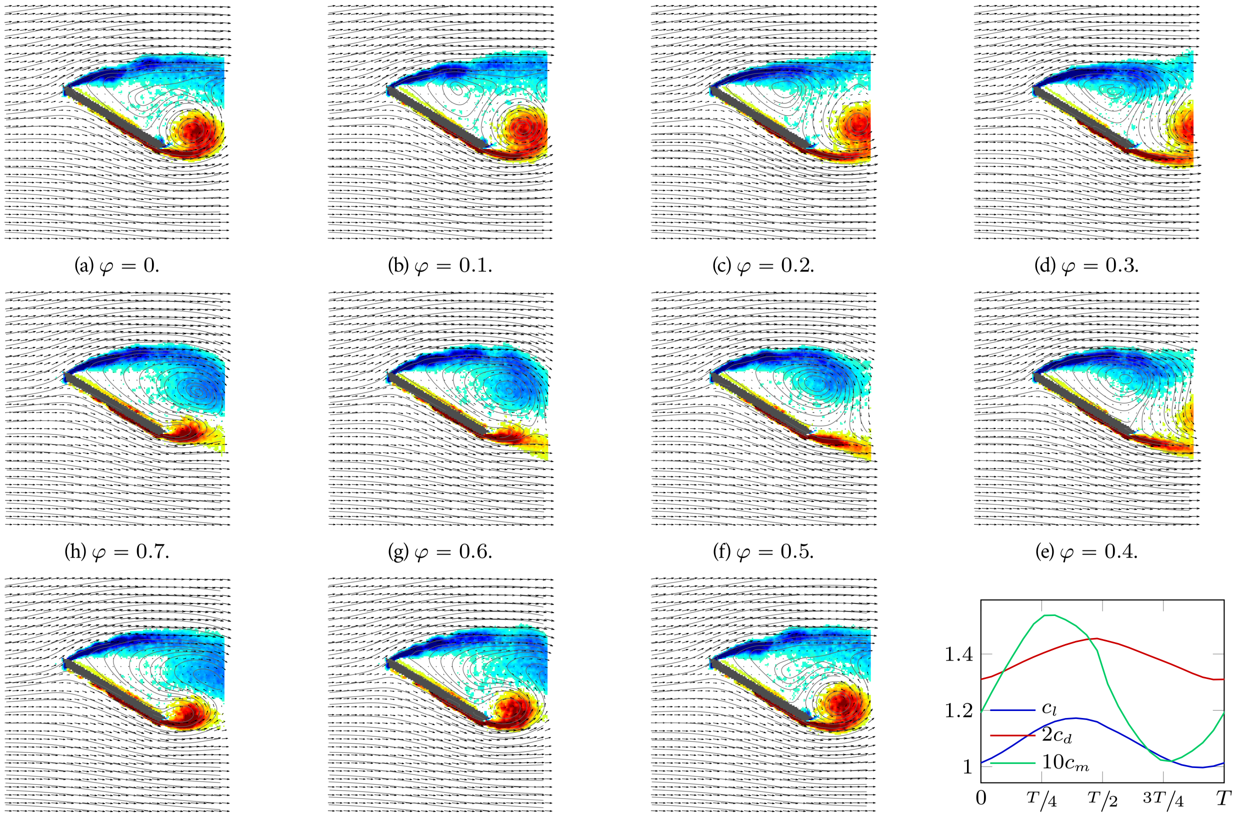

(a) $\varphi = 0.$

(b) $\varphi = 0.1.$

(c) $\varphi = 0.2.$

(d) $\varphi = 0.3.$

(h) $\varphi = 0.7.$

(g) $\varphi = 0.6.$

(f) $\varphi = 0.5.$

(e) $\varphi = 0.4.$

(i) $\varphi = 0.8.$

(j) $\varphi = 0.9.$

(k) $\varphi = 1.$

(l) Load coefficients.

Figure 4.16: Phase-averaged PIV velocity and vorticity fields for a small amplitude pitching cycle at a mean angle $\overline{\alpha} = 30^\circ$. The red and blue fields correspond, respectively, to positive and negative vorticity, i.e. counter-clockwise and clockwise vortices. The field of view corresponds to a square of size $2c$ centered on the plate center. The corresponding variation of the load coefficients for one oscillation period T is also shown (l).

mum lift occurs at $\varphi = 0.4$ and $\varphi = 0.9$ while drag extrema take place $0.05T$ later. As the flow is separated, the total drag consists mostly of pressure drag. Considering only this contribution, the lift and drag time responses should be in phase (Lam and Wei, 2010). Therefore, the observed shift is due to the contribution of friction. As the flow does not vary much along the lower surface of the plate, it can be concluded that the temporal load variations are mainly caused by the flow topology and dynamics along the upper surface. In particular, the flow corresponding to the maximum lift is shown in Fig. 4.16e. At this phase of the cycle, the TE vortex has been shed into the wake and the LE vortex lies along the entire upper surface. The negative pressure associated with the vortex causes a large suction force perpendicular to the plate which leads to large lift and drag. For subsequent phases of the cycle, the emergence and growth of the TE vortex leads to the shedding of the LE vortex. This reduces the suction along the upper surface and consequently leads to the decrease of lift and drag. The minimum lift corresponds to $\varphi = 0.9$, i.e. the end of the growing phase of the TE vortex and the beginning of its shedding. As the TE vortex is shed, the LE vortex has more space to grow. The time responses of the fluid dynamic forces are thus mainly caused by the variation of pressure induced by the LE vortex. However, the time response of the pitching moment coefficient is due to the suction caused by both the LE and TE vortices. In particular, c_M is minimum at $\varphi = 0.8$, for which the TE vortex is located close to the TE of the plate, causing a large suction at this location. The suction caused by the TE vortex is probably the most important contribution to the pitching moment as the LE vortex is being shed into the wake and thus located far from the plate upper surface. As c_M is defined positive nose-up, a high suction along the rear part of the upper surface leads to a negative contribution to the pitching moment. After the shedding of the TE vortex into the wake, the pitching moment increases. Its maximum is achieved at $\varphi = 0.3$ for which, as shown in Fig. 4.16d, the LE vortex lies along the upper surface. The maximum pitching moment is then probably caused by the combination of an asymmetry in the suction due to the LE vortex and the pressure along the lower surface being higher near the LE.

	$\overline{c_L}$	c_L'	$\overline{c_D}$	c_D'	$\overline{c_M}$	c_M'
$\overline{\alpha} = 30^\circ$	1.08	0.079	0.69	0.044	0.13	0.019
$\overline{\alpha} = 45^\circ$	1.07	0.210	1.15	0.224	0.12	0.020

Table 4.4: Time-average and standard deviation of the load coefficients for a plate undergoing small pitching oscillations at large incidence and $\mathrm{Re} = 4 \times 10^4$.

The phase-averaged flow fields and loads for a mean angle $\overline{\alpha} = 45^\circ$ are presented in Fig. 4.17. The same behavior as for the smaller incidence is observed. Increasing the mean incidence $\overline{\alpha}$ increases the characteristic length of the wake which scales with $c \sin \alpha$ (Fage and Johansen, 1927). Therefore, the field of view should be larger to be able to visualize the entire shedding phenomenon. Nonetheless, the main mechanisms described above are still present. In particular, at $\varphi = 0.8$, the TE vortex is sufficiently far downstream to allow the emergence of the LE vortex. Then, the LE vortex grows and moves downstream, as depicted by Figs. 4.17i to 4.17c. At $\varphi = 0.3$, the rolling-up of the lower shear layer creates a new TE vortex. As this TE vortex grows, the LE vortex is shed into the wake. This is visible in Fig. 4.17d to Fig. 4.17h.

The corresponding loads are depicted in Fig. 4.16l. It appears that the time response is less smooth than for the loads measured at $\overline{\alpha} = 30^\circ$. This is possibly due to vibrations of the plate occurring at $\overline{\alpha} = 45^\circ$, but also to an increase of the vortex strength. Finally, at this incidence, the pressure contributes equally to the lift and drag. As reported in Tab. 4.4, the mean lift and drag have similar values and the differences in their time response are probably due to friction.

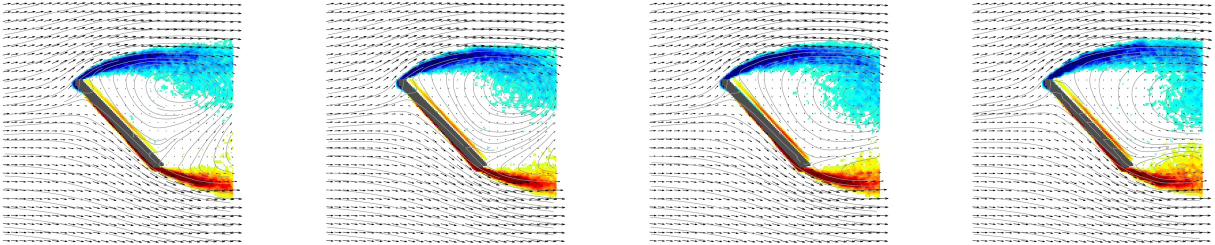

(a) $\varphi = 0.$ (b) $\varphi = 0.1.$ (c) $\varphi = 0.2.$ (d) $\varphi = 0.3.$

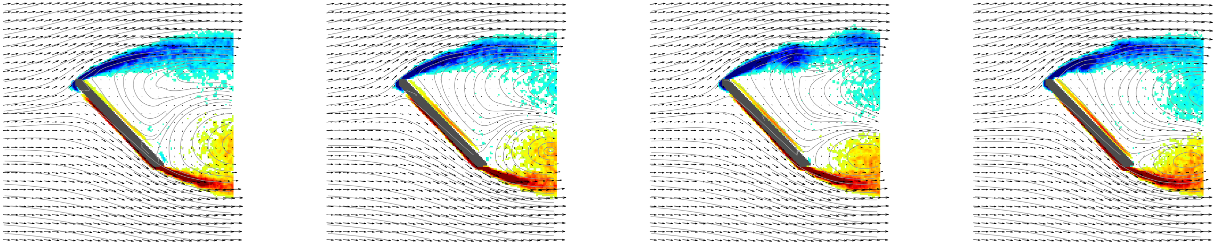

(h) $\varphi = 0.7.$ (g) $\varphi = 0.6.$ (f) $\varphi = 0.5.$ (e) $\varphi = 0.4.$

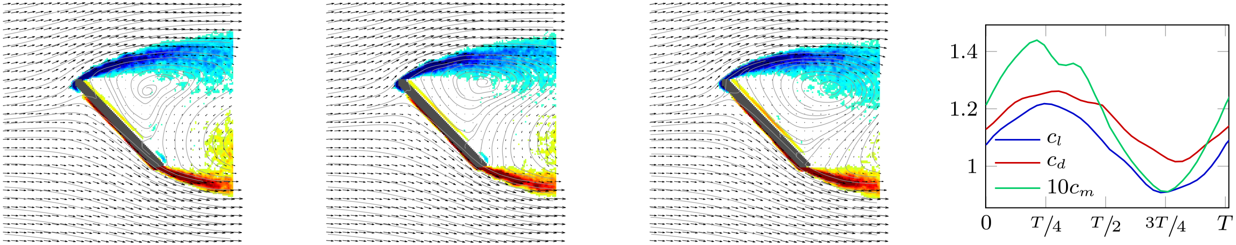

(i) $\varphi = 0.8.$ (j) $\varphi = 0.9.$ (k) $\varphi = 1.$ (l) Load coefficients.

Figure 4.17: Phase-averaged PIV velocity and vorticity fields for a small amplitude pitching cycle at a mean angle $\overline{\alpha} = 45^\circ$. The red and blue fields correspond, respectively, to positive and negative vorticity, i.e. counter-clockwise and clockwise vortices. The field of view corresponds to a square of size $2c$ centered on the plate center. The corresponding variation of the load coefficients for one oscillation period T is also shown (l).

4.5 Impact of user-defined parameters in the INSE and NOCA methods

The goal of the present chapter is to assess the INSE and NOCA indirect load calcluation methods. These formulations are applied to the different flows described in Sec. 4.4. Before discussing their accuracy, the effects of the user-defined parameters appearing in the INSE and NOCA methodologies are studied.

The user-defined parameters can be categorized into two types: the parameters related to the input PIV fields, and those related to the INSE and NOCA methods themselves. The parameters related to the PIV fields are first studied in Sec. 4.5.1. In particular, this section describes the effects of: i) the number of PIV images used in the averaging procedure, ii) the spatial resolution of the PIV measurements and, for unsteady phenomena, iii) the number of phases sampled within a pitching/shedding cycle. Then, in Sec. 4.5.2, the effects of the user-defined parameters appearing in the NOCA and INSE methodologies are investigated. Four different parameters are studied: i) the size and location of the control surface $\mathcal{S}$, ii) the mathematical formulation of the volume term in the NOCA approach, iii) the position of the origin for the location vector x_i in the NOCA method, and iv) the threshold value $\Gamma_2^{\mathrm{thres}}$ for the pressure correction in the INSE methodology.

To perform a relevant analysis, the different user-defined parameters cannot be modified simultaneously. Therefore, unless otherwise specified, the default values given below are used. The average PIV fields are obtained from 200 snapshots. The control surface $\mathcal{S}$ surrounding the plate is a square of side length $2c$ centered around the plate, as shown in Fig. 4.18. This surface is divided into points distant by $\Delta x = {}^{c}\!/_{85}$ which form a uniform cartesian calculation grid. For the large and small amplitude pitching plate cases, a cycle is divided into 20 phases and an averaged PIV fields is computed for each of those. In the context of the NOCA approach, formulation (2.43) is used for the calculation of forces. Therefore, the initial temporal term that consists of a volume integral is rewritten as surface integrals. Conversely, to improve the accuracy of the methodology, the calculation of the pitching moment involves formulation (2.66) where the volume integral is retained. The origin of location vector x_i appearing in Eqs. (2.43) and (2.66) is set at a horizontal distance of $0.925c$ downstream of the plate center. It is represented by the black dot labeled I in Fig. 4.18. Finally, for the INSE approach, Γ_2 is calculated through Eq. (2.68), where length l is chosen as $l = 0.138c$. The threshold on Γ_2 used for the pressure correction is set to $\Gamma_2^{\mathrm{thres}} = 0.05$.

It is known that the estimated loads given by the indirect formulations applied on two adjacent contours $\mathcal{C}_\infty$ can vary significantly (Albrecht et al., 2012). In order to limit that effect, the aerodynamic coefficients obtained in this work are presented in terms of statistics of the nondimensionalized loads calculated on several contours. More specifically, the control surface is associated with twelve additional surfaces that are up to $0.15c$ narrower, as illustrated in Fig. 4.18 by the shaded zones along the right boundary. The load coefficients presented are thus calculated by ensemble averaging the results obtained from the corresponding thirteen control surfaces. In addition, the standard deviation associated with these different surfaces is presented as it measures the sensitivity of the results to $\mathcal{S}$.

4.5.1 Parameters defining the PIV fields

This section studies the effects of the user-defined parameters required to define the PIV fields. In particular, the effects of the number of images used to compute statistics and the spatio-temporal resolution of PIV fields are investigated.

4.5.1.1 Number of PIV images for averaging

The impact of the number of PIV images used to obtain averaged PIV fields is investigated by applying the two indirect methodologies to velocity fields obtained from 50, 100, 150 and 200 snapshots. The results presented below are obtained by applying the INSE approach but similar conclusions can be drawn from the NOCA methodology.

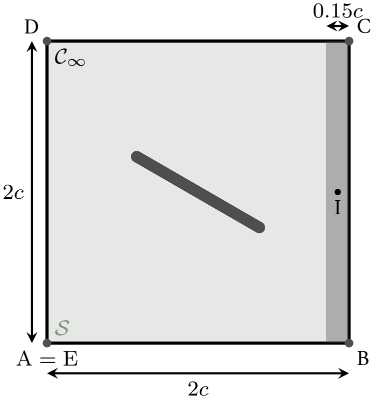

Figure 4.18: Schematic view of the default location of the control surface with respect to the plate. The small disc denoted I represents the location considered as origin in the NOCA method.

For the large amplitude pitching plate, Fig. 4.19 shows that the time response of the lift and drag coefficients are very similar for the four numbers of images considered. The pitching moment coefficient results are not shown here as they are very similar to those obtained for the drag. The mean and RMS calculated from the time responses plotted in Fig. 4.19 are almost the same for the different number of snapshots considered. A maximum relative difference of 4% is calculated by comparing the statistics obtained from the time responses corresponding to 50, 100 and 150 snapshots with those corresponding to 200 snapshots. Therefore, 50 images would already be enough to obtain a good estimation of the load coefficients. Surprisingly, this number differs significantly from the results presented by Gharali and Johnson (2014) who reported a minimum of 500 images required for a similar case.

For the static plate, the convergence analysis (not shown) indicates that the PIV mean flow field based on 50 snapshots leads to a reasonable estimation of the mean coefficients. Nonetheless, 150 images are needed to compute standard deviations, i.e., sensitivity to the control surface location, similar to the results obtained with the maximum number of snapshots. Note that the number of images required to obtain converged statistics increases compared to the large amplitude pitching case. This is probably because the coherence between snapshots decreases.

Finally, for the small amplitude pitching plate case, the mean coefficients are similar whether computed with PIV fields obtained from 50, 100, 150 or 200 images. Nonetheless, it seems that increasing the number of snapshots leads to a decrease of the noise in the coefficient responses, as depicted in Fig. 4.20.

4.5.1.2 Spatial resolution

Spatial resolution includes three aspects: i) the magnification of the camera lens in the PIV setup, ii) the size of the interrogation windows in the PIV processing and iii) the spacing of the grid on which the INSE and NOCA approaches are applied. The magnification is related to the PIV setup. More precisely, a PIV image consists of a fixed number of pixels. A physical length is thus divided into several pixels corresponding to the magnification produced by the camera lens. The size of the field of view captured by each PIV image varies with this magnification: the larger the field of view, the lower the magnification. Gharali and Johnson (2014) applied the INSE method to PIV fields obtained with several magnifications. They demonstrated that a lower magnification can be used to increase the possibility to find a location for the downstream boundary of $\mathcal{S}$ that is not in the vortical region (see Sec. 4.5.2). However, they showed that the lower spatial resolution

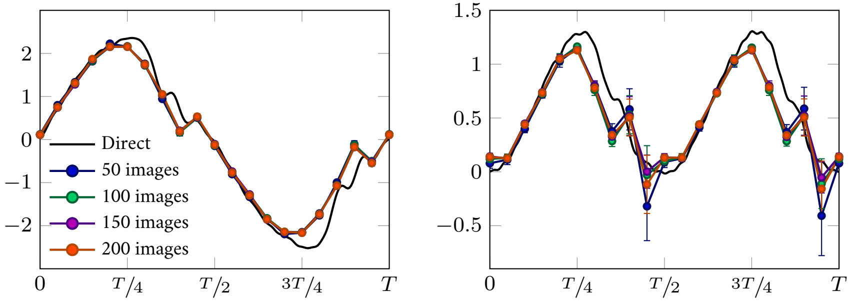

(a) c_l.

(b) c_d.

Figure 4.19: Impact of the number of snapshots on the variation of the lift and drag coefficients within a pitching period T for large amplitude plate oscillations around a mean angle of attack of 0°: indirect calculation using INSE (symbols) and direct measurements (thick continuous line). The error bars correspond to the sensitivity of the results to the control surface used in the indirect method.

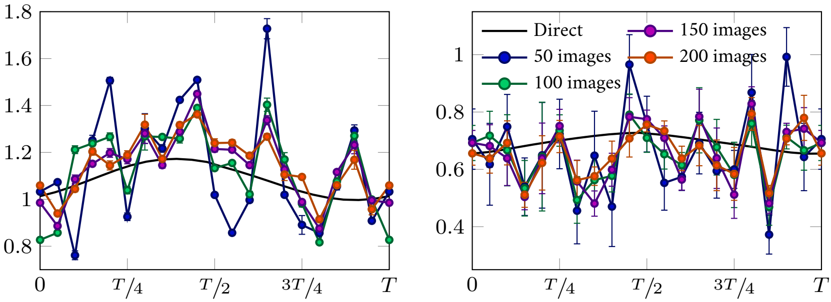

(a) c_l.

(b) c_d.

Figure 4.20: Impact of the number of snapshots on the variation of the lift and drag coefficients within a pitching period T for small amplitude plate oscillations around a mean angle of attack of 30°: indirect calculation using INSE (symbols) and direct measurements (thick continuous line). The error bars correspond to the sensitivity of the results to the control surface used in the indirect method.

could be problematic for moving bodies. The setting of the size of the PIV interrogation windows is required for the PIV process described in Algo. 1. In particular, a small interrogation window for the second pass captures smaller scales. This is explained in more details in Sec. 2.3.1. Finally, the PIV fields are obtained on a grid having a prescribed spacing Δx. Because the indirect calculations use the same grid, a larger Δx introduces larger discretization errors.

In the present work, the magnification is constant and its impact on the indirectly computed loads is not studied. On the other hand, the size of the interrogation windows and the grid spacing are varied. More precisely, the results obtained by applying the INSE and NOCA formulations on two PIV grids are compared. The first one corresponds to the default parameters. As stated in Sec. 4.2, the grid spacing is $\Delta x = c/85$ and the size of the first and second pass interrogation windows are 64×64 pixels and 32×32 pixels, respectively. The second grid is obtained by increasing the grid spacing while the overlap of the first pass interrogation windows IWa_0 and

IWb_0 is kept constant. In particular, the grid spacing of the second grid is $\Delta x = {}^{c}/_{42}$ while the size of IW_0 and IW_1 are 128×128 pixels and 64×64 pixels, respectively. The second grid is then coarser and its dynamic range is reduced compared to the first default grid. This procedure leads to a smoother field than the one that would result from selecting every second point of the first grid.

The time response of the lift and drag coefficients calculated by applying the INSE method in the context of the large amplitude pitching plate are depicted in Fig. 4.21. It appears that the indirect calculation is not severely impacted by the increase of Δx. Moreover, similar conclusions can be drawn for the results obtained from the NOCA approach and those associated with the small amplitude pitching plate (not shown). Therefore, in combination with the work of Gharali and Johnson (2014), it can be concluded that the effect of magnification on the indirect load computation is stronger than that of a decrease of dynamic range or an increase of grid spacing.

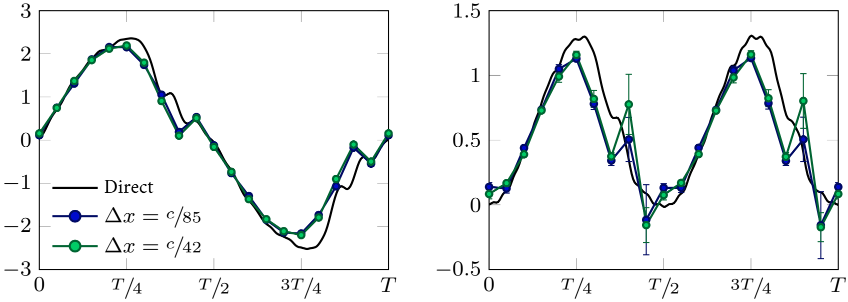

(a) c_l. (b) c_d.

Figure 4.21: Impact of the spatial resolution on the variation of the lift and drag coefficients within a pitching period T for large amplitude plate oscillations around a mean angle of attack of $0°$: indirect calculation using INSE (symbols) and direct measurements (thick continuous line). The error bars correspond to the sensitivity of the results to the control surface used in the indirect method.

4.5.1.3 Temporal resolution

The temporal resolution is studied by varying the size of the time-step that discretizes one cycle of the shedding/pitching phenomena. More precisely, the INSE and NOCA methods are applied for: i) $\Delta T = {}^{T}/_{20}$, ii) $\Delta T = {}^{T}/_{10}$ and iii) $\Delta T = {}^{T}/_{5}$. Note that the variation of the time-step is considered only in the computation of the temporal derivative. Therefore, the loads are still calculated for each of the 20 phases in the shedding/pitching cycle. The impact of the temporal resolution is studied on both the large and small amplitude pitching plate cases and the corresponding results are presented in Figs. 4.22 and 4.23.

For the large amplitude pitching case, the time response for the lift and drag coefficients estimated through the INSE approach are depicted in Fig. 4.22. The effect of Δt on the pitching moment is similar to the effect on drag (not shown). Increasing the temporal resolution clearly improves the predictions, especially for the drag. Moreover, larger discrepancies are observed between time instances ${}^{3T}/_{10}$ and ${}^{T}/_{2}$, and ${}^{8T}/_{10}$ and T. As discussed in Sec. 4.4.1, these time instances correspond to the shedding of the LE vortex. As visible in Fig. 4.8, this shedding is associated with rapid flow variations.

The effect of the time resolution on the estimated loads for the small amplitude pitching case differs significantly from the previous case, as shown Fig. 4.23. Increasing the time resolution does not seem to improve the results. This is possibly due to the noise present in the PIV fields, the number of snapshots, and/or an insufficient spatial resolution.

Despite the inconclusive results of the second case, it is evident that a sufficient time resolution is required to accurately capture the load variation. While these results have been obtained from the INSE method, similar conclusions can be drawn for the NOCA method.

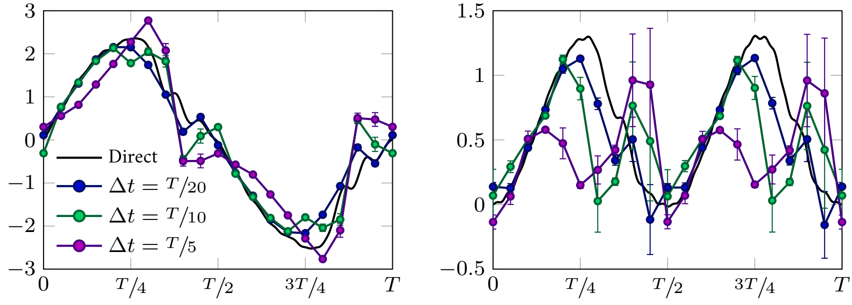

(a) c_l.

(b) c_d.

Figure 4.22: Impact of the temporal resolution on the variation of the lift and drag coefficients within a pitching period T for large amplitude plate oscillations around a mean angle of attack of 0°: indirect calculation using INSE (symbols) and direct measurements (thick continuous line). The error bars correspond to the sensitivity of the results to the control surface used in the indirect method.

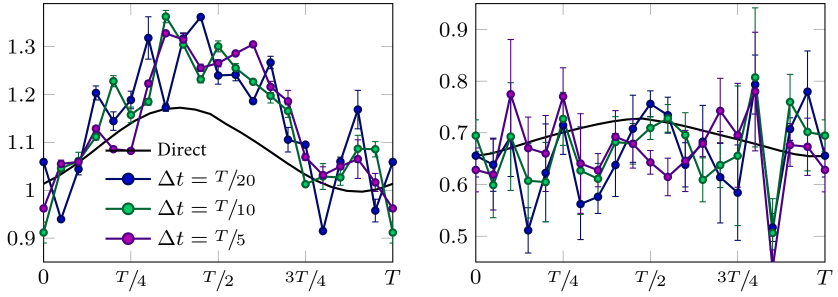

(a) c_l.

(b) c_d.

Figure 4.23: Impact of the temporal resolution on the variation of the lift and drag coefficients within a pitching period T for small amplitude plate oscillations around a mean angle of attack of 30°: indirect calculation using INSE (symbols) and direct measurements (thick continuous line). The error bars correspond to the sensitivity of the results to the control surface used in the indirect method.

4.5.2 Parameters appearing in the INSE and NOCA approaches

This section presents the effects of the user-defined parameters explicitly appearing in the INSE and NOCA formulations. First, the effect of the choice of the control surface $\mathcal{S}$ in both methodologies is discussed. Then, in the context of the NOCA method, the effects of the mathematical formulation of the temporal term and of the origin of the vector location are investigated. Finally, the effect of $\Gamma_2^{\mathrm{thres}}$ in the INSE methodology is studied.

4.5.2.1 Size and location of the control surface $\mathcal{S}$

The effects of $\mathcal{S}$, in particular its size and location, are studied by applying the INSE and NOCA methodologies to the large amplitude pitching plate test case. The study is conducted by varying: i) the upstream edge noted D-E in Fig. 4.18, ii) the upper and lower edges noted A-B and C-D and, finally, iii) the downstream edge B-C. The different edges are then moved within the limitation of the available PIV window $\mathcal{S}_{max}$ depicted in Fig. 4.2c. In particular, for each case three different surfaces are considered, as illustrated in Fig. 4.24. As explain before, each of these three control surfaces is associated with additional surfaces that are up to $0.15c$ narrower, as illustrated in Fig. 4.24 by the shaded zones. The results are then reported in terms of statistics where the standard deviation measures the sensitivity to the location of the upstream edge. The results of these three cases obtained with the INSE method are presented in Figs. 4.25, 4.26 and 4.28. A similar sensitivity to $\mathcal{S}$ is observed for the NOCA formulation.

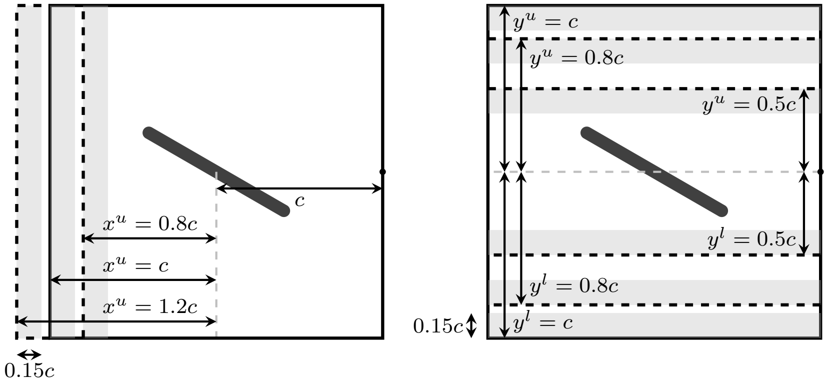

(a) Upstream edge study.

(b) Upper and lower edges study.

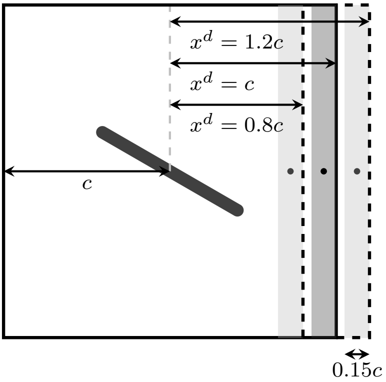

(c) Downstream edge study.

Figure 4.24: Schematic view of the location of the control surfaces with respect to the plate. The solid lines define the border of the default contour chosen to compare the indirect methods and the dashed lines denote the additional contours used in the parameter study. The small black discs represent the locations considered for the origin in the NOCA method.

The sensitivity of the lift and drag estimations to the upstream edge D-E is shown in Fig.4.25. The variation of the pitching moment is not depicted but it shows a sensitivity similar that of the

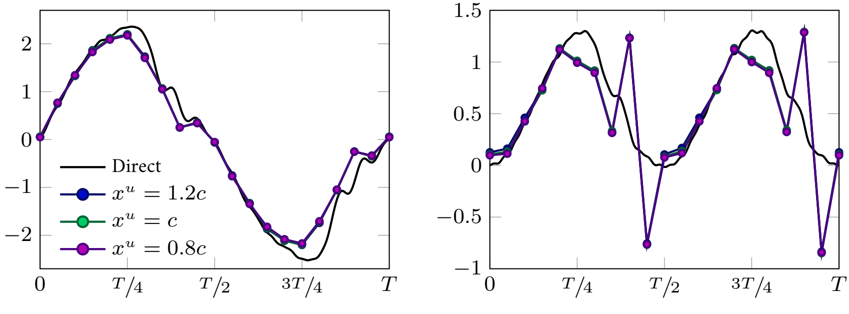

(a) c_l. (b) c_d.

Figure 4.25: Impact of the upstream edge of the control surface location on the variation of the aerodynamic coefficients within a pitching period T for large amplitude plate oscillations about a pivot axis at the plate center: indirect calculations using INSE with $\Gamma_2^{\text{thres}} = 0$ and different edge D-E positions (symbols) and direct measurements (thick continuous line). The error bars correspond to the sensitivity of the results to the control surface used in the indirect methods.

lift coefficient. The results are almost insensitive to the location of the upstream edge. As also reported by David et al. (2009) and Gharali and Johnson (2014), this insensitivity of the aerodynamic coefficients to x^u is expected since the flow is very smooth in this location.

Figure 4.26 shows the sensitivity of the aerodynamic coefficient response to the location of the upper and lower edges. It appears that the results obtained for $y^u = c$ and $y^u = 0.8c$ are mostly similar, only small differences are visible between ${}^{7T}\!/_{20}$ and ${}^{9T}\!/_{20}$, and between ${}^{17T}\!/_{20}$ and ${}^{19T}\!/_{20}$. However, the results obtained for $y^u = 0.5c$ differ considerably. The discrepancies for the lift and drag coefficients are large between ${}^{2T}\!/_{10}$ and ${}^{4T}\!/_{10}$ and between ${}^{7T}\!/_{10}$ and ${}^{9T}\!/_{10}$. Large error bars also indicate a higher sensitivity to a small change in the location of the right edge. As discussed in Sec. 4.4.1, a large vortex emerges at the leading edge, grows and is then shed into the wake. When $y^u = 0.5c$, the upper and lower edges are so close to the body that they may be crossed by this large vortex, which induces error in the load estimation. In particular, the errors in the pressure calculation appearing in the INSE method are not compensated by the pressure correction step as the error is supposed to be only generated along the downstream edge (see Sec. 2.3.2.2). The results obtained with the NOCA approach also show this behavior although the method does not explicitly require the knowledge of pressure. Figure 4.27 depicts the flow field at two phases. In Fig. 4.27a, the leading edge vortex is small and the upper and lower edges are then located away from the vorticity region. However, in Fig. 4.27b, the leading edge vortex is large enough to perturb the calculation along the upper edge if $y^u = 0.5c$. Nonetheless, when $y^u = 0.8c$ or $y^u = c$, this edge is located far enough from the body. This demonstrates that the aerodynamic coefficients are not very sensitive to the location of the upper and lower edges, as long as they are far enough from the body, i.e. outside the high vorticity regions. This observation was also reported by David et al. (2009) and Gharali and Johnson (2014).

Figure 4.28 shows the sensitivity of the aerodynamic coefficients to the downstream edge. Note that the results are computed by the INSE method in which the pressure correction is applied to the entire edge B-C, i.e., $\Gamma_2^{\text{thres}} = 0$. The main differences are observed between ${}^{7T}\!/_{20}$ and ${}^{5T}\!/_{10}$, and between ${}^{17T}\!/_{20}$ and T. At these phases, the leading edge vortex is located in the wake and crosses the downstream edge (see Fig. 4.8). The lift coefficient is only weakly impacted by the choice of x^d, as depicted in Fig. 4.28a. The effects on the pitching moment coefficient are larger, as seen in Fig. 4.28c. However, the variation of the error with x^d does not exhibit any clear trend. Finally, as shown in Fig. 4.28b, it seems that choosing the downstream edge closer to the body slightly improves the drag estimation as indicated by the smaller discontinuous jumps. However,

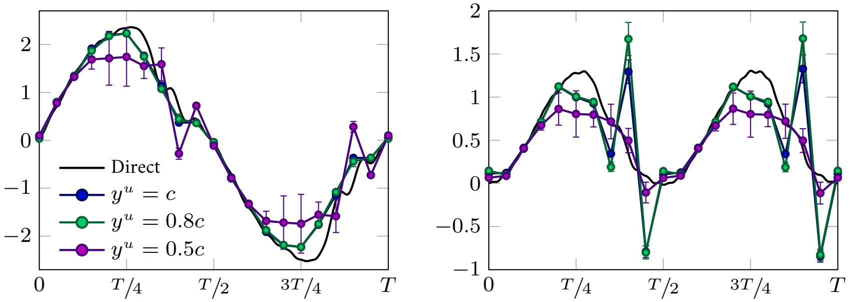

(a) c_l.

(b) c_d.

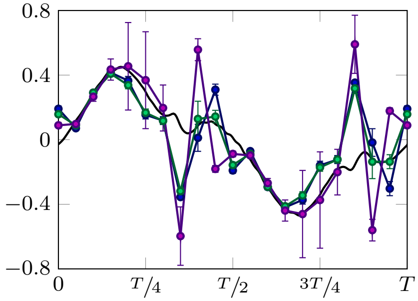

(c) c_m.

Figure 4.26: Impact of the upper and lower edges of the control surface location on the variation of the aerodynamic coefficients within a pitching period T for large amplitude plate oscillations about a pivot axis at the plate center: indirect calculations using INSE with $\Gamma_2^{\text{thres}} = 0$ and different edge B-C positions (symbols) and direct measurements (thick continuous line). The error bars correspond to the sensitivity of the results to the control surface used in the indirect methods.

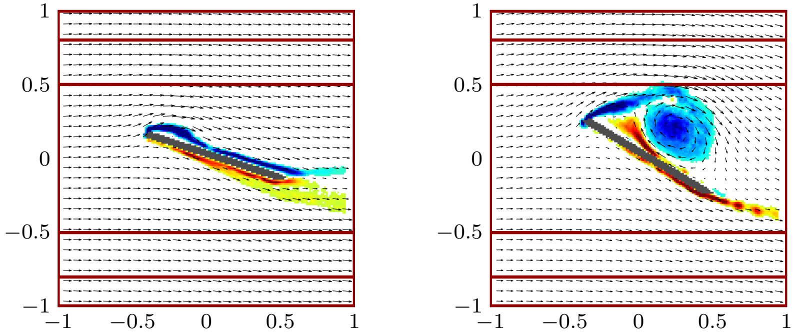

(a) $0.05T$.

(b) $0.25T$.

Figure 4.27: Phase-averaged PIV velocity and vorticity fields at two phases in the large amplitude pitching cycle. The red and blue fields correspond, respectively, to positive and negative vorticity, i.e. counter-clockwise and clockwise vortices. The red boxes correspond to three different control surfaces.

additional studies demonstrate that the downstream edge cannot be located too close to the body because the sensitivity to a small change in the surface location increases in this case. This sensitivity of the drag to the choice of x^d was also observed by David et al. (2009) and Gharali and Johnson (2014). Moreover, Gharali and Johnson (2014) reported that this sensitivity can be reduced by increasing the size of the PIV window in order to find a location for the downstream boundary far from vortical structures. To this end, Gharali and Johnson (2014) proposed to decrease the magnification factor of the PIV camera lens increasing then the size of the field of view. However, they also reported that the resulting decrease in spatial resolution may become problematic.

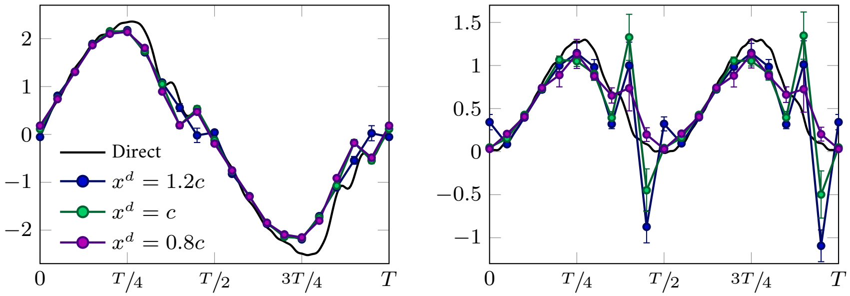

(a) c_l.

(b) c_d.

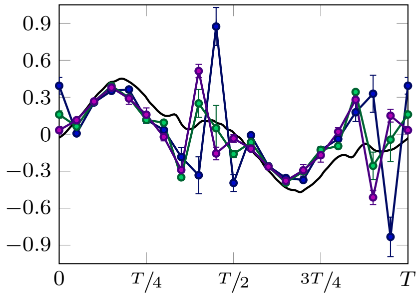

(c) c_m.

Figure 4.28: Impact of the downstream edge of the control surface location on the variation of the aerodynamic coefficients within a pitching period T for large amplitude plate oscillations about a pivot axis at the plate center: indirect calculations using INSE with $\Gamma_2^{\mathrm{thres}} = 0$ and different edge B-C positions (symbols) and direct measurements (thick continuous line). The error bars correspond to the sensitivity of the results to the control surface used in the indirect methods.

4.5.2.2 Temporal term in the NOCA formulation

In the NOCA formulation the temporal term appearing in the integral Navier-Stokes equations (2.36) is written in terms of surface integrals using only the borders of the control volume. As explained in App. A.2, this is mathematically expressed as

$$-\,\mathrm{d}_t \int_{\mathcal{V}} \mathbf{u}\,\mathrm{d}\mathcal{V} = \oint_{\mathcal{S}_\infty} \mathbf{n}\cdot\boldsymbol{\gamma}^{Ft}\,\mathrm{d}\mathcal{S} - \mathrm{d}_t \oint_{\mathcal{S}_b} \mathbf{n}\cdot(\rho\mathbf{u}\mathbf{x})\,\mathrm{d}\mathcal{S}. \tag{4.5}$$

A comparison between the lift and drag time responses obtained from the NOCA method using a volume or a surface integral formulation for the temporal term is shown in Fig. 4.29. No significant differences are observed. Note that as stated in Sec. 2.3.3.2, the pitching moment is always calculated based on a volume integral formulation.

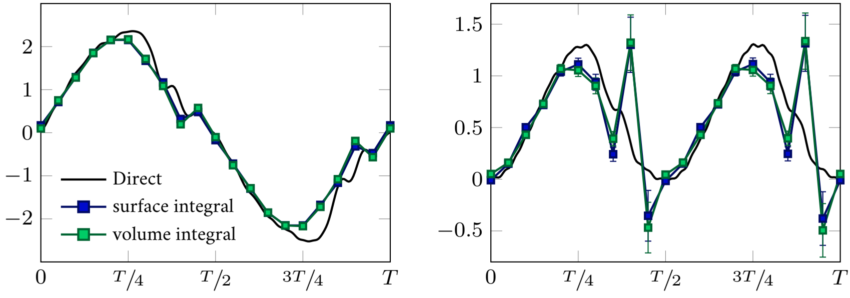

(a) c_l.

(b) c_d.

Figure 4.29: Impact of the mathematical formulation of the temporal term as either volume or surface integral on the variation of the aerodynamic coefficients within a pitching period T for large amplitude plate oscillations about a pivot axis at the plate center: indirect calculations using NOCA (symbols) and direct measurements (thick continuous line). The error bars correspond to the sensitivity of the results to the control surface used in the indirect methods.

4.5.2.3 Origin of location vector x_i in the NOCA formulation

Although the results obtained with the NOCA method should be in theory independent of the choice of the origin, they depend quite strongly on it in practice. This is particularly true for turbulent flows but this dependence was also demonstrated by Noca et al. (1999) for a laminar case. This impact is illustrated here with the large amplitude pitching plate test case. Figure 4.30 depicts the three origin locations considered here. The default origin is labelled I, while the locations II and III aim to study the effect of a horizontal and vertical modification of the origin location, respectively.

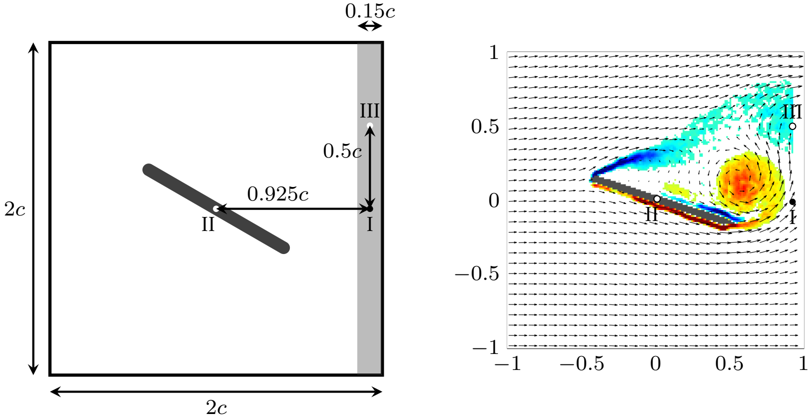

(a) With respect to the control surface.

(b) With respect to the flow at $0.4T$.

Figure 4.30: Schematic views of the locations considered for the study of the effect of the origin in the NOCA method. The different origins are represented by the small discs denoted I to III.

Figure 4.31 shows the time response of the lift and drag coefficients. The results for the pitching moment are not presented here but their sensitivity to the origin is similar to that of the lift. In Fig. 4.31a, it appears that the lift is only impacted by a horizontal modification of the origin location. An origin located farther from the downstream edge (II compared to I and III) leads to higher discrepancies with the experimental results. In particular, the origin denoted II leads to spurious oscillations and jumps in the time response of c_l. Figure 4.31b shows the same behavior for the drag coefficient regarding locations I and II. Compared to location I, location III leads to a reduction of the first jump in c_d but an increase in the amplitude of the second one. As shown in Fig. 4.30b, a vortex core is located near point III at the phase corresponding to the first jump. Assuming that the largest errors occur in the wake region where vorticity is large, these results indicate that the contribution from this region is smaller when the distance $\|\mathbf{x}\|$ in Eqs. (2.46) and (2.67) is small. Having an origin in the critical region thus reduces the overall error and provides a better estimation of the drag. Consequently, it should be possible to further improve the NOCA results by adapting the location of the origin of x_i to the flow topology.

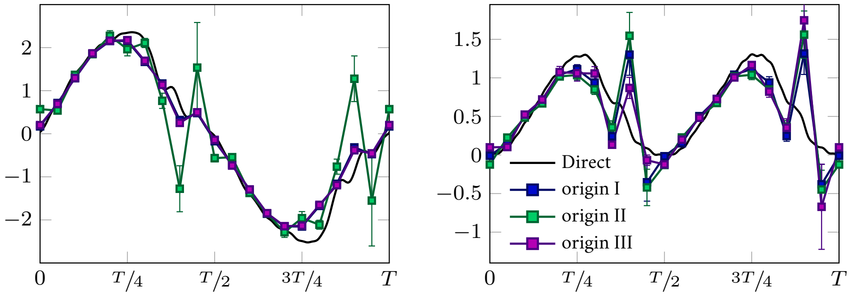

(a) c_l.

(b) c_d.

Figure 4.31: Impact of the origin defining the location vector x_i on the variation of the aerodynamic coefficients within a pitching period T for large amplitude plate oscillations about a pivot axis at the plate center: indirect calculations using NOCA with different origin locations (symbols) and direct measurements (thick continuous line). The error bars correspond to the sensitivity of the results to the control surface used in the indirect methods.

4.5.2.4 Threshold value Γ_2^{thres} in the INSE formulation

The pressure correction step appearing in the INSE methodology requires a threshold value Γ_2^{thres}. As described in Sec. 2.3.2.2, this value is used to determine the part of the downstream edge B-C where the pressure correction is applied. Several values of Γ_2^{thres} are considered for three different control surfaces differing by the location of their downstream edge x^d (see Fig. 4.24c).

Figure 4.32 shows the results obtained for the drag coefficient. The lift and pitching moment coefficient are not shown because they are not impacted by a variation of Γ_2^{thres}. As shown by Fig. 4.32a for the default control surface, an increase of Γ_2^{thres}, i.e., a decrease of the portion of the downstream edge where the pressure correction is applied, reduces the amplitude of the jumps. Nonetheless, increasing Γ_2^{thres} above 0.05 does not seem to further improve the results. Moreover, Fig. 4.32b and Fig. 4.32c show that the impact of Γ_2^{thres} decreases when the downstream edge moves closer to the body.

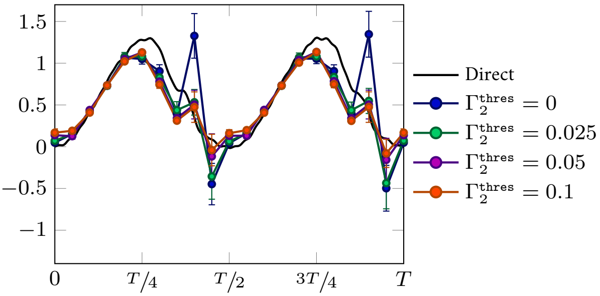

(a) $x^d = c$.

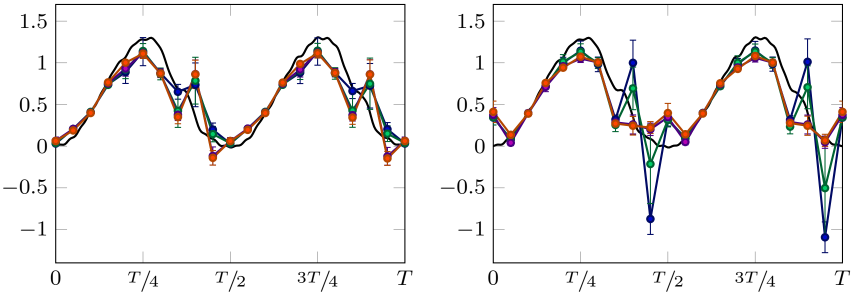

(b) $x^d = 0.8c$.

(c) $x^d = 1.2c$.

Figure 4.32: Impact of the threshold value Γ_2^{thres} on the variation of the drag coefficient within a pitching period T for large amplitude plate oscillations about a pivot axis at the plate center: indirect calculations using INSE (symbols) and direct measurements (thick continuous line). The error bars correspond to the sensitivity of the results to the control surface used in the indirect methods. Three positions x^d of the downstream edge are considered.

4.6 Evaluation of the indirect methods for computing aerodynamic loads

The present section describes the results obtained by using the INSE and NOCA formulations to compute the loads on the large amplitude pitching plate, the static plate and the small pitching plate. The two-dimensional lift and drag coefficients, and the pitching moment coefficient about the mid-chord are computed and compared to three-dimensional direct measurements. The accuracy of the indirect methods is discussed, and their limitations are highlighted. For all results, the choice of the user-defined parameters is based on the guidelines provided previously and corresponds to the default values introduced at the beginning of Sec. 4.5.

4.6.1 Large amplitude pitching plate

The time responses of the load coefficients during a complete cycle of the large amplitude motion are shown in Fig. 4.33. The loads are indirectly computed using both the INSE and NOCA formulations for the three cases corresponding to the three locations of the pivot axis. Note that the symmetry around the half-period is a direct consequence of the PIV field stitching procedure. The results compare rather well with direct measurements. As shown from Fig. 4.10 to Fig. 4.11, the loads are very well estimated during the middle stage of the upstroke and downstroke, i.e. when the plate increases its relative incidence with respect to the freestream. These phases correspond to the growth of the leading edge vortex. Conversely, for other parts of the cycle, the amplitude

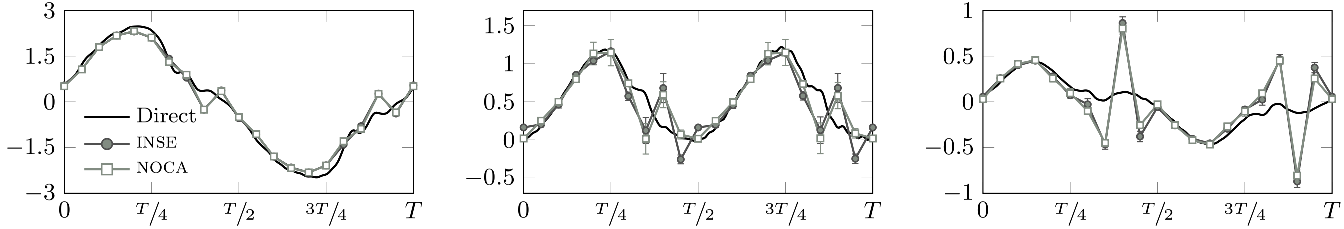

(a) Pivot at LE: c_l.

(b) Pivot at LE: c_d.

(c) Pivot at LE: c_m.

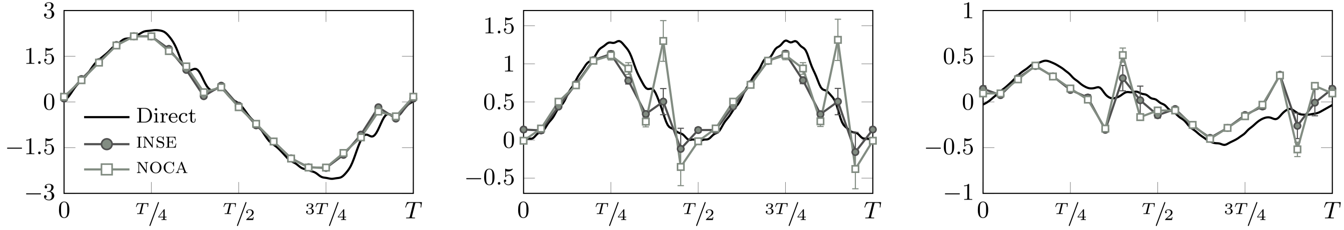

(d) Pivot at center: c_l.

(e) Pivot at center: c_d.

(f) Pivot at center: c_m.

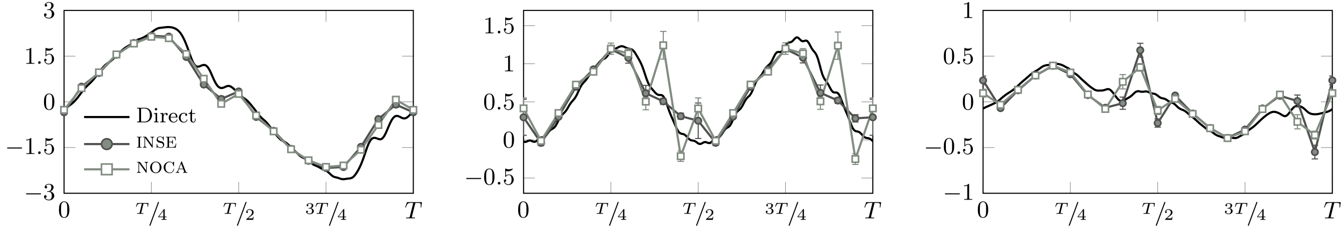

(g) Pivot at TE: c_l.

(h) Pivot at TE: c_d.

(i) Pivot at TE: c_m.

Figure 4.33: Variation of the aerodynamic coefficients within a pitching period T for large amplitude plate oscillations about different pivot axes at $\mathrm{Re} = 2 \times 10^4$: indirect calculations (symbols) and direct measurements (thick continuous line). The error bars correspond to the sensitivity of the results to the control surface used in the indirect methods.

of the lift is slightly underestimated while the accuracy of the drag and pitching moment coefficients decreases. Similar results were obtained by Gharali and Johnson (2014). Both the drag and pitching moment, and to a much lesser extent the lift, exhibit discontinuous jumps. The amplitude of these jumps depends on the method and, as described in Sec. 4.5, the chosen values for user-defined parameters. In particular, the difference in the jump amplitude observed between the INSE and NOCA methods is due to the pressure correction step applied in the former methodology. Moreover, the location of the discontinuous jumps changes with the position of to the pivot axis, as clearly visible by comparing Figs. 4.33f and 4.33i. This is due to the change in the flow topology when varying the pivot location, as described in Sec. 4.4. Note that for a pivot axis located at the LE or TE, the last term in Eq. (2.45) contributes to the lift coefficient. However, this contribution corresponds to less than 0.3% of the maximum lift and the impact of the body motion can thus be considered as negligible.

The discontinuous jumps observed in Fig. 4.33 are linked to the shedding of vortices into the wake. As previously discussed and also highlighted by Gharali and Johnson (2014), a vortex that crosses the integration path in the wake impacts the results. Figures 4.8, 4.10 and 4.11 show the velocity and vorticity fields during half a pitching cycle for a field of view that corresponds to the control surface $\mathcal{S}$. The comparison of the coefficient responses with the flow fields shows that the accuracy of the load estimation decreases with the increase of flow disturbance on the downstream edge of $\mathcal{S}$, a jump in the estimation appearing when vortices cross this edge. The increased measurement noise associated with regions of strong vorticity probably induces an increase in numerical errors. As an example, for a pivot axis located at LE, Fig. 4.10 shows that the large leading edge vortex still located near the plate at $^{3T}/_{10}$ is convected downstream and crosses the downstream edge at $^{7T}/_{20}$ and to a lesser extent at $^{4T}/_{10}$. These phases correspond to the large discrepancies visible in Figs. 4.33b and 4.33c.

Time-averaged and root-mean-square statistics of the aerodynamic coefficients are summarized in Tab. 4.5 and should be analyzed in light of Fig. 4.33. The mean lift and moment coefficients are both close to zero. This result is expected as the pitching motion is symmetric with respect to the freestream but also because two velocity fields distant in time by half a cycle are built from the same PIV snapshots. The mean and RMS of the drag coefficient are generally lower than expected because of the underestimation of their response amplitude. Similarly, the RMS value of the lift coefficient estimated by both indirect methods is slightly lower than the direct measurements. Finally, the RMS value of the moment coefficient is artificially improved by the presence of the jumps in its time response.

In conclusion, both indirect methods are able to estimate reasonably well the aerodynamic coefficients of a flat plate undergoing a large amplitude pitching motion. However, the NOCA method is more sensitive to noise even if the user-defined parameters are carefully chosen. Nonetheless, the estimated load responses must be considered with caution for detached flows especially when a vortex crosses the downstream edge of the control surface.

4.6.2 Static plate

The mean load coefficients calculated for the static plate using indirect methods are shown in Tab. 4.6, together with the mean results obtained from direct measurements. Due to the time-averaging used in this case, the major contribution to the term $\overline{u'_i u'_j}$ stems from the unsteady flow dynamics and not from the turbulence itself. As described above, the standard deviation is computed from the results obtained using different control surfaces $\mathcal{S}$.

Albrecht et al. (2013) studied a similar flow using the INSE and NOCA approaches. Their results were shown to be highly sensitive to the choice of indirect approach. They concluded that NOCA should be used for the lift, while INSE provides better results for the drag. Moreover, a high sensitivity to the location of $\mathcal{S}$ was reported. The present work leads to different conclusions. First, the results show that the two indirect methodologies can provide a reasonably good estimation of the mean load coefficients for both angles of attack. In particular, the mean lift is predicted with a maximal relative error of about 2%. The relative error on the mean drag coefficient is higher for

	Pivot at leading edge					
	$\overline{c_l}$	c_l^{RMS}	$\overline{c_d}$	c_d^{RMS}	$\overline{c_m}$	c_m^{RMS}
INSE	0.03	1.45	0.48	0.64	0.00	0.40
NOCA	0.03	1.45	0.50	0.65	0.00	0.37
Direct	-0.01	1.57	0.54	0.68	-0.01	0.24
	Pivot at center					
	$\overline{c_l}$	c_l^{RMS}	$\overline{c_d}$	c_d^{RMS}	$\overline{c_m}$	c_m^{RMS}
INSE	0.01	1.36	0.49	0.63	0.01	0.22
NOCA	0.01	1.36	0.54	0.75	0.00	0.26
Direct	-0.05	1.56	0.60	0.75	-0.01	0.25
	Pivot at trailing edge					
	$\overline{c_l}$	c_l^{RMS}	$\overline{c_d}$	c_d^{RMS}	$\overline{c_m}$	c_m^{RMS}
INSE	-0.02	1.35	0.57	0.68	0.01	0.27
NOCA	-0.01	1.36	0.61	0.77	0.01	0.23
Direct	-0.02	1.55	0.58	0.74	0.00	0.22

Table 4.5: Mean and RMS values of the aerodynamic coefficients for large amplitude plate oscillations around different pivot axes at $\mathrm{Re} = 2 \times 10^4$ computed with the indirect methods and obtained from direct measurements.

both methodologies with a maximum of 13% at an angle of attack of 30°. The relative error is 25% for the mean pitching moment coefficient at an angle of attack of 45°, an error that should be considered in light of the relatively small value of the directly measured coefficient. Finally, the sensitivity to the control surface is low and similar for the two methods, as shown by the low standard deviations.

In conclusion, the INSE and NOCA methodologies are both able to provide an accurate indirect estimation of the mean load coefficients. Moreover, they exhibit a similarly low sensitivity to the location of the control surface $\mathcal{S}$.

4.6.3 Small amplitude pitching plate

The INSE and NOCA methods are now applied to the plate undergoing small amplitude pitching oscillations around a large incidence. First, the estimates from the indirect formulations are presented and the discrepancies with the direct measurements are discussed. Then, the DMD is used as a pre-processing step to reduce the noise in the PIV field and therefore improve the indirect estimations of load coefficients. Finally, the causes of the discrepancies between direct and indirect results are investigated.

4.6.3.1 Estimation from INSE and NOCA methods

The time responses of the phase-averaged load coefficients are shown in Fig. 4.34 for a mean angle of attack of 30° and 45°. They are very noisy whether calculated by INSE or NOCA. For $\overline{\alpha} = 30^\circ$, only global trends can be seen for the lift coefficient computed by both the NOCA and INSE methods. The noise in the drag and pitching moment response is even higher, so that only mean values are meaningful. Additionally, the large error bars in Fig. 4.34c indicate a strong sensitivity of the results to the choice of the control surface. The results corresponding to $\overline{\alpha} = 45^\circ$ exhibit the same

	Angle of attack 30°		
	$\overline{c_l}$	$\overline{c_d}$	$\overline{c_m}$
INSE	1.00 ± 0.00	0.56 ± 0.04	0.12 ± 0.01
NOCA	1.00 ± 0.00	0.57 ± 0.04	0.12 ± 0.01
Direct	0.99	0.63	0.12
	Angle of attack 45°		
	$\overline{c_l}$	$\overline{c_d}$	$\overline{c_m}$
INSE	1.00 ± 0.01	1.12 ± 0.07	0.15 ± 0.01
NOCA	0.99 ± 0.02	1.13 ± 0.07	0.16 ± 0.02
Direct	1.01	1.09	0.12

Table 4.6: Mean value of the aerodynamic coefficients for a static plate at an incidence angle of 30° and 45° and $\mathrm{Re} = 4 \times 10^4$ computed with the indirect methods and obtained from direct measurements. The standard deviations indicated for the indirect calculations represent the sensitivity of the results to the choice of control surface $\mathcal{S}$.

	Angle of attack					
	30° ± 0.77°			45° ± 1.33°		
	$\overline{c_l}$	$\overline{c_d}$	$\overline{c_m}$	$\overline{c_l}$	$\overline{c_d}$	$\overline{c_m}$
INSE	1.15	0.66	0.10	1.10	1.12	0.10
NOCA	1.15	0.68	0.11	1.09	1.11	0.10
Direct	1.08	0.69	0.13	1.07	1.15	0.12

Table 4.7: Mean values of the aerodynamic coefficients for small amplitude plate oscillations around a mean angle of attack of 30° and 45° at $\mathrm{Re} = 4 \times 10^4$ computed with the indirect methods and obtained from direct measurements. Results are shown for the original data (without DMD pre-processing).

type of behavior although the global trend of the drag response is better estimated. Finally, despite the noise in the load responses, the time averaged of the load coefficients are well approximated, as shown in Tab. 4.7.

4.6.3.2 Application of DMD as a pre-processing step

As shown in Fig. 4.34, the time responses of the indirectly estimated load coefficients are very noisy. This noise probably originates in the PIV velocity. Therefore, the phase-averaged PIV fields are filtered by applying DMD (see Sec. 2.4). Only the first three modes are retained to approximate the original fields. These modes correspond to the mean flow, the shedding/pitching frequency and its first harmonic.

This pre-processing step leads to the smoother responses depicted in Fig. 4.35. The qualitative behavior of the lift and drag time responses is well predicted for $\overline{\alpha} = 30°$ and $\overline{\alpha} = 45°$, respectively (Figs. 4.35a, 4.35d). However, several quantitative discrepancies remain. In particular, the maximum lift obtained with the NOCA method for $\overline{\alpha} = 30°$ is overestimated and slightly shifted in time compared to the direct measurements. The behavior of the other load coefficient responses

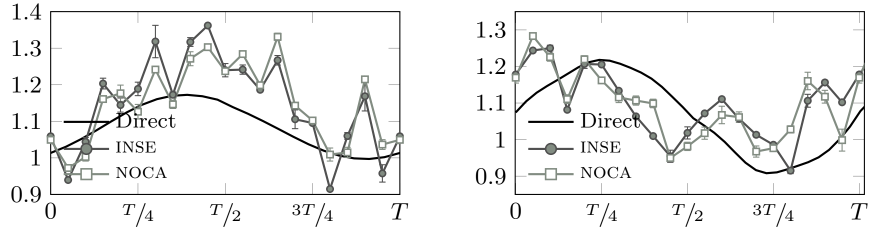

(a) c_l for $\overline{\alpha} = 30^\circ$.

(b) c_l for $\overline{\alpha} = 45^\circ$.

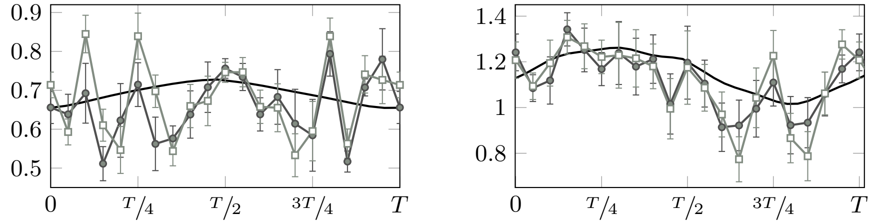

(c) c_d for $\overline{\alpha} = 30^\circ$.

(d) c_d for $\overline{\alpha} = 45^\circ$.

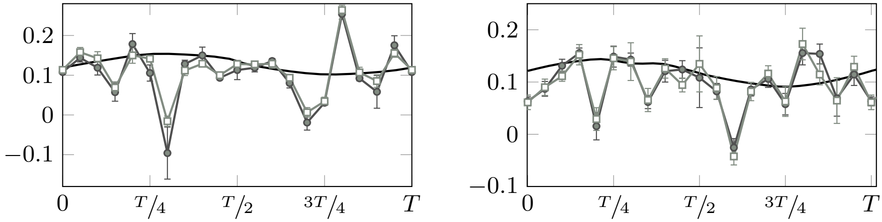

(e) c_m for $\overline{\alpha} = 30^\circ$.

(f) c_m for $\overline{\alpha} = 45^\circ$.

Figure 4.34: Variation of the aerodynamic coefficients within a pitching period T for small amplitude plate oscillations around a mean angle of attack of 30° and 45° at $\mathrm{Re} = 4 \times 10^4$ without DMD pre-processing: indirect calculation (symbols) and direct measurements (thick continuous line). The error bars correspond to the sensitivity of the results to the control surface used in the indirect method.

is not improved by the DMD pre-processing (Figs. 4.35c, 4.35e, 4.35b and 4.35f). The noise in the PIV fields is probably too high to determine the frequency content of their responses.

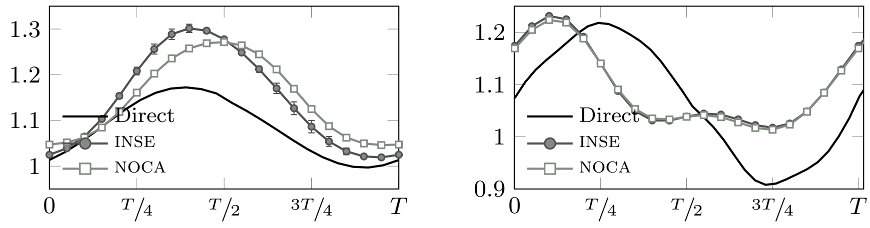

(a) c_l for $\overline{\alpha} = 30^\circ$.   (b) c_l for $\overline{\alpha} = 45^\circ$.

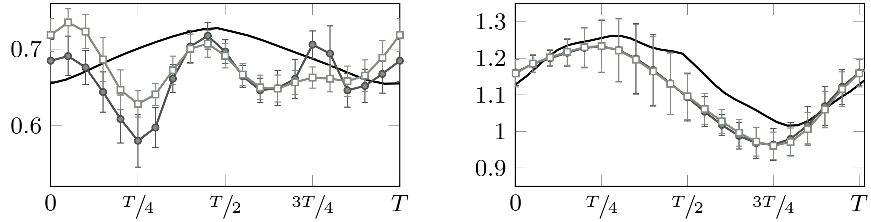

(c) c_d for $\overline{\alpha} = 30^\circ$.   (d) c_d for $\overline{\alpha} = 45^\circ$.

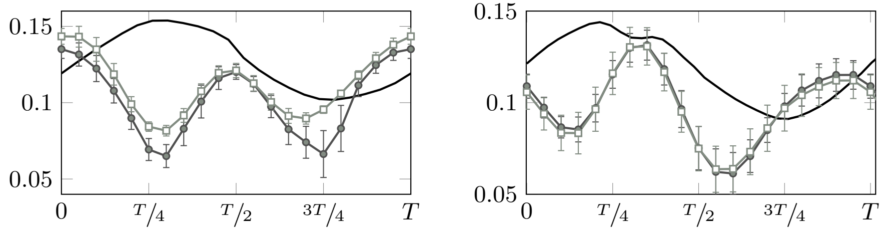

(e) c_m for $\overline{\alpha} = 30^\circ$.   (f) c_m for $\overline{\alpha} = 45^\circ$.

Figure 4.35: Variation the aerodynamic coefficients within a pitching period T for small amplitude plate oscillations around a mean angle of attack of 30° and 45° at $\mathrm{Re} = 4 \times 10^4$ with DMD pre-processing: indirect calculation (symbols) and direct measurements (thick continuous line). The error bars correspond to the sensitivity of the results to the control surface used in the indirect method.

4.6.3.3 Three-dimensional flow and phase-averaging

As reported by David et al. (2009), these unsatisfactory estimations provided by the indirect methods can be partially explained by three-dimensional effects. Three-dimensional features are induced by massive flow separation and lead to a decrease of the flow coherence along the span, as discussed in Sec. 4.4.3. Additionally, experimental measurements and DDES simulations show that the flow strongly varies from one shedding period to the next, and that the shedding phenomenon does not occur at a precise constant frequency.

Dye visualization was performed for a plate undergoing small forced oscillations. Because the flow visualization is not synchronized with the plate kinematics and because the amplitude and period of oscillations are very small, it is challenging to identify the different phases of the cycle in the recorded movies. This problem is overcome using CFD simulations. Figure 4.36 presents the pressure coefficient at the mid-span of the plate at the same phase of the pitching motion but for different cycles. Each of the Figs. 4.36a to 4.36d depicts a pressure field that corresponds to a large LE vortex standing along the upper surface and a TE vortex being shed into the wake. Nonetheless, the location of the flow features is very different for the four cycles considered here.

This lack of coherence between the snapshots is a source of noise in the averaged PIV fields. Moreover, the two sets of data for the top and bottom sides of the plate do not match well in the overlapping regions, introducing additional noise in the velocity field during the stitching phase. These different noise contributions can explain why the application of INSE and NOCA methods leads to the unsatisfactory results depicted in Figs. 4.34 and 4.35. The convergence study performed on the number of snapshots that are used to compute the PIV flow fields at each phase supports these conclusions (see Sec. 4.5.1). In particular, increasing the number of snapshots decreases the noise in the estimated load response. Therefore, better results can be expected if a larger number of PIV images is used for each phase.

Finally, the case of the plate undergoing large amplitude oscillations is investigated for comparison purposes. Figure 4.37 depicts dye flow visualization images at a specific phase of the motion for four different cycles. It can be observed that the the location of the flow features is much more similar from one cycle to the next compared to the small amplitude pitching case (see Fig. 4.36). This is due to the large amplitude of the imposed pitching motion that increases flow coherence along the span. The resulting flow is more two-dimensional, which explains the more accurate results obtained in Sec. 4.6.1.

4.7 Conclusions and future work

This chapter has investigated the indirect calculation of two-dimensional loads from PIV measurements in the context of detached flows. Two formulations of the momentum balance have been studied: one using the integral Navier-Stokes equations and a second that uses the flux equation proposed by Noca et al. (1999). These methodologies have been tested on two main cases: the flow around a flat plate undergoing a large amplitude pitching motion and the flow around a flat plate at large incidence. The results obtained through the INSE and the NOCA methods have been compared to each other and to fluid dynamic loads acquired directly. Moreover, the effects of the user-defined parameters related to the two formulations and the PIV measurements have been determined. Finally, numerical simulations have been performed to further study the different flows and understand the limitation of the indirect methodologies.

The combined experimental and numerical approach has led to a better insight in the flow dynamics for the cases considered.

- The flow around the plate undergoing large amplitude pitching oscillations is characterized by load coefficients larger than those generated by a static plate at similar incidence. This corresponds to the dynamic stall phenomenon. The flow is attached during approximately half of the cycle, while the incidence increases. During this phase, a large vortex forms at the leading edge, grows and is convected downstream. As the incidence angle decreases, the leading edge vortex is shed into the wake. Then, the trailing edge free shear layer rolls to form a vortex which is subsequently also shed. This flow is mostly two-dimensional and periodic in time.
- The flow around a plate at large incidence angle consists of the growth, convection and shedding of both leading and trailing edge vortex. The leading edge vortex emerges from several vortices that grew in the leading edge free shear layer. They agglomerate and merge into a large vortex that covers the entire upper surface of the plate. As the leading edge vortex is shed into the wake, a smaller vortex grows at the trailing edge from the rolling up of the shear layer. The trailing edge vortex is shed into the wake as a new leading edge vortex starts to develop. Therefore, the interaction between the two vortices is critical and determine their respective size and dynamics. This type of flow exhibits a lack of coherence

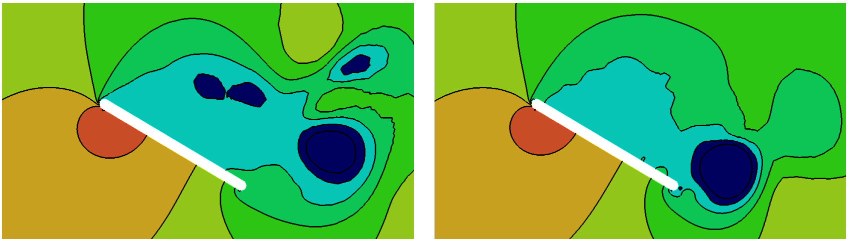

(a) 32nd pitching cycle. (b) 39th pitching cycle.

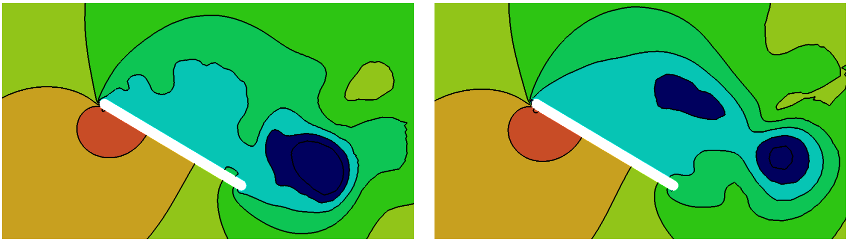

(c) 46th pitching cycle. (d) 54th pitching cycle.

Figure 4.36: Pressure coefficient field on a xy-plane located at mid-span of a plate undergoing small oscillations around $\overline{\alpha} = 30^\circ$. The results are obtained through DDES with a span length $s = 7.5c$ and the iso-surfaces corresponds to C_p varying from -1.8 to 1 (blue to red). The phase $\varphi = 0.25$ is presented for different cycles.

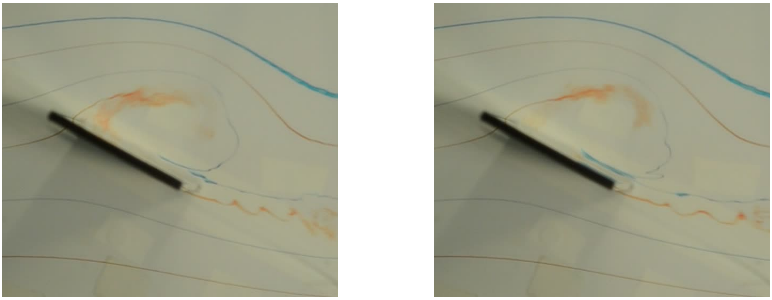

(a) 3rd pitching cycle. (b) 4th pitching cycle.

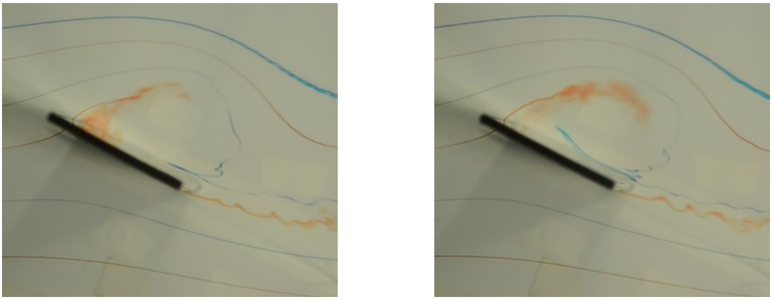

(c) 5th pitching cycle. (d) 6th pitching cycle.

Figure 4.37: Dye visualization of the flow around a plate undergoing large amplitude oscillations around $\overline{\alpha} = 0^\circ$. The phase $\varphi = 0.3$ corresponding to $\alpha = 28.5^\circ$ is presented for different cycles.

in the third dimension that increases with the span of the plate. Because of these three-dimensional effects, the flow is not perfectly periodic in time.

The NOCA and INSE methodologies have been applied to these test cases and the effects of the different user-defined parameters have been investigated. From these studies, several conclusions have been drawn.

- The indirect methods are able to provide an accurate estimation of the mean load coefficients for the detached flows considered. The phase-averaged time response of the load coefficients can be determined with reasonable accuracy if the phase-averaged PIV velocity fields are sufficiently converged. In the present work, satisfying results were obtained for the large amplitude pitching plate test case, which is mostly two-dimensional. However, even a qualitatively meaningful time response could not be obtained for the plate at large incidence angle. It has been argued that the three-dimensional effects result in poorly converged phase-averaged PIV fields. The noise in these fields is most likely amplified by the stitching procedure needed to obtain the required view of the flow around the plate.
- It has been demonstrated that the INSE and NOCA methodologies behave similarly. In particular, the pitching moment is estimated with the same accuracy both through the INSE method and the new formulation derived in the present work. However, to obtain the best performance of the indirect computation methodologies, the user-defined parameters have to be chosen carefully.
- The sensitivity analysis performed on the user-defined parameters has shown that the accuracy of the time response estimated indirectly is very sensitive to the convergence of the phase-averaged PIV fields. Moreover, as previously reported by Gharali and Johnson (2014), the downstream edge of the control surface $\mathcal{S}$ should be located as far as possible from the vortical zone. If this is not possible, it has been shown that the accuracy of the indirect calculation decreases when a vortex crosses this edge. This is mostly due to errors appearing in the estimation of the pressure contribution and can be improved by carefully choosing the threshold value $\Gamma_2^{\mathrm{thres}}$ and the origin of the location vector x_i in the NOCA and the INSE formulations, respectively.

This work has been limited by several simplifications and hypotheses. Moreover, additional studies could be performed.

- The three-dimensional features of the flow around a plate at large incidence have been studied only qualitatively. The DDES simulations were shown to provide accurate predictions that could be used to further investigate this aspect of the flow.
- The determination of the pressure contribution is critical to the accuracy of the load estimation. The pressure correction performed in the INSE methodology could be improved by using the knowledge of the flow dynamics. In particular, a new correction method could be designed by applying the INSE formulation on numerical results for which the pressure and the loads are known. A weighted-correction based on flow features such as Γ_2, ω_z or $\partial_i p$ could be considered. To further improve the load estimation provided by the NOCA method, the origin of the location vector x_i could be set at the vortex core and then be function of time. Additionally, the post-processing stitching step applied to PIV data and required to obtain a complete view of the flow around the body should be avoided as it introduces additional noise. Therefore, the PIV setup should be designed to prevent the shadow created on one side of the body. To this end, a transparent model could be used or the laser beam could be split to illuminate both sides of the body. If adaptations of the experimental setup are not possible, the stitching process could be improved. A possible procedure is the use of a sub-grid translation of the averaged PIV fields acquired at each side of the body. The rotation and deformation of the PIV fields could also be considered.

- Finally, two-dimensional flow has been assumed all along the present work. For the phenomena exhibiting significant three-dimensional effects, a three-dimensional instantaneous approach should be considered. Schneiders et al. (2016) and Laskari et al. (2016) reported promising results for the determination of the instantaneous pressure field from 3C3D PIV.

CHAPTER 5

Conclusion

The main focus of this thesis was the study of detached flows around bluff bodies. As discussed in Chap. 1, this aspect is of primary importance in wind engineering where the knowledge of building aerodynamics is needed to understand and control undesirable aeroelastic phenomena. In the present work, two canonical geometries have been investigated: a 4:1 rectangular cylinder and a flat plate at large incidence or undergoing large amplitude pitching motion. The rectangular cylinder geometry has been chosen as it approximates several elongated civil engineering structures such as bridges and towers. Both numerical and experimental approaches have been applied to this study. The flows around a flat plate with different configurations have been selected as test cases to assess an indirect load measurement technique that uses PIV velocity fields. In particular, the capabilities of the two-dimensional INSE and NOCA approaches, both based on the momentum balance, have been tested. These indirect approaches are well suited for analyzing aeroelastic phenomena where the structural response of the moving bodies contaminates the direct load measurements. In addition to PIV experiments, numerical simulations have been used to better understand the limitations of the indirect methodologies.

The rectangular cylinder at several incidence angles has been studied in Chap. 3 through dynamic pressure measurements along a cross-section combined with URANS and DDES simulations. The conclusions and perspectives of this work have been discussed in detail in Sec. 3.9. In summary, this simple geometry involves complex flow separation-reattachment phenomena that is highly sensitive to the freestream velocity. In particular, the mean lift slope $\overline{c_l}_\alpha$ increases rapidly with the Reynolds number in the range $3.1 \times 10^4 \leqslant \mathrm{Re} \leqslant 7.6 \times 10^4$. This increase was found to be linked to an increase/decrease of the suction along the upper/lower surfaces of the rectangular cylinder, respectively. Moreover, it has been shown that the detached flow around a 4:1 cylinder is very challenging to capture numerically. In particular, both URANS and DDES simulations overestimate the experimental lift. This is mainly due to an overestimation of the suction along the upper surface. Despite discrepancies in the pressure intensity, URANS is able to accurately estimate the main features of the flow for incidences lower than the stall angle. In particular, the global spatio-temporal variation of vortices is correctly captured. It has been shown that DDES is surprisingly not able to provide an accurate estimation of the flow as it incorrectly estimates the chordwise location of vortices. However, DDES performs better for post-stall angles as it captures the characteristic decrease in suction along the upper surface and the resulting decrease in lift. The original contributions of the research work presented in Chap. 3 are:

- to provide experimental measurements for different incidence angles of the spatio-temporal pressure coefficient along a cross-section of the 4:1 rectangular cylinder;
- to demonstrate that the variation of the mean lift coefficient with Reynolds number is not caused by a variation in the reattachment point location along the lower surface, but rather due to a modification of the size/strength of the corresponding mean recirculation bubble;

- to show that DDES is not able to correctly estimate the flow around a 4:1 rectangular cylinder neither at zero nor higher incidences, at least for the classical numerical setup considered here.

Finally, several questions remain open and additional studies should be performed to further understand key aspects.

- Where does the high sensitivity of the flow come from?
  Additional studies should be performed to better identify the causes of this sensitivity and the different parameters influencing the flow. In particular, PIV experiments should be conducted to investigate the variation of the flow features with the Reynolds number and then determine the cause of the strong variation in lift. The effect of the freestream turbulence should also be further studied and the uncertainties associated with experimental measurements should be considered.
- Why is DDES not able to accurately estimate the flow?
  URANS performs better than DDES to simulate the flow around the rectangular cylinder although the latter should provide a more accurate representation of turbulence and thus of the flow features. Further work should be carried out to understand the causes of DDES failure and to determine an accurate numerical approach. This work has shown that the DDES results strongly differ when varying the maximum grid spacing in the "focus region" Δ_0. Consequently, additional simulations could be performed with a finer Δ_0. However, LES results reported by Patruno et al. (2016) for a 5:1 rectangular cylinder also exhibit significant discrepancies compared to experiments. This seems to suggest that even a finer mesh and a more accurate approach would not lead to better results. The effect of numerical dissipation, which Mannini et al. (2011) identified as a key factor, of the freestream turbulence and of the span length could also be investigated.

Chapter 4 discussed the capabilities of the INSE and NOCA approaches to indirectly estimate the loads by using PIV velocity fields. The conclusions are detailed in Sec. 4.7. To summarize, it has been demonstrated that the two indirect methodologies perform similarly for all the cases considered. In particular, the new formulation established in Sec. 2.3.3.2 for the calculation of the pitching moment provides similar results to the INSE method. Both the INSE and NOCA approaches are able to accurately estimate the mean loads for the detached flows considered here. The phase-averaged time response can also be estimated with reasonable accuracy as long as the corresponding PIV fields are sufficiently converged, i.e. for a sufficient number of PIV snapshots acquired at the same phase. This has been demonstrated in the context of the flow around a flat plate at high incidence. The imposed low amplitude pitching motion at the shedding frequency allows the measurement of phase-averaged PIV fields. Because of its low amplitude, this imposed motion does not significantly impact the flow, which has been shown to remain three-dimensional and not perfectly periodic. It was found that the accuracy of the load estimates calculated by the two indirect methods is generally negatively impacted by the decrease in spanwise flow coherence due to three-dimensional effects and the lack of a clear single shedding frequency. In that respect, the present results could be improved by using more snapshots, and thus phase-averaged PIV fields that are better converged. The magnification of the camera in the PIV setup has been shown to be critical for ensuring sufficient spatial resolution. A value of 18 pixels/mm seems to be sufficient to obtain accurate results for the flows investigated in this work. The number of phases in a cycle should be adapted to the time response of the flow. To this end, the temporal resolution could be varied within the cycle based on a preliminary analysis of the flow. The effects of additional user-defined parameters have been investigated. It has been shown that the location of the control surface downstream edge has the most significant effect on the accuracy of the indirect load estimations, particularly whenever it is crossed by a vortex. The indirect approaches perform better if this downstream edge is located far away from the vorticity zones. However, this strategy is not always possible because of the limited size of the PIV window. For such cases, the user-defined parameters impacting the estimation of the pressure contribution have to carefully chosen. More precisely, the threshold value $\Gamma_2^{\mathtt{thres}}$ in the INSE method should be increased as the downstream edge moves closer to the body. Moreover, the origin of the location vector x_i in the NOCA method should be defined as close as possible to the vortex center. Finally, as far as it is possible, the PIV setup should be designed to provide a complete view of the flow around the body. This removes the need for an additional post-processing step that introduces additional noise in the measurements. In summary, the original contributions of the present work are:

- the derivation and validation of a new formulation for the indirect calculation of moments that does not require the knowledge of pressure, in the same spirit as the NOCA method for the force estimation;
- the detailed comparison of the INSE and NOCA capabilities using several detached flows;
- practical guidelines for setting the user-defined parameters of the indirect estimation, and a quantitative assessment of the impact of these user-defined parameters, in particular of the origin of the location vector x_i in the NOCA approach.

Finally, the two indirect methodologies could be further improved. In particular, a pressure correction step that is based on the flow physics could be developed for the INSE approach by using the knowledge of the flow features. A possible strategy towards this goal would be to rely on numerical simulations as they provide information about all flow quantities everywhere. Additionally, the control surface, and the origin of the location vector x_i required in the NOCA method could vary with the vortex core location.

This thesis has demonstrated the added value of integrating numerical and experimental studies. The two approaches are complementary and enable a deeper understanding of the physics. The comparison of numerical and experimental results obtained for the flow around a flat plate at high incidence has demonstrated that the DDES approach is able to provide an accurate estimation of the flow features. Therefore, the pressure and velocity fields provided by the simulations can be used to further study specific aspects that would be elusive to available experimental techniques, such as the three-dimensional effects or the origin of the frequency content. In turn, the additional physical insights provided by CFD can be used to design an experiment focused on these aspects. On the other hand, one should be very cautious with simulations without experimental validation. Relying solely on numerical results can lead to incorrect conclusions. This is well illustrated by the two cases considered here. While DDES leads to good results for the flat plate at high angle of attack, it fails to provide accurate predictions in the case of the rectangular cylinder. Both cases involve massively separated flow, for which DDES should yield good predictions, or at least better than those obtained by URANS. This is clearly not the case for the rectangular cylinder, and, without experimental validation, the DDES results would have been considered as the most accurate ones. This clearly demonstrates the need for validation, even for simple geometries.

In conclusion, this thesis provides original and useful contributions towards a better understanding of separated flows around bluff bodies. Nevertheless, much remains to do, especially in the context of realistic civil engineering applications that involve higher Reynolds numbers and more complex geometries.

APPENDIX A

Indirect calculation of loads from PIV measurements

A.1 Vector identities

The derivation of Noca's flux equation involves the following vector identities

$$\begin{aligned}
\mathbf{a} &= \nabla\cdot(\mathbf{a}\mathbf{x}) - (\nabla\cdot\mathbf{a})\,\mathbf{x}, && \text{(A.1)}\\
\mathbf{x}\times(\nabla\times\mathbf{a}) &= (\mathcal{N}-1)\mathbf{a} + \nabla(\mathbf{x}\cdot\mathbf{a}) - \nabla\cdot(\mathbf{x}\mathbf{a}), && \text{(A.2)}\\
\nabla\times(\mathbf{x}\times\phi\mathbf{I}) &= -\,\phi(\mathcal{N}-1)\mathbf{I} - (\mathbf{x}\cdot\nabla\phi)\mathbf{I} + \mathbf{x}\nabla\phi, && \text{(A.3)}\\
\mathbf{x}\times(\mathbf{n}\times[\mathbf{a}\times\mathbf{x}]) &= \mathbf{n}\cdot(\mathbf{x}\,[\mathbf{x}\times\mathbf{a}]) && \text{(A.4)}\\
\mathbf{x}\times(\mathbf{x}\times[\mathbf{a}\times\mathbf{n}]) &= \mathbf{n}\cdot\left(\{[\mathbf{a}\times\mathbf{I}]\cdot\mathbf{x}\}\,\mathbf{x} - \|\mathbf{x}\|^2\,[\mathbf{a}\times\mathbf{I}]\right) && \text{(A.5)}\\
\mathbf{x}\times(\mathbf{n}\times[\mathbf{a}\times\mathbf{b}]) &= \mathbf{n}\cdot(\mathbf{b}\,[\mathbf{x}\times\mathbf{a}] - \mathbf{a}\,[\mathbf{x}\times\mathbf{b}]) && \text{(A.6)}\\
\mathbf{x}\times(\mathbf{n}\times\mathbf{a}) &= \mathbf{n}\,(\mathbf{x}\cdot\mathbf{a}) - \mathbf{n}\cdot(\mathbf{x}\mathbf{a}) && \text{(A.7)}
\end{aligned}$$

where $\mathbf{x}$ is the location vector, $\mathbf{a}$, $\mathbf{b}$ and ϕ are arbitrary vectors and scalar, respectively, $\mathbf{I}$ is the unit tensor and $\mathcal{N}$ is the number of spatial dimensions. These identities can be proven straightforwardly using index notation.

A.2 Derivation of Noca's flux equation

In tensor notation, the Noca's flux equation is written as

$$\mathbf{F} = \oint_{\mathcal{S}_\infty} \mathbf{n}\cdot\left(\boldsymbol{\gamma}^{Ft} + \boldsymbol{\gamma}^{Fp} - \rho\mathbf{u}\mathbf{u} + \boldsymbol{\tau}\right)\,\mathrm{d}\mathcal{S} - \mathrm{d}_t \oint_{\mathcal{S}_b} \mathbf{n}\cdot(\rho\mathbf{u}\mathbf{x})\,\mathrm{d}\mathcal{S}, \tag{A.8}$$

with

$$\begin{aligned}
\boldsymbol{\gamma}^{Ft} &= -\,\rho(\partial_t\mathbf{u})\mathbf{x}\\
\boldsymbol{\gamma}^{Fp} &= \frac{\rho}{2}\|\mathbf{u}\|^2\mathbf{I} + \frac{\rho}{\mathcal{N}-1}\left[\boldsymbol{\omega}(\mathbf{x}\times\mathbf{u}) - \mathbf{u}(\mathbf{x}\times\boldsymbol{\omega})\right]\\
&\quad - \frac{\rho}{\mathcal{N}-1}\left[(\mathbf{x}\cdot\partial_t\mathbf{u})\mathbf{I} - \mathbf{x}\partial_t\mathbf{u}\right]\\
&\quad + \frac{1}{\mathcal{N}-1}\left[\mathbf{x}\cdot(\nabla\cdot\boldsymbol{\tau})\mathbf{I} - \mathbf{x}(\nabla\cdot\boldsymbol{\tau})\right]
\end{aligned} \tag{A.9}$$

where $\mathbf{u}$ is the velocity, $\boldsymbol{\omega}$ the vorticity, $\mathbf{x}$ the location vector, ρ the constant density, $\boldsymbol{\tau}$ the viscous stress and $\mathbf{I}$ the unit tensor. The space dimensionality $\mathcal{N}$ can be 2 or 3. It is assumed that there is no flow through the body surface $\mathcal{S}_b$. Moreover, the external surface $\mathcal{S}_\infty$ unlike $\mathcal{S}_b$ is considered constant in time. As sketched in Fig. A.1, the unit vector normal to the surface is defined positive outward.

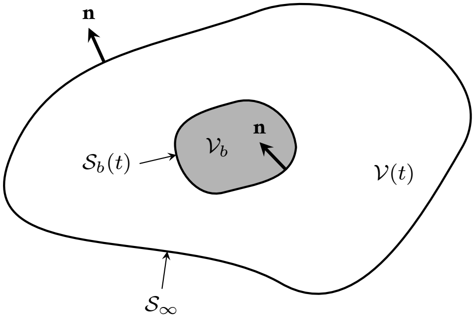

Figure A.1: Domain of integration for the determination of aerodynamic forces on a body (in dark gray) using momentum-based approaches.

With these assumptions, the Noca's flux equation can be derived from the integral formulation of the Navier-Stokes equations,

$$\mathbf{F} = -\mathrm{d}_t \int_{\mathcal{V}} \rho \mathbf{u} \, \mathrm{d}\mathcal{V} + \oint_{\mathcal{S}_\infty} \mathbf{n} \cdot \left[-p\mathbf{I} - \rho \mathbf{u}\mathbf{u} + \boldsymbol{\tau} \right] \, \mathrm{d}\mathcal{S}, \tag{A.10}$$

where p is the pressure and $\mathcal{V}$ the volume enclosed between the surfaces $\mathcal{S}_\infty$ and $\mathcal{S}_b$.

The derivation done by Noca et al. (1999) consists of two steps: first the elimination of pressure, then the elimination of volume integrals. Note that the original derivation was done for the general case where the surface $\mathcal{S}_\infty$ is a function of time and where there can have a flow through the body.

Elimination of the pressure

Using the so-called pressure identity

$$(\mathcal{N} - 1) \oint_{\mathcal{S}} p\mathbf{n} \, \mathrm{d}\mathcal{S} = - \oint_{\mathcal{S}} \mathbf{x} \times (\mathbf{n} \times \nabla p) \, \mathrm{d}\mathcal{S}, \tag{A.11}$$

derived in Sec. A.3 and the differential form of Navier-Stokes equations, the pressure gradient can be written as

$$\nabla p = -\rho \partial_t \mathbf{u} - \nabla\left(\frac{\rho}{2} \|\mathbf{u}\|^2\right) + \rho \mathbf{u} \times \boldsymbol{\omega} + \nabla \cdot \boldsymbol{\tau}, \tag{A.12}$$

as $(\mathbf{u}\cdot\nabla)\mathbf{u} = \nabla(\frac{1}{2}\mathbf{u}\cdot\mathbf{u}) - \mathbf{u}\times\boldsymbol{\omega}$. The pressure term becomes then

$$\begin{aligned}
-\oint\limits_{\mathcal{S}_\infty} p\mathbf{n}\,\mathrm{d}\mathcal{S} = &-\frac{\rho}{\mathcal{N}-1}\oint\limits_{\mathcal{S}_\infty}\mathbf{x}\times(\mathbf{n}\times\partial_t\mathbf{u})\ \mathrm{d}\mathcal{S}\\
&-\frac{\rho}{2\,(\mathcal{N}-1)}\oint\limits_{\mathcal{S}_\infty}\mathbf{x}\times\left(\mathbf{n}\times\nabla\|\mathbf{u}\|^2\right)\ \mathrm{d}\mathcal{S}\\
&+\frac{\rho}{\mathcal{N}-1}\oint\limits_{\mathcal{S}_\infty}\mathbf{x}\times(\mathbf{n}\times[\mathbf{u}\times\boldsymbol{\omega}])\ \mathrm{d}\mathcal{S}\\
&+\frac{1}{\mathcal{N}-1}\oint\limits_{\mathcal{S}_\infty}\mathbf{x}\times(\mathbf{n}\times[\nabla\cdot\boldsymbol{\tau}])\ \mathrm{d}\mathcal{S}.
\end{aligned}$$

Then, applying again the pressure identity in conjunction with Eqs. (A.6) and (A.7), the integral Navier-Stokes equations (A.10) can be written as

$$\mathbf{F} = -\mathrm{d}_t\int_{\mathcal{V}}\rho\mathbf{u}\,\mathrm{d}\mathcal{V} + \oint\limits_{\mathcal{S}_\infty}\mathbf{n}\cdot\left[\boldsymbol{\gamma}^{Fp} - \rho\mathbf{u}\mathbf{u} + \boldsymbol{\tau}\right]\ \mathrm{d}\mathcal{S},$$

with

$$\begin{aligned}
\boldsymbol{\gamma}^{Fp} = &\frac{\rho}{2}\|\mathbf{u}\|^2\mathbf{I} + \frac{\rho}{\mathcal{N}-1}\left[\boldsymbol{\omega}(\mathbf{x}\times\mathbf{u}) - \mathbf{u}(\mathbf{x}\times\boldsymbol{\omega})\right]\\
&-\frac{\rho}{\mathcal{N}-1}\left[(\mathbf{x}\cdot\partial_t\mathbf{u})\mathbf{I} - \mathbf{x}\partial_t\mathbf{u}\right]\\
&+\frac{1}{\mathcal{N}-1}\left[\mathbf{x}\cdot(\nabla\cdot\boldsymbol{\tau})\mathbf{I} - \mathbf{x}(\nabla\cdot\boldsymbol{\tau})\right].
\end{aligned}$$

Unlike the integral form of the Navier-Stokes equations, it does not explicitly require the pressure. However, an integration over the entire volume $\mathcal{V}$ remains. The purpose of the second step of the derivation is to transform this volume integral into surface integrals.

Elimination of the volume integral

The volume integral appearing in Eq. (A.10) can be expressed in terms of surface integrals using Gauss' theorem and taking advantage of vector identity (A.1). This leads successively to

$$\begin{aligned}
-\mathrm{d}_t\int_{\mathcal{V}}\mathbf{u}\,\mathrm{d}\mathcal{V} &= -\,\mathrm{d}_t\oint\limits_{\mathcal{S}_\infty+\mathcal{S}_b}\mathbf{n}\cdot(\mathbf{u}\mathbf{x})\ \mathrm{d}\mathcal{S},\\
&= \oint\limits_{\mathcal{S}_\infty}\mathbf{n}\cdot\boldsymbol{\gamma}^{Ft}\,\mathrm{d}\mathcal{S} - \mathrm{d}_t\oint\limits_{\mathcal{S}_b}\mathbf{n}\cdot(\rho\mathbf{u}\mathbf{x})\,\mathrm{d}\mathcal{S},
\end{aligned}$$

with

$$\boldsymbol{\gamma}^{Ft} = -\rho(\partial_t\mathbf{u})\mathbf{x}.$$

Noca's flux equation is thus retrieved.

Simplification in case of rigid body motion

In case of a rigid body motion, the time derivative of the body surface integral appearing in Eq. (A.8) can be expressed as a function of the motion parameters only (Noca, 1997). If the body displacement can be decomposed into a rigid translation at velocity $\mathbf{u}^t$ and a rotation at angular velocity $\dot{\boldsymbol{\alpha}}^r$, defined negative according to right-hand rule, the velocity of the body surface $\mathbf{u}^b$ is

$$\mathbf{u}^b = \mathbf{u}^t + \dot{\boldsymbol{\alpha}}^r \times (\mathbf{x}^r - \mathbf{x}), \tag{A.13}$$

where $\mathbf{x}^r$ is the location vector of the center of rotation. Using the Gauss' theorem, the term of interest becomes successively,

$$\begin{aligned}-\mathrm{d}_t \oint_{\mathcal{S}_b} \rho \mathbf{n} \cdot (\mathbf{u}\mathbf{x})\, \mathrm{d}\mathcal{S} &= \mathrm{d}_t \int_{\mathcal{V}_b} \rho \nabla \cdot \left(\mathbf{u}^b \mathbf{x}\right)\, \mathrm{d}\mathcal{V}, \\ &= \rho \mathrm{d}_t \int_{\mathcal{V}_b} \underbrace{\nabla \cdot \left[\mathbf{u}^t \mathbf{x}\right]}_{I} + \underbrace{\nabla \cdot \left[\left(\dot{\boldsymbol{\alpha}}^r \times \{\mathbf{x}^r - \mathbf{x}\}\right) \mathbf{x}\right]}_{II}\, \mathrm{d}\mathcal{V},\end{aligned}$$

where $\mathcal{V}_b$ is the body volume as sketched in Fig. A.1. Examining the two terms separately leads to

$$\begin{aligned} I &= \mathbf{u}^t, \\ II &= \dot{\boldsymbol{\alpha}}^r \times (\mathbf{x}^r - \mathbf{x}), \end{aligned}$$

since $\mathbf{u}^t$ and $\dot{\boldsymbol{\alpha}}^r$ and $\mathbf{x}^r$ are constant in space. Moreover, $\mathbf{u}^t$ and $\dot{\boldsymbol{\alpha}}^r$ are constant on $\mathcal{V}_b$, so that

$$-\mathrm{d}_t \oint_{\mathcal{S}_b} \rho \mathbf{n} \cdot (\mathbf{u}\mathbf{x})\, \mathrm{d}\mathcal{S} = \rho \mathrm{d}_t \left[\mathbf{u}^t \underbrace{\int_{\mathcal{V}_b} \mathrm{d}\mathcal{V}}_{III} + \underbrace{\int_{\mathcal{V}_b} (\mathbf{x} - \mathbf{x}^r)\, \mathrm{d}\mathcal{V}}_{IV} \times \dot{\boldsymbol{\alpha}}^r \right],$$

where III is the body volume and IV the first moment of volume calculated with respect to the pivot point. The latter can be linked to the position of the centroid $\overline{\mathbf{x}}^r$ of $\mathcal{V}_b$ with respect to the pivot point

$$\overline{\mathbf{x}}^r \mathcal{V}_b = \int_{\mathcal{V}_b} (\mathbf{x} - \mathbf{x}^r)\, \mathrm{d}\mathcal{V}.$$

Finally, since only $\mathbf{u}^t$ and $\dot{\boldsymbol{\alpha}}^r$ vary in time, the body surface integral becomes

$$-\mathrm{d}_t \oint_{\mathcal{S}_b} \rho \mathbf{n} \cdot (\mathbf{u}\mathbf{x})\, \mathrm{d}\mathcal{S} = \rho \mathcal{V}_b \mathrm{d}_t \mathbf{u}^t + \rho \mathcal{V}_b \overline{\mathbf{x}}^r \times \mathrm{d}_t \dot{\boldsymbol{\alpha}}^r.$$

A.3 Derivation of the pressure identity

The pressure identity Eq. (A.11)

$$(\mathcal{N} - 1) \oint_{\mathcal{S}} p \mathbf{n}\, \mathrm{d}\mathcal{S} = - \oint_{\mathcal{S}} \mathbf{x} \times (\mathbf{n} \times \nabla p)\, \mathrm{d}\mathcal{S} \tag{A.11}$$

rewritten here for convenience, can be derived from the Impulse-Momentum identity for a simply-connected domain (Noca et al., 1997). If the domain is multiply-connected, this derivation fails since the volume integrals are ill-defined in some parts of $\mathcal{V}$ (Noca et al., 1997). Another derivation starts from the vector identity Eq. (A.3) multiplied by the normal vector $\mathbf{n}$ and integrated over a surface $\mathcal{S}$:

$$\begin{aligned}\int_{\mathcal{S}} \mathbf{n} \cdot [\nabla \times (\mathbf{x} \times \phi \mathbf{I})]\, \mathrm{d}\mathcal{S} = &- (\mathcal{N} - 1) \int_{\mathcal{S}} \phi \mathbf{n}\, \mathrm{d}\mathcal{S} \\ &- \int_{\mathcal{S}} \mathbf{n}(\mathbf{x} \cdot \nabla \phi) - (\mathbf{n} \cdot \mathbf{x}) \nabla \phi\, \mathrm{d}\mathcal{S}.\end{aligned}$$

The integrand of the second term on the right-hand side can be transformed using Eq. (A.7)

$$\mathbf{n}(\mathbf{x}\cdot\nabla\phi)-(\mathbf{n}\cdot\mathbf{x})\nabla\phi=\mathbf{x}\times(\mathbf{n}\times\nabla\phi).$$

In case of a single-valued scalar field ϕ, the left-hand side term becomes, using Stokes' theorem,

$$\oint_{\mathcal{S}}\mathbf{n}\cdot[\nabla\times(\mathbf{x}\times\phi\mathbf{I})]\ \mathrm{d}\mathcal{S}=\oint_{\mathcal{C}}(\mathbf{x}\times\phi\mathbf{I})\cdot\mathbf{t}\,\mathrm{d}\mathcal{C},$$

where $\mathbf{t}$ is tangent to curve $\mathcal{C}$. If the surface $\mathcal{S}$ is closed, $\mathcal{C}$ tends infinitesimally to a point, so that the above integral vanishes. Using these simplifications, the identity

$$(\mathcal{N}-1)\oint_{\mathcal{S}}\phi\mathbf{n}\,\mathrm{d}\mathcal{S}=-\oint_{\mathcal{S}}\mathbf{x}\times(\mathbf{n}\times\nabla\phi)\,\mathrm{d}\mathcal{S}$$

is obtained and, with $\phi=p$, the pressure identity is retrieved.

A.4 Derivation of extended pressure identity

The extended pressure identity can be written as

$$-\oint_{\mathcal{S}}p\,(\mathbf{n}\times\mathbf{x})\ \mathrm{d}\mathcal{S}=\frac{1}{\mathcal{N}}\oint_{\mathcal{S}}\mathbf{x}\times[\mathbf{x}\times(\nabla p\times\mathbf{n})]\ \mathrm{d}\mathcal{S},\tag{A.14}$$

Note that the domain enclosed by $\mathcal{S}$ can be multiply-connected.

The identity (A.14) can be derived from the pressure identity (A.11). Therefore, if $\mathbf{r}$ is an arbitrary position vector and assuming an arbitrary scalar field ψ_{pi} so that $\psi_{pi}=\phi r_q\epsilon_{piq}$, it can be written successively

$$\begin{aligned}(\mathcal{N}-1)\oint_{\mathcal{S}}\phi\,(\mathbf{n}\times\mathbf{r})\ \mathrm{d}\mathcal{S} &= (\mathcal{N}-1)\oint_{\mathcal{S}}\phi n_i r_q\epsilon_{piq}\ \mathrm{d}\mathcal{S},\\ &= (\mathcal{N}-1)\oint_{\mathcal{S}}\psi_{pi}n_i\ \mathrm{d}\mathcal{S},\\ &= -\oint_{\mathcal{S}}x_j n_l\partial_m\psi_{pi}\epsilon_{ijk}\epsilon_{klm}\ \mathrm{d}\mathcal{S}.\end{aligned}$$

Using

$$\partial_m\psi_{pi}=(r_q\partial_m\phi+\phi\delta_{mq})\,\epsilon_{piq},$$

the identity becomes

$$(\mathcal{N}-1)\oint_{\mathcal{S}}\phi\,(\mathbf{n}\times\mathbf{r})\ \mathrm{d}\mathcal{S}=-\oint_{\mathcal{S}}\mathbf{r}\times[\mathbf{x}\times(\nabla\phi\times\mathbf{n})]\ \mathrm{d}\mathcal{S}-\oint_{\mathcal{S}}\phi\,(\mathbf{n}\times\mathbf{x})\ \mathrm{d}\mathcal{S}.$$

Finally, assuming that $\mathbf{r}=\mathbf{x}$ and with $\phi=p$, Eq. (A.14) is retrieved.

APPENDIX B

Detached flow around a 4:1 rectangular cylinder

B.1 Sensitivity analysis on the dynamic pressure correction

Dynamic pressure is measured with a multi-channel DPMS transducer which is connected to the pressure taps with tubes. Each tube forms a pneumatic line that acts as a filter and causes amplitude and phase distortions of the unsteady pressure signal measured. To retrieve the original unsteady pressure, a correction should be applied and the methodology proposed by Bergh and Tijdeman (1965) is used for that purpose. As shown by Rigo (2017), this method performs accurately when applied to data acquired with the particular DPMS transducer used for the experiments described in Sec. 3.2. The correction is based on a FRF modeling the pneumatic line by linking the true and measured C_p. The theoretical expression of this FRF depends on many physical parameters that are subject to uncertainty. The sensitivity of the corrected C_p to these uncertainties is studied in this section.

Bergh and Tijdeman (1965) identified the most significant parameters appearing in the FRF as the atmospheric pressure p_{atm}, the pressure transducer volume V_s, the tube length l_t and the tube internal diameter d_t. Their nominal values for the experiments described in Sec. 3.2 are presented in Tab. B.1 and the results discussed in Chap. 3 were established on this basis. However, these parameters are subject to uncertainty. In particular, V_s is not known precisely, measurement errors impact p_{atm}, l_t and d_t, and p_{atm} could vary during the experiment. Additionally, Bergh and Tijdeman (1965) showed that the values of the physical parameters may have to be slightly modified to obtain a theoretical FRF modeling accurately the pneumatic line. A sensitivity analysis is then conducted to determine how uncertainties impact C_p. First, the variation range of each

Parameter set	l_t [m]	d_t [mm]	p_{atm} [Pa]	V_s [mm^3]
Nominal values	1.34	1.32	99 250	0
LENGTH	$1.33 - 1.35$	1.32	99 250	0
DIAMETER	1.34	1.25	99 250	0
PRESSURE	1.34	1.32	$98\,250 - 100\,250$	0
VOLUME	1.34	1.32	99 250	150
MIXED A	1.35	1.25	98 250	150
MIXED B	1.33	1.32	100 250	0

Table B.1: Nominal values of physical parameters and parameter sets corresponding to the sensitivity analysis.

physical parameter is determined. Then, the different FRF associated with the boundaries of these ranges are calculated, and the corresponding corrections are applied to the measured C_p. Finally, the effects of uncertainties are analyzed through the variation of C_p'. Initially, the variation of each parameter is considered separately. In a second time, the uncertainties are combined to obtain the highest variation of C_p'.

The uncertainty ranges are determined from the potential measurement errors, the parameter analysis made by Bergh and Tijdeman (1965), and the DPMS transducer characterization performed by Rigo (2017). The subsequent sets of parameters that define the different FRF are listed in Tab. B.1. The measurement error on the tube length is assumed to be below $1\mathrm{cm}$. The set of parameters called LENGTH is thus determined by varying the nominal l_t by less than 1%. Bergh and Tijdeman (1965) reported that the measured d_t has often to be slightly reduced (around 5%) to obtain an accurate theoretical FRF. Therefore, the parameter set DIAMETER corresponds to a reduction of 5% of the documented internal diameter. The parameter set PRESSURE is associated with a variation of the atmospheric pressure. The latter was measured twice during the experimental session, which allows to assume that p_{atm} does not vary more than within $1\mathrm{kPa}$, i.e., 1% of its nominal value. The transducer volume is the most difficult physical parameter to determine. Rigo (2017) measured $V_s = 100\,\mathrm{mm}^3$, but had also to assume $V_s = 0\,\mathrm{mm}^3$ to obtain a theoretical FRF modeling accurately the pneumatic line. Therefore, for the parameter set VOLUME, the upper limit of V_s is supposed to be $150\,\mathrm{mm}^3$, which corresponds to an increase of 50% compared to the measurement performed by Rigo (2017).

The Bode plots of the theoretical FRF computed with the sets of parameters reported in Tab. B.1 are depicted in Fig. B.1. It shows that the uncertainties associated with the tube diameter and the transducer volume significantly impact the FRF. In particular, its amplitude is modified by a reduction of d_t and an increase of V_s, the latter modifying also slightly the peak distortion location in the frequency spectrum. Conversely, the uncertainties on the tube length and the atmospheric pressure do not have significant effect. Finally, the FRF phase is only modified by a variation of volume.

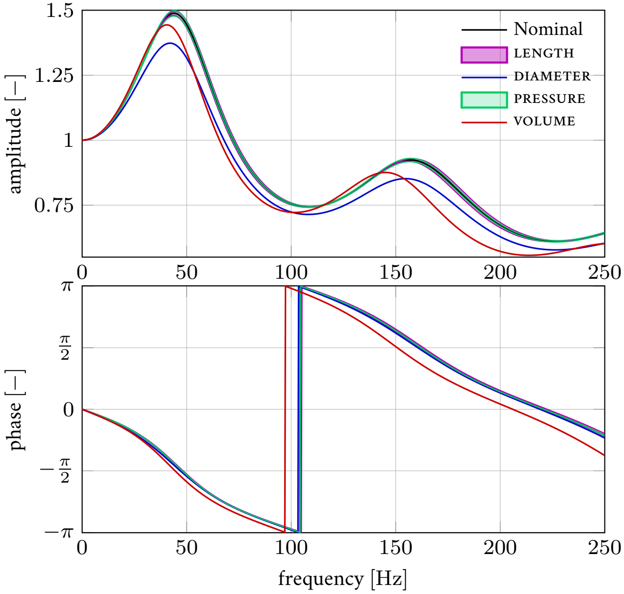

Figure B.1: Bode plots of the theoretical FRF associated with the parameter sets in Tab. B.1.

As discussed in Sec. 3.2.2.3, the peaks of distortion caused by the pneumatic line are located in the frequency range of the studied phenomena. Therefore, the FRF variations impact the corrected C_p. This is illustrated in Fig. B.2 that shows the C_p' distribution obtained after correction with the different FRF depicted in B.1. In particular, Figs. B.2a and B.2b confirm that C_p is only impacted by uncertainties on V_s and d_t. Both an increase of the transducer volume and a decrease of the tube diameter lead to an increase of C_p', with respect to the nominal case. This is consistent with the increase in the FRF amplitude depicted in Fig. B.1. To have an idea of the maximum variation of C_p', the boundary values of the parameter ranges are combined to obtained the largest increase/decrease of C_p'. The subsequent sets of parameters are called MIXED A and MIXED B, respectively, and they are reported in Tab. B.1. The standard deviation of the corrected C_p obtained from these two sets are depicted in Figs. B.2c and B.2d. It appears that the most critical combination of uncertainties (MIXED A) leads to an increase of maximum 20% of C_p'. However, this increase does not take place similarly all along the rectangle surface. In particular, Fig. B.2c shows that the uncertainties have no impact on C_p' at $\overline{r} \approx 0.55$, the frequency spectrum of C_p at this location being probably not in the frequency range of large signal distortions. Finally, the global shape of C_p', i.e., the location of minimum and maximum, is not modified.

In conclusion, this sensitivity analysis shows that the nominal physical parameters used in Chap. 3 could lead to an underestimation of the temporal variation of C_p around $\overline{C_p}$. Under the worst scenario, this underestimation could be of the order of 20%. However, since the global shape of C_p' is conserved, it can be assumed that the overall dynamics of C_p is correctly captured. Moreover, many of the studies reported in Chap. 3 are based on the distribution of $\overline{C_p}$ which is not impacted by the pneumatic line. Therefore, it can be concluded that the conclusions drawn in Chap. 3 are robust to uncertainties.

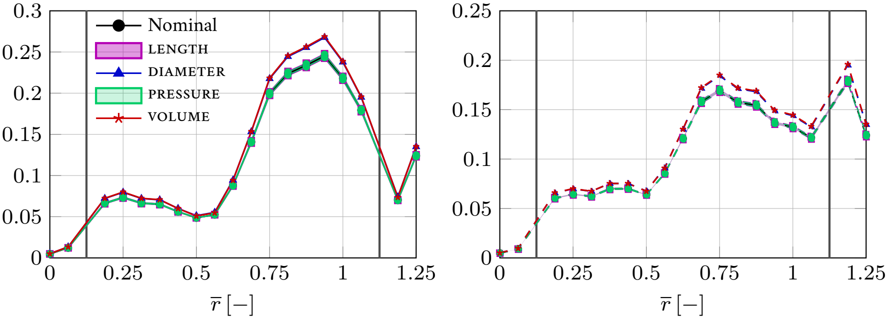

(a) C_p' along upper side. (b) C_p' along lower side.

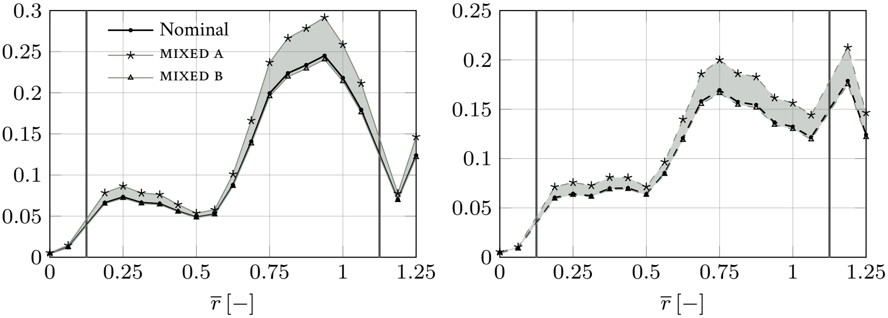

(c) C_p' along upper side. (d) C_p' along lower side.

Figure B.2: Sensitivity to the theoretical FRF parameters of the standard deviation of C_p along the rectangle surface obtained experimentally at $\alpha = 2^\circ$ and $\mathrm{Re} = 4.2 \times 10^4$. Each parameters are considered separately (Figs. (a) and (b)) and together (Fig. (c) and Fig. (d)) The vertical gray lines represent the leading and trailing edges and the coordinate $\overline{r}$ is defined in Fig. 3.4.

APPENDIX C

Detached flow around a flat plate

C.1 Kinematic description

The one associated with the small amplitude pitching case consists of three different parts. The plate incidence is first linearly increased to achieve the main angle of attack $\overline{\alpha}$, i.e. 30° or 45°. Then, the desired small amplitude sinusoidal motion is imposed an repeated 117 times. Finally, the plate goes back linearly to zero incidence. For the static case, the kinematic is the same that the one described above, except that no motion is imposed. Therefore, the plate holds its position during approximately 117 shedding periods. The large pitching amplitude kinematic consists of 14 sinusoidal motions of 30° amplitude around a mean incidence of 0°. For implementation reasons, it begins and finishes by a linear motion from 0° to 30° or -30°, respectively, followed by a return to zero incidence.

C.2 Kinematic files

This section provides some examples of input files required by COSMOS software. They impose to the rotary stage the three motions describe in Sec. C.1, i.e., the kinematics corresponding to the large and small amplitudes pitching plate and the static plate. In the following files, the most used commands are `SmMx` and `ImMy`, which imposes at motor `m` a speed of `x` step/s and a number of steps `y` to cover. Detailed information about the Velmex language can be found in the VXM Stepping Motor Controller User's Manual (Velmex INC, 2004).

C.2.1 Kinematic corresponding to the large amplitude pitching plate

```
E,
;Program 1
;----------
PM-1,
S1M3268, I1M151,
S1M3247, I1M150,
S1M3225, I1M149,
S1M3182, I1M147,
S1M3139, I1M145,
S1M3074, I1M142,
S1M2987, I1M138,
S1M2900, I1M134,
S1M2814, I1M130,
```

```
S1M2706, I1M125,
S1M2576, I1M119,
S1M2446, I1M113,
S1M2316, I1M107,
S1M2165, I1M100,
S1M1991, I1M92,
S1M1840, I1M85,
S1M1667, I1M77,
S1M1472, I1M68,
S1M1299, I1M60,
S1M1104, I1M51,
S1M909, I1M42,
S1M714, I1M33,
S1M519, I1M24,
S1M303, I1M14,
S1M108, I1M5,
S1M108, I1M-5,
S1M303, I1M-14,
S1M519, I1M-24,
S1M714, I1M-33,
S1M909, I1M-42,
S1M1104, I1M-51,
S1M1299, I1M-60,
S1M1472, I1M-68,
S1M1667, I1M-77,
S1M1840, I1M-85,
J2,
;
;Program 2
;----------
PM-2,
S1M1991, I1M-92,
S1M2165, I1M-100,
S1M2316, I1M-107,
S1M2446, I1M-113,
S1M2576, I1M-119,
S1M2706, I1M-125,
S1M2814, I1M-130,
S1M2900, I1M-134,
S1M2987, I1M-138,
S1M3074, I1M-142,
S1M3139, I1M-145,
S1M3182, I1M-147,
S1M3225, I1M-149,
S1M3247, I1M-150,
S1M3268, I1M-151,
U5,                         ;sync point at 0.49992*2PI => output 1 high
S1M3268, I1M-151,
U4,                         ;sync point => output 1 low
S1M3247, I1M-150,
S1M3225, I1M-149,
S1M3182, I1M-147,
```

```
S1M3139, I1M-145,
S1M3074, I1M-142,
S1M2987, I1M-138,
S1M2900, I1M-134,
S1M2814, I1M-130,
S1M2706, I1M-125,
S1M2576, I1M-119,
S1M2446, I1M-113,
S1M2316, I1M-107,
S1M2165, I1M-100,
S1M1991, I1M-92,
S1M1840, I1M-85,
S1M1667, I1M-77,
S1M1472, I1M-68,
S1M1299, I1M-60,
S1M1104, I1M-51,
J3,
;
;Program 3
;----------
PM-3,
S1M909, I1M-42,
S1M714, I1M-33,
S1M519, I1M-24,
S1M303, I1M-14,
S1M108, I1M-5,
S1M108, I1M5,
S1M303, I1M14,
S1M519, I1M24,
S1M714, I1M33,
S1M909, I1M42,
S1M1104, I1M51,
S1M1299, I1M60,
S1M1472, I1M68,
S1M1667, I1M77,
S1M1840, I1M85,
S1M1991, I1M92,
S1M2165, I1M100,
S1M2316, I1M107,
S1M2446, I1M113,
S1M2576, I1M119,
S1M2706, I1M125,
S1M2814, I1M130,
S1M2900, I1M134,
S1M2987, I1M138,
S1M3074, I1M142,
S1M3139, I1M145,
S1M3182, I1M147,
S1M3225, I1M149,
S1M3247, I1M150,
S1M3268, I1M151,
;
```

```
;MAIN PROGRAM in 0
;-----------------
PM-0,
;
;Delay for bias
;--------------
P150,
;
;First motion form 0deg to 30deg then return to in 6s
;-----------------------------------------------------
A1M2,
U5,                         ;beginning of starting motion => output 1 high
S1M800,
I1M-2400,
I1M2400,
U4,                         ;end of starting motion => output 1 low
;
;Kinematic: multiple sines
;-------------------------
A1M127,
U7, setPA200,
LM0,
JM1,
L21,
U92,
;
;Last motion form 0deg to -30deg then return to in 6s
;-----------------------------------------------------
A1M2,
U5,                         ;beginning of last motion => output 1 high
S1M800,
I1M2400,
I1M-2400,
U4,                         ;end of last motion => output 1 low
;
;Delay for bias
;--------------
P150,
```

C.2.2 Kinematic corresponding to the small amplitude pitching plate

```
E,
;Program 1
;----------
PM-1,
S1M421, I1M10,
S1M379, I1M9,
S1M379, I1M9,
S1M337, I1M8,
S1M295, I1M7,
S1M253, I1M6,
S1M211, I1M5,
S1M168, I1M4,
```

```
S1M84, I1M2,
S1M42, I1M1,
S1M42, I1M-1,
S1M84, I1M-2,
S1M168, I1M-4,
S1M211, I1M-5,
S1M253, I1M-6,
S1M295, I1M-7,
S1M337, I1M-8,
S1M379, I1M-9,
S1M379, I1M-9,
S1M421, I1M-10,
U5,                        ;sync point at 0.5*2PI => output 1 high
S1M421, I1M-10,
U4,                        ;sync point => output 1 low
S1M379, I1M-9,
S1M379, I1M-9,
S1M337, I1M-8,
S1M295, I1M-7,
S1M253, I1M-6,
S1M211, I1M-5,
S1M168, I1M-4,
S1M84, I1M-2,
S1M42, I1M-1,
S1M42, I1M1,
S1M84, I1M2,
S1M168, I1M4,
S1M211, I1M5,
S1M253, I1M6,
J2,
;
;Program 2
;----------
PM-2,
S1M295, I1M7,
S1M337, I1M8,
S1M379, I1M9,
S1M379, I1M9,
S1M421, I1M10,
;
;MAIN PROGRAM in 0
;-----------------
PM-0,
;
;Delay for bias
;--------------
P150,
;
;First motion form 0deg to 30deg in 3s
;-------------------------------------
A1M2,
U5,                        ;beginning of starting motion => output 1 high
```

```
S1M800,
I1M-2400,
U4,                        ;end of starting motion => output 1 low
;
;Kinematic: multiple sines
;------------------------
A1M127,
U7, setPA200,
LM0,
JM1,
L117,
U92,
;
;Final motion form 30deg to 0deg in 3s
;-------------------------------------
A1M2,
U5,                        ;beginning of final motion => output 1 high
S1M800,
I1M2400,
U4,                        ;end of final motion => output 1 low
;
;Delay for bias
;-------------
P150,
```

C.2.3 Kinematic corresponding to the static plate

```
E,
;MAIN PROGRAM in 0
;----------------
PM-0,
;
;Delay for bias
;-------------
P150,
;
;First motion form 0deg to 30deg in 3s
;------------------------------------
A1M2,
U5,                        ;beginning of starting motion => output 1 high
S1M800,
I1M-2400,
U4,                        ;end of starting motion => output 1 low
;
;Delay for acquisition
;--------------------
P1100,
;
;Final motion from 30deg to 0deg in 3s
;------------------------------------
A1M2,
U5,                        ;beginning of final motion => output 1 high
S1M800,
```

```
I1M2400,
U4,                        ;end of final motion => output 1 low
;
;Delay for bias
;--------------
P150,
```

C.3 Synchronization of the plate kinematics on the PIV sampling

To phase-average the PIV velocity fields, several pairs of images have to be acquired at the same phase of the motion. To this end, the nominal laser pulsing frequency f_{l_0} has to be adjusted to obtain a sampling frequency f_s as close as possible to the kinematic frequency f_k. Moreover, the camera shutter has to be opened at a specific phase of the motion.

The first condition is enforced by skipping some laser pulses, i.e. artificially reducing the laser frequency. The frequency divider N_{f_l} is determined by rounding the ratio of the laser nominal frequency f_{l_0} to the kinematic frequency f_k. The sampling frequency f_s is then $^1/_{f_s} = {}^{N_{f_l}}/_{f_k}$ which has to be lower than the maximal sampling frequency f_s^{max}. If it is not, the frequency divider has to be increased as kN_{f_l} until the criterion is achieved, k being an integer. Finally, since the frequency divider is an integer, the obtained frequency is not exactly the same as the kinematic frequency. Therefore, after a certain number of cycles, the sampled phase differs from the desired one. As it varies with f_k, this drift has to be quantified for each kinematics.

The second condition is enforced by delaying the kinematics with respect to the laser pulses. The delay is determined by synchronizing two signals as illustrated in Fig. C.1. The first one comes from the camera shutter. The rising edge corresponds to the camera shutter opening, i.e., when the first laser pulse occurs and the first of the images pair is acquired. The falling edge of the camera signal appears after the sampling of the first image but before the sampling the second one. The period of this signal is the sampling period $T_s = {}^1/_{f_s}$. The second signal is sent by the stepper motor. As explained in Sec. 4.2.2, its rising edge corresponds to a chosen phase of the kinematics which has period $T_k = {}^1/_{f_k}$. To determine the delay of the kinematics Δ_k, the falling edge of the camera signal has to be aligned with the rising edge of the kinematics. This is illustrated by the vertical gray lines in Fig. C.1.

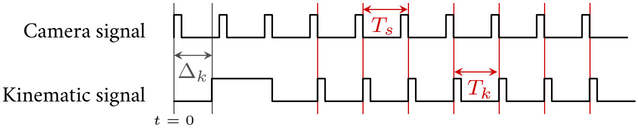

Figure C.1: Schematic view of the determination of Δ_k, the delay in kinematics required to obtain PIV images at a specific phase in the motion.

Bibliography

Adrian RJ, Yao CS (1984) Development of pulsed laser velocimetry for measurement of turbulent flow. In: Reed X, Patterson G, Zakin J (eds) Proceedings of the Eighth Symposium on Turbulence, Univ of Missouri-Rolla,Rolla, MO, USA, pp 170–186

Albrecht T, del Campo V, Weier T, Gerbeth G (2012) Comparison of PIV-based methods for airfoil loads evaluation. In: 16th International Symposium on Applications of Laser Techniques to Fluid Mechanics, Lisbon, Portugal, July, vol 9, p 12

Albrecht T, del Campo V, Weier T, Metzkes H, Stiller J (2013) Deriving forces from 2D velocity field measurements. The European Physical Journal Special Topics 220(1):91–100

Anderson JDJ (1999) A History of Aerodynamics And Its Impact on Flying Machines. Cambridge University Press

Anderson JDJ (2010) Fundamentals of Aerodynamics. McGraw-Hill Education

Andrianne T (2012) Experimental and numerical investigations of the aeroelastic stability of bluff structures. PhD thesis, University of Liege

Anthoine J, Arts T, Boerrigter HL, Buchlin JM, Carbonano M, Degrez G, Dénos R, Fletcher D, Olivari D, Riethmuller M, Van den Braembussche R (2009) Measurement Techniques in Fluid Dynamics – An Introduction. VKI LS

Arslan T, Pettersen B, Andersson HI (2011) Calculations of the flow around rectangular shaped floating structures. In: Proceedings of the 13th International Conference on Wind Engineering (ICWE)

Baik YS (2011) Unsteady force generation and vortex dynamics of pitching and plunging airfoils at low reynolds number. PhD thesis, University of Michigan

Baik YS, Bernal LP, Granlund K, Ol MV (2012) Unsteady force generation and vortex dynamics of pitching and plunging aerofoils. Journal of Fluid Mechanics 709:37–68

Baldwin BS, Barth TJ (1990) A one-equation turbulence transport model for high reynolds number wall-bounded flows. TM 102847, NASA

Barlow JB, Rae WH, Pope A (1999) Low-Speed Wind Tunnel Testing. John Wiley

Bartoli G, Bruno L, Buresti G, Ricciardelli F, Salvetti M, Zasso A (2008) BARC overview document

Bergh H, Tijdeman H (1965) Theoretical and experimental results for the dynamic response of pressure measuring systems. Tech. rep., Nationaal Lucht-en Ruimtevaartlaboratorium

Billah KY, Scanlan RH (1991) Resonance, Tacoma Narrows bridge failure, and undergraduate physics textbooks. American Journal of Physics 59(2):118–124

Blocken B, Persoon J (2009) Pedestrian wind comfort around a large football stadium in an urban environment: CFD simulation, validation and application of the new Dutch wind nuisance standard. Journal of Wind Engineering and Industrial Aerodynamics 97(5–6):255–270

Bomphrey RJ, Taylor GK, Thomas ALR (2009) Smoke visualization of free-flying bumblebees indicates independent leading-edge vortices on each wing pair. Experiments in Fluids 46(5):811–821

Boussinesq J (1877) Essai sur la théorie des eaux courantes. Imprimerie nationale, Paris

Bradshaw P (1973) Effects of streamline curvature on turbulent flow. Tech. Rep. AGARD-169, NATO, AGARD

Bradshaw P (1987) Turbulent secondary flows. Annual review of fluid mechanics 19(1):53–74

Breuer M, Jovičić N (2001) Separated flow around a flat plate at high incidence: an LES investigation. Journal of Turbulence 2:N18

Breuer M, Jovičić N, Mazaev K (2003) Comparison of DES, RANS and LES for the separated flow around a flat plate at high incidence. International Journal for Numerical Methods in Fluids 41(4):357–388

Bruno L, Fransos D, Coste N, Bosco A (2010) 3D flow around a rectangular cylinder: A computational study. Journal of Wind Engineering and Industrial Aerodynamics 98(6-7):263–276

Bruno L, Salvetti MV, Ricciardelli F (2014) Benchmark on the aerodynamics of a rectangular 5:1 cylinder: An overview after the first four years of activity. Journal of Wind Engineering and Industrial Aerodynamics 126:87–106

Casey M, Wintergerste T (2000) Special interest group on "Quality and trust in industrial CFD": Best practice guidelines, version 1. European Research Community on Flow, Turbulence and Combustion

Chan J, Havard D, Rawlins C, Diana G, Cloutier L, Lilien JL, Hardy C, Wang J, Goel A (2009) EPRI Transmission Line Reference Book: wind-induced Conductor Motion. EPRI

Chen KK, Tu JH, Rowley CW (2012) Variants of dynamic mode decomposition: Boundary condition, Koopman, and Fourier analyses. Journal of Nonlinear Science 22(6):887–915

Chien KY (1982) Predictions of channel and boundary-layer flows with a low-Reynolds-number turbulence model. AIAA Journal 20(1):33–38

Da Silva A (2015) The pont de Normandie

Dabiri JO, Bose S, Gemmell BJ, Colin SP, Costello JH (2014) An algorithm to estimate unsteady and quasi-steady pressure fields from velocity field measurements. Journal of Experimental Biology pp jeb–092,767

David L, Jardin T, Farcy A (2009) On the non-intrusive evaluation of fluid forces with the momentum equation approach. Measurement Science and Technology 20(9):095,401

Dudderar TD, Simpkins PG (1977) Laser speckle photography in a fluid medium. Nature 270:45–47

Durbin PA, Pettersson Reif BA (2011) Statistical theory and modeling for turbulent flows. John Wiley & Sons

Edwards BF, Smith DH (2002) River meandering dynamics. Phys Rev E 65:046,303

Fage A, Johansen FC (1927) On the flow of air behind an inclined flat plate of infinite span. Proceedings of the Royal Society of London Series A 116:170–197

Feeny BF, Kappagantu R (1998) On the physical interpretation of proper orthogonal modes in vibrations. Journal of sound and vibration 211(4):607–616

Ferziger JH, Perić M (1996) Computational methods for fluid dynamics. Springer Science & Business Media

Gardner AD, Klein C, Sachs WE, Henne U, Mai H, Richter K (2014) Investigation of three-dimensional dynamic stall on an airfoil using fast-response pressure-sensitive paint. Experiments in Fluids 55(9):1807

van Gent PL, Michaelis D, van Oudheusden BW, Weiss PE, de Kat R, Laskari A, Jeon YJ, David L, Schanz D, Huhn F, Gesemann S, Novara M, McPhaden C, Neeteson NJ, Rival DE, Schneiders JFG, Schrijer FFJ (2017) Comparative assessment of pressure field reconstructions from particle image velocimetry measurements and Lagrangian particle tracking. Experiments in Fluids 58(4):33

Geuzaine C, Remacle JF (2009) Gmsh: A 3-D finite element mesh generator with built-in pre- and post-processing facilities. International Journal for Numerical Methods in Engineering 79(11):1309–1331

Gharali K, Johnson DA (2014) PIV-based load investigation in dynamic stall for different reduced frequencies. Experiments in Fluids 55(8):1803

Goulart PJ, Wynn A, Pearson D (2012) Optimal mode decomposition for high dimensional systems. In: 2012 IEEE 51st IEEE Conference on Decision and Control (CDC), pp 4965–4970

Graftieaux L, Michard M, Grosjean N (2001) Combining PIV, POD and vortex identification algorithms for the study of unsteady turbulent swirling flows. Measurement Science and Technology 12(9):1422

Granlund KO, Ol MV, Bernal LP (2013) Unsteady pitching flat plates. Journal of Fluid Mechanics 733

Grilli M, Schmid PJ, Hickel S, Adams NA (2012) Analysis of unsteady behaviour in shockwave turbulent boundary layer interaction. Journal of Fluid Mechanics 700:16–28

Güner H (2015) Delayed detached-eddy simulations for separated flows. Master's thesis, Université de Liège

Gurka R, Liberzon A, Hefetz D, Rubinstein D, Shavit U (1999) Computation of pressure distribution using PIV velocity data. In: Workshop on particle image velocimetry, vol 2

Hannachi A, Jolliffe IT, Stephenson DB (2007) Empirical orthogonal functions and related techniques in atmospheric science: A review. International Journal of Climatology 27(9):1119–1152

Hirsch C (2007) Numerical computation of internal and external flows: The fundamentals of computational fluid dynamics. Butterworth-Heinemann

Holmström I (1963) On a method for parametric representation of the state of the atmosphere. Tellus 15(2):127–149

Huang S, Li QS, Xu S (2007) Numerical evaluation of wind effects on a tall steel building by CFD. Journal of Constructional Steel Research 63(5):612–627

Irwin PA (2008) Bluff body aerodynamics in wind engineering. Journal of Wind Engineering and Industrial Aerodynamics 96(6–7):701–712

Irwin PA (2010) Vortices and tall buildings: A recipe for resonance. Physics today 63(9):68–69

Johnson FT, Tinoco EN, Yu NJ (2005) Thirty years of development and application of CFD at Boeing Commercial Airplanes, Seattle. Computers & Fluids 34(10):1115–1151

Jones BM (1936) The measurement of profile drag by the pitot-traverse method. HM Stationery Office

Karhunen K (1946) Zur Spektraltheorie stochastischer Prozesse. Ann Acad Sci Finnicae, Ser A 1:34

Kirby M, Sirovich L (1990) Application of the Karhunen-Loeve procedure for the characterization of human faces. IEEE Transactions on Pattern Analysis and Machine Intelligence 12(1):103–108

Kolmogorov A (1941) The local structure of turbulence in incompressible viscous fluid for very large Reynolds numbers (in russian). Dokl Akad Nauk SSSR 30:299–303

Kosambi DD (1943) Statistics in function space. J Indian Math Soc 7(1):76–88

Kurtulus DF, Scarano F, David L (2007) Unsteady aerodynamic forces estimation on a square cylinder by TR-PIV. Experiments in Fluids 42(2):185–196

Lam KM, Leung MYH (2005) Asymmetric vortex shedding flow past an inclined flat plate at high incidence. European Journal of Mechanics - B/Fluids 24(1):33–48

Lam KM, Wei CT (2010) Numerical simulation of vortex shedding from an inclined flat plate. Engineering Applications of Computational Fluid Mechanics 4(4):569–579

Laskari A, de Kat Rd, Ganapathisubramani B (2016) Full-field pressure from snapshot and time-resolved volumetric PIV. Experiments in Fluids 57(3):44

Leitl BM, Meroney RN (1997) Car exhaust dispersion in a street canyon. Numerical critique of a wind tunnel experiment. Journal of Wind Engineering and Industrial Aerodynamics 67:293–304

Li Y, Tang H, Lin Q, Chen X (2017) Vortex-induced vibration of suspenders in the wake of bridge tower by numerical simulation and wind tunnel test. Journal of Wind Engineering and Industrial Aerodynamics 164:164–173

Liang YC, P LH, Lim SP, Lin WZ, Lee KH, Wu CG (2002) Proper orthogonal decomposition and its applications–Part I: Theory. Journal of Sound and Vibration 252(3):527–544

Lin JC, Rockwell D (1996) Force identification by vorticity fields: techniques based on flow imaging. Journal of Fluids and Structures 10(6):663–668

Loeve M (1945) Fonctions aléatoires du second ordre. Comptes Rend Acad Sci (Paris) 220

Löhner R, Haug E, Michalski A, Muhammad B, Drego A, Nanjundaiah R, Zarfam R (2015) Recent advances in computational wind engineering and fluid-structure interaction. Journal of Wind Engineering and Industrial Aerodynamics 144:14–23

Lumley JL (1967) The structure of inhomogeneous turbulent flows. In: Turbulence and Radio Wave Propagation, A. M. Yaglom and V. I. Tatarsky, Nauka, Moscow, USSR, pp 166–176

Lumley JL (1970) Stochastic Tools in Turbulence. Academic Press, New York and London

Mannini C, Šoda A, Schewe G (2010) Unsteady RANS modelling of flow past a rectangular cylinder: Investigation of Reynolds number effects. Computers & Fluids 39(9):1609–1624

Mannini C, Šoda A, Schewe G (2011) Numerical investigation on the three-dimensional unsteady flow past a 5:1 rectangular cylinder. Journal of Wind Engineering and Industrial Aerodynamics 99(4):469–482

Massa L, Kumar R, Ravindran P (2012) Dynamic mode decomposition analysis of detonation waves. Physics of Fluids 24(6):066,101

Matsumoto M, Shirato H, Araki K, Haramura T, Hashimoto T (2003) Spanwise coherence characteristics of surface pressure field on 2-D bluff bodies. Journal of Wind Engineering and Industrial Aerodynamics 91(1–2):155–163

McCroskey WJ (1981) The phenomenon of dynamic stall. Tech. rep., NASA and US Army Research and Technology Laboratories

McLachlan BG, Bell JH (1995) Pressure-sensitive paint in aerodynamic testing. Experimental Thermal and Fluid Science 10(4):470–485

Mellen C, Rodi W, Froelich J (2002) Lessons from the European LESFOIL project on LES of flow around an airfoil. In: 40th AIAA Aerospace Sciences Meeting & Exhibit, American Institute of Aeronautics and Astronautics

Melling A, Whitelaw JH (1976) Turbulent flow in a rectangular duct. Journal of Fluid Mechanics 78(2):289–315

Menter F (1993) Zonal two equation k-ω turbulence models for aerodynamic flows. In: 24th Fluid Dynamics Conference, American Institute of Aeronautics and Astronautics

Menter F, Esch T (2001) Elements of industrial heat transfer predictions. In: 16th Brazilian Congress of Mechanical Engineering (COBEM), pp 26–30

Menter FR (1992) Influence of freestream values on k-ω turbulence model predictions. AIAA journal 30(6):1657–1659

Menter FR (1994) Two-equation eddy-viscosity turbulence models for engineering applications. AIAA journal 32(8):1598–1605

Menter FR, Kuntz M (2004) Adaptation of eddy-viscosity turbulence models to unsteady separated flow behind vehicles. In: The aerodynamics of heavy vehicles: trucks, buses, and trains, Springer, pp 339–352

Menter FR, Kuntz M, Langtry R (2003) Ten years of industrial experience with the SST turbulence model. Turbulence, heat and mass transfer 4(1):625–632

Messaris GA, Hadjinicolaou M, Karahalios GT (2016) Unsteady fluid flow in a slightly curved pipe: A comparative study of a matched asymptotic expansions solution with a single analytical solution. Physics of Fluids 28(8):081,901

Meynart R (1983) Mesure de champs de vitesse d' écoulements fluides par analyse de suites d'images obtenues par diffusion d'un feuillet lumineux,. PhD thesis, Université Libre de Bruxelles

Mizota A T & Okajima (1981) Experimental studies of unsteady flows around rectangular prisms. In: Proceedings of the Japan Society of Civil Engineers, 312, pp 49–57

Molon A (2014) Burj khalifa

Moran J (2003) An Introduction to Theoretical and Computational Aerodynamics. Dover Publications, Inc

Muld TW, Efraimsson G, Henningson DS (2012) Flow structures around a high-speed train extracted using Proper Orthogonal Decomposition and Dynamic Mode Decomposition. Computers & Fluids 57:87–97

Nakaguchi H, Hashimoto K, Muto S (1968) An experimental study on aerodynamic drag of rectangular cylinders. The Journal of the Japan Society of Aeronautical Engineering 16(168):1–5

Nakamura Y, Mizota T (1975) Torsional flutter of rectangular prisms. Journal of Engineering Mechanics 101(EH2)

Nimmervoll D (2013) Burn out

Noca F (1997) On the evaluation of time-dependent fluid-dynamic forces on bluff bodies. PhD thesis, California Institute of Technology

Noca F, Shiels D, Jeon D (1997) Measuring instantaneous fluid dynamic forces on bodies, using only velocity fields and their derivatives. Journal of Fluids and Structures 11(3):345–350

Noca F, Shiels D, Jeon D (1999) A comparison of methods for evaluating time-dependent fluid dynamic forces on bodies, using only velocity fields and their derivatives. Journal of Fluids and Structures 13(5):551–578

Obukhov A (1960) On statistically orthogonal decompositions of empirical functions. Izv Akad Nauk SSSR Ser Geophys 3:432–439

Okajima A (1983) Flow around a rectangular cylinder with a section of various width/height ratios.

Wind Engineers, JAWE 1983(17):1–19

Otsuki Y, Washizu K, Tomizawa H, Ohya A (1974) A note on the aeroelastic instability of a prismatic bar with square section. Journal of Sound and Vibration 34(2):233–248

van Oudheusden BW (2013) PIV-based pressure measurement. Measurement Science and Technology 24(3):032,001

van Oudheusden BW, Scarano F, Casimiri EWF (2006) Non-intrusive load characterization of an airfoil using PIV. Experiments in Fluids 40(6):988–992

van Oudheusden BW, Scarano F, Roosenboom EW, Casimiri EW, Souverein LJ (2007) Evaluation of integral forces and pressure fields from planar velocimetry data for incompressible and compressible flows. Experiments in Fluids 43(2-3):153–162

Païdoussis MP, Price SJ, de Langre E (2014) Fluid-Structure Interactions: Cross-Flow-Induced Instabilities. Cambridge University Press

Patel VC, Sotiropoulos F (1997) Longitudinal curvature effects in turbulent boundary layers. Progress in Aerospace Sciences 33(1):1–70

Patruno L (2015) Accuracy of numerically evaluated flutter derivatives of bridge deck sections using RANS: Effects on the flutter onset velocity. Engineering Structures 89:49–65

Patruno L, Ricci M, de Miranda S, Ubertini F (2016) Numerical simulation of a 5:1 rectangular cylinder at non-null angles of attack. Journal of Wind Engineering and Industrial Aerodynamics 151:146–157

Pope SB (2000) Turbulent flows. IOP Publishing

Prandtl L (1905) Über flüssigkeitsbewegung bei sehr kleiner reibung. In: Krazer A (ed) Verhandlungen des dritten internationalen Mathematiker-Kongresses in Heidelberg vom 8. bis 13. August 1904, BG Teubner

Prasad AK (2000) Stereoscopic particle image velocimetry. Experiments in Fluids 29(2):103–116

Pugachev V (1953) The general theory of correlation of random functions. Izv Akad Nauk SSSR Ser Mat 15(5):401–420

Pullin DI, Perry AE (1980) Some flow visualization experiments on the starting vortex. Journal of Fluid Mechanics 97(2):239–255

Raffel M, Willert CE, Kompenhans J, et al. (2013) Particle image velocimetry: a practical guide. Springer

Reckzeh D (2003) Aerodynamic design of the high-lift-wing for a Megaliner aircraft. Aerospace Science and Technology 7(2):107–119

Reynolds O (1895) On the dynamical theory of incompressible viscous fluids and the determination of the criterion. Philosophical Transactions of the Royal Society of London A: Mathematical, Physical and Engineering Sciences 186:123–164

Richardson LF (1922) Weather prediction by numerical process. Cambridge University Press

Rigo F (2017) Unsteady pressure measurement around aerodynamic bodies: Development of a calibration apparatus and wind tunnel testing. Master's thesis

Rival D, Prangemeier T, Tropea C (2009) The influence of airfoil kinematics on the formation of leading-edge vortices in bio-inspired flight. Experiments in Fluids 46(5):823–833

Rodi W, Scheuerer G (1986) Scrutinizing the k-ε turbulence model under adverse pressure gradient conditions. Journal of Fluids Engineering 108(2):174–179

Roukhovetz LV (1963) On the optimal treatment of vertical distributions of several meteorological quantities. Izv Akad Nauk SSSR Ser Geophys 4:626–636

Scarano F, Riethmuller ML (1999) Iterative multigrid approach in PIV image processing with discrete window offset. Experiments in Fluids 26(6):513–523

Schewe G (2013) Reynolds-number-effects in flow around a rectangular cylinder with aspect ratio 1:5. Journal of Fluids and Structures 39:15–26

Schmid PJ (2010) Dynamic mode decomposition of numerical and experimental data. Journal of Fluid Mechanics 656:5–28

Schneiders JFG, Pröbsting S, Dwight RP, van Oudheusden BW, Scarano F (2016) Pressure estimation from single-snapshot tomographic PIV in a turbulent boundary layer. Experiments in Fluids 57(4):53

Shimada K, Ishihara T (2002) Application of a modified $k - \varepsilon$ model to the prediction of aerodynamic characteristics of rectangular cross-section cylinders. Journal of fluids and structures 16(4):465–485

Smagorinsky J (1963) General circulation experiments with the primitive equations: I. the basic experiment*. Monthly weather review 91(3):99–164

Sohankar A, Norberg C, Davidson L (1999) Simulation of three-dimensional flow around a square cylinder at moderate Reynolds numbers. Physics of Fluids 11(2):288–306

Spalart PR (2000) Trends in turbulence treatments. In: Fluids 2000 Conference and Exhibit, American Institute of Aeronautics and Astronautics, Fluid Dynamics and Co-located Conferences

Spalart PR, Allmaras SR (1994) A one-equation turbulence model for aerodinamic flows. La Recherche Aerospatiale 1:5–21

Spalart PR, Rumsey CL (2007) Effective inflow conditions for turbulence models in aerodynamic calculations. AIAA journal 45(10):2544–2553

Spalart PR, Streett C (2001) Young-Person' s Guide to Detached-Eddy Simulation Grids. Tech. rep.

Spalart PR, Jou WH, Strelets M, Allmaras SR, others (1997) Comments on the feasibility of LES for wings, and on a hybrid RANS/LES approach. Advances in DNS/LES 1:4–8

Spalart PR, Deck S, Shur ML, Squires KD, Strelets MK, Travin A (2006) A new version of detached-eddy simulation, resistant to ambiguous grid densities. Theoretical and computational fluid dynamics 20(3):181–195

Stefanakis TS, Dias F, Dutykh D (2011) Local run-up amplification by resonant wave interactions. Phys Rev Lett 107:124,502

Sterenborg JJHM, Lindeboom RCJ, Simão Ferreira CJ, van Zuijlen AH, Bijl H (2014) Assessment of PIV-based unsteady load determination of an airfoil with actuated flap. Journal of Fluids and Structures 45:79–95

Stokes AN, Welsh MC (1986) Flow-resonant sound interaction in a duct containing a plate, II: Square leading edge. Journal of Sound and Vibration 104(1):55–73

Strouhal V (1878) Über eine besondere Art der Tonerregung. Annalen der Physik 241(10):216–251

Tamura T, Itoh Y, Kuwahara K (1993) Computational separated-reattaching flows around a rectangular cylinder. Journal of Wind Engineering and Industrial Aerodynamics 50:9–18

Tamura T, Miyagi T, Kitagishi T (1998) Numerical prediction of unsteady pressures on a square cylinder with various corner shapes. Journal of Wind Engineering and Industrial Aerodynamics 74-76:531–542

Tan BT, Thompson MC, Hourigan K (2005) Evaluating fluid forces on bluff bodies using partial velocity data. Journal of Fluids and Structures 20(1):5–24

Theodorsen T (1935) General theory of aerodynamic instability and the mechanism of flutter.

Tech. Rep. 496, NACA

Tropea C, Yarin AL, Foss JF (2007) Springer handbook of experimental fluid mechanics, vol 1. Springer Science & Business Media

Tu JH, Rowley CW, Luchtenburg DM, Brunton SL, Kutz JN (2014) On dynamic mode decomposition: Theory and applications. Journal of Computational Dynamics 1(2):391–421

Unal M, Lin JC, Rockwell D (1997) Force prediction by PIV imaging: a momentum-based approach. Journal of Fluids and Structures 11(8):965–971

University of Washington Libraries Special Collections Division (2017) Tacoma narrows bridge showing man running off roadway during collapse.

Vandenheede R, Bernal LP, Morrison CL, Humbert S (2012) Parameter space exploration of bio-inspired hover kinematics. In: 42nd AIAA Fluid Dynamics Conference and Exhibit, New Orleans, USA, 25-28 June 2012; AIAA 2012-3155, American Institute of Aeronautics and Astronautics (AIAA)

Velmex INC (2004) VXM Stepping Motor Controler - User' s Manual

Washizu K, Ohya A, Otsuki Y, Fujii K (1978) Aeroelastic instability of rectangular cylinders in a heaving mode. Journal of Sound and Vibration 59(2):195–210

Weber R, Visser BM, Boysan F (1990) Assessment of turbulence modeling for engineering prediction of swirling vortices in the near burner zone. International Journal of Heat and Fluid Flow 11(3):225–235

Weller HG, Tabor G, Jasak H, Fureby C (1998) A tensorial approach to computational continuum mechanics using object-oriented techniques. Computers in physics 12(6):620–631

Wilcox DC (1993) Turbulence modeling for CFD. DCW industries, Inc., La Canada, CA

Xu M, Sun G, Kim CJ (2014) Infinite lifetime of underwater superhydrophobic states. Phys Rev Lett 113:136,103

Yu D, Kareem A (1998) Parametric study of flow around rectangular prisms using LES. Journal of Wind Engineering and Industrial Aerodynamics 77-78:653–662

Yu HT (2014) Unsteady aerodynamics of pitching flat plate wings. PhD thesis, University of Michigan